A High Gain Tri-reflector Antenna Configuration for Beam Scanning

by

Paul Christian Werntz

Dissertation submitted to the Faculty of the
Virginia Polytechnic Institute and State University
in partial fulfillment of the requirements for the degree of
Doctor of Philosophy
in
Electrical Engineering

APPROVED:

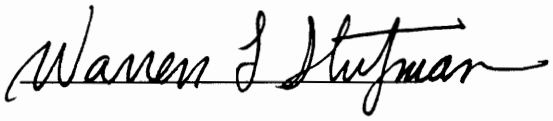

Dr. W. L. Stutzman, Chairman

Dr. G. S. Brown

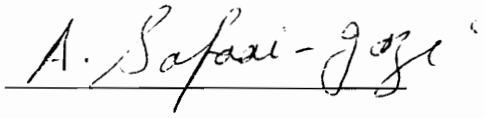

Dr. A. Safaai-Jazi

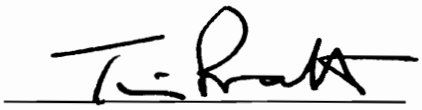

Dr. T. Pratt

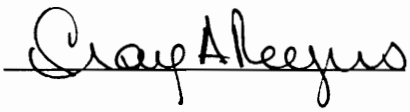

Dr. C. A. Rogers

April 1993
Blacksburg, Virginia

A High Gain Tri-reflector Antenna Configuration for Beam Scanning

by

Paul Christian Werntz

(Abstract)

High resolution earth observation from geostationary orbit offers several advantages compared to traditional low earth orbit systems. Among the advantages are decreased time to scan the visible geo-disk and the ability to stare at a particular event.

The following work is concerned with the design of a reflector antenna configuration for passive remote sensing and suitable for use on a geostationary platform; however, the resultant configuration is not limited to this application. The specific goal is the design of a reflector antenna configuration capable of precision beam scanning over a range of several degrees in all directions while minimizing vibration and inertial torque such as to have minimal effect on the other instruments sharing the platform. Desirable characteristics of such a reflector configuration are: a stationary feed consisting of a single element or a small array; simple reflector motions; and high primary aperture utilization for all scan directions (high illumination efficiency).

This dissertation documents the development of a novel tri-reflector antenna configuration which addresses the design goals outlined above. The reflector configuration has been named the conjugate tri-reflector. The conjugate tri-reflector consists of a parabolic primary reflector an elliptical secondary reflector and a shaped tertiary reflector. Beam scanning is performed entirely by motion of the relatively small tertiary reflector. The proposed reflector configuration offers substantial improvement in scan performance compared to that achieved by feed displacement with a prime focus parabolic reflector and has a much higher aperture efficiency than comparable spherical reflector configurations.

Acknowledgements

To begin, work on and complete a project of this magnitude requires inspiration and encouragement. I would like to thank my advisor Warren Stutzman for supplying these two necessary ingredients. I have had the privilege of working with Warren Stutzman since my first year in graduate school in 1986 and sincerely appreciate his endless support, advice and patience.

My committee members Timothy Pratt, Gary Brown, Ahmad Safaai-Jazi and Craig Rogers were charged with the torturous task of reading through an early version of this document, in addition to attending a 7:00 am oral defense, and responded by supplying many valuable suggestions and comments. I would, therefore, like to extend my deepest appreciation to these gentlemen for their valuable assistance.

I would like to express my gratitude to NASA Langley for funding this project and thank Thomas Campbell, M.C. Bailey and Cliff Schroeder for their support and assistance. Also, I would like to thank Peter Foldes for suggesting that we investigate the reflector configuration which became the topic of this dissertation.

Most of ones life is spent at work and I was privileged to spend this time with some very special people. Particularly Koichiro Takamizawa and Fatim Haidara with whom I have shared the small confines of 621 Whittemore for the last seven years. Also, Mike Barts, Jim LaPean and Bing Shen with whom I have had many valuable conversations. Special thanks go to Cynthia Marshall who has helped me in innumerous ways. Our trips to the copy room were often the highlight of my day.

Finally, I would like to thank my parents Carl and Margaret Werntz for their constant love, support and understanding.

Table of Contents

List of Figures

List of Tables

Chapter 1

Introduction

High gain antenna systems capable of producing narrow beamwidths are useful for applications pertaining to point to point communications and high resolution remote sensing. The use of a large aperture reflector offers the most economical method of obtaining the electrically large aperture dimensions necessary for high gain. In many, if not most, applications the reflector antenna configuration must be able to scan the main beam over a given region of space. In communications applications varying traffic demands dictate scan coverage and in remote sensing applications beam scanning is necessary in order to collect data over a given region.

The following work is concerned with the design of an antenna configuration for passive remote sensing and suitable for use on a geostationary platform; however, the resultant configuration is not limited to this application. The specific goal is the design of a reflector antenna configuration capable of precision beam scanning over a range of several degrees in all directions while minimizing vibration and inertial torque such as to have minimal effect on other instruments sharing the platform. Desirable characteristics of such a reflector configuration are: a stationary feed consisting of a single element or a small array; simple reflector motions; and high primary aperture utilization for all scan directions (high illumination efficiency). The motivation behind this set of design goals is discussed in Chapter 6.

This report documents the development of a novel tri-reflector configuration which addresses the design goals outlined above. The reflector

configuration has been named the conjugate tri-reflector for reasons discussed in Chapter 6. The conjugate tri-reflector consists of a parabolic primary reflector an elliptical secondary reflector and a shaped tertiary reflector. Beam scanning is performed entirely by tertiary reflector motion. The proposed reflector configuration offers substantial improvement in scan performance compared to that achieved by feed displacement with a prime focus parabolic reflector and has a much higher aperture efficiency than comparable spherical reflector configurations. For high gain applications a phased array feed can be used to compensate for scan induced phase errors.

Chapters 2 through 5 present useful background information including: fundamental concepts of reflector antenna operation; concepts necessary to the design of array feeds; and a detailed literature review of beam scanning reflector antenna configurations. In Chapter 6 the conjugate tri-reflector is presented, the operational principals are discussed and geometrical optics (G.O.) synthesis and analysis methods are developed. In Chapter 7 G.O. is used to compare several example tri-reflector configurations and to evaluate the effects of allowing different types of tertiary reflector motion. In Chapter 8 physical optics performance results are presented which verify the G.O. results. Conclusions and recommendations are presented in Chapter 9.

Chapter 2

Reflector Antenna Fundamentals

Convergent lenses and most types of reflector antennas are examples of focused aperture antennas. In this chapter fundamental principles of focused aperture antennas are presented and the relationships between the scalar field intensity at the focal plane, aperture plane and far-field are examined. Also presented are fundamental concepts of lens aberration theory which are useful for developing an appreciation of antenna performance.

2.1 Principles of Focused Aperture Antennas

Viewed in the transmitting mode a common property shared by all focused aperture antennas is the ability to convert a spherical wave diverging from a feed antenna located at the focal point to a plane wave propagating through the aperture along the axis of the antenna. In optics this process is often termed collimation, referring to the fact that geometrical optics rays, which are at all points perpendicular to the phase front, are parallel (columns) for a plane wave. The simplest focused reflector configuration is a single parabolic reflector. A cross-section of a parabolic reflector with focal length F is shown in Fig. 2.1-1. The surface of this reflector is given by

$$z = \frac{x^2 + y^2}{4F} \tag{2.1-1}$$

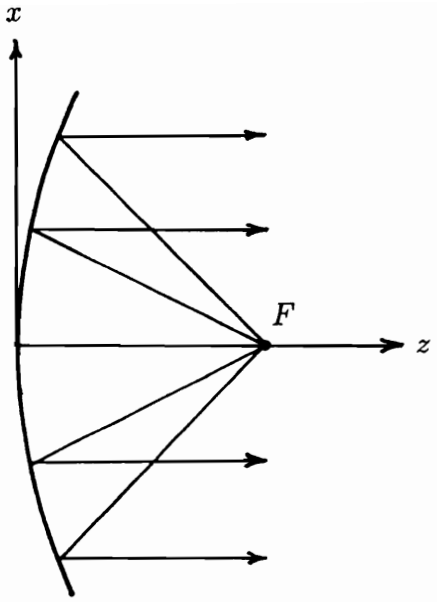

Figure 2.1-1. Cross-section of a parabolic reflector with focal point F showing collimation of transmit rays.

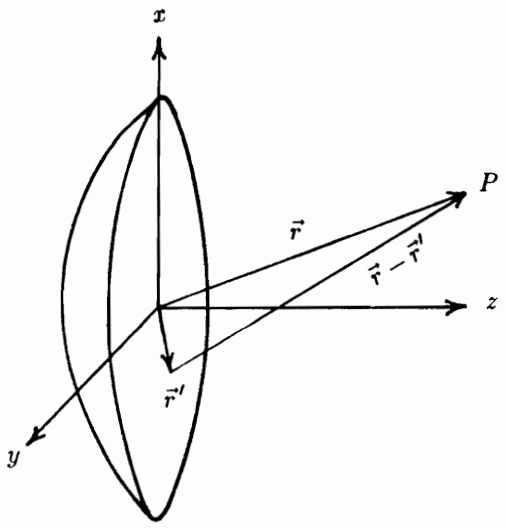

Figure 2.1-2. Diagram of the geometry used for (2.1-1). Vector $\vec{r}'$ is the position vector to points in the aperture plane which is located in the $z = 0$ plane and vector $\vec{r}$ is the position vector to the observation point P.

where the focal point, also denoted by F, is located on the z-axis. In Fig. 2.1-1 rays are shown for the parabolic reflector in the transmitting mode. In the receiving mode the process is reversed and incident parallel rays are focused to the point F.

An important property of focused aperture antennas is the approximate Fourier transform relationship between the aperture plane field distribution and both the far-field radiation pattern and the focal plane field distribution. This property can be easily shown. Using Huygen's principle a scalar solution $\psi(\vec{r})$ can be obtained for the radiated field at observation point P located a vector distance $\vec{r}$ away from the coordinate origin O as a result of a monochromatic disturbance across an aperture plane described by the source function $\psi'(\vec{r}')$ (here $\vec{r}'$ is the position vector from the coordinate origin to the aperture plane). This geometry is shown in Fig. 2.1-2. The radiated field is given by [2]

$$\begin{aligned}\psi(\vec{r}) &= \int_{aperture} \psi'(\vec{r}')\ A(\vec{r},\vec{r}')\ \mathrm{G}(\vec{r},\vec{r}')\ d\vec{r}' \\ &= \int_{aperture} \psi'(\vec{r}')\ A(\vec{r},\vec{r}')\ \frac{e^{-jk|\vec{r}-\vec{r}'|}}{|\vec{r}-\vec{r}'|}\ d\vec{r}',\end{aligned} \tag{2.1-2}$$

where the integral is performed over the aperture plane and in general the source term $\psi'(\vec{r}')$ is complex. In terms of linear system theory $\mathrm{G}(\vec{r},\vec{r}')$ represents the system impulse response or scalar Green's function and is the field radiated by a point source. The radiated field is the system response from the extended source $\psi'(\vec{r}')$ and is obtained by the convolution of the impulse response with the extended source. The function $A(\vec{r},\vec{r}')$ is called the inclination (or obliquity) factor and is dependent on the source polarization [2]. If $\vec{r}$ and $\vec{r}'$ are restricted to a small angular region in the neighborhood of the reflector axis, then $A(\vec{r},\vec{r}')$ will remain essentially constant and (2.1-1) can be written as [2]

$$\psi(\vec{r}) = C\int_{aperture} \psi'(\vec{r}')\ \frac{e^{-jk|\vec{r}-\vec{r}'|}}{|\vec{r}-\vec{r}'|}\ d\vec{r}'. \tag{2.1-3}$$

If the observation point is suitably far removed from the antenna aperture, then the term $|\vec{r} - \vec{r}'|$ is slowly varying over the extent of the integral and the term in the denominator of (2.1-3), which only affects the amplitude of the wave, can be considered to be constant and extracted from the integral. The term in the exponent, however, is multiplied by $\frac{2\pi}{\lambda}$ and affects the phase of the radiation. This term always has a significant effect on the integral and cannot be ignored. Under these conditions equation (2.1-3) can be rewritten as:

$$\psi(\vec{r}) \simeq \frac{C}{R} \int_{aperture} \psi'(\vec{r}') \, e^{-jk|\vec{r}-\vec{r}'|} d\vec{r}'. \tag{2.1-4}$$

where $R = |\vec{r} - \vec{r}'|$. If both $\vec{r}$ and $\vec{r}'$ are written in rectangular coordinates, the exponential term becomes

$$|\vec{r} - \vec{r}'| = [(x - x')^2 + (y - y')^2 + z^2\,]^{\frac{1}{2}}$$

$$= r\left[1 + \frac{x'^2 + y'^2}{r^2} - \frac{2(xx' + yy')}{r^2}\right]^{\frac{1}{2}}, \tag{2.1-5}$$

where $r = |\vec{r}| = (x^2 + y^2 + z^2)^{\frac{1}{2}}$. If the distance between the observation point and the aperture plane is much greater than the maximum dimension of the aperture, then the r^2 term in the denominators of (2.1-5) is much larger than the terms in the numerators. Under this condition (2.1-5) can be expanded in a binomial series and approximated by the first two terms giving

$$|\vec{r} - \vec{r}'| \approx r + \frac{x'^2 + y'^2}{2r} - \frac{x'x + y'y}{r}. \tag{2.1-6}$$

Antenna problems are customarily divided into three groups depending on the distance of the observation point from the source. The first group occurs when the observation point is so close to the antenna aperture that (2.1-6) does not adequately approximate (2.1-5). This is termed the near-field region. The other two groups depend on the relative magnitude of the last two terms of (2.1-6) [2]. The region where r is large enough that the term $(x'^2 + y'^2)/(2r)$ can be neglected

is termed the Fraunhofer or far-field region. The region in which this term cannot be neglected is termed the Fresnels region. In addition to the far-field region the term $(x'^2 + y'^2)/(2r)$ can also be neglected at the focal point of an antenna. The similarities between the far-field approximation and the focal point approximation are now discussed.

2.1.1 Far-Field Approximation

The far-field approximation can be made if the distance between the antenna aperture and the observation point P is increased such that

$$\frac{k(x'^2 + y'^2)_{max}}{2r} \ll 1 \tag{2.1-7}$$

where the term $(x'^2 + y'^2)_{max}$ can be approximated by the maximum dimension of the aperture squared, $D^2{}_{max}$. Recalling that $k = 2\pi/\lambda$ and substitution into (2.1-7) leads to

$$r \gg \frac{\pi D^2{}_{max}}{\lambda}. \tag{2.1-8}$$

If this condition is met, then (2.1-6) becomes

$$|\vec{r} - \vec{r}'| \approx r - \frac{x'x + y'y}{r}. \tag{2.1-9}$$

Substitution into (2.1-4) leads to

$$\psi(\vec{r}) = \frac{Ce^{-jkr}}{R} \int_{aperture} \psi'(x', y')\, e^{jk\left(\frac{x'x + y'y}{r}\right)}\, dx'dy'. \tag{2.1-10}$$

Equation (2.1-10) has the form of a Fourier transform and, therefore, implies a Fourier transform relationship between the radiated far field and the antenna's aperture plane field distribution.

2.1.2 Focal Point Approximation

A second circumstance under which the term $(x'^2 + y'^2)/(2r)$ in (2.1-6) can be neglected occurs when calculating the diffraction pattern in the focal region of a focused aperture antenna [2]. When viewed in the receiving mode a focused aperture antenna converts an incident plane wave into a converging spherical wave of radius F. This is shown for a parabolic reflector in Fig. 2.1-3. Here P is a plane wave incident on the reflector; S is a reflected spherical wave; ρ is the radial height to an arbitrary point on S; and Δz is the axial distance of the point on S from the origin. From the Pythagorean theorem

$$(F - \Delta z)^2 + \rho^2 = F^2 \quad \text{or} \quad 2\Delta z F = (\rho^2 - \Delta z^2). \tag{2.1-11}$$

If Δz is small compared to ρ, Δz^2 can be ignored compared to ρ^2 on the right side of (2.1-11). For reflector antennas this corresponds to a large F/D ratio where F is the focal length and D is the diameter of the reflector. Under this condition

$$\Delta z \approx \frac{\rho^2}{2F}, \tag{2.1-12}$$

which is referred to as the "sagittal' approximation, and the phase change introduced at the aperture of the antenna due to the focusing effect is

$$\phi = k\Delta z = k\,\frac{x'^2 + y'^2}{2F} \tag{2.1-13}$$

and the source function $\psi'(x'^2, y'^2)$ in (2.1-4) is multiplied by the additional term

$$e^{j\phi} = e^{jk\frac{x'^2 + y'^2}{2F}} \tag{2.1-14}$$

For $r = F$ (2.1-14) exactly cancels the second term in (2.1-6). Therefore, the field at any point on the plane passing through the focal point F (focal plane) is given by

$$\psi(x,y,F) = \frac{ke^{-jkF}}{R} \int_{aperture} \psi'(x',y')\, e^{jk\left(\frac{xx' + yy'}{F}\right)}\, dx'dy'. \tag{2.1-15}$$

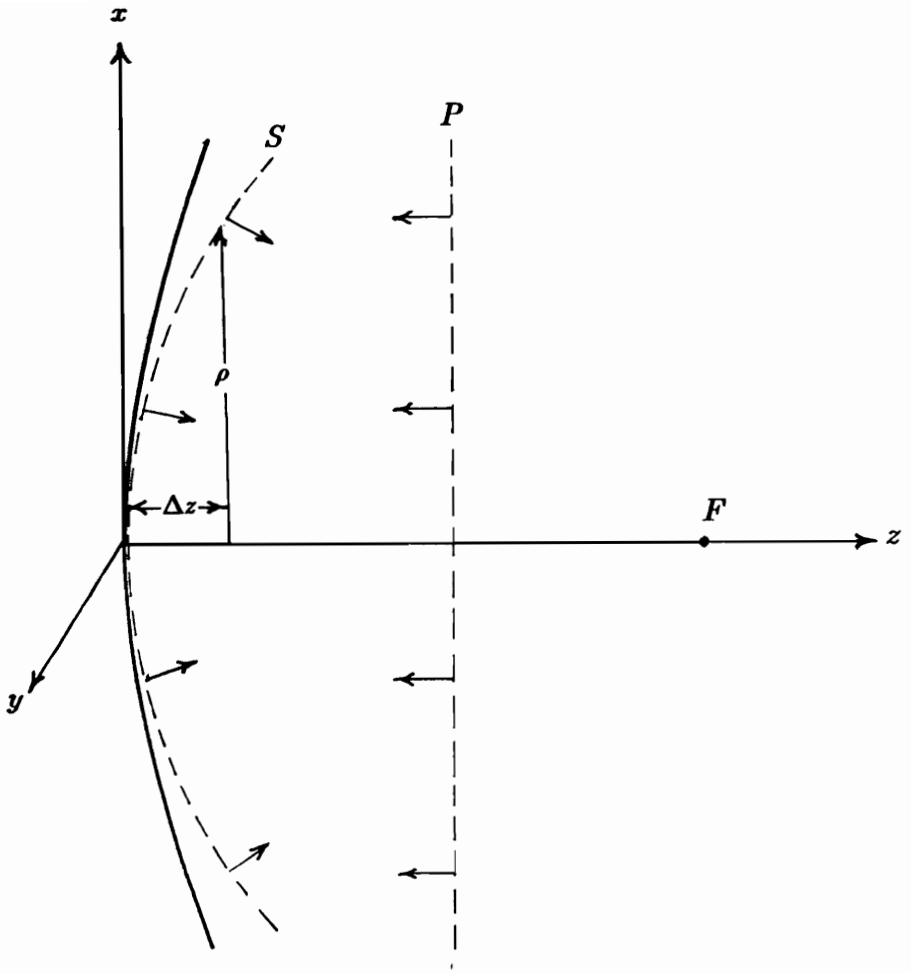

Figure 2.1-3. A parabolic reflector with focal point F converts incident plane wave P into the reflected spherical wave S which is convergent on F. The radial distance to any point on S is given by ρ and Δz is the axial distance of the point on S from the coordinate origin.

Equation (2.1-15) is identical to (2.1-10) if r is replaced by F. Therefore, near the axis of a focused aperture antenna with a large F/D ratio both the far-field and the focal plane field distributions are related to the aperture plane field distribution by a Fourier transform. This similarity is expected because the far-field condition of parallel rays corresponds to a focus point at infinity.

2.2 Lens Aberration Theory

The term "aberration" is used by optical designers for any imperfection caused by a lens in reproducing the image of an object [3]. For antenna engineers, however, the emphasis is on phase error. Phase error is defined as the deviation of the phase of a wavefront compared to a reference (desired) wavefront. Usually the comparison is made over the aperture plane where the desired wavefront is a plane wave and the phase is easiest to represent.

For reflector antennas phase error can result from errors in the feed illumination pattern, displacement of the feed from the focal point, or from reflector surface errors. Using geometrical optics rays can be traced from the feed to the aperture plane and a pathlength error ΔL can be defined as the difference in path length between any arbitrary ray and a reference ray. In most cases the reference ray is defined as the ray which exits through the center of the aperture. The resultant phase error is related to the pathlength error by

$$\Delta P = \frac{2\pi}{\lambda} \Delta L. \tag{2.2-1}$$

The pathlength error across the aperture plane can be expressed in cylindrical coordinates by the function $\Delta L(\rho, \phi)$, where the center of the coordinate system is at the center of the aperture plane. To visualize the effects of different types of pathlength errors it is helpful to expand the pathlength error function in a power series in ρ and $cos\phi$. This is the approach taken by Schwartzchild [1] and the resultant power series is known as the expansion of the perturbation eikonal of Schwartzchild. The five lowest order terms in this

expansion represent five "primary aberrations" also known as Seidel aberrations and are given by [1]:

$$\Delta L(\rho,\phi) = \alpha\rho\cos\phi + \beta\rho^2 + \gamma\rho^2\cos(2\phi) + \delta\rho^3\cos\phi + \varepsilon\rho^4. \qquad (2.2\text{-}2)$$

The five Seidel aberrations in the above equation are respectively identified as: distortion; curvature of field; astigmatism; coma; and spherical aberration. The surfaces resulting from each of these aberrations are shown in Fig 2.2-1 [3]. It has been shown that any aberration function of small amplitude can be approximated by the Seidel aberrations [3].

The adverse far-field radiation pattern effects caused by each of the Seidel aberrations can be demonstrated by reducing the problem to a two-dimensional case. This corresponds to an infinite cylindrical reflector extending along the y-axis with a finite parabolic cross section along the x-axis and an aperture field distribution which is a function of only x such that the primary aberrations can be found by setting $\phi = 0^\circ$ in (2.2-2). For this case the distortion term degenerates into the linear error term αx, the curvature of field and astigmatism terms degenerate into the quadratic error term βx^2, the coma term degenerates into the cubic error term δx^3 and the spherical term degenerates into the quartic (fourth-order) error term ϵx^4. The five primary aberrations, therefore, degenerate into four types of errors: linear, quadratic, cubic and quartic [3].

The linear error term αx does not perturb the far-field radiation pattern, but scans the beam by angle [3]

$$\theta_s = sin^{-1}\left(\frac{\alpha}{2a}\right) \qquad (2.2\text{-}3)$$

where a is the linear dimension (width) of the aperture. Associated with the scan angle is a gain loss due to a reduction of the projected aperture by $cos\theta_s$.

The quadratic error term βx^2 raises sidelobe levels and causes null filling between lobes. Since the errors are symmetric with respect to the center of the aperture, pattern degradation will be symmetric about the $\theta = 0$ axis [3]. Following the analysis by Silver [4] the far-field pattern of a two-dimensional aperture with quadratic phase errors is given by

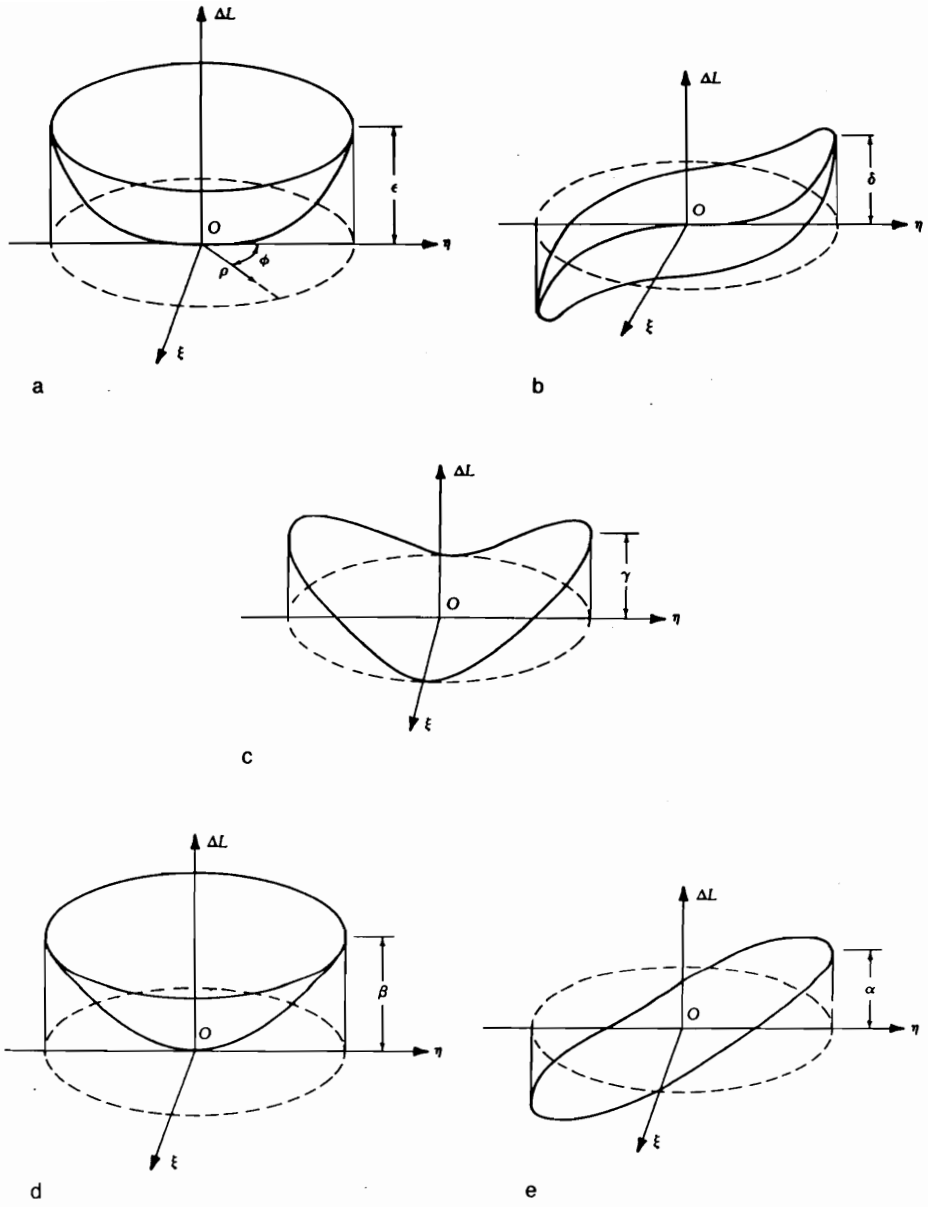

Figure 2.2-1. Surfaces corresponding to the five primary aberrations [3]. (a) Spherical aberration: $\Delta L = \epsilon\rho^4$. (b) Coma: $\Delta L = \delta\rho^3 cos\phi$. (c) Astigmatism: $\Delta L = \gamma\rho^2 cos^2\phi$ (similar to $\rho^2 cos2\phi$ in nature). (d) Curvature of field: $\Delta L = \beta\rho^2$. (e) Distortion: $\Delta L = \alpha\rho \cos\phi$.

$$q(u) = \frac{a}{2} \int_{-1}^{1} f(x)\, e^{j(ux - k\beta x^2)}\, dx \tag{2.2-4}$$

where a is the linear dimension of the aperture, $f(x)$ is a symmetric aperture amplitude distribution, $u = (\frac{\pi a}{\lambda}) sin\,\theta$ and $k = \frac{2\pi}{\lambda}$. For small values of β the far-field power pattern can be expressed as [3]

$$P(u) \approx \frac{a^2}{4} \left\{ g_0{}^2(u) + [k\beta\, g_0{}''(u)]^2 \right\} \tag{2.2-5}$$

where $g_0(u)$ is the pattern in absence of phase errors ($\beta = 0$) and $g_0{}''(u)$ is the second derivative of $g_0(u)$. The far-field patterns of a uniform amplitude aperture distribution with $k\beta = 0$, $\pi/4$ and $\pi/2$ are shown in Fig. 2.2-2. For β sufficiently large the main beam becomes bifurcated with maxima occurring on either side of the $\theta = 0$ axis [3].

Using a similar technique for the cubic error term δx^3, the far-field power pattern is given by [3]

$$P(u) \approx \frac{a^2}{4} [g_0(u) + k\delta\, g_0{}''(u)]^2. \tag{2.2-6}$$

The effect of this phase error is to scan the beam and reduce peak gain. In addition the main lobe loses symmetry and the sidelobes become asymmetrical. That is, the sidelobes decrease on the side of the main lobe near $\theta = 0$ and increase on the other side of the main lobe. The enlarged first sidelobe is referred to as the coma lobe. The far-field patterns of a uniform amplitude aperture distribution with $k\delta = 0$, $\pi/4$ and $\pi/2$ are shown in Fig. 2.2-3 [3].

For an aperture with quartic errors εx^4 the far-field power pattern is given by [3]

$$P(u) \approx \frac{a^2}{4} \left\{ g_0{}^2(u) + k\left[\varepsilon g_0{}^{(4)}(u)\right]^2 \right\}. \tag{2.2-7}$$

Comparison with (2.2-4) indicates that the effects of quartic phase errors are similar to that of quadratic phase errors. The far-field patterns of a uniform amplitude aperture distribution with $k\varepsilon = 0$, $\pi/4$ and $\pi/2$ are shown in Fig. 2.2-4

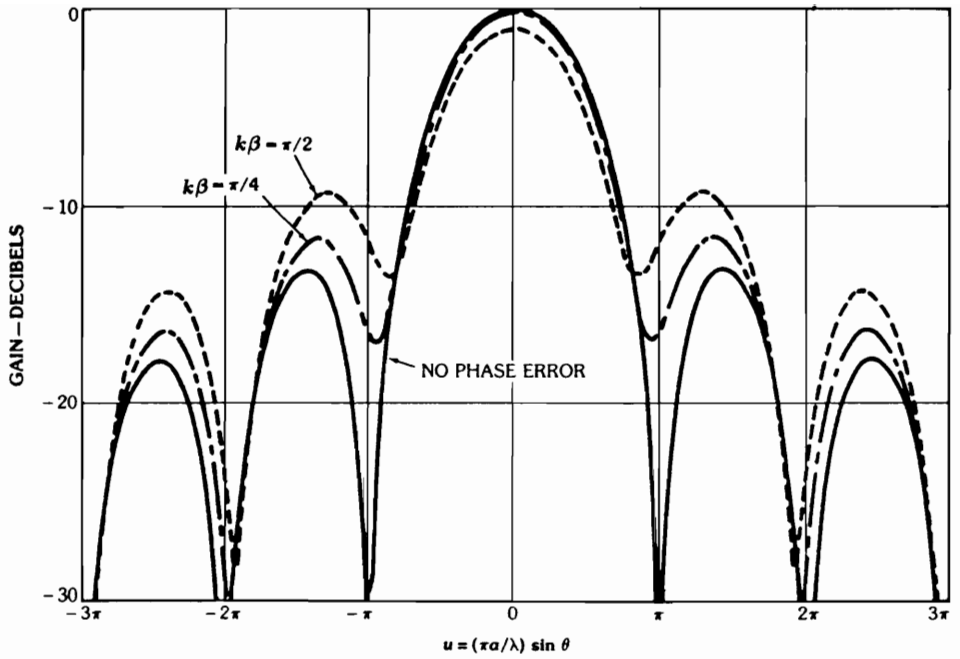

Figure 2.2-2. Pattern degradation due to quadratic phase error (one dimensional case) [3].

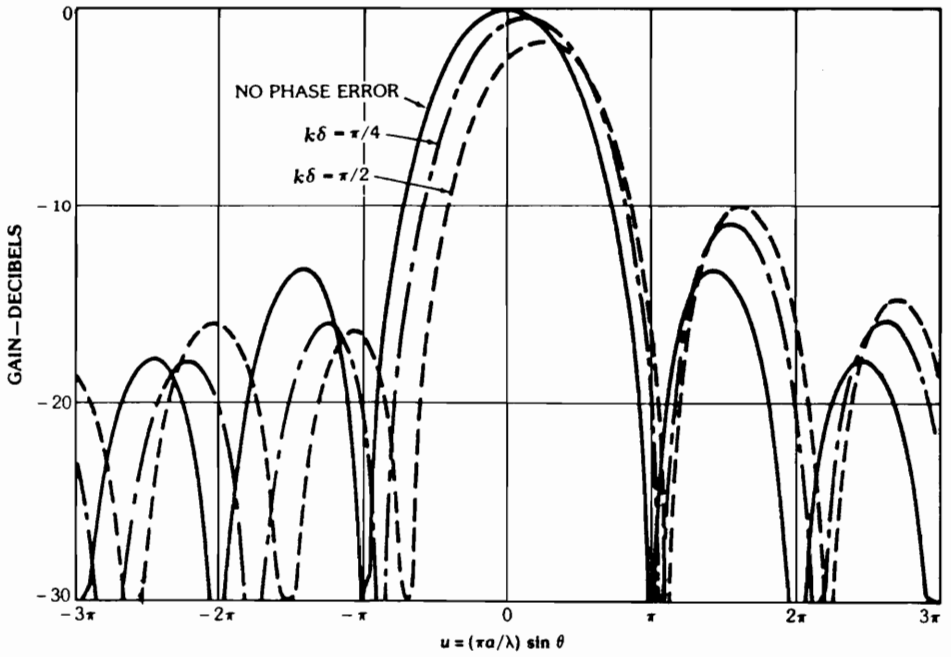

Figure 2.2-3. Pattern degradation due to cubic phase error (one dimensional case) [3].

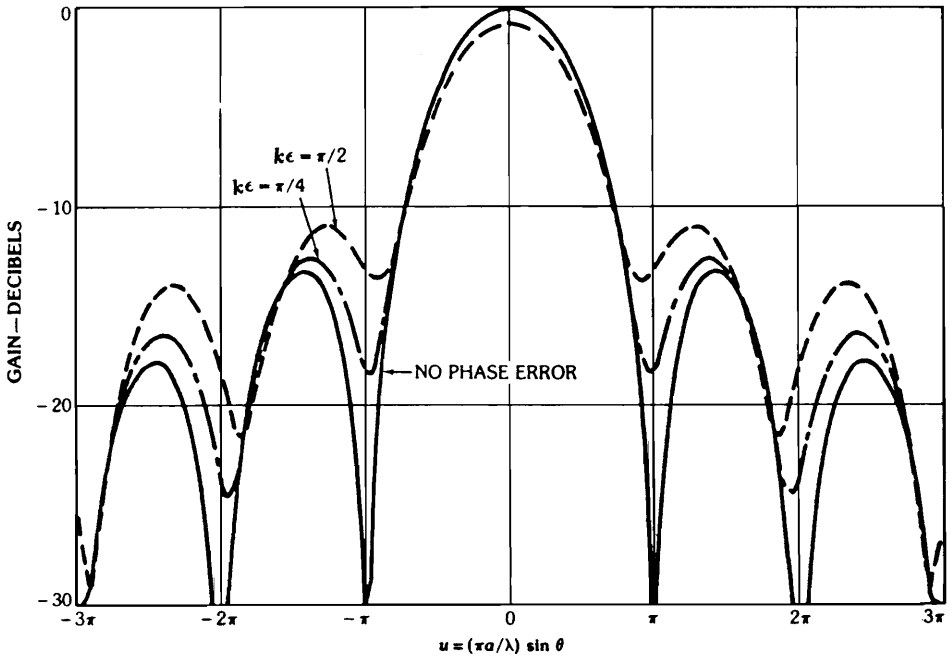

Figure 2.2-4. Pattern degradation due to quartic phase error (one dimensional case) [3].

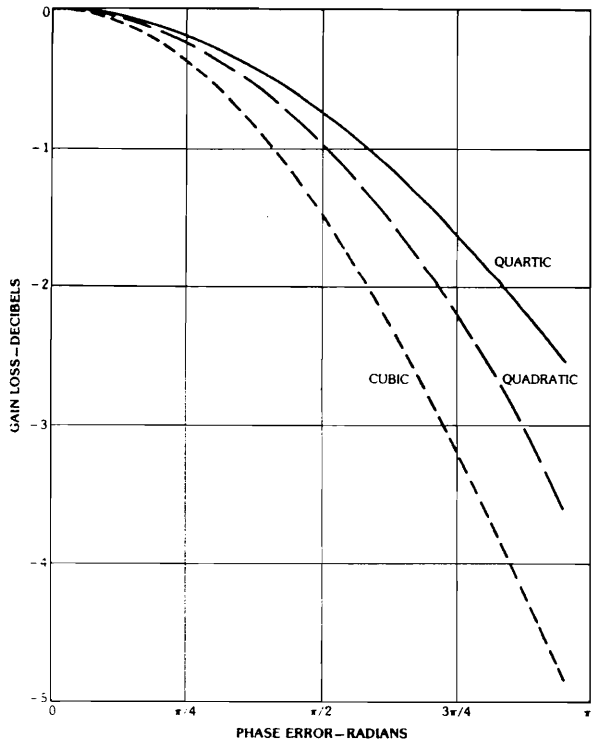

Figure 2.2-5. Gain loss due to quadratic, cubic and quartic phase errors considered individually (one dimensional case) [3].

[3]. It may be noted that for the same peak error the effects of quartic phase errors are less pronounced than that for quadratic phase errors because the total error over the aperture is less.

The gain loss effects of quadratic, cubic and quartic phase errors are demonstrated in Fig. 2.2-5 for the case of a two-dimensional aperture [3]. From this figure it is evident that gain loss is most sensitive to cubic phase errors (those resulting from coma aberration). It is also noted that sidelobe degradation is most sensitive to cubic phase errors due to the appearance of the large asymmetric coma lobe. Quadratic phase errors can be corrected by axially displacing the feed from the focus point. This defocusing technique cannot be used to compensate for cubic or fourth order errors [3].

2.3 References

1. M. Born and E. Wolf, *Principles of Optics*, The Macmillan Company: New York, 1964.

2. Renolds, DeVelis, Parrent and Thompson, *The New Physical Optics Notebook: Tutorials in Fourier Optics*, The Society for Optical Engineering: Bellingham, Washington, 1987.

3. Y. T. Lo and S.W. Lee, *Antenna Handbook*, Van Nostrand Reinhold Co.: New York, 1981.

4. S. Silver, *Microwave Antenna Theory and Design*, Peter Peregrinus Ltd.: London, reprinted 1986.

5. C. Balanis, *Antenna Theory and Design*, Harper & Row, Inc.: 1982.

6. W. Stutzman and G. Thiele, *Antenna Theory and Design*, John Wiley & Sons, Inc.: New York, 1981.

Chapter 3

Array Feed Compensation Techniques

Phase errors and their effects on the resulting radiation pattern were discussed in the previous chapter. In this chapter techniques for correcting phase errors using phased array feeds are presented. The advantages of using an array feed can be explained by viewing a focused reflector system in the receiving mode.

The aperture field distribution produced by a distant source is a plane wave with uniform amplitude and phase. For a focused reflector system this illumination produces the most compact focal plane field distribution possible; a result which follows from the Fourier transform relationship between the aperture plane field distribution and the focal plane field distribution as discussed in Sec. 2.1. If the reflector has surface errors, the resulting phase errors, which have approximately twice the surface error magnitude, cause the focal plane field distribution to be less focused and to spread [2]. Figure 3-1(a) shows the focal plane field distribution for a parabolic reflector along with mean focal plane distribution envelopes for the same reflector with random surface errors with *rms* variations of $\epsilon = \lambda/18$ and $\epsilon = \lambda/9$ [2]. If the plane wave does not arrive from the boresight direction, which is the scanned condition, phase errors cause the focal plane field distribution to spread and the maximum intensity position to shift away from the focal point. Typical field distributions in the focal region of a parabolic reflector resulting from an off-boresight incident plane wave are shown in Fig. 3-1(b) [1].

The goal of array feed compensation is to match the feed to the focal

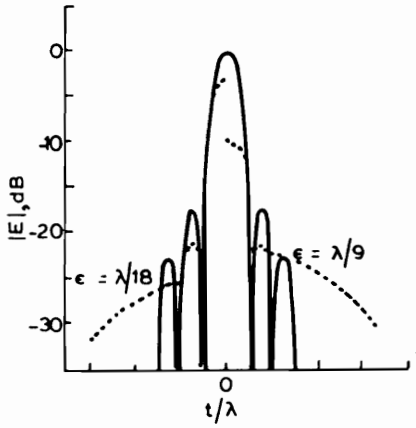

(a)

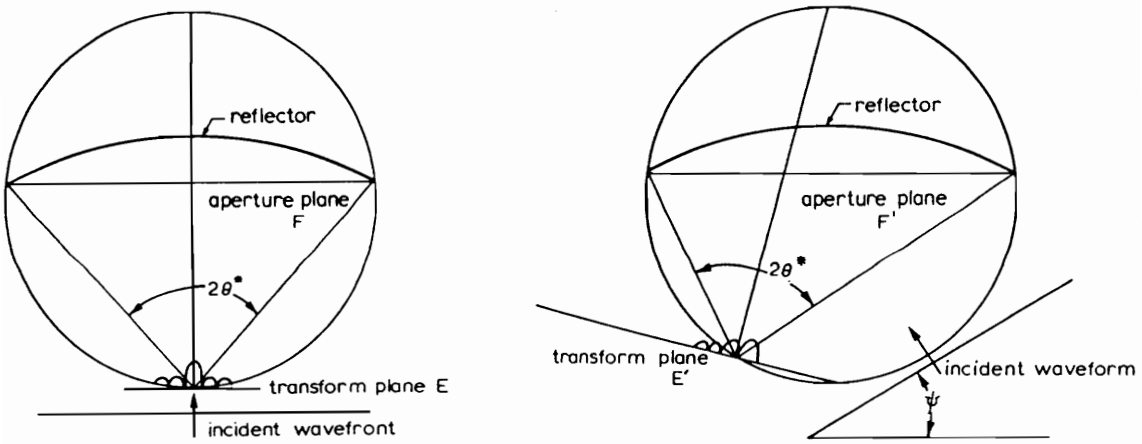

(b)

Figure 3-1. Demonstration of the effects of random surface errors and off-axis reception of an incident wave front. (a) The mean focal plane distribution envelopes for a reflector with random surface errors with *rms* variations of $\epsilon = \lambda/18$ and $\epsilon = \lambda/9$ [2]. (b) Typical focal plane distributions for axial and off axis reception of an incident wavefront [1].

plane field distribution of the reflector when operated in the receive mode such that the maximum amount of power is transmitted to the receiver (analogous to impedance matching). For this application the advantages of using an array feed are clear. An array feed covers a larger area of the focal region, as opposed to a single horn feed, and is therefore able to capture more of the focal plane energy distribution. In addition, by varying the magnitude and phase of the array feed element excitations, an array feed can be used to compensate for changes in the focal plane field distribution due to both reflector surface errors and beam scanning. The concept of matching a feed to the focal plane field distribution has been formalized in the conjugate field match technique. This technique is now presented.

3.1 The Conjugate Field Match (CFM) Technique

The conjugate field match technique is based on maximizing the power received by one antenna due to the power radiated by a second antenna or, more generally, an incoming wave. For a lossless antenna the time-average power P_R available at the antenna terminals is given by [7]

$$P_R = S_{AV}\, A_e \tag{3.1-1}$$

where S_{AV} is the time-averaged power density of the incoming wave and A_e is the effective aperture of the receiving antenna. The effective aperture A_e is related to the physical aperture A_p by [7]

$$A_e = \epsilon_{ap}\, A_p \tag{3.1-2}$$

where ϵ_{ap} is the aperture efficiency. Substitution of (3.1-2) into (3.1-1) and rearranging terms leads to the following equation for aperture efficiency:

$$\epsilon_{ap} = \frac{P_R}{S_{AV}\, A_p}. \tag{3.1-3}$$

The antenna gain is related to the aperture efficiency and the physical antenna aperture area by [7]

$$G = \epsilon_{ap} A_p \, \frac{4\pi}{\lambda^2}. \tag{3.1-4}$$

Figure 3.1-1 depicts a system consisting of a transmitting antenna 2 and a receiving antenna 1. According to Robieux's theorem [4] the time-averaged power transferred to antenna 1 from antenna 2 is given by

$$P_R = \frac{|\frac{1}{2}\int\int_{S_1} (\vec{E}_1 \times \vec{H}_2 - \vec{E}_2 \times \vec{H}_1) \cdot d\vec{S}_1|^2}{Re\int\int_{S_1} (\vec{E}_1 \times \vec{H}_1^*) \cdot d\vec{S}_1} \tag{3.1-5}$$

where $\vec{E}_1$ and $\vec{H}_1$ are the transmit fields radiated by antenna 1, $\vec{E}_2$ and $\vec{H}_2$ are the transmit fields radiated by antenna 2 and the integrals are performed over the closed surface S_1 surrounding antenna 1. If the receiving antenna is located in the focal region of a reflector as shown in Fig. 3.1-2, then the received power is given by

$$P_R = \frac{|\frac{1}{2}\int\int_{S_1} (\vec{E}_1 \times \vec{H}_{2s} - \vec{E}_{2s} \times \vec{H}_1) \cdot d\vec{S}_1|^2}{Re\int\int_{S_1} (\vec{E}_1 \times \vec{H}_1^*) \cdot d\vec{S}_1} \tag{3.1-6}$$

where $\vec{E}_{2s}$ and $\vec{H}_{2s}$ are the fields scattered by the reflector surface due to transmitting antenna 2. If it is assumed that transmitting antenna 2 is far enough away such that the incident fields $\vec{E}_2$ and $\vec{H}_2$ are planar across the reflector aperture, then the time-averaged power density incident on the aperture of the reflector is given by

Figure 3.1-1. System consisting of receiving antenna 1 surrounded by closed surface S_1 and transmitting antenna 2.

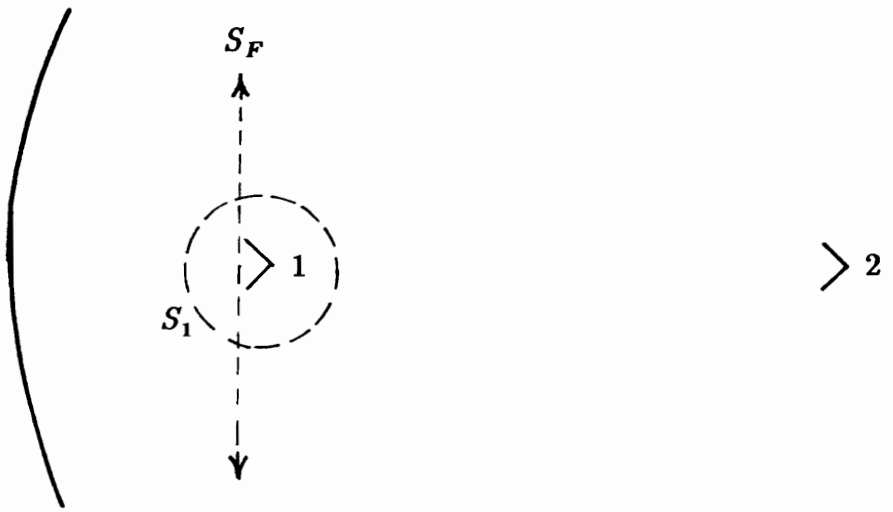

Figure 3.1-2. System consisting of a transmitting antenna 2 and receiving antenna 1 surrounded by closed surface S_1 and located in the focal region of a reflector antenna. Also shown is the focal plane S_F.

$$S_{AV} = \frac{Re\int\int_{S_R} (\vec{E}_2 \times \vec{H}_2^*) \cdot d\vec{S}_R}{A_p} \tag{3.1-7}$$

where A_p is physical area of the reflector aperture and the integral is taken across the reflector aperture plane. Substitution of (3.1-6) and (3.1-7) into (3.1-3) leads to the following expression for the reflector aperture efficiency:

$$\epsilon_{ap} = \frac{|\int\int_{S_1} (\vec{E}_1 \times \vec{H}_{2s} - \vec{E}_{2s} \times \vec{H}_1) \cdot d\vec{S}_1|^2}{2[Re\int\int_{S_1} (\vec{E}_1 \times \vec{H}_1^*) \cdot d\vec{S}_1] \, [Re\int\int_{S_R} (\vec{E}_2 \times \vec{H}_2^*) \cdot d\vec{S}_R]}. \tag{3.1-8}$$

It is noted that a similar expression has been obtained by Wood [5,6]. If a focal plane S_F is defined as shown in Fig. 3.1-2, then (3.1-8) can be approximated by

$$\epsilon_{ap} \simeq \frac{|\int_{\infty}\int_{\infty} (\vec{E}_1 \times \vec{H}_{2s} - \vec{E}_{2s} \times \vec{H}_1) \cdot d\vec{S}_F|^2}{2[Re\int_{\infty}\int_{\infty} (\vec{E}_1 \times \vec{H}_1^*) \cdot d\vec{S}_F] \, [Re\int_{\infty}\int_{\infty} (\vec{E}_{2s} \times \vec{H}_{2s}^*) \cdot d\vec{S}_F]} \tag{3.1-9}$$

where it has been assumed that most of the power transmitted by antenna 1 and most of the power scattered by the reflector surface due to incident fields $\vec{E}_2$ and $\vec{H}_2$, crosses the focal plane surface S_F. From (3.1-9) it is seen that ϵ_{ap} has a maximum value of unity under the conditions $\vec{E}_1 = \vec{E}_{2s}^*$ and $\vec{H}_1 = \vec{H}_{2s}^*$. Therefore, if antenna 1 radiates the complex conjugate of the focal plane field distribution due to a plane wave incident from the direction of antenna 2, then the gain of the reflector/feed combination is maximized in the direction of antenna 2. Such a feed is said to be conjugate matched to the reflector focal plane field distribution.

It is noted that for plane waves the electric field is orthogonal to the

magnetic field and, in addition, these fields are related to each other by [7]

$$|\frac{\vec{E}}{\vec{H}}| = Z_0 \tag{3.1-10}$$

where Z_0 is the intrinsic impedance of free space. Under the condition of planar fields over the surface of integration in (3.1-9), which is approximately valid for focused apertures, the orthogonality of electric and magnetic fields and (3.1-10) can be used to express (3.1-9) as

$$\epsilon_{ap} \simeq \frac{|\int\int_{\infty\infty} (\vec{E}_1 \cdot \vec{E}_{2s})\, dS_F|^2}{\int\int_{\infty\infty} |\vec{E}_1|^2\, dS_F \int\int_{\infty\infty} |\vec{E}_{2s}|^2\, dS_F}. \tag{3.1-11}$$

Equation (3.1-11) is identical to the expression obtained by Midgley [3] who used a reradiation approach.

From (3.1-9) and (3.1-11) it is seen that a perfect conjugate match requires that the feed extend over the entire focal plane and that the feed match the focal plane field distribution at all locations along the focal plane. While such a feed is, in general, impossible to obtain, an array feed can be used to conjugate match the focal plane distribution at a number of discrete locations corresponding to the feed element positions. There are two ways to determine the required conjugate field match (CFM) element excitations: direct conjugate field matching (DCFM) and indirect conjugate field matching (ICFM). These are outlined in the following two sections. A more detailed comparison of these techniques is presented by Smith [8].

3.1.1 Direct Conjugate Field Matching (DCFM)

In DCFM the array feed element excitations are found directly from the focal plane field distribution. When the focal plane field distribution is calculated using numerical methods the technique is referred to as theoretical DCFM. This technique is well documented in existing literature [9,10,11]. It is noted that CFM was presented in terms of matching a feed to a reflector with a

uniform amplitude aperture distribution. This produces the highest possible gain but also results in high sidelobe levels (-17.6 dB for a circular aperture). To decrease sidelobe level, at the expense of a wider main beamwidth and decreased gain, theoretical DCFM can be used to match an array feed to a reflector with a tapered aperture distribution. This is achieved by assuming the incoming wave is amplitude tapered at the edges of the aperture.

A disadvantage of using theoretical DCFM is the need for very accurate reflector surface data in order to calculate the focal plane field distribution. This constraint can be eliminated by directly measuring the reflector focal plane field distribution. This is called experimental DCFM and has been performed by Rahmat-Samii [12,13].

3.1.2 Indirect Conjugate Field Matching (ICFM)

In ICFM the array feed element excitations are found using a far-field computer program [14,10,11]. To obtain CFM element excitations corresponding to a given beam scan direction direction (θ', ϕ') the reflector is illuminated from each feed location using a normalized feed element pattern and the corresponding phase and amplitude of the far-field pattern in the (θ', ϕ') direction is calculated. By reciprocity if each element is excited with the complex conjugate of the far-field value obtained above, then the element excitations will be conjugate matched to the focal plane distribution and gain will be maximized in the (θ', ϕ') direction [9,10]. ICFM can also be used to match the array feed to a reflector with a tapered aperture distribution by using a fictitious feed illumination amplitude taper when computing the element excitations [11].

An advantage of using ICFM compared to DCFM is that the element patterns are accounted for leading to a potentially better match. A disadvantage of ICFM is the difficulty in implementing the technique with measured far-field data, particularly when electrically large reflectors are considered.

3.2 Alternative Array Compensation Techniques

With the CFM techniques described in the preceding section the array element excitations are calculated in such a way as to give maximum gain if the feed elements are equally spaced and have identical patterns (this is shown in Sec. 3.2.3). For the case where a specific aperture plane field distribution or far-field pattern is desired, there is no guarantee that using CFM techniques for any given array will produce the best approximation possible. For this case it is advantageous to use a feed array synthesis technique which accounts for the feed array dimensions, element locations and element patterns. Three such techniques are "the least squared error technique" the "pattern synthesis compensation technique" and "directivity optimization". These are now discussed.

3.2.1 The Least Squared Error Technique

The least squared error technique was developed by M.C. Bailey [15] for computing the array element excitations of a given feed array such that the best approximation (in a least squared error sense) to a desired complex-valued aperture plane field distribution is achieved. This technique was initially applied to the problem of surface distortion compensation. The computational algorithm, which is presented in detail below, is to match the actual aperture field produced by the feed array to the desired aperture field at discrete points. The method of least squares is then used to compute the feed array element excitations [15]. It has been noted that the method could also be used to calculate the excitation coefficients that approximate a desired far-field pattern [15].

To apply the algorithm it is necessary to specify the location of each of N array feed elements and the phase and amplitude of the aperture field distribution corresponding to each of the N feed elements considered individually. The desired complex-valued aperture field $F_d(x,y)$ is then

approximated in the aperture plane, which is taken to be the xy-plane, at I discrete points by [15]

$$F_d(x_i,y_i) \simeq \sum_{n=1}^{N} A_n\, f_n(x_i,y_i), \qquad i = 1,2,3,\ldots,I \tag{3.2-1}$$

where N is the number of feed elements, A_n is the n^{th} element excitation and $f_n(x_i,y_i)$ is the normalized field at location (x_i,y_i) due to the n^{th} feed element. The number of field points in the aperture I must be large enough to accurately represent the aperture plane distribution. The feed array can be of any geometry. The complex array element excitations A_n are found such that the desired aperture field $F_d(x,y)$ is approximated in a least-squared sense by the N-element feed array [15]. An outline of the least squared procedure is now presented.

The quantity ε is defined as a measure of the error between $F_d(x,y)$ and the approximation in (3.2-1) and is given by [15]

$$\varepsilon = \sum_{i=1}^{I} [F_d(x_i,y_i) - \sum_{n=1}^{N} A_n\, f_n(x_i,y_i)]^2. \tag{3.2-2}$$

Minimizing ε with respect to A_n for $m = 1,2,3,\ldots,N$ gives [15]

$$\frac{\delta\varepsilon}{\delta A_n} = -2\sum_{i=1}^{I}\left[f_m(x_i,y_i)\left(F_d(x_i,y_i) - \sum_{n=1}^{N} A_n\, f_n(x_i,y_i)\right)\right] = 0 \tag{3.2-3}$$

which yields N equations with N unknowns. Defining [15]

$$B_m = \sum_{i=1}^{I} f_m(x_i,y_i)\; F_d(x_i,y_i) \tag{3.2-4}$$

$$S_{mn} = \sum_{i=1}^{I} f_m(x_i,y_i)\; f_n(x_i,y_i) \tag{3.2-5}$$

and using (3.2-4) and (3.2-5) in (3.2-3), allows the problem to be expressed in matrix form as follows:

$$\begin{bmatrix} A_1 \\ - \\ - \\ A_N \end{bmatrix} = \begin{bmatrix} S_{11} & S_{12} & - & S_{1N} \\ S_{21} & S_{22} & - & S_{2N} \\ - & - & - & - \\ S_{N1} & S_{N2} & - & S_{NN} \end{bmatrix}^{-1} \begin{bmatrix} B_1 \\ - \\ - \\ B_N \end{bmatrix} \tag{3.2-6}$$

Equation (3.2-6) is used to solve for the element excitations A_N.

As Bailey notes, this technique does not maximize gain or sidelobes; it yields the best approximation in a least squared sense to a desired aperture field distribution within the pattern correction limits of the finite N-element array feed [15]. To date this method has only been applied using computed aperture field data; however, with a near field range it is possible that measured aperture field data could be used.

3.2.2 The Pattern Synthesis Compensation Technique

The pattern synthesis compensation technique is based on the iterative sampling method (ISM). ISM was originally formulated to synthesize radiation patterns with desired characteristics for line sources, linear arrays, rectangular apertures and rectangular arrays [16,17,18,19].

Pattern synthesis begins with an original secondary far-field pattern that is an approximation to the desired pattern [8]. The first iteration adds a series of correction patterns to the original approximate pattern. The individual correction pattern beam maxima are scanned to the locations where the pattern deviates from the desired pattern most and are then amplitude and phase weighted to properly correct the pattern at those points. Scanning of the correction beams is accomplished by adding displaced feeds, where displacement is relative to the feed position which produces the desired beam direction, or by a feed array weighted to electronically scan the correction beams in the desired directions. If the resulting pattern is not satisfactory after one iteration, more iterations are applied. For example, if the original pattern contains a sidelobe in a direction where a null is desired, a correction beam is steered to the same direction as the sidelobe and weighted to have a magnitude equal to that of the

unwanted sidelobe but 180° out of phase with it. This causes the sidelobe to be canceled by the correction beam when the excitation is added to the original excitation. The correction pattern will also affect the rest of the pattern because it has sidelobes and, therefore, subsequent iterations may be necessary for further improvement.

The total corrected pattern is the sum of the weighted correction patterns and the original pattern. The amplitude and phase data for the correction patterns are related to the necessary currents on the antenna from which the required feed positions or array element excitations can be established. A detailed description of the pattern synthesis compensation technique is now presented.

Figure 3.2-1 shows the geometry of an infinite cylindrical reflector with a y-polarized array feed [8]. For the i^{th} iteration the total correction pattern of the reflector is [8]

$$\Delta F^{(i)}(u) = \sum_n a_n^{(i)}\, G(u, u_n^{(i)}) \tag{3.2-7}$$

where $G(u, u_n^{(i)})$ is a normalized correction pattern produced by the reflector for the n^{th} array excitation, $a_n^{(i)}$ is the correction pattern weight, $u = sin\ \theta$ and $u_n^{(i)}$ is where the main beam of the n^{th} correction pattern is centered. After I iterations the resultant improved pattern is [8]

$$F^{(k)}(u) = F^{(0)} + \sum_{i=1}^{I} \Delta F^{(i)}(u). \tag{3.2-8}$$

Each normalized correction pattern for the cylindrical reflector is related to the current on the reflector surface $g_{mn}^{(i)}$ by the following integration over the reflector surface [8]:

$$G(u, u_n^{(i)}) = \kappa \int_{S_0} \sum_m g_{mn}^{(i)} (\vec{H}_{inc}, s_0, x, z) e^{jk(\vec{\rho} \cdot \hat{R}_1)}\, ds \tag{3.2-9}$$

where κ is a constant, $\vec{H}_{inc}$ is the magnetic field incident on the reflector surface due to the m^{th} feed, $\vec{\rho}$ is a position vector locating the integration points on the

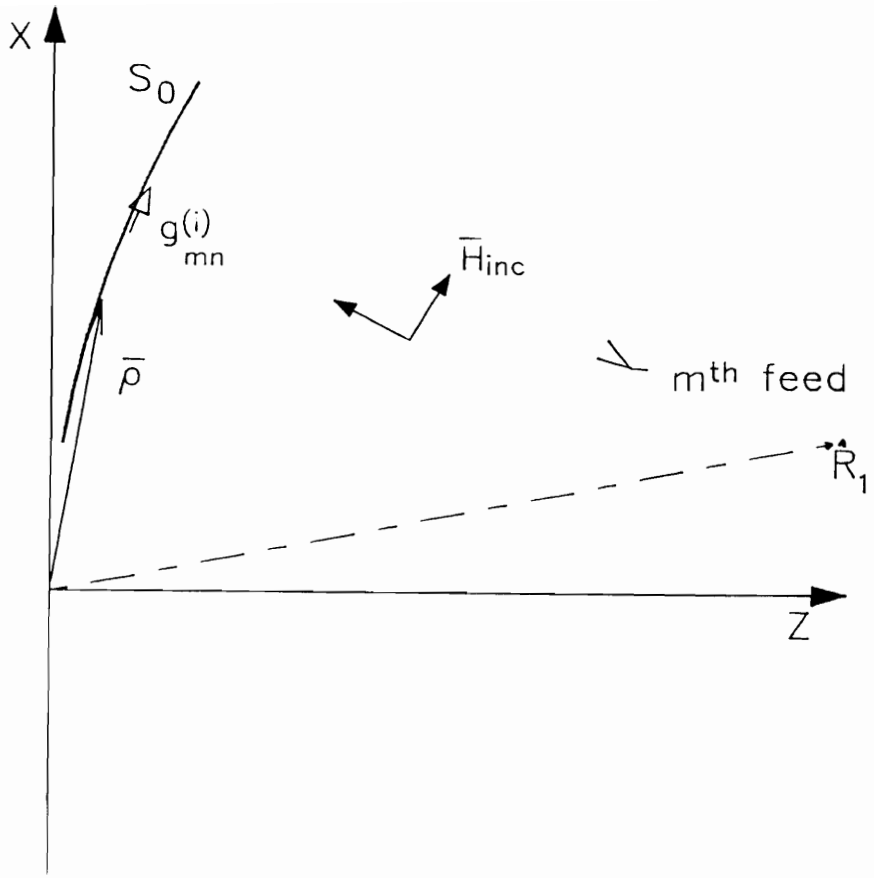

Figure 3.2-1. ISM cylindrical reflector geometry [8].

reflector surface and $\widehat{R}_1$ is a unit vector in the direction of the observation point. If the correction patterns are scanned by displacing the feeds, then the values of $g_{mn}^{(i)}$ in (3.2-9) are all zero except for the one that produces the n^{th} scanned correction beam [8]. If the correction beams are scanned electronically, then $g_{mn}^{(i)}$ is the induced current due to the m^{th} array feed element that has been amplitude and phase weighted to compositely produce the n^{th} scanned correction beam when superimposed with the induced currents due to the rest of the array elements [8]. The total correction current contribution due to the m^{th} feed for the i^{th} iteration is [8]

$$\Delta f_{ref,m}^{(i)} = \sum_n a_n^{(i)} \, g_{mn}^{(i)} \tag{3.2-10}$$

and the total current on the reflector surface due to the m^{th} feed after I iterations is [8]

$$f_{ref,m}^{(k)} = f_{ref,m}^{(0)} + \sum_{i=1}^{I} \Delta f_{ref,m}^{(i)} . \tag{3.2-11}$$

Therefore, once the weighting coefficients $a_n^{(i)}$ are found (3.2-10) and (3.2-11) are used to find the total current on the reflector due to the m^{th} feed element and the relationship between the feed element and the reflector surface current, which must be know to apply (3.2-9), is used to find the element excitation coefficient.

Figure 3.2-2 shows the elements of the n^{th} correction beam weighting scheme for the i^{th} iteration at $u_n^{(i)}$ [8]. In this figure $F^{(i-1)}(u)$ is the corrected pattern at the $i-1$ iteration, $G(u, u_n^{(i)})$ is the correction pattern with peak at $u_n^{(i)}$ and $F_d(u_n^{(i)})$ is the desired corrected pattern level at $u_n^{(i)}$. Assuming $F_d(u_n^{(i)})$ to be real and positive, the real-valued amplitude of $a_n^{(i)}$ is [8]

$$\alpha_n^{(i)} = \frac{F_d(u_n^{(i)}) - |F^{(i-1)}(u_n^{(i)})|}{|\mathrm{G}(u - u_n^{(i)})|} \tag{3.2-12}$$

where $\alpha_n^{(i)}$ can be positive or negative (the phase of $\alpha_n^{(i)}$ is 0° or 180 °). It is noted

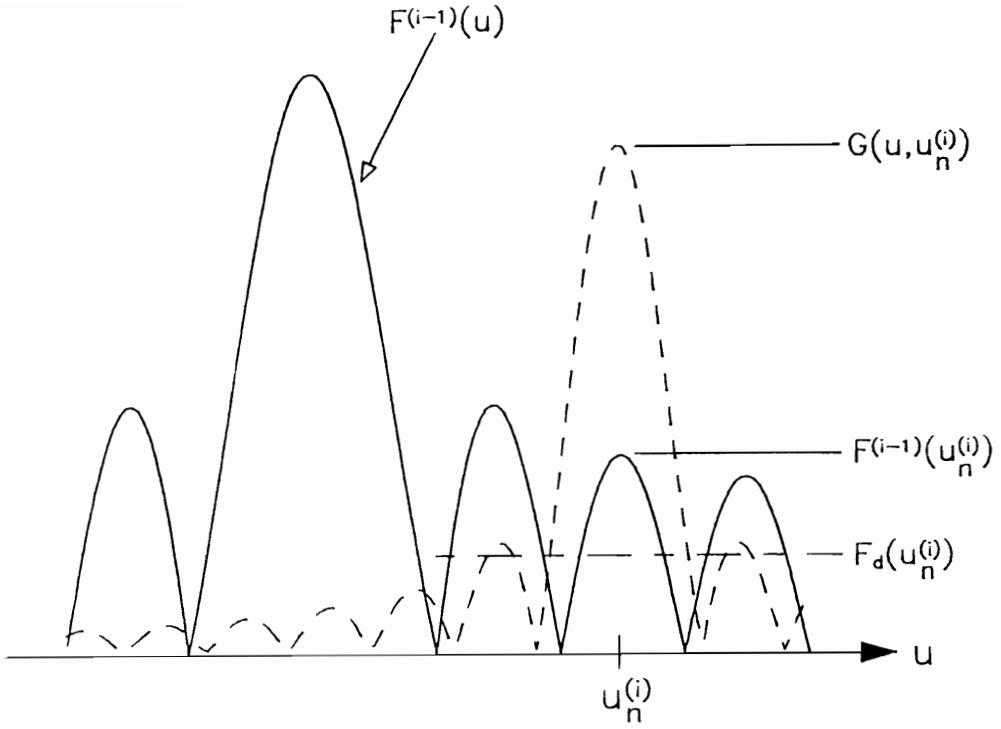

Figure 3.2-2. Representation of elements used in the ISM weighting scheme for i^{th} iteration at $u_n^{(i)}$ [8]. The $F^{(i-1)}(u_n^{(i)})$ is the corrected pattern at the $i-1^{th}$ iteration. $G(u, u_n^{(i)})$ is the correction pattern with the peak at $u_n^{(i)}$. $F_d(u_n^{(i)})$ is the desired correction pattern level at $u_n^{(i)}$.

that the correction pattern beam must be either in phase or out of phase with $F^{(i-1)}(u_n^{(i)})$. Therefore, the phase of the weighting coefficient $a_n^{(i)}$ must satisfy [8]

$$\phi_G + \phi_a + \begin{bmatrix} 0^\circ \\ \pm 180^\circ \end{bmatrix} = \phi_F \tag{3.2-13}$$

where ϕ_G, ϕ_F and ϕ_a are the phases of $G(u, u_n^{(i)})$, $F^{(i-1)}(u_n^{(i)})$ and $a_n^{(i)}$, respectively. The terms in (3.2-13) can be rearranged to yield

$$\phi_a = \phi_F - \phi_G - \begin{bmatrix} 0^\circ \\ \pm 180^\circ \end{bmatrix} \tag{3.2-14}$$

and the complete correction pattern weighting for the n^{th} correction beam and i^{th} iteration is

$$a_n^{(i)} = \alpha_n^{(i)} \, e^{j\phi_a}. \tag{3.2-15}$$

It is noted that the three-dimensional formulation is similar to the above two-dimensional formulation except for the three-dimensional case the surface integral in (3.2-9) becomes a double integral and the patterns and current distributions become bivariate [8].

3.2.3 Directivity optimization

Directivity optimization is a method for obtaining array element excitations such that the directivity of the reflector/feed combination is optimized [14]. For a given reflector and M element array feed, with fixed feed positions and element patterns, the maximum directivity of the reflector/feed combination can be formulated in terms of a linear optimization problem with unknown array element excitation coefficients $\{I_1, I_2, \ldots, I_M\}$ [14]. A closed form solution for $\{I_1, I_2, \ldots, I_M\}$ can then be obtained by straight forward

differentiation [14].

For a given observation direction (θ', ϕ') and reference polarization $\widehat{R}'$ the following row matrix is defined [14]:

$$\langle E = [E_1, E_2, \ldots, E_M] \tag{3.2-16}$$

where $\{E_m\}$ are the complex valued scalar secondary far-field patterns in the observation direction due to each feed element. The values of $\{E_m\}$ can be calculated or measured and mutual coupling effects can be included when establishing these values. The scalar fields $\{E_m\}$ are related to the vector fields $\{\vec{E}_m\}$ by

$$E_m = \widehat{R}' \cdot \vec{E}_m. \tag{3.2-17}$$

The combined far-field pattern of the M element array feed after scattering from the reflector, for the specified reference polarization, is given by [14]

$$\langle EI \rangle = \sum_{m=1}^{M} E_m I_m \tag{3.2-18}$$

where $I\rangle$ is a column matrix of the complex array element excitation coefficients $\{I_1, I_2, \ldots, I_M\}$ [14].

The optimization problem is to obtain the excitation coefficients which maximize directivity in the observation direction (θ', ϕ') for the given feed array geometry and the reference polarization $\widehat{R}'$. For a planar array feed the total time-average radiated power is given by [14]

$$P_{rad} = \frac{1}{Z_0} \int_0^{\pi/2} \int_0^{2\pi} \vec{E}_a(\vec{r}) \cdot \vec{E}_a^*(\vec{r})\, r^2 \sin\theta \, d\theta \, d\phi \tag{3.2-19}$$

where $\vec{E}_a(\vec{r})$ is the electric field produced by the array and Z_0 is the intrinsic impedance of free space. The electric field produced by the array is the sum of the complex weighted electric fields produced by each individual array element

$I_m \vec{E}_m$ multiplied by the appropriate phase factor

$$\vec{E}_a(\vec{r}) = \sum_{m=1}^{M} I_m \, \vec{E}_m(\vec{r}) \, e^{jk\hat{u} \cdot \vec{\rho}_m} \tag{3.2-20}$$

where $\vec{\rho}_m = x_m\hat{x} + y_m\hat{y} + z_m\hat{z}$ is the position vector to the m^{th} array element with $\hat{z}_m$ perpendicular to the plane of the array and

$$\hat{u} = sin\theta \; cos\phi \; \hat{x} + sin\theta \; sin\phi \; \hat{y} + cos \; \theta \; \hat{z}. \tag{3.2-21}$$

Substitution of (3.2-20) into (3.2-19) leads to

$$P_{rad} = \sum_{m=1}^{M} \sum_{n=1}^{N} I_m \, I_n^* \, \{\frac{1}{Z_0} \int_0^{\pi/2} \int_0^{2\pi} \vec{E}_m(\vec{r}) \cdot \vec{E}_n^*(\vec{r})$$

$$e^{jk\hat{u} \cdot (\vec{\rho}_m - \vec{\rho}_n)} \, r^2 \, sin\theta \; d\theta \; d\phi\}. \tag{3.2-22}$$

If the quantity in parenthesis is designated A_{mn}, then the above can be rewritten

$$P_{rad} = \sum_{m=1}^{M} \sum_{n=1}^{N} I_m \, I_n^* \, A_{mn} = \langle I^* A \; I \rangle \tag{3.2-23}$$

where I_m is the dimensionless excitation coefficient of element m and A is an $M \times M$ square matrix.

In the observation direction (θ', ϕ') the directivity for the reference polarization is [14]

$$D = \frac{4\pi \, \langle EI \rangle^2}{Z_0 \, \langle I^* A \; I \rangle}. \tag{3.2-24}$$

The excitation coefficients corresponding to maximum directivity are obtained within a constant of proportionality by setting the derivative of D with respect to the real and imaginary parts of I_m equal to zero $(\partial D/\partial re(I_m) = 0,$ $\partial D/\partial im(I_m) = 0, \; m = 1,\ldots,M)$ and solving for the required excitation coefficients. The result is [14]:

$$I\rangle_{opt} = (A^*)^{-1}\, E^*\rangle. \tag{3.2-25}$$

Since, in general, both matrices A and $E\rangle$ are complex valued, so are the optimum excitations in (3.2-25) [14]. The optimum (maximum) directivity then follows from substitution of (3.2-25) into (3.2-24) [14]:

$$D_{opt} = \frac{4\pi}{Z_0}\langle E^* A^{-1} E\rangle. \tag{3.2-26}$$

The element excitation coefficients corresponding to a conjugate field match are given by

$$CFM\colon\ I\rangle = E^*\rangle \tag{3.2-27}$$

and the corresponding directivity is [14]

$$D_{CFM} = \frac{4\,\pi\langle E^* E\rangle^2}{Z_0\langle E^* A\, E\rangle}. \tag{3.2-28}$$

A comparison of (3.2-26) and (3.2-28) leads to the conclusion that CFM gives the optimum gain under the condition [14]

$$\begin{cases} A_{mm} = a \text{ (constant)}, & \text{for all } m = n \\ A_{mn} = 0, & \text{if } m \neq n, \end{cases} \tag{3.2-29}$$

which requires that all feed elements have identical patterns and be equally spaced.

3.3 Summary of Array Compensation Techniques

This section presents a summary of the five techniques for obtaining array element excitations discussed in Secs. 3.1 and 3.2.

Direct Conjugate Field Matching (DCFM)

Application: DCFM is used to obtain the element excitations for a given array feed which produce maximum gain for arrays consisting of equally spaced elements with identical element patterns. Modified DCFM can be used to approximate a desired aperture distribution, however, in this case there is no guarantee that the best solution has been obtained.

Required Data: In order to use DCFM an accurate means of calculating or measuring the phase and amplitude of the reflector antenna's focal plane field distribution is necessary.

Comments: DCFM is limited because it does not directly account for element patterns or mutual coupling effects between elements. DCFM does provide a means for estimating the optimum location of the array feed elements. If dual polarized feed elements are considered, DCFM can be used to obtain the phase and amplitude of both feed element polarizations to reduce cross-polarization in the secondary pattern.

Indirect Conjugate Field Matching (ICFM)

Application: ICFM is used to obtain the feed element excitations for a given array feed which produce maximum gain for arrays consisting of equally spaced elements with identical element patterns. Modified ICFM can be used to approximate a desired aperture distribution, however, in this case there is no guarantee that the best solution has been obtained.

Required Data: In order to use ICFM an accurate means of calculating or measuring the phase and amplitude of the secondary far-field radiation pattern is necessary.

Comments: ICFM does not lend itself to the use of experimental data because of the difficulty in accurately measuring the phase and amplitude of the secondary far-field pattern. ICFM is an improvement over DCFM because it directly accounts for element patterns and can be formulated to account for mutual coupling between elements. If dual polarized feed elements are considered DCFM can be used to obtain the phase and amplitude of both feed element polarizations to reduce cross-polarization in the secondary pattern.

The Least Squared Error Technique

Application: The least squared error technique is used to obtain the feed element excitations for a given array feed such that the best approximation, in a least squared sense, to the desired aperture field distribution is achieved.

Required data: In order to use the least squared error technique an accurate means of calculating or measuring the phase and amplitude of the reflector aperture plane field distribution is necessary.

Comments: The least squared error technique lends itself to the use of experimental data because of the ease with which the aperture plane field distribution can be measured using a near field range. The least squared error technique directly accounts for element patterns and can be formulated to account for mutual coupling between elements. No data exists for the use of the least squared error technique with dual polarized feed elements to reduce cross polarization in the secondary pattern.

The Pattern Synthesis Compensation Technique

Application: The pattern synthesis compensation technique is used to obtain the feed element excitations or positions for an array feed such that a

desired far-field secondary pattern is synthesized.

Required Data: In order to use the pattern synthesis compensation technique an accurate means of calculating or measuring the phase and amplitude of the secondary far-field radiation pattern is necessary.

Comments: The pattern synthesis compensation technique does not lend itself to the use of experimental data because of the difficulty in accurately measuring the phase and amplitude of the secondary far-field pattern. The pattern synthesis compensation technique directly accounts for the element radiation patterns and can be formulated to account for mutual coupling between elements. It also provides a means for obtaining optimum element positions. No data exists for the use of the pattern synthesis compensation technique with dual polarized feed elements to reduce cross polarization in the secondary pattern.

Directivity Optimization

Application: Directivity optimization is used to obtain the feed element excitations which maximizes the directivity of the secondary radiation pattern.

Required Data: In order to use directivity optimization an accurate means of calculating or measuring the phase and amplitude of the secondary far-field pattern is necessary.

Comments: Directivity optimization does not lend itself to the use of experimental data because of the difficulty in accurately measuring the phase and amplitude of the far-field radiation pattern. Directivity optimization directly accounts for the element radiation patterns and mutual coupling between elements. No data exists for the use of directivity optimization with dual polarized feed elements to reduce cross polarization in the secondary pattern.

3.4 The Double Fourier Transform Technique

Methods for obtaining array element excitations to compensate for phase errors created by distorted reflector surfaces or scanning the main beam were discussed in Secs. 3.1 and 3.2. It is noted that the focal plane field distribution tends to vary rapidly in both amplitude and phase and, therefore, to match the focal plane field distribution the phase and amplitude of a feed array will also vary rapidly in both phase and amplitude. The rapid amplitude variation poses problems when trying to coherently add the signals from each element. Brennon [20] has shown that when coherently adding signals from several channels with different signal-to-noise ratios, the maximum resultant signal to noise ratio is obtained if the gain of each channel is made directly proportional to the RMS signal (voltage or current) in that channel with the constant of proportionality the same for each channel. Therefore, a correctly designed multiple element feed requires suitable amplitude weighting for each channel, which involves impedance-changing circuits. It is extremely difficult to make variable phasing and combining processes which maximize the resultant signal-to-noise ratio because the amplitude and phase across the array feed is highly dependent on scan direction, reflector surface errors and the frequency of operation.

A solution proposed by Rudge and Davies [2] exploits the Fourier transform relationship between the aperture field distribution and the focal plane field distribution. A second spatial Fourier transform is performed on the focal plane distribution by an array feed placed on the aperture plane. The output of this second Fourier transform approximates the reflector's aperture plane field distribution and, hence, has an approximately constant magnitude across the output terminals. For the case of scanned or distorted reflectors the phase across the output terminals will not be uniform, due to phase errors, so phase shifters are used before combining the signals.

The initial hardware implementation of the double Fourier transform technique was restricted to one dimension with experimentation being performed on a variable-profile parabolic cylinder reflector with $F/D = 0.5$ [2]. This allowed the compensation method to be experimentally implemented via Butler matrix feed. The Butler matrix is a device consisting of a matrix of fixed phase

shifters and couplers, which are lossless in ideal form, whose output is a sampled spatial Fourier transform of the field distribution applied to the input. Figure 3.4-1(a) shows an example of the Fourier transform on a hypothetical focal plane distribution [2]. Rudge and Davies [2] used phase shifters after the Butler matrix to achieve a conjugate match with the focal plane field distribution and a second Butler matrix to recombine the signals. This is shown in Fig. 3.4-1(b) [2]. It is noted that the phase shifters could also be used to achieve the element excitations calculated from the least squared error technique, the pattern synthesis technique or directivity optimization.

A benefit of using Rudge and Davies' technique is that only the phase shifters have to be changed for different focal plane distributions and, therefore, active phase shifters under adaptive control could be used to continuously correct for changing phase errors due to changing reflector surface errors or different scan directions [2]. In their conclusions Rudge and Davies note that for three-dimensional reflectors a two-dimensional array feed is required and Butler matrices would probably be too hard to build, too lossy and too expensive. They suggest seeking alternative methods of performing the second Fourier transform such as a microwave lens or an additional reflector [2].

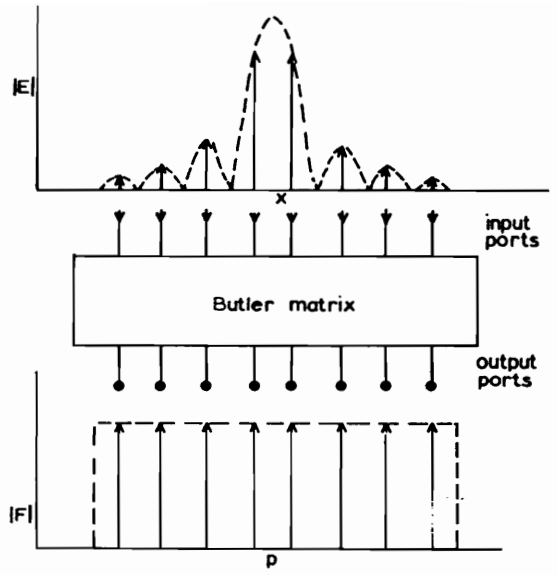

(a)

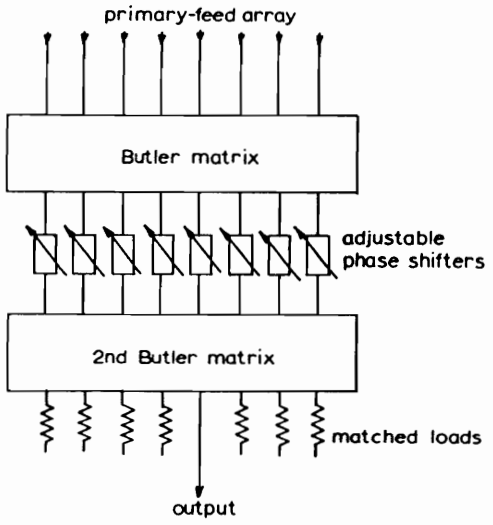

(b)

Figure 3.4-1. (a) Sampled Fourier transform performed by a Butler matrix. $|E|$ represents the value of the focal plane field at the input of the matrix, $|F|$ represents the value after transformation by the matrix [2]. (b) Schematic diagram for Rudge and Davies' experimental 8-element array feed system. The top Butler matrix performs a Fourier transform on the focal plane distribution. The phase shifters are used to coherently phase the output signals of the matrix. The second Butler matrix is used to recombine the coherent signals [2].

3.5 References

1. A. W. Rudge and M. J. Withers, "New Technique for Beam Steering with Fixed Parabolic Reflectors," *Proc. IEE*, vol. 118, no. 7, pp. 857-867 July 1971.

2. A. W. Rudge and D. E. W. Davies, "Electronically Controllable Primary Feed for Profile Error Compensation of Large Parabolic Reflectors," *Proc. IEE*, vol. 117, no. 2, pp. 351-358, February 1970.

3. D. Midgley, "A Theory of Receiving Aerials Applied to the Radiation of an Electromagnetic Horn," *Proc. IEE*, vol. 108 B, no. 42, pp. 645-650, November 1961.

4. J. Robieux, "Lois Generales ds la Laison entre Radiateurs d'Ondes," *Ann. Radioelectr.*,vol. 44, pp. 187-229, 1959.

5. P. J. Wood, "Field Correlation Theorem with a Application to Reflector Aerial Diffraction Problems," *Electron. Lett.*, vol. 6, pp. 326-327, May 1970.

6. P. J. Wood, *Reflector Antenna Analysis and Design*, Peter Peregrinus Ltd.: London, 1980.

7. W. L. Stutzman and G. A. Thiele, *Antenna Theory and Design*, John Wiley & Sons, Inc.: New York, 1981.

8. W. T. Smith and W. L. Stutzman, "Feasibility Study of a Synthesis Procedure for Array Feeds to Improve Radiation Performance of Large Distorted ReflectorAntennas," Semiannual Status Report, EE. Satcom 90 -2, August 1990.

9. R. J. Acosta, "Compensation of Reflector Surface Distortions Using Conjugate Field Matching," *1986 IEEE AP-S Symposium*, Philadelphia, Pa, June 1986.

10. J. J. Blank and W.A. Imbriale, "Array Feed Synthesis for Correction of Reflector Distortion and Vernier Beamsteering," *The Telecommunications and Data Acquisition Progress Report*, 42-86, April-June 1986.

11. Y. Rahmat-Sami, "A Generalized Reflector/Array Surface Compensation Algorithm for Gain and Sidelobe Control," *1987 IEEE AP-S International Symposium*, Blacksburg, Virginia, June 1987.

12. Y. Rahmat-Samii, "Large Antenna Measurement and Compensation Techniques," *11th ESTEC Antenna Workshop on Antenna Measurements*,Gothenburg Sweden, pp. 57-68, June 1988.

13. Y. Rahmat-Samii, "Reflector Antenna Distortion Compensation by Array Feeds: An Experimental Implementation," *Electronics Letters*, vol. 24, no. 18, pp. 1188-1190, September 1988.

14. P. T. Lam, S.W. Lee, D.C.D. Chang and K.C. Lang, "Directivity Optimization of a Reflector Antenna with Cluster Feeds: A Closed Form Solution," *IEEE Trans. on Ant. and Prop.*, vol. 33, no. 11, pp. 1163-1174, November 1985.

15. M. C. Bailey, "Electronic Compensation for Reflector Surface Distortion to Improve Radiation Pattern Characteristics of Antenna," *NASA Technical Memorandum*, No. 100652, 1988.

16. W. L. Stutzman, "Synthesis of Shaped Beam Radiation Patterns Using the Iterative Sampling Method," *IEEE Trans. on Ant. and Prop.*, vol. 19, no. 1, pp. 36-41, January 1971.

17. W. L. Stutzman, "Sidelobe Control of Antenna Patterns," *IEEE Trans. on Ant. and Prop.*, vol 20, no. 1, pp. 102-104, January 1972.

18. W. L. Stutzman and E.L. Coffey, "Radiation Pattern Synthesis of Planar Antennas Using the Iterative Sampling Method," *IEEE Trans. on Ant. and Prop.*, vol. 23, no. 6, pp. 764-769, November 1975.

19. W. L. Stutzman, "Shaped-Beam Synthesis of Nonuniformly Spaced Linear Arrays," *IEEE Trans. on Ant. and Prop.*, vol. AP 22, no. 4, pp. 499-501, July 1972.

20. D. G. Brennon, "On the Maximum Signal/Noise Ratio Realizable for Several Noisy Channels," *Proc. Inst. Radio Eng.*, 1955, 43, pp. 1530.

21. M. Born and E. Wolf, *Principles of Optics*, The Macmillan Company: New York, 1964.

Chapter 4

Parabolic Reflectors

The parabolic reflector is the most studied reflector shape. A single parabolic reflector has the ability of focusing an incident plane wave to a small region about the focal point. Although parabolic reflectors exhibit poor scanning performance they are useful for many applications requiring scanning over a narrow angular region. In this chapter the lens aberration theory presented in Chapter 2 and the phased array compensation techniques presented in Chapter 3 are applied to the parabolic reflector with an emphasis on scan performance. Also, multiple reflector configurations involving parabolic main reflectors are discussed.

4.1 Parabolic Reflector Beam Scanning with a Displaced Feed

A focus-fed parabolic reflector produces a secondary radiation pattern peak along its axis (e.g. the z-axis in Fig. 4.1-1). This secondary beam can be scanned off axis by a combination of a lateral (parallel to the focal plane) and axial (perpendicular to the focal plane) translation of a single feed element. Ruze [1] used scalar analysis to formulate expressions for the phase error caused by displacing the feed of an axis-symmetric parabolic reflector from the focal

point. This analysis is now presented.

Consider a paraboloid with diameter $2a$ described by a spherical coordinate system centered at the focal point as shown in Fig. 4.1-1. The secondary far-field in the direction of the observation point P, which is specified by the spherical coordinates (θ, ϕ), can be found by the following integration over the induced current on the reflector surface:

$$\vec{E}(\theta,\phi) = \int_{surface} [\vec{J}_s(\vec{\rho}) - \hat{R} \cdot \vec{J}_s(\vec{\rho})\ \hat{R}]\ e^{jk\vec{\rho}\cdot\hat{R}}\ d\vec{\rho} \tag{4.1-1}$$

where $\vec{J}_s$ is the induced surface current, $\vec{\rho}$ is the position vector to points on the reflector surface and $\hat{R}$ is the unit vector in the direction of observation point P. All leading constants in (4.1-1) have been suppressed. When the reflector is large with respect to the wavelength, as is usually the case, the surface can be considered locally flat and the surface current can be approximated by [2]

$$\vec{J}_s \approx 2\hat{n} \times \vec{H}_i \tag{4.1-2}$$

where $\hat{n}$ is the unit normal to the surface of the reflector and $\vec{H}_i$ is the illuminating magnetic field arising from the feed. Equation (4.1-2) is often referred to as the physical optics (P.O.) approximation.

The surface current in (4.1-1) is a complex-valued quantity. The phase of the current is found from the path length from the feed to the surface of the reflector. It is helpful to introduce the following variables [1]:

$$\vec{f}(\vec{\rho})\ e^{-j\Phi'} = \vec{J}_s(\vec{\rho}) - \hat{R} \cdot \vec{J}_s(\vec{\rho})\ \hat{R} \tag{4.1-3}$$

where ρ is the pathlength from the focal point F to the surface of the reflector as shown in Fig. 4.1-1 and $\Phi' = k\rho$.

The surface integral in (4.1-1) can be reduced to a two-dimensional aperture integration by introducing integration variables ϕ' and $r = \rho \sin\theta'$, which are shown in Fig. 4.1-1. Making this variable substitution and applying (4.1-3) results in the following equation for the secondary far-field pattern [1]:

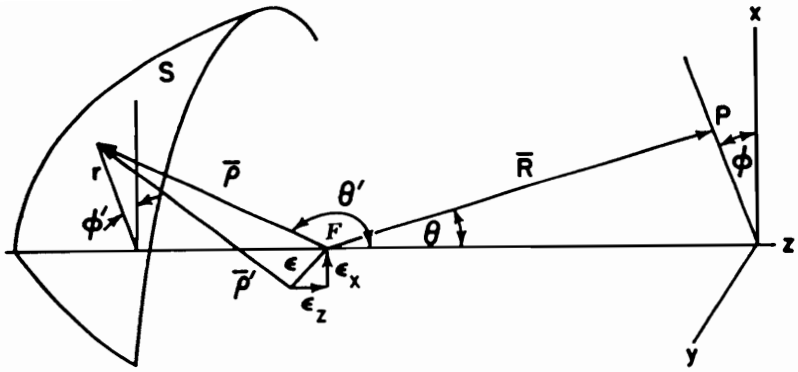

Figure 4.1-1. Paraboloid described by a spherical coordinate system centered at the focal point [1].

$$\vec{E}(\theta,\phi) = \int_0^{2\pi}\int_0^{a} \vec{f}(r,\phi')\, e^{jk(\rho - \hat{\rho}\cdot\hat{R}_o)}\, r\, dr\, d\phi' \tag{4.1-4}$$

where $\vec{f}(r,\phi')$ plays the role of an effective aperture field distribution. If the feed is displaced a lateral distance ϵ from the focus, then the field in the (θ,ϕ) direction is given by [1]

$$\vec{E}(\theta,\phi) = \int_0^{2\pi}\int_0^{a} \vec{f}(r,\phi')\, e^{jk(\rho' - \vec{\rho}'\cdot\hat{R}_o)}\, r\, dr\, d\phi' \tag{4.1-5}$$

where it is assumed that the magnitude of the aperture field distribution remains unchanged.

The following geometric relations are useful for analyzing the behavior of the phase factor in (4.1-5) (see Fig. 4.1-1) [1]:

$$\rho = \frac{2F}{1-\cos\theta'} = F\left(1+\left(\frac{r}{2F}\right)^2\right) \tag{4.1-6a}$$

$$\vec{\rho} = \rho\,[\cos\phi'\,\sin\theta'\,\hat{x} + \sin\phi'\,\sin\theta'\,\hat{y} + \cos\theta'\,\hat{z}] \tag{4.1-6b}$$

$$\hat{R}_0 = \cos\phi\,\sin\theta\,\hat{x} + \sin\phi\,\sin\theta\,\hat{y} + \cos\theta\,\hat{z} \tag{4.1-6c}$$

$$\vec{\rho}' = \vec{\rho} + \epsilon_x\,\hat{x} + \epsilon_z\,\hat{z} \tag{4.1-6d}$$

$$\rho' = \rho\left\{1 + \frac{2\epsilon_x}{\rho}\cos\phi'\,\sin\theta' + \frac{2\epsilon_z}{\rho}\cos\theta' + \frac{\epsilon^2}{\rho^2}\right\}^{\frac{1}{2}} \tag{4.1-6e}$$

If the displacements are small compared to the focal length, then

$$\frac{\epsilon_x}{\rho} < \frac{\epsilon_x}{F} \ll 1 \tag{4.1-7}$$

and the phase factor in (4.1-5) can be written as follows by substitution from (4.1-6) and neglecting terms higher than the square of the parameters above [1]:

$$\rho' - \vec{\rho}' \cdot \hat{R}_o \simeq 2F - \epsilon_x \cos\phi \sin\theta - \epsilon_z \cos\theta$$

$$- \rho \sin\theta' \sin\theta \cos(\phi' - \phi) + \epsilon_x \cos\phi' \sin\theta'$$

$$+ \epsilon_z \cos\theta' + \frac{\epsilon_x^2}{2\rho} + \rho \cos\theta'(1 - \cos\theta)$$

$$- \frac{\epsilon_x^2}{2\rho} \cos^2\phi' \sin^2\theta'. \tag{4.1-8}$$

The first three terms in the above expression are independent of the integration coordinates and can be taken out of the integral, these terms represent the phase pattern of the far field [1]. The next term is the phase factor of a smooth parabolic reflector with a feed at its focus [1]. The fifth term in (4.1-8) represents distortion and coma aberration. This can be shown by applying the following expansion [1]:

$$\sin\theta' = \frac{r}{\rho} = \frac{r}{F\left[1 + \left(\frac{r}{2F}\right)^2\right]}$$

$$= \frac{r}{F}\left[1 - \left(\frac{r}{2F}\right)^2 + \left(\frac{r}{2F}\right)^4 - \cdots\right]. \tag{4.1-9}$$

Substitution of (4.1-9) into the fifth term of (4.1-8) allows the phase factor due to this term, PF_5, to be written as [1]

$$PF_5 = u_s r \cos\phi' \left[1 - \left(\frac{r}{2F}\right)^2 + \left(\frac{r}{2F}\right)^4 - \cdots\right] \tag{4.1-10}$$

where

$$u_s = \frac{\epsilon_x}{F} = \tan\theta_s \tag{4.1-11}$$

is a measure of feed squint [1]. The first term in (4.1-10) is identical in form to the distortion term in (2.2-2) where $\phi = \phi'$, $\rho = r$ and $\alpha = u_s$. Distortion is shown graphically in Fig. 2.2-1(e). For the two-dimensional case (i.e. for infinite cylindrical reflectors) this term can be expressed as a linear function of

$x = r\cos\phi'$. The linear phase error resulting from this term scans the beam by angle θ_s in the xz-plane, where θ_s is given by (2.2-3) with $\alpha = u_s$. The second term in (4.1-10) has the same form as the coma aberration term in (2.2-2) where $\phi = \phi'$, $\rho = r$ and $\delta = u_s/(2F)^2$. Coma aberration is shown graphically in Fig. 2.2-1(b). For the two-dimensional case this gives rise to cubic phase errors. The asymmetric pattern degradation effects which result from cubic phase errors are shown in Fig. 2.2-3. The remaining terms in (4.1-10) are higher order coma terms and for reflectors with high F/D ratios cause negligible contribution to beam distortion [1].

The sixth through eighth phase factor terms in (4.1-8) introduce constant phase terms, field curvature terms, which are proportional to r^2, and higher terms of even order [1]. This can be shown by expanding the terms in ρ using (4.1-6 a) resulting in

$$PF_{6\text{-}8} = \epsilon_z\left[1 - \frac{2F}{\rho}\right] + \frac{\epsilon_x^2}{2\rho} + (\rho - 2F)(1 - \cos\theta). \tag{4.1-12}$$

The r^2 and higher order dependence in (4.1-12) can be obtained by using (4.1-6 a) to write ρ in terms of r^2 and expanding in a binomial series as is done in (4.1-9). This leads to

$$\begin{aligned} PF_{6\text{-}8} &= \epsilon_z\left(1 - 2\left[1 - \left(\frac{r}{2F}\right)^2 + \left(\frac{r}{2F}\right)^4 + \cdots\right.\right. \\ &\quad + \frac{\epsilon_x^2}{2F}\left(1 - \left(\frac{r}{2F}\right)^2 + \left(\frac{r}{2F}\right)^4 + \cdots\right. \\ &\quad + F\left[1 + \left(\frac{r}{2F}\right)^2\right](1 - \cos\theta). \end{aligned} \tag{4.1-13}$$

Field curvature is shown graphically in Fig. 2.2-1(d). For the two-dimensional case this gives rise to quadratic phase errors. The symmetrical pattern degradation effects resulting from quadratic phase errors are shown in Fig. 2.2-2.

Field curvature can be eliminated by axially refocusing the feed. This result can be obtained from (4.1-8) by setting all the field curvature terms to zero resulting in the relation [1]

$$\epsilon_z = \frac{\epsilon_x^2}{2F}. \tag{4.1-14}$$

The surface defined by (4.1-14) is referred to as the Petzval surface.

By similar expansions of $sin\theta'$ and $1/\rho$ the final phase factor term in (4.1-8) can be shown to introduce astigmatism and higher order terms as follows:

$$PF_9 = \frac{-2\epsilon_x^2}{F} cos^2\phi' \left[\left(\frac{r}{2F}\right)^2 - 3\left(\frac{r}{2F}\right)^4 + \cdots \right]. \tag{4.1-15}$$

Astigmatism is illustrated graphically in Fig. 2.2-1(c). For the two-dimensional case this gives rise to quadratic phase errors.

Following [1], the ratio of phase error due to astigmatism to phase error due to coma at the edge of the reflector, were the effects of aberration are worst, is

$$\frac{\Phi_{astigmatism}}{\Phi_{coma}} = \frac{2u_s\left(\frac{F}{D}\right)}{\left[1 + \frac{1}{16}\left(\frac{D}{F}\right)^2\right]^2}. \tag{4.1-16}$$

For reflectors with small F/D values coma aberration dominates while for reflectors with large F/D values astigmatism becomes the limiting factor. For large F/D values the Petzval surface losses its utility and the feed locus becomes poorly defined [1].

Rusch and Ludwig [3] used physical optics (P.O.) to obtain the feed motion path which produces the maximum scan-gain and compared this path with the Petzval surface. In this investigation an axis-symmetric parabolic reflector was considered with $F/D = 0.433$ and $D = 34\ \lambda$. The geometry is shown in Fig. 4.1-2(a) [3]. The coordinate origin is located at the reflector focal point and the z-axis corresponds to the reflector axis of symmetry. Figure 4.1-2(b) shows the xz-plane focal field distributions resulting from y-polarized plane waves incident from scan angles of 0°, 8° and 16° where scanning is confined to the xz-plane (H-plane scanning) [3]. In this figure amplitude

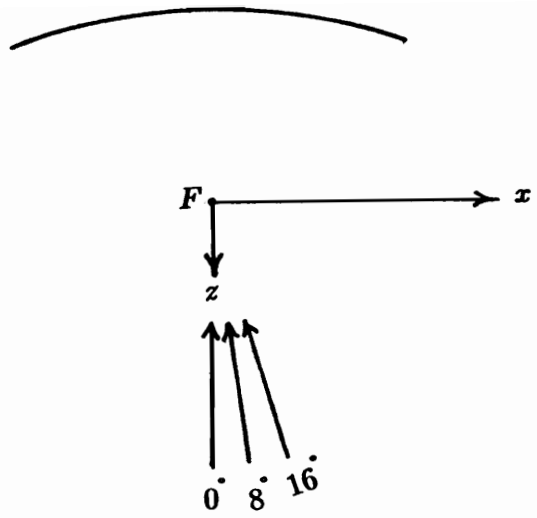

(a)

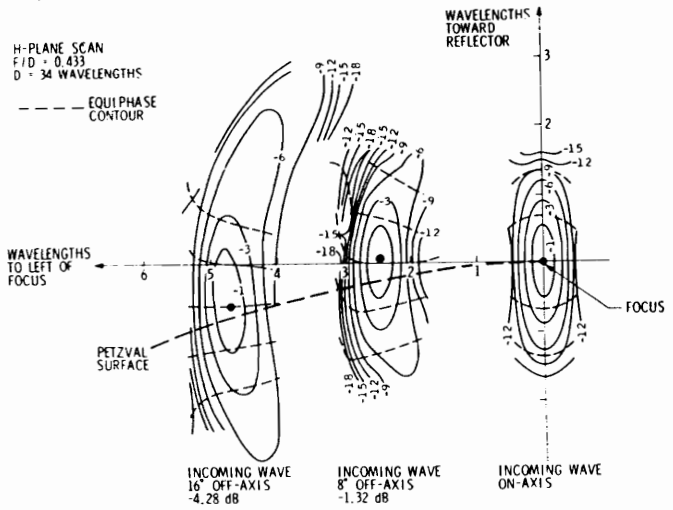

(b)

Figure 4.1-2. Phase and Amplitude contours in the focal region plane-of-scan for a receiving parabolic reflector. (a) Geometry of reflector and incident wave cases. (b) Focal region amplitude contours [3].

contours are depicted by solid lines and phase contours, which are separated by 180 electrical degrees, are depicted by dashed lines. The maximum intensity points for 8° and 16° incidence are, respectively, 1.32 and 4.28 dB below the maximum intensity at the focal point for axial incidence [3]. For scanned incidence the amplitude and phase contours distort and spread, and at the maximum intensity point for each angle of incidence the constant phase contour is approximately parallel to the aperture plane (perpendicular to the reflector axis) [3]. It is noted that the maximum intensity points do not follow the Petzval surface.

Reciprocity permits the contours in Fig. 4.1-2(b) to be interpreted in terms of the secondary pattern produced by a y-polarized infinitesimal electric dipole feed [3]. For example, if the desired scan direction is 8°, then the set of corresponding amplitude and phase contours on which the transmitting dipole is placed will yield the phase and amplitude of the field in that scan direction. Placing the dipole at the maximum intensity point will result in the maximum possible field being transmitted in the 8° scan direction. This field will be 1.32 dB below the power radiated in the boresight direction when the dipole is located at the focal point.

When directional feeds are used it is expected that the optimum gain for a given feed position is achieved by orienting the feed pattern to minimize the amount of power that misses the reflector surface (spillover). For a displaced feed this can be achieved by repointing the feed such that the feed maximum bisects the angle subtended by the edges of the reflector. However, analysis has consistently shown that unless spillover is excessively large (on the order of several dB) a higher gain is achieved for moderate F/D values when the feed axis is parallel to the boresight axis of the reflector [3]. An explanation for this phenomena can be obtained by observation of the constant phase contours in Fig. 4.1-2(b). The constant phase contours at the maximum intensity points are nearly perpendicular to the reflector boresight axis. Consequently, by reciprocity, scan loss will be minimized when the feed phase front is parallel to the constant phase contour which corresponds to a feed pointing direction that is parallel to the reflector boresight axis.

Rusch and Ludwig [3] investigated the use of directional feeds with the

axis-symmetric parabolic reflector. Three directional feed patterns and a dipole feed were considered [3]. The directional feeds had $cos^n\theta$ electric field patterns with $n = 1, 2$ and 3. A plot of the resultant maximum gain contours, calculated with the feed pointing angle parallel to the reflector boresight axis, is shown in Fig. 4.1-3(a) [3]. The curve for the dipole passes through the maximum intensity points shown in Fig. 4.1-2(b). The Petzval surface is also shown in Fig. 4.1-3(a). The maximum-gain contours are slightly displaced towards the focal-plane side of the Petzval surface and converge towards the Petzval surface as feed directivity is increased. A plot of scan loss versus scan angle obtained by moving the different feeds along the corresponding maximum-gain contours is shown in Fig. 4.1-3(b) [3]. For this plot scan angle is given in terms half-power beamwidths for the 34 λ aperture. Also plotted in Fig. 4.1-3(b) is the component of scan loss due exclusively to power missing the reflector surface. This spillover loss amounts to a fraction of a dB in all cases indicating that most of the scan loss is due to phase errors.

4.1.1 Beam Deviation Factor

A useful parameter when dealing with parabolic reflector beam scanning is the beam deviation factor (BDF) which is defined as

$$BDF = \frac{\theta_F}{\theta_B} \tag{4.1-17}$$

where θ_B and θ_F are the beam scan angle and feed tilt angle, respectively, as shown in Fig. 4.1-4 [4]. The BDF depends on the equivalent curvature of the reflector surface. In the limit of a flat plate reflector the BDF goes to unity.

For small feed displacements the direction of the beam maximum occurs when the illumination weighted squared phase error is a minimum. Ruze [1] used this principle to derive the following expression for the BDF of an axis-symmetric parabolic reflector with feed motion restricted to the Petzval surface:

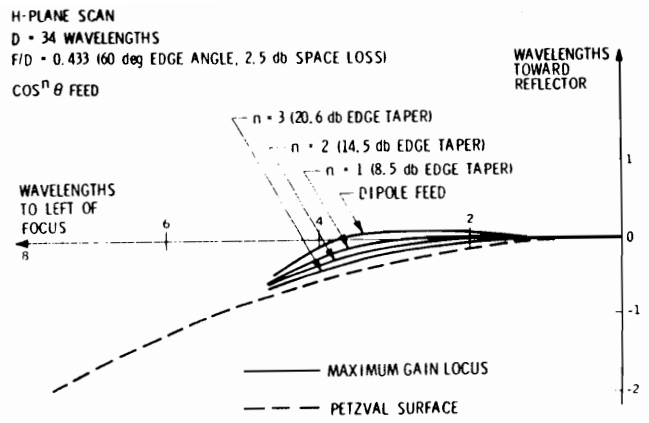

(a)

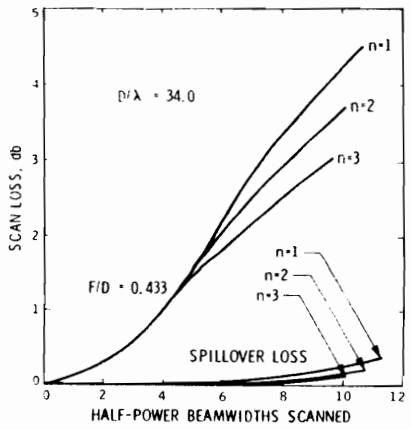

(b)

Figure 4.1-3. Scanning by displacement of a directional feed for an axis-symmetric parabolic reflector with $F/D = 0.433$ and $D = 34\ \lambda$ [3]. (a) Comparison of maximum transmit-gain contours and Petzval surface. (b) Comparison of total scan loss and spillover loss due to displacing but not axially repointing the feed.

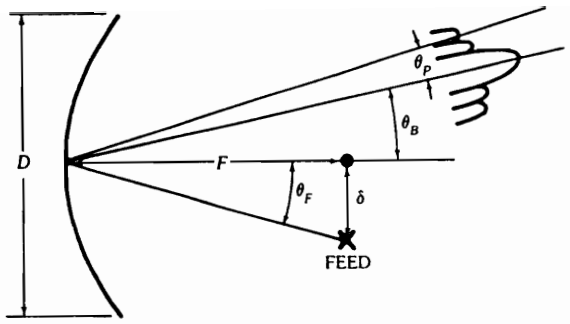

Figure 4.1-4. Definition of feed tilt angle θ_F and beam scan angle θ_B [4].

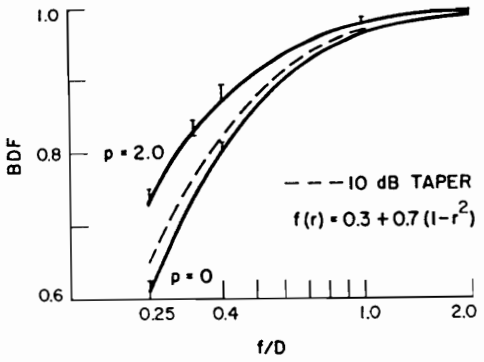

Figure 4.1-5. Beam deviation factor versus F/D value for three different illumination tapers [1].

$$\text{BDF} = \frac{\int_0^a \frac{f(r)\, r^3}{1+\left(\frac{r}{2F}\right)^2}\, dr}{\int_0^a f(r)\, r^3\, dr} \tag{4.1-18}$$

where $f(r)$ is the aperture amplitude distribution and a is the reflector radius. The derivation of (4.1-18) uses the phase factor expansion (4.1-8) with the last term, which gives rise to astigmatism, excluded. This truncation limits the range of validity of (4.1-18) to small scan angles and small F/D values as evident from (4.1-16). It has been noted that for large scan angles and large F/D values Ruze's results more closely follow the results for a parabolic cylinder [5]. Ruze [1] used (4.1-18) to compute BDF versus F/D for three different illumination tapers: a parabolic taper given by $f(r) = (1-r^2)^p$ with $p = 0$ and 2; and a parabolic on a pedestal taper with a 10 dB edge taper given by $f(r) = 0.3 + 0.7(1-r^2)$. These results are shown in Fig. 4.1-5. In all cases the BDF approaches unity in the limit of very large F/D values, as expected.

Lo [4] derived the following useful approximation for the BDF of an axis-symmetric parabolic reflector with a lateral feed displacement δ:

$$\text{BDF} = \frac{sin^{-1}(\delta/F)\{[1+k(\frac{D}{4F})^2]/[1+(\frac{D}{4F})^2]\}}{tan^{-1}(\delta/F)} \tag{4.1-19}$$

where D is the diameter of the reflector, F is the focal length and k is an empirically determined constant such that $0 < k < 1$. Usually k lies in the range of $0.3 < k < 0.7$ with k increasing for higher aperture tapers [4]. For small values of δ/F (4.1-19) can be simplified to [4]

$$\text{BDF} = \frac{1+k\left(\frac{D}{4F}\right)^2}{1+\left(\frac{D}{4F}\right)^2}. \tag{4.1-20}$$

4.1.2 Numerical Results for Scanning by Feed Displacement

Mrstik [5] performed an analysis aimed at establishing the relationship between gain loss and F/D ratio for axis-symmetric parabolic reflectors. For this analysis G.O. was used to compute the root-mean squared (RMS) path-length variation for rays traced from the feed to the aperture plane. The optimum feed positions for beam scanning were obtained by iteratively locating the z-displacement ϵ_z that minimizes the pathlength variation for a given x-displacement ϵ_x [5]. This geometry is shown in Fig. 4.1-1.

Two types of reflector configurations were analyzed by Mrstik: axis-symmetric point fed paraboloids and line-fed parabolic cylinders. The beam deviation factor versus F/D value calculated by Mrstik is shown in Fig. 4.1-6(a) [5]. For parabolic cylinders the beam deviation factor depends more strongly on aperture illumination and is in all cases closer to unity.

For both the axis-symmetric paraboloid and the parabolic cylinder curves of maximum scan angle versus normalized aperture diameter such that scan induced gain loss does not exceed 1 dB were generated [5]. Results for the axis-symmetric paraboloid with F/D values of 1 to 100 are shown in Fig. 4.1-6(b) [5]. Larger scan angles are possible for the tapered aperture distribution because the effective aperture diameter is reduced.

Examples of scanned beams are shown in Figs. 4.1-7 and 4.1-8 [4]. Figure 4.1-7 shows the secondary radiation patterns for an axis-symmetric reflector with $F/D = 0.4$ with the main beam scanned from 0 to 10 half-power beamwidths (HPBW) off axis [4]. The effects of coma aberration can be observed by the appearance of the large first sidelobe on the axis side of the main beam. This is commonly referred to as the coma lobe. In addition to the appearance of the coma lobe, the main beam broadens with increasing scan and the first sidelobe on the other side decreases, changes sign, and merges with the main beam and second sidelobe [4]. Figure 4.1-8 shows secondary radiation patterns for an axis-symmetric reflector with $F/D = 1$ with the main beam scanned from 0 to 10 HPBW off axis [4]. Comparison with Fig. 4.1-7 shows the improved scanning characteristics associated with reflectors with higher F/D values [4].

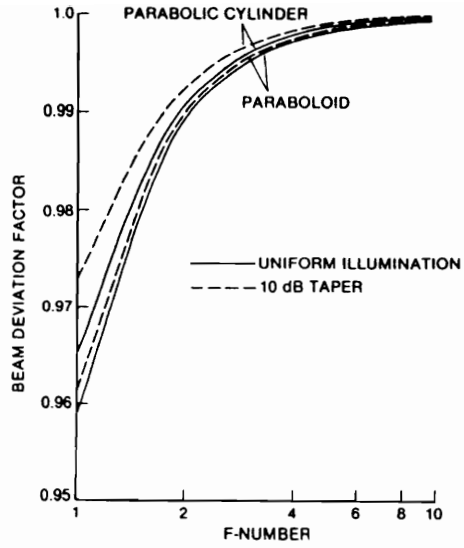

(a)

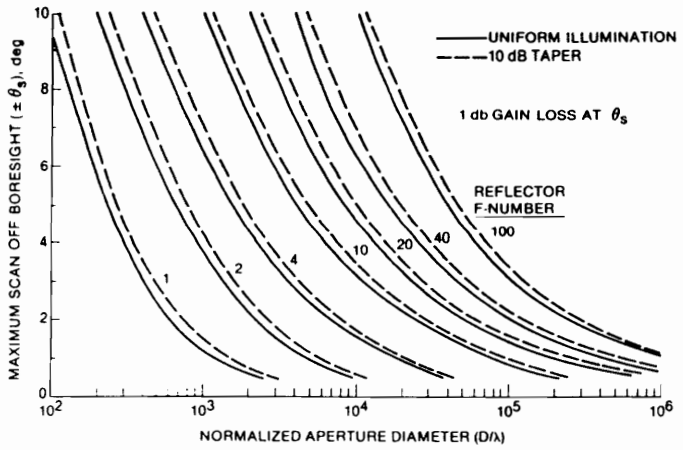

(b)

Figure 4.1-6. Numerical results obtained by Mrstik for an axis-symmetric parabolic reflector [5]. (a) Beam deviation factor versus F/D ratio (F number). (b) Maximum scan angle for 1 dB gain loss; axis-symmetric parabolic reflector antenna.

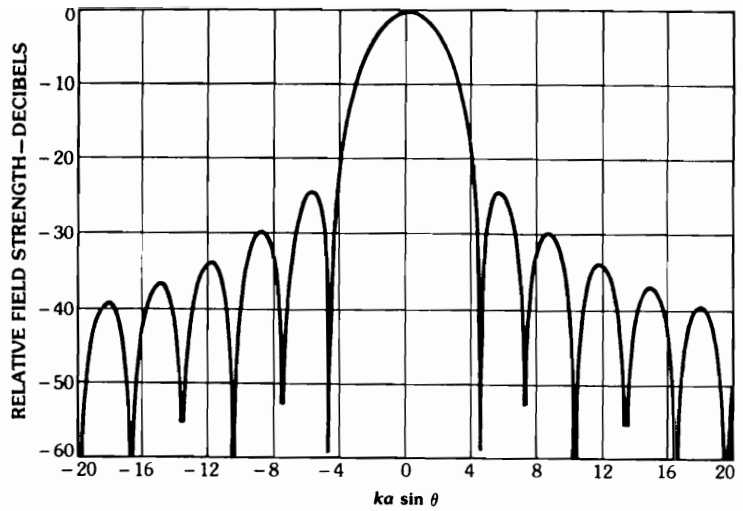

(a)

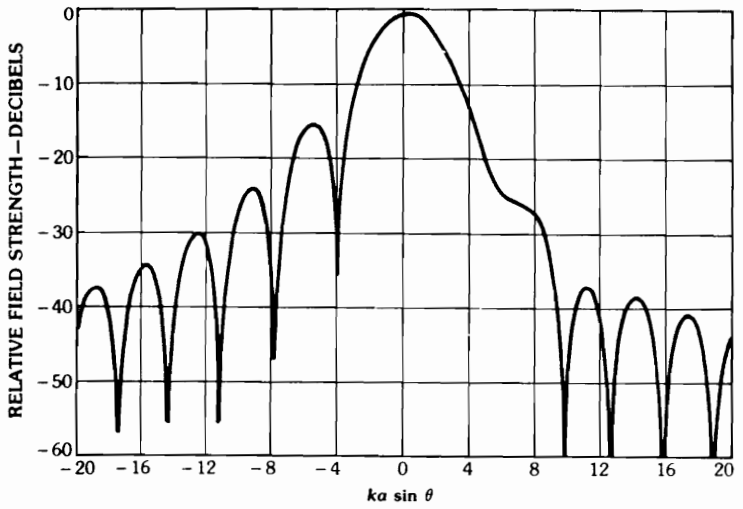

(b)

Figure 4.1-7. Axis-symmetric parabolic reflector far-field patterns for $\phi = 0^\circ$ as a function of lateral feed displacement in terms of the number of beamwidths scanned (F/D = 0.4, ET = -10 dB, BDF = 0.82) [4]. (a) 0 HPBW. (b) 2 HPBW. (c) 6 HPBW. (d) 10 HPBW.

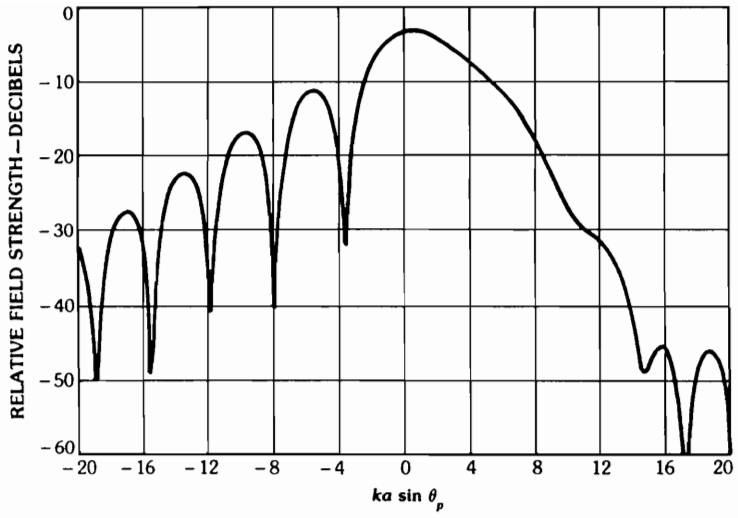

(c)

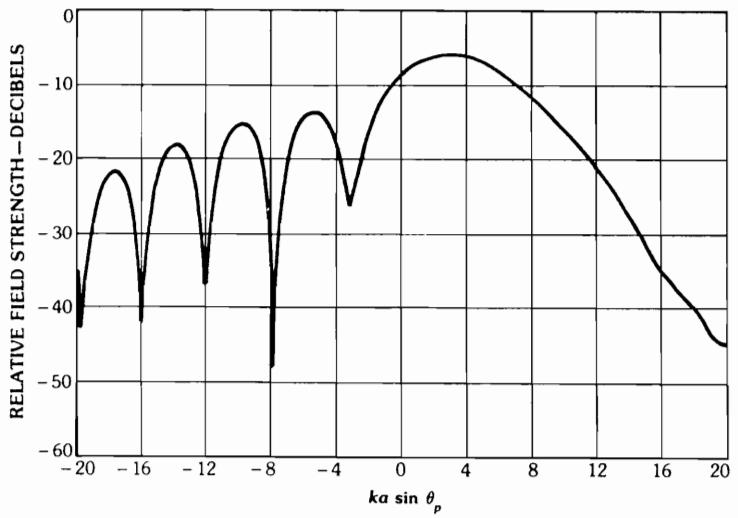

(d)

Figure 4.1-7 (continued).

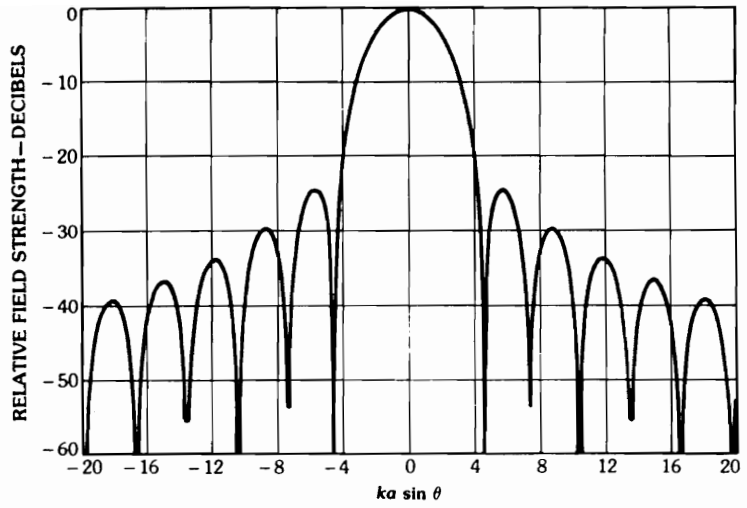

(a)

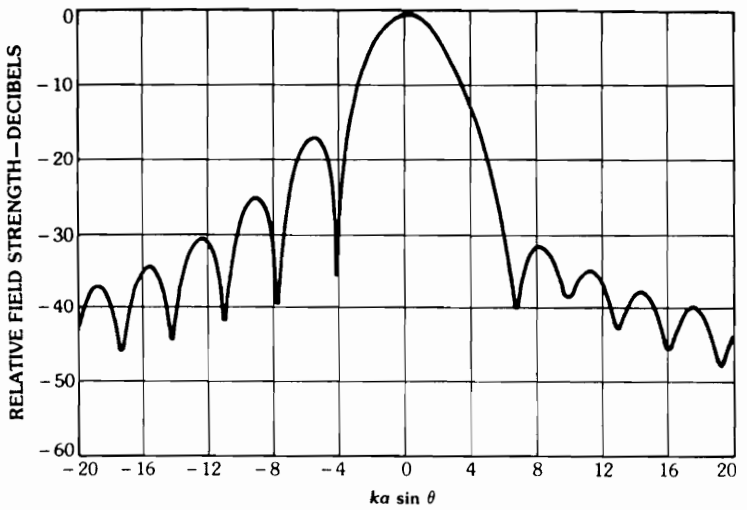

(b)

Figure 4.1-8. Axis-symmetric parabolic reflector far-field patterns for $\phi = 0^{\circ}$ as a function of lateral feed displacement in terms of the number of beamwidths scanned (F/D = 1.0, ET = -10 dB, BDF = 0.966) [4]. (a) 0 HPBW. (b) 2 HPBW. (c) 6 HPBW. (d) 10 HPBW.

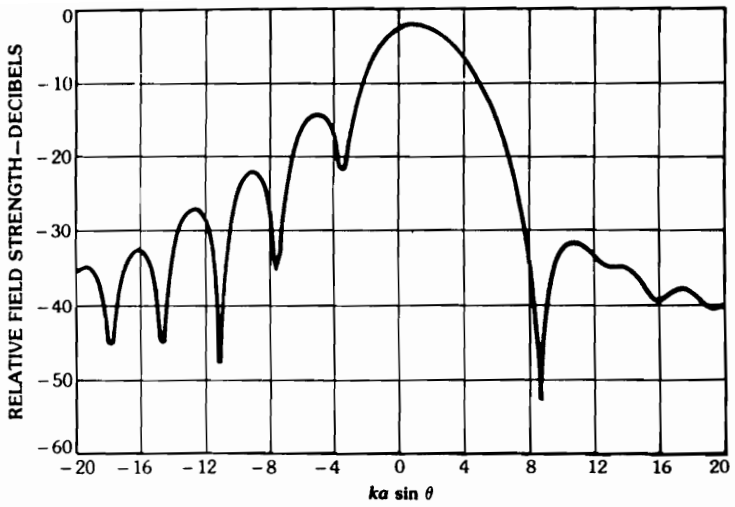

(c)

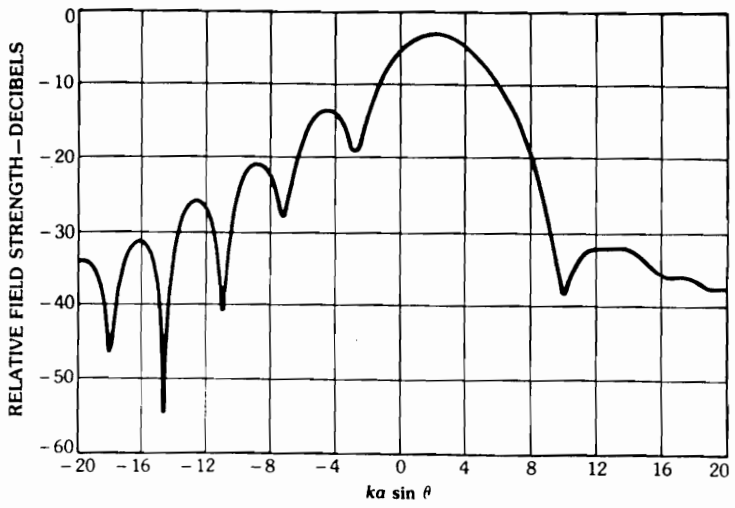

(d)

Figure 4.1-8 (continued).

A general result for parabolic reflectors is that for a given reflector diameter better scan performance can be achieved with a larger F/D value. This conclusion is evident from Fig. 4.1-6(b) and is demonstrated by the patterns in Figs. 4.1-7 and 4.1-8. Drawbacks to using reflectors with high F/D values are that they require larger support structures for the feed and larger feed motions to achieved a given angular scan as compared to reflectors with lower F/D values. The larger feed motions are a result of the beam deviation factor approaching unity for large F/D values.

4.1.3 Offset Reflectors

Previous discussions only applied to axis-symmetric parabolic reflectors. For axis-symmetric configurations the feed antenna or subreflector is located in front of the aperture producing blockage. Aperture blockage can be reduced (efficiency increased) by offsetting the feed assembly. In general an offset reflector is constructed from a sector of an axis-symmetric parent reflector. For example an offset parabolic reflector can be formed by intersecting a parent paraboloid of revolution with a circular or elliptic cone with its tip at the focal point [4]. The geometry of an offset reflector is shown in Fig. 4.1-9(a) [4]. The parameters shown on this figure are defined below:

F = focal length
D = reflector diameter
H = offset height ($H = -D/2$ for axis-symmetric reflectors)
d = offset height of the circular projected aperture center = $D/2 + H$
ψ_u = angle subtended to the upper tip = $2\ tan^{-1}[(D+H)/2F]$
ψ_c = angle subtended to the center of the center of the projected aperture = $2\ tan^{-1}[(D/2+H)/2F]$
ψ_L = angle subtended to the lower tip = $2\ tan^{-1}[H/2F]$
ψ_B = angle subtended in the bisect direction = $(\psi_u + \psi_L)/2$
ψ_s = half-angle subtended to the upper and lower tips = $(\psi_u + \psi_L)/2$

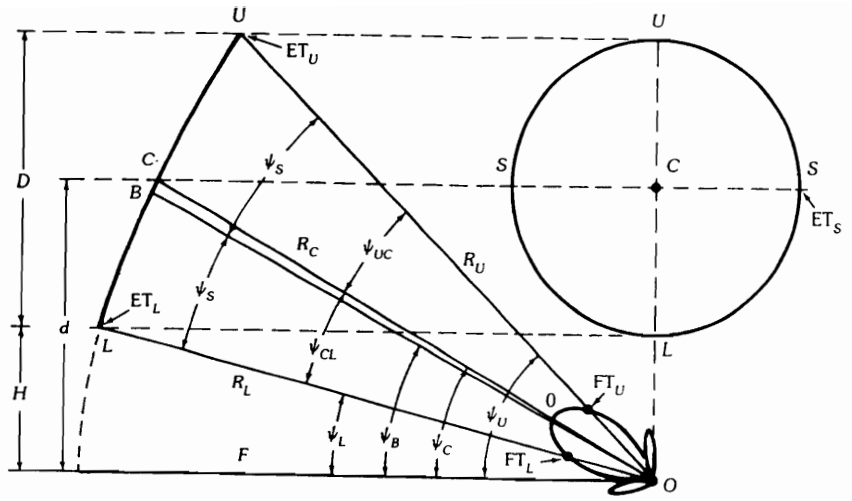

(a)

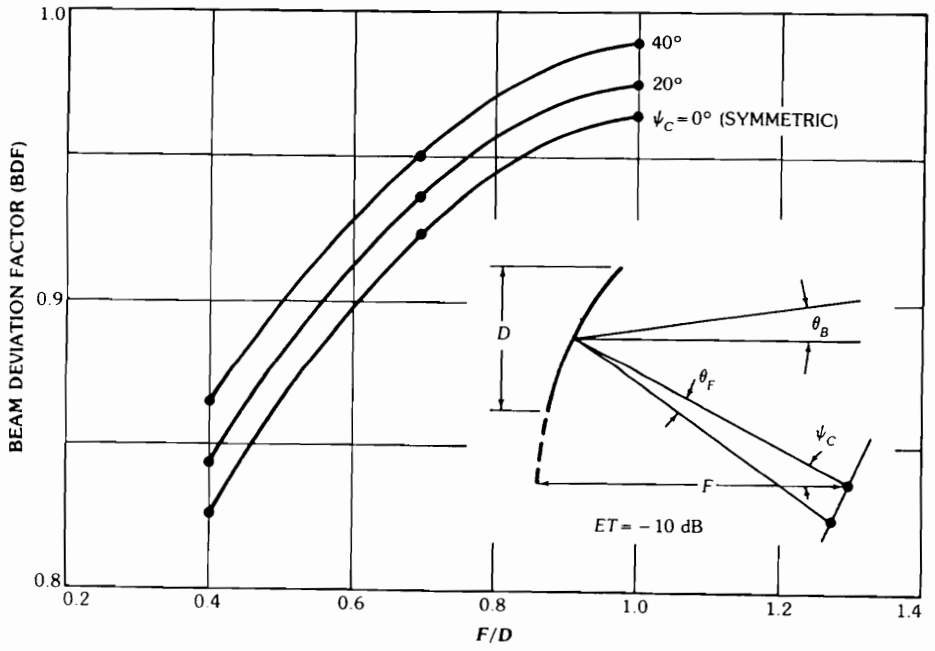

(b)

Figure 4.1-9. Offset parabolic reflectors. (a) Geometry of an offset parabolic reflector antenna [4]. (b) Angle definitions for the BDF of an offset paraboloid and BDF versus F/D value for different offset angles ψ_c [4].

ψ_{sc} = half-angle subtended to the right and left sides =

$$\sin^{-1}\left[\frac{D}{\sqrt{(H+D/2)^2+(D/2)^2+\left[\frac{(D/2)^2+(H+D/2)^2}{2F}-F\right]}}\right]$$

D_p = parent parabola diameter = $2(D+H)$ for $H \geq -D/2$.

The phase errors created by small feed displacements with offset reflectors are better characterized by the ratio of the focal length to the parent reflector diameter, F/D_p [4]. This value is given in terms of reflector diameter and offset height by

$$F/D_p = \frac{F}{2(D+H)}. \tag{4.1-21}$$

For scanning applications the offset height H should be kept as small as possible as evident from Fig. 4.1-6(b) with F/D replaced by F/D_p. The BDF of an offset reflector expressed in terms of the angles defined in Fig. 4.1-9(b), as a function of F/D value for different offset angles ψ_c, are shown in Fig. 4.1-9(b) [4]. It is noted that offset reflectors usually exhibit better scanning characteristics for negative scan directions ($\theta_B < 0$) because of the increase in the area of the projected aperture.

4.1.4 Polarization Considerations

Polarization purity is required for many communication and remote sensing applications and a high isolation between orthogonally polarized modes is desirable. Cross-polarization is a measure of polarization isolation. Cross-polarization in the far-field radiation pattern is introduced in two ways: from the geometrical configuration of the reflector(s) and feed position; and from cross-polarization in the feed radiation pattern. The latter contribution will not be considered here.

Figure 4.1-10 shows a typical electric field distribution in the aperture of

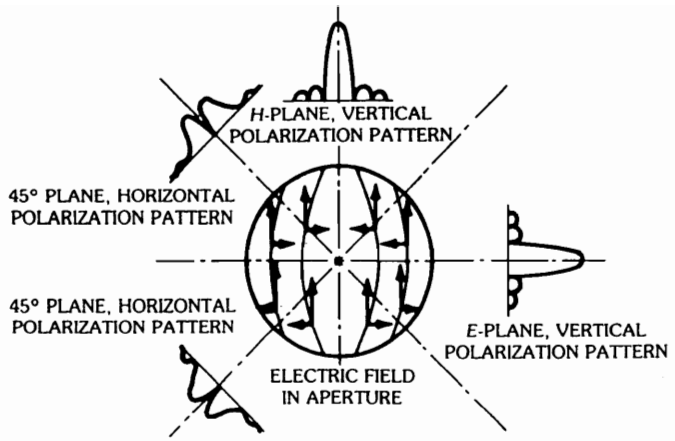

Figure 4.1-10. Typical electrical field vector directions in the aperture of an axis-symmetric parabolic reflector feed by a vertically polarized feed [4].

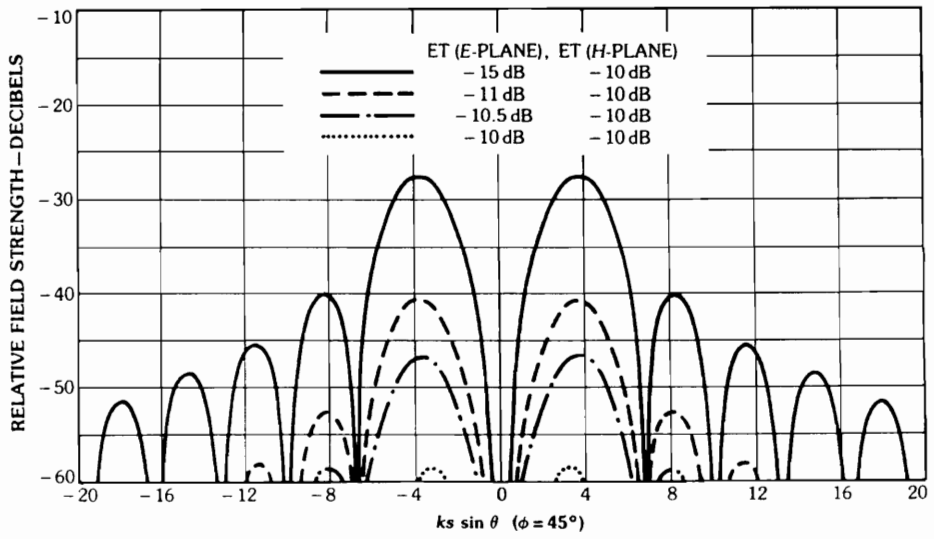

Figure 4.1-11. Cross-polarized fields in the $\phi = 45^\circ$ plane (normalized with respect to the peak) for an axis-symmetric reflector ($F/D = 0.3$) illuminated by a linearly polarized feed with three types of unbalanced E- and H-plane patterns and one balanced pattern [4]. The relative edge tapers (ET) of the feed patterns considered are indicated on the top of the figure.

an axis-symmetric parabolic reflector illuminated by a balanced vertically polarized feed [4]. This figure demonstrates the mechanism of cross-polarization generation. In both the E and H planes the horizontal field components, which give rise to cross-polarization, cancel due to reflector symmetry and no cross-polarization is generated in these planes. In the 45° planes, however, the symmetry is not present, the horizontal field components do not cancel and cross-polarization is produced. Typical 45°-plane cross-polarization patterns are shown in Fig. 4.10. For an axis-symmetric parabolic reflector illuminated by a linearly polarized feed cross-polarization is maximum in the 45° planes [4].

A feed is called unbalanced if it has different E- and H-plane patterns. The aperture field distribution produced by an unbalanced feed is not symmetric resulting in increased cross-polarization. The 45°-plane cross-polarization patterns produced by an axis-symmetric parabolic reflector fed by a balanced feed and several types of unbalanced feeds are shown in Fig. 4.1-11 [4]. Cross-polarization is also dependent on F/D value and edge taper. A higher F/D value, which corresponds to a flatter reflector, produces less cross-polarization. There is no cross-polarization in the limit of a flat plate, $F/D \to \infty$. Likewise, a higher edge taper corresponds to an effective increase in F/D value, since the illuminated diameter is decreased, and therefore reduces cross polarization.

In contrast to axis-symmetric parabolic reflectors which have very low levels of cross-polarization offset reflectors fed by linearly polarized feeds can have very high levels of cross-polarization, even for balanced feeds [4]. For offset reflectors the amount of cross-polarization is least in the plane of symmetry and greatest in the plane orthogonal to the plane of symmetry, where these planes are the xz-plane and the yz-planes respectively as shown in Fig. 4.1-9(a) [4]. For offset parabolic reflectors cross-polarization depends on the feed pointing angle and increases with the angle between the feed axis and the axis of the parent paraboloid, ψ [4]. In Fig. 4.1-12 cross-polarized fields in the $\phi = 90^\circ$ plane are shown versus feed-axis tilt angle ψ for an offset parabolic reflector with a diameter of $D = 100\ \lambda$ and an offset hight of $H = 20\ \lambda$. In practice, in order to reduce spillover, the feed axis is usually tilted toward the center of the reflector by the bisect angle ψ_B, which is defined as the average of the angles subtended by the upper and lower edges of the reflector. Levels of cross-polarization for

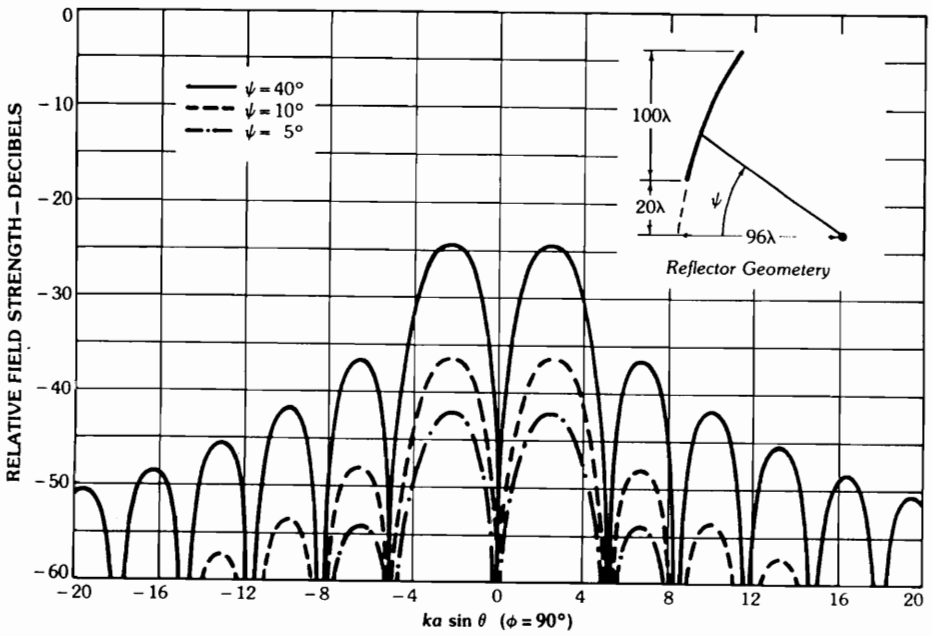

Figure 4.1-12. Cross-polarized fields in the $\phi = 90^{\circ}$ plane (normal to the offset plane) for an offset parabolic reflector illuminated by a balanced linearly polarized feed for various feed-axis tilt angles ψ [4].

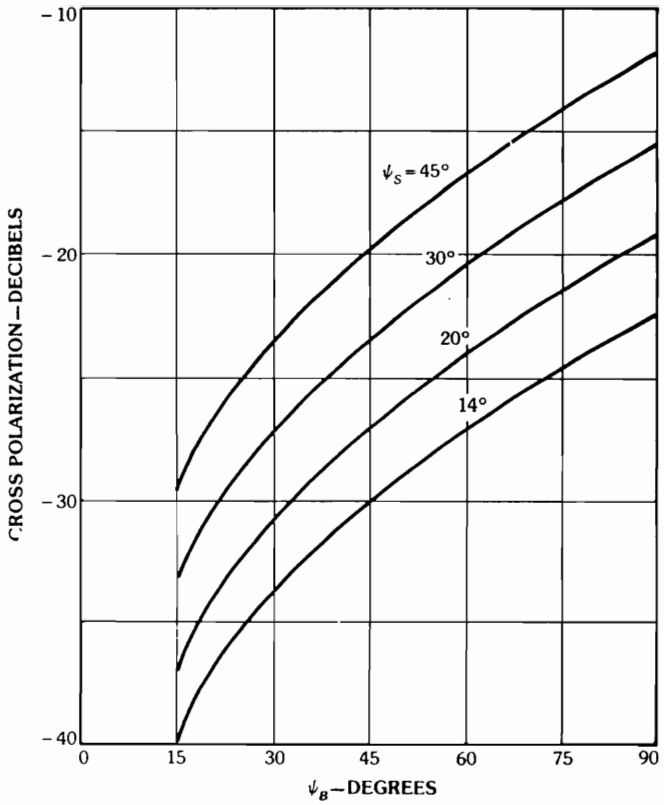

Figure 4.1-13. Maximum cross-polarization level of an offset parabolic reflector illuminated by a balanced linearly polarized feed [4].

different values of bisection angle ψ_B and half-angle ψ_s (see Fig. 4.1-9(a)) are shown in Fig. 4.1-13 [4]. It is noted that the bisection angle is a measure of reflector offset and the half angle is a measure of reflector curvature; therefore, Fig. 4.1-13 shows that cross-polarization increases both with increasing reflector offset and increasing reflector curvature.

Both axis-symmetric and offset reflectors produce low levels of cross-polarization when illuminated by a balanced circularly polarized feed, however, offset reflectors produce beam squinting which is a shift of the main beam from the reflector axis [4]. The amount of squint depends both on the reflector geometry and the feed tilt angle and squint increases for combinations which produce higher levels of cross-polarization for a linearly polarized feed [4]. The following expression is a good approximation for the beam squint angle θ_s [4]:

$$\theta_s = \mp \sin^{-1}\left(\frac{\sin \psi_B}{4\pi(F/\lambda)}\right) \tag{4.1-22}$$

where the $\mp$ signs are for right and left circularly polarized cases, respectively.

4.2 Electronic Scanning

The scan capability of a parabolic reflector with a single displaced feed element is very limited and is dependent on the F/D value [1,4]. Phase errors associated with beam scanning cause the focal plane field distribution to shift from the reflector focal point and spread as discussed in Chapter 3. This energy can be recaptured and scan characteristics can be improved by using a distributed feed system such as a phased array feed. When using an array feed it is possible to scan the beam using a large stationary array or a small movable array. Both of these cases are now discussed.

4.2.1 Beam Scanning with Stationary Array Feeds

The advantages of using a stationary array feed, particularly for space

applications, is that there are no moving parts and it is possible to form multiple beams. The disadvantage is that a large array must be used to intercept the focal plane energy distribution which moves during scanning as is shown in Fig. 4.1-2(b) [3].

A comprehensive investigation of beam scanning using a stationary array feed with an axis-symmetric parabolic reflector was performed by Blank and Imbraile [6]. This investigation lead to simple "rules of thumb" for the optimum choice of planar array feed configuration (number and type of elements). The reflector configuration addressed consists of a single reflector with a circular diameter D and a maximum subtended angle $\widehat{\psi}$ as shown in Fig. 4.2-1(a) [6]. The feeds considered are a single circular element, which is used as a reference for gain calculations, and a triangular grid array of 7, 19 or 37 elements as shown in Fig. 4.2-1(b) [6]. The elements of each array are identical and have circularly symmetric unidirectional electric-field radiation patterns of the form [6]

$$f(\psi) = cos^q(\psi). \tag{4.2-1}$$

The minimum spacing between element centers d_e is related to the exponent q in (4.2-1) by [6]

$$d_e = \sqrt{\frac{q+0.5}{b}} \tag{4.2-2}$$

where the value of b depends on the type of element used and d_e is given in wavelengths. In this investigation Blank and Imbraile [6] considered two types of elements: circular waveguides with $b = 2.07$, and radiators with a higher effective aperture, such as disk-on-rod elements, for which $b = 2.47$ was used. Spacing element centers greater than d_e apart would imply gain loss since the "open" areas left between the elements would not be available to capture the incident energy; therefore, in the investigation, all elements spacings were set to d_e [6]. The array diameter d_f of such a "well packed" feed array is given by [6]

$$d_f = kd_e \tag{4.2-3}$$

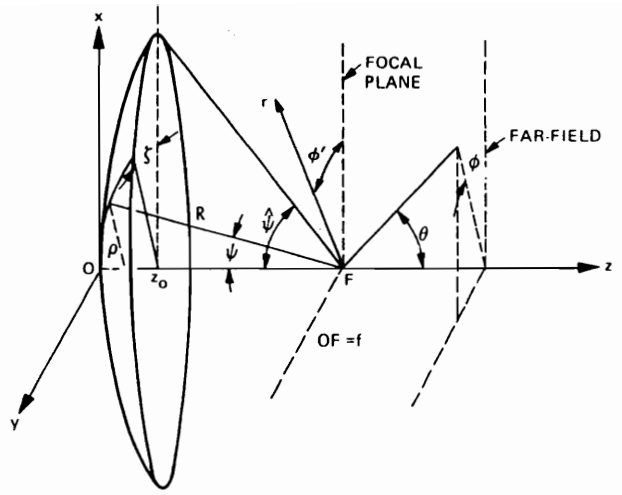

(a)

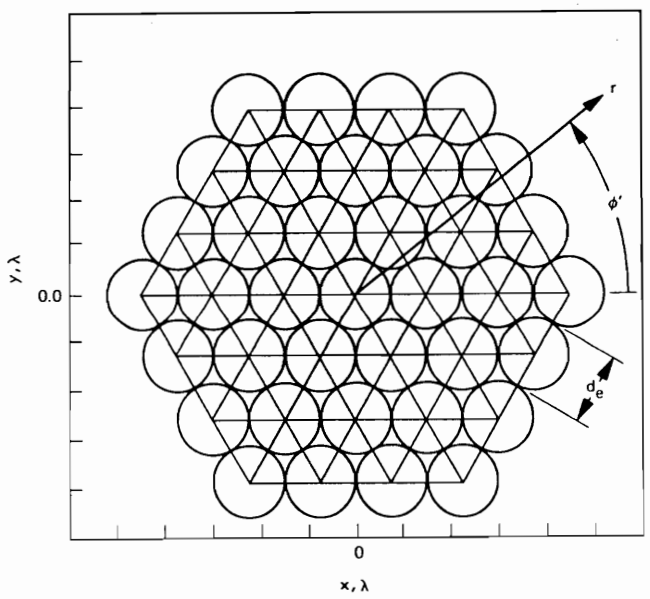

(b)

Figure 4.2-1. Geometrical parameters of the parabolic reflector and array feed used by Blank and Imbraile [6]. (a) Reflector parameters. (b) Triangular grid array of circular elements showing the focal plane coordinates r, ϕ'.

where $k = 1, 2, 3$ and 7 corresponds to feed element numbers $N = 1, 7, 19$ and 37, respectively.

Blank and Imbraile [6] also considered the effects of reflector surface distortions of the form

$$\Delta z = \epsilon \rho^s cos(L\zeta) \tag{4.2-4}$$

where ϵ is the maximum deviation in wavelengths, s is a real number, ρ is the distance from the z-axis to a point on the reflector surface normalized to the reflector radius, L is the integer number of periodic scallops in the distorted reflector and ζ is the angle shown in Fig. 4.2-1(a). Blank and Imbraile [6] performed analysis for the following parameter values: $\epsilon = 0.0$, 0.12 and 0.2; $s = 1$ and 2; and $L = 3$. These values are based on typical data for gravity-induced distortions as a function of pointing angle for large ground-based reflectors [6].

For distorted reflectors the optimum choice of the element diameter d_e for maximum on-axis gain with a given number of array elements, N, depends on the need for greater or lesser granularity and/or greater or lesser aperture area to match the array feed to the focal plane field distribution [6]. For a 7 element array feed and the gravitational distortion parameters listed above the element diameter which gives the maximum on-axis gain, d_{e7}, is approximately equal to the diameter required by a single feed element to achieve a -10 dB edge taper, d_{e1} [6]. For an 18 or 37 element array feed and the gravitational distortion parameters listed above the element diameters which give maximum on-axis gain, d_{e18} and d_{e37}, are approximately equal to one third of the diameter required by a single feed element to achieve a -10 dB edge taper, $d_{e1}/3$ [6]. The optimum element diameters can be expressed as a function of reflector F/D value and element efficiency b as follows [6]:

$$\mathrm{d}_{e7} \simeq \mathrm{d}_{e1} \simeq \sqrt{\frac{9.2}{b}} \left(\frac{F}{D}\right) \tag{4.2-5 a}$$

$$d_{e19} = d_{e37} \simeq \sqrt{\frac{9.2}{b}} \left(\frac{F}{3D}\right). \tag{4.2-5 b}$$

The corresponding array configurations for $N = 1, 7, 19$ and 37 elements are

shown in Fig. 4.2-2(a) [6].

Calculated gain loss as a function of scan angle (in half-power beamwidths) for an axis-symmetric parabolic reflector with $F/D = 1$ and distortion parameters $\epsilon = 0,\ 0.12\ \lambda,\ 0.2\ \lambda,\ s = 2$ and $L = 3$ are shown in Fig. 4.2-2(b) [6]. The optimum element diameters for maximum on-axis gain for this reflector where found to be $d_{e7} = 2.1\ \lambda$, $d_{e19} = 0.8\ \lambda$ and $d_{e37} = 0.71\ \lambda$, which approximately satisfy (4.2-5) [6]. Comparison of the results in Fig. 4.2-2(b) with the array diameters shown in Fig. 4.2-2(a) indicate that the maximum possible scan angle for a given array (scan limit) is dictated by the angle for which the focal plane distribution shifts past the outer elements of the array. The array with the largest diameter, that with $N = 7$ elements, can achieve scan angles of approximately 2.25 HPBW, while the array with the smallest diameter, that with $N = 19$ elements, can only achieve scan angles of approximately 1.5 HPBW.

It is noted from Fig. 4.2-2(b) that scan performance for the 7-element array is not continuous over the whole scan range. This is because the element spacings for this array are too coarse to continuously match the focal plane field distribution over the scan range. Blank and Imbraile [6] state that for continuous scanning the far-field beam crossovers of two adjacent elements should not be lower than their 3 dB points, which corresponds to one half-power beamwidth [6]. To achieve this the elements spacings must satisfy the following relationship [6]:

$$d_e \leq \frac{1.16\ \lambda}{\text{BDF}}\left(\frac{F}{D}\right) \tag{4.2-6}$$

where BDF is the reflector beam deviation factor. It is noted that the restrictions imposed on d_e by (4.2-6) are not always consistent with the requirements for maximum on-axis gain. For example, with $F/D = 1$ and a -10 dB edge taper Fig. 4.1-6(a) gives BDF $\simeq 0.96$ for which (4.2-6) gives $d_e \leq 1.2\ \lambda$; however, for this reflector and a 7 element array feed on-axis gain is maximized for $d_{e7} \simeq 2.1\ \lambda$ which does not satisfy (4.2-6) and, therefore, results in "stepped" beam scanning as is shown in Fig. 4.2-2(b). For a 37 element array feed on-axis gain is maximized for $d_{e37} \simeq 0.71\ \lambda$ which satisfies (4.2-6) and, therefore, allows continuous beam scanning over the entire scan range as shown

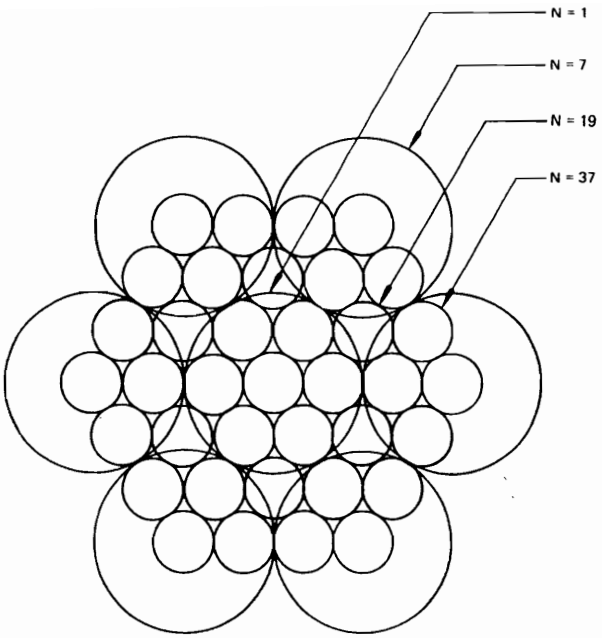

(a)

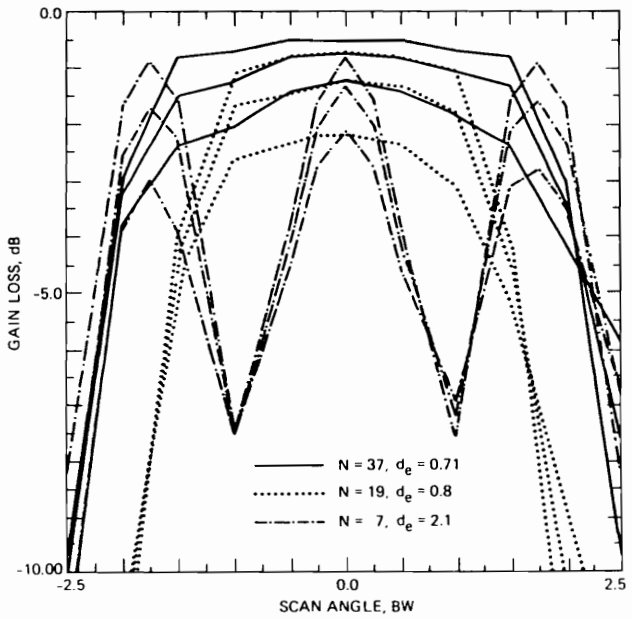

(b)

Figure 4.2-2. Array fed parabolic reflector results obtained by Blank and Imbraile [6]. (a) Optimum array feed configurations for $N = 1$, 7, 19 and 37 elements. (b) Gain loss as a function of scan angle ($F/D = 1.0$, $\epsilon = 0$, 0.12 λ, 0.2 λ, $s = 2$ and $L = 3$.

in Fig. 4.2-2(b).

4.2.2 Beam Scanning with Movable Array Feeds

Beam scanning with a movable array feed allows for the use of a smaller array since the array can be continuously repositioned to the optimum location to capture the focal plane energy distribution. Mechanically, however, a movable array increases complexity and is particularly undesirable for space applications where the inertial torque created by moving a massive feed assembly must be accounted for. The added calibration (for radiometers) and reliability problems which result from the use of flexible cables necessary for a movable feed must also be considered.

Rudge and Withers [7] pioneered the use of movable array feeds. They noted that the Fourier transform relation between the reflector aperture distribution and the focal plane field distribution remains valid for incident plane waves inclined (scanned) with respect to the reflector boresight direction. However, for such inclined incident waves the Fourier transform relationship is expressed between the reflector aperture plane and one of a set of transform planes which are normally inclined to the centerline of the angular cone subtended by the perimeter of the reflector aperture (i.e. the subtended angle at the new "focal point" must remain constant and equal to $2\theta^*$) [7]. The locus of transform planes and associated electric field distributions for a plane wave incident from the boresight direction and a plane wave incident from the scan angle ψ are shown in Fig. 3-1(b) [7]. Although the Fourier transform relationship is maintained for scanned incidence significant distortion of the focal plane field distribution, particularly coma aberration, is observed due to phase errors introduced by the reflector surface.

Rudge and Withers [7] constructed an experimental configuration for operation at 5 GHz with a cylindrical offset parabolic reflector having a width of 1.8 m and an F/D value of 0.5. This configuration is shown in Fig. 4.2-3. The array feed system is a linear array of eight elements and the feed network was designed to produce a sampled Fourier transform on the input field as discussed in Sec. 3.4 [7]. The experimental array configuration introduced an insertion loss

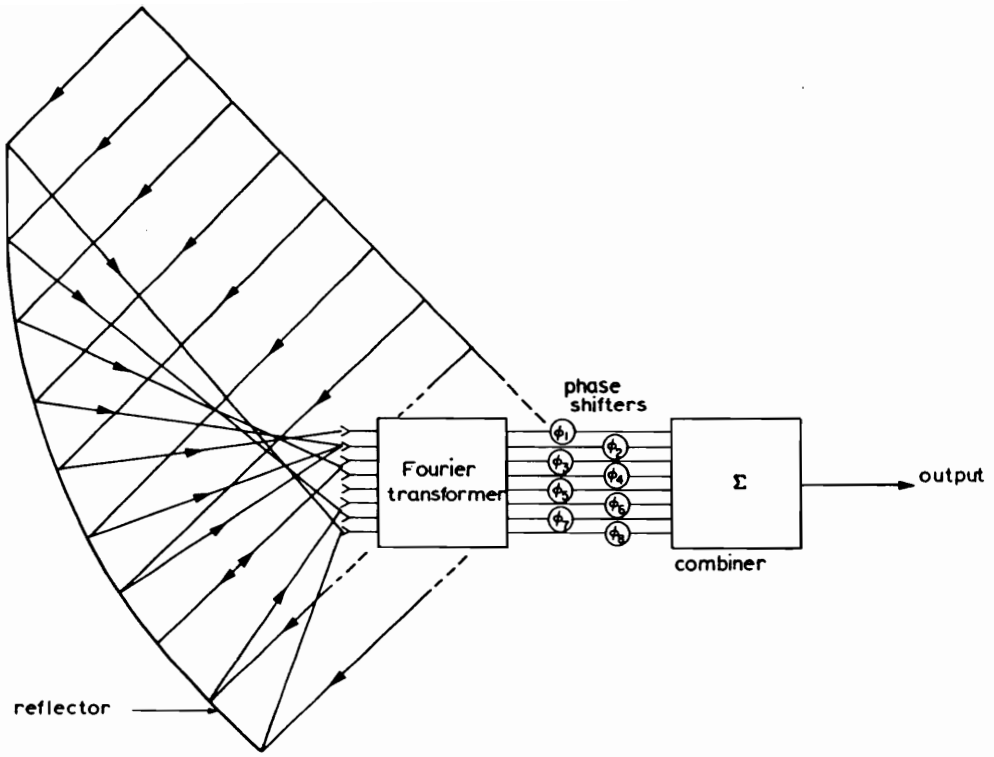

Figure 4.2-3. Schematic of experimental cylindrical reflector configuration and adaptive primary-feed block used by Rudge and Withers [7]. The reflector diameter is 1.8 m and $F/D = 0.5$ [7].

on the order of 1 dB and was mounted on a movable carriage to permit the aperture plane of the array to be moved around the focal region [7].

For each scan angle the feed array position and element excitations were obtained by experimental iteration [7]. The reflector configuration was moved so that the target transmitter made an angle of ψ with the reflector boresight. The feed array was then moved along the $2\theta^*$ locus (see Fig. 3-1(b)) and placed at the point corresponding to the highest output power. The array feed phase shifters were then adjusted to maximize the output power. With the new element phases the array feed was again moved along the $2\theta^*$ locus until a new point giving the highest output power was reached. The phase shifters were then readjusted to maximize output power at the new point. This procedure was repeated until the array location and element excitations corresponding to the maximum received power were obtained. The following three measurements were then performed:

a. Secondary radiation pattern with a single feed place at the center of the array.

b. Transform field distribution across the plane of the array.

c. Secondary radiation pattern with the array feed.

The results of these measurements for $\psi = 0^\circ$ and $\psi = 15^\circ$ are shown in Fig. 4.2-4(a)-(c).

The measurements are in close agreement with theory. Comparison of Figs. 4.2-4(a) and (b) demonstrated the predicted double Fourier transform relationship between the far-field radiation pattern and the transform plane field distribution. For the array feed a scan range of $\pm 15^\circ$ is observed with less than 0.5 dB gain loss. Comparison of Figs. 4.2-4(a) and (c) indicate a slightly higher sidelobe level in the boresight direction for the array feed. This is the result of increased aperture blockage due to the array feed [7].

Hung and Mittra [8] performed a numerical investigation into the scan capabilities of an axis-symmetric parabolic reflector fed by a small movable array

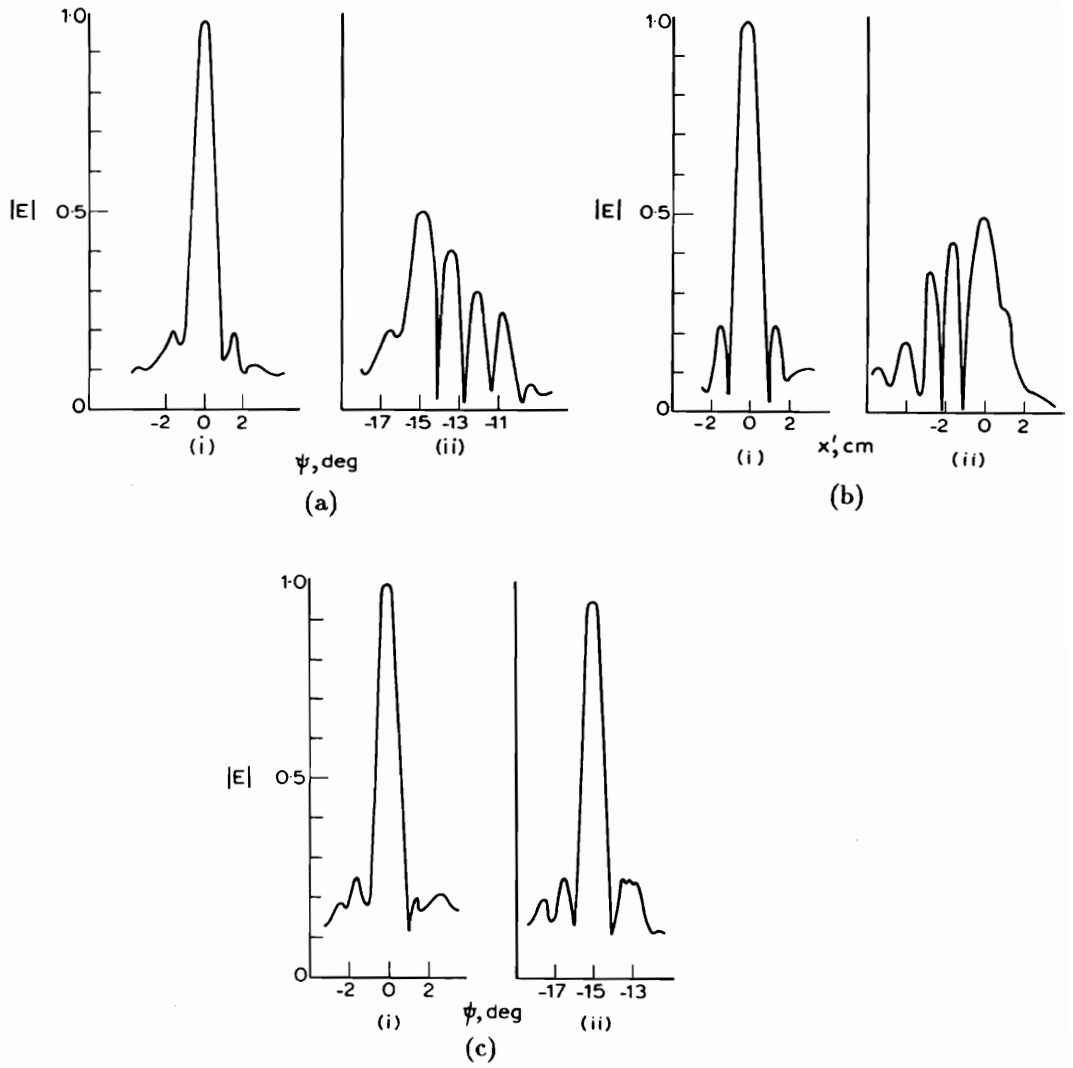

Figure 4.2-4. Experimental results obtained by Rudge and Withers for the reflector configuration shown in Fig. 4.2-3 at 5 GHz [7].

(a). Scanned pattern with conventional single-element primary feed. (i) Feed on axis. (ii) Feed offset to scan the beam by 15°.

(b). Transform plane field distributions. (i) Focal plane with target transmitter along antenna boresight. (ii) Reflector transform plane with target transmitter offset 15°.

(c). Steered-antenna radiation pattern with adaptive (array) primary feed (i) Primary feed center at focal point (boresight). (ii) Primary feed center offset to scan the beam by 15°.

feed. The reflector geometry used by Hung and Mittra is identical to that shown in Fig. 4.1-2. The reflector diameter is 360 in (9.14 m) with $F/D = 0.48$ [8]. The focal region field distribution was calculated using reciprocity by repeatedly computing the radiated far field of the reflector in the intended scan direction for different feed locations in the focal region [8]. The far-field patterns were calculated using a Fourier-Bessel series technique in which the physical optics currents on the reflector surface are expanded in terms of elementary sinusoidal functions using a fast Fourier transform algorithm and the surface integration is carried out analytically in terms of the Fourier-Bessel series [8]. Calculations were performed at $f = 19.17$ GHz corresponding to an aperture diameter of $D = 548\ \lambda$ [8].

The array size, position and feed element spacings were determined from the focal region distribution [8]. The array used is a 27 element RN^2 array with interelement spacings of 0.01 m and identical TE_{11} mode circular horn elements [8]. The array center was located at the point corresponding to maximum intensity in the focal region distribution and the element excitations corresponded to the complex conjugate of the focal plane distribution at the element locations. Secondary patterns of the parabolic reflector fed by both a single horn and the 27 element array feed are shown in Fig. 4.2-5 for the boresight direction and scan directions of 2.5° and 5° [8]. For the 27 element array feed improvement in both gain and sidelobe level is observed compared to the results for the single horn; however, for the array feed considerable coma is observed in both the 2.5° and 5.0° scan directions indicating that further improvement could be expected by the use of a larger feed array.

Lam et al. [9] performed a comparison of directivity optimization and CFM. The reflector configuration considered consisted of an offset parabolic reflector with diameter $D = 108.15\ \lambda$, focal length $F = 94.87\ \lambda$ and offset height $H = 16.87\ \lambda$ [9]. The diameter of the parent reflector is $D_p = 2(D + H) = 250\ \lambda$ and $F/D_p = 0.38$, which is considered a deep dish [9]. Beam scanning to 2.85° (five half-power beamwidths) was accomplished using a 7-element feed array. The center of the feed array was placed at the position corresponding to maximum gain in the 2.85° direction for a single feed [9]. The feed elements used were y-polarized with identical $cos^q(\theta)$ element patterns [9]. The element

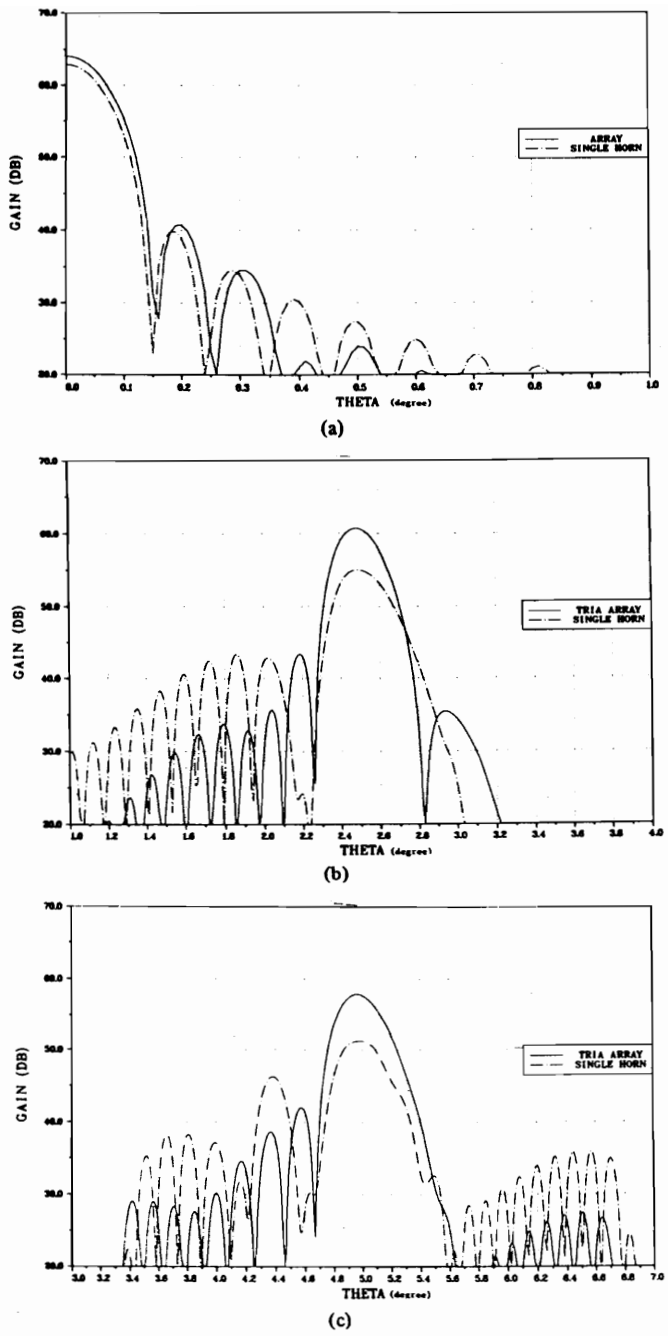

Figure 4.2-5. Secondary patterns obtained by Hung and Mittra at $f = 19.17$ GHz with an axis-symmetric parabolic reflector with diameter $D = 9.14$ m and $F/D = 0.48$ [8]. Results are shown for a single displaced feed element and a movable array feed with 27 elements spaced 0.01 m apart [8]. (a) Boresight operation. (b) Beam scanned by 2.5°. (c) Beam scanned by 5.0°.

patterns were asymmetrical with the E-plane pattern defined by q_E and the H-plane pattern defined by q_H [9]. Results were calculated for both "low" q elements and more directive "high" q elements. Both cases showed similar characteristics.

The values used for the low q elements, which are more reasonable for the interelement spacings considered, are $q_E = 1.0$ and $q_H = 0.0$ [9]. It is noted that the original results published in reference [9] are in error and corrected results appear in reference [10]. For interelement spacing of $d = 0.4\ \lambda$ the directivity obtained by CFM was 45.883 dB and the directivity obtained by directivity optimization was 46.985 dB, the difference being 1.102 dB [10]. For $d = 0.5\ \lambda$ the directivity obtained by CFM was 48.049 dB and the directivity obtained by directivity optimization was 48.605 dB, the difference being 0.556 dB [10]. For spacings of $d > \lambda$ the difference in directivity obtained by the two methods becomes negligible [9].

4.3 Dual Reflector Configurations

Microwave dual reflector antennas evolved from their optical counterparts often used in telescopes. The addition of a second reflector creates an additional parameter which can be varied to tailor the reflector configuration for a specific need. For example, a subreflector placed between the main reflector and the focal point can be used to fold the optics and reduce the overall length of the reflector configuration while creating a better feed position. Also, a subreflector can be used to increase the effective F/D value of a reflector configuration to improve scan performance and increase magnification. For offset reflectors a subreflector can be used to decrease cross-polarization [12].

Dual reflector configurations can be divided into two categories: Cassegrain configurations and Gregorian configurations. For Cassegrain configurations the subreflector is placed between the main reflector and the focal point (or focal region for defocused main reflectors). For Gregorian configurations the main reflector focal point (or focal region) is placed between

the two reflector surfaces.

4.3.1 Classical Dual Reflector Configurations

Classical dual reflector configurations are comprised of a parabolic main reflector and either a hyperbolic or an elliptic subreflector corresponding to a Cassegrain or a Gregorian configuration, respectively. An axis-symmetric Cassegrain configuration is shown in Fig. 4.3-1 [11]. One of the two focal points of the hyperbolic subreflector is the real focal point of the configuration and is located at the desired feed location, the other focal point is a virtual focal point and is located at the focus of the parabolic main reflector. For Gregorian configurations one of the two focal points of the elliptic subreflector is the real focal point of the configuration and is located at the desired feed position, the other is a virtual focal point and is located at the focus of the parabolic main reflector.

The seven parameters shown in Fig. 4.3-1 are related by the following three equations [11]:

$$tan\left(\frac{\phi_v}{2}\right) = \pm\frac{D_m}{4F_m} \tag{4.3-1}$$

$$\frac{1}{tan\,\phi_v} = \frac{1}{tan\,\phi_r} = 2\frac{F_c}{D_s} \tag{4.3-2}$$

$$1 - \frac{sin\left(\frac{\phi_v - \phi_r}{2}\right)}{sin\left(\frac{\phi_v + \phi_r}{2}\right)} = \frac{2L_v}{F_c} \tag{4.3-3}$$

where the positive sign in (4.3-1) applies to Cassegrain configurations and the negative sign applies to Gregorian configurations. In a typical case the parameters D_m, F_m, F_c and ϕ_r are determined by consideration of antenna performance and space limitations and ϕ_v, D_s and L_v are then calculated. It is important to note that the value of the parameter ϕ_r, which determines the

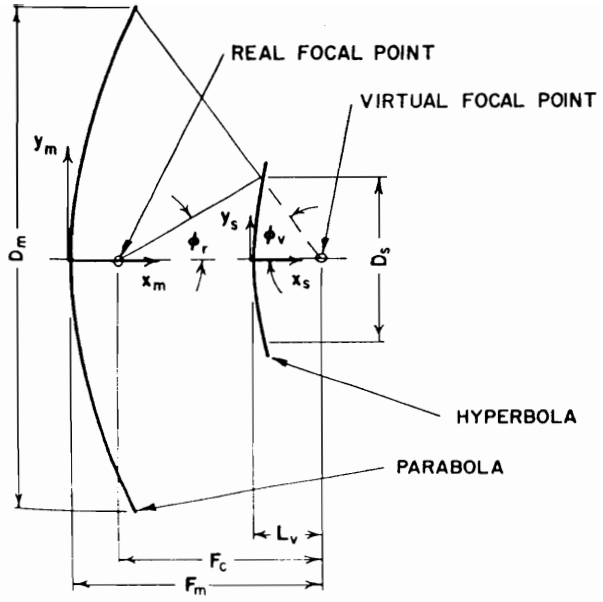

Figure 4.3-1. Geometry of an axis-symmetric classical Cassegrain reflector configuration [11].

required beamwidth of the feed pattern, can be specified independently of the ratio F_m/D_m, which determines the shape of the main reflector.

The surface of the main reflector is given by the equation

$$x_m = \frac{y_m^2}{4F_m} \tag{4.3-4}$$

The surface of the subreflector is given by the equation [11]

$$x_s = a\left[\sqrt{1+\left(\frac{y_s}{b}\right)^2} - 1\right] \tag{4.3-5}$$

where

$$e = \frac{sin\left(\frac{\phi_v + \phi_r}{2}\right)}{sin\left(\frac{\phi_v - \phi_r}{2}\right)}$$

$$a = \frac{F_e}{2e}$$

$$b = a\sqrt{e^2 - 1}$$

and parameter e is the subreflector eccentricity. For Cassegrain configurations (hyperbolic subreflectors) $e > 1$, while for Gregorian configurations (elliptic subreflectors) $0 < e < 1$ [11].

There are two equivalence concepts which are helpful in predicting the performance of classical Cassegrain and Gregorian configurations: the virtual feed concept and the equivalent paraboloid concept.

4.3.1.1 The Virtual Feed Concept

With the virtual feed concept the combination of real feed and subreflector are replaced by a virtual feed at the focal point of the main reflector. Thus, the antenna configuration becomes an ordinary single reflector having the same main reflector but a different feed [11]. This is shown in Fig. 4.3-2(a) for an axis-symmetric Cassegrain configuration. If both the real and virtual feeds

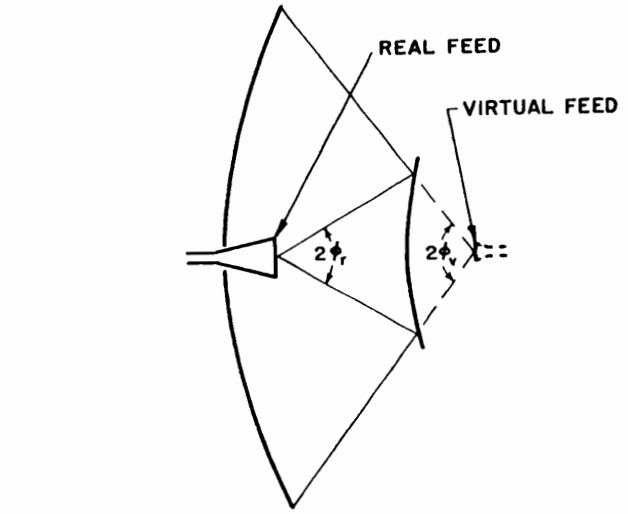

(a)

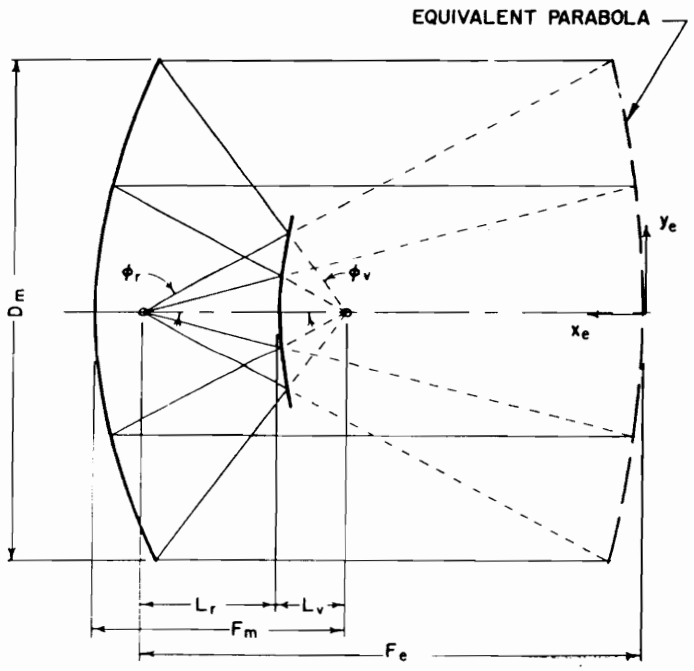

(b)

Figure 4.3-2. (a) Virtual feed concept for classical Cassegrain reflector system [11]. (b) Equivalent parabola concept for classical Cassegrain reflector system [11].

had dimensions much larger than a wavelength, then the configuration of the virtual feed could be determined by finding the optical image of the real feed in the subreflector [11]. This may be useful for array feeds; however, this condition seldom exists for single feeds and diffraction effects of the feed at the surface of the subreflector must be considered. For both Cassegrain and Gregorian configurations the virtual feed usually has a broader beamwidth for the same edge taper ($\phi_v > \phi_r$) and, therefore, has a smaller effective aperture. There are several microwave antenna applications for which the ability to obtain a different effective aperture from that of the feed is helpful. For example, for wide band applications it is difficult to reduce the overall size of the feed aperture to a wavelength or less and maintain efficiency over the bandwidth. On the other hand, a large feed aperture requires a long focal length for efficient utilization of the main reflector aperture, which increases the size of the antenna structure. This problem can be solved by use of a Cassegrain configuration which can incorporate a large real feed while employing a short focal length for the main reflector [11].

4.3.1.2 The Equivalent Paraboloid Concept

The equivalent paraboloid concept has proved useful in predicting the beam scan characteristics of classical Cassegrain and Gregorian configurations for small feed displacements and small scan angles. With this concept the combination of main reflector and subreflector are replaced by a single equivalent parabolic reflector at a certain distance from the real focal point [11]. The equivalent paraboloid for an axis-symmetric Cassegrain configuration is shown in Fig. 4.3-2(b). The equivalent paraboloid, based on ray analysis, can be defined by the following set of equations [11]:

$$\frac{D_m}{4F_e} = tan\left(\frac{\phi_r}{2}\right) \tag{4.3-6}$$

$$x_e = \frac{y_e^2}{4F_e} \tag{4.3-7}$$

$$\pm\frac{F_e}{F_m}=\frac{tan\left(\frac{\phi_r}{2}\right)}{tan\left(\frac{\phi_r}{2}\right)}=\frac{L_r}{L_v}=\frac{e+1}{e-1}. \tag{4.3-8}$$

where e is the subreflector eccentricity as defined for (4.3-5). Equations (4.3-6) and (4.3-7) describe the equivalent paraboloid in terms of its equivalent focal length F_e [11]. Equation (4.3-8) presents alternate expressions for the quantity F_e/F_m, the ratio of the equivalent focal length to the focal length of the main reflector. In (4.3-8) the positive sign applies to Cassegrain configurations and the negative sign applies to Gregorian configurations [11].

Rusch et al. [12] studied the derivation and application of the equivalent paraboloid concept for offset Cassegrain and Gregorian configurations. The geometries used for this study are shown in Fig. 4.3-3 [12]. The main reflector has focal length F and the subreflector has eccentricity e and interfocal distance $2c$ [12]. Four Cartesian coordinates are shown in Fig. 4.3-3 [12]: x-y-z, centered at the paraboloid/subreflector focus with the z-axis colinear with the axis of the parent paraboloid; x_s-y_s-z_s, also centered at the paraboloid/subreflector focus with the z_s-axis colinear with the axis of the parent subreflector (z_s possess through both subreflector focal points); x_β-y_β-z_β, centered at the second focus of the subreflector with the z_β-axis colinear with the z_s-axis; and x_f-y_f-z_f, also centered at the second focus of the subreflector with the z_f-axis, which is the feed boresight direction, rotated by angle α with respect to the z_s-axis. The angle α, which is the angle between the feed boresight axis and the parent subreflector axis, is called the feed tilt angle. The angle β, which is the angle between the parent main reflector axis and the parent subreflector axis, is called the subreflector tilt angle.

The surface of the main reflector is given by [12]

$$\rho_p=\frac{2F}{1+\alpha\ cos\theta} \tag{4.3-9}$$

and the surface of the subreflector is given by [12]

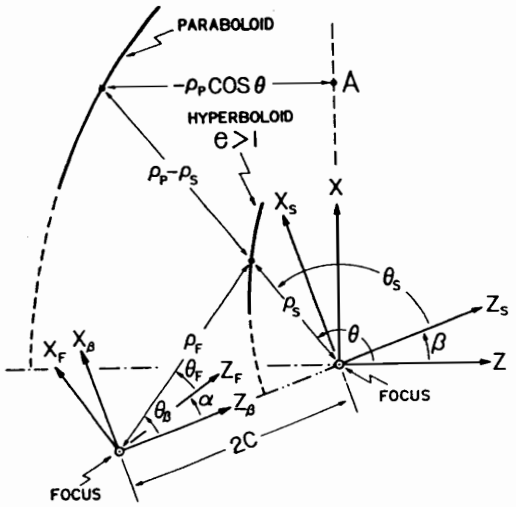

(a)

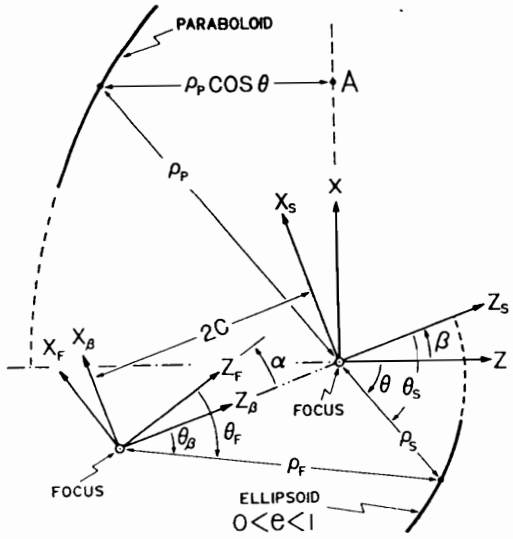

(b)

Figure 4.3-3. Offset classical Cassegrain and Gregorian reflector geometries used by Rusch et al. [12]. (a) Cassegrain. (b) Gregorian.

$$\rho_s = \frac{1}{\alpha}\left(\frac{2C}{e} - \rho_f\right) \tag{4.3-10}$$

where the parameter σ takes the value -1 for Cassegrain configurations and $+1$ for Gregorian configurations, and e is the eccentricity as defined for (4.3-5). Equations (4.3-9) and (4.3-10) are more general than (4.3-4) and (4.3-5) because they allow for offset configurations where the axis of the feed, subreflector and main reflector are tilted with respect to each other. Additional useful relationships are [12]

$$\rho_f = \frac{c}{e} \times \frac{e^2 - 1}{e\,cos\theta_\beta - 1} \tag{4.3-11}$$

$$tan\,\frac{\theta_\beta}{2} = \frac{|\,e-1\,|}{e+1}\left(tan\frac{\theta_s}{2}\right)^{\sigma}. \tag{4.3-12}$$

Equivalent paraboloids for the offset Cassegrain and Gregorian configurations are shown in Fig. 4.3-4 [12]. The surface of the equivalent paraboloid, given in the x_f-y_f-z_f coordinate system, can be calculated by the following equations [12]:

$$\rho_{eq} = \frac{2\,F_{eq}}{1 + cos\theta_f} \tag{4.3-13}$$

and

$$F_{eq} = F \times \frac{|e^2 - 1|}{(e^2+1) - 2e\,cos\beta} \tag{4.3-14}$$

In configurations where the main reflector has a circular projected aperture it is usually desirable to orient the feed boresight axis, z_f, along the axis of the equivalent parent paraboloid. This makes the equivalent paraboloid axis-symmetric and reduces cross polarization [12]. However, this could produce an excessive amount of spillover since, in general, the equivalent paraboloid axis is not aligned with the subreflector angular center. With reference to Fig. 4.3-4 [12], for a given main reflector offset angle θ_0 (θ_0 is the angle to the center of the main reflector) it is possible to find a subreflector tilt angle β and feed tilt angle

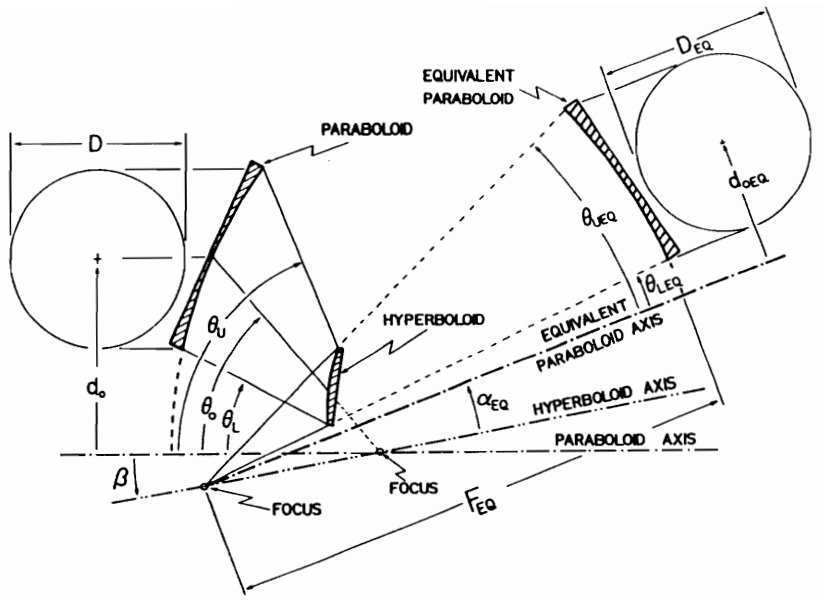

(a)

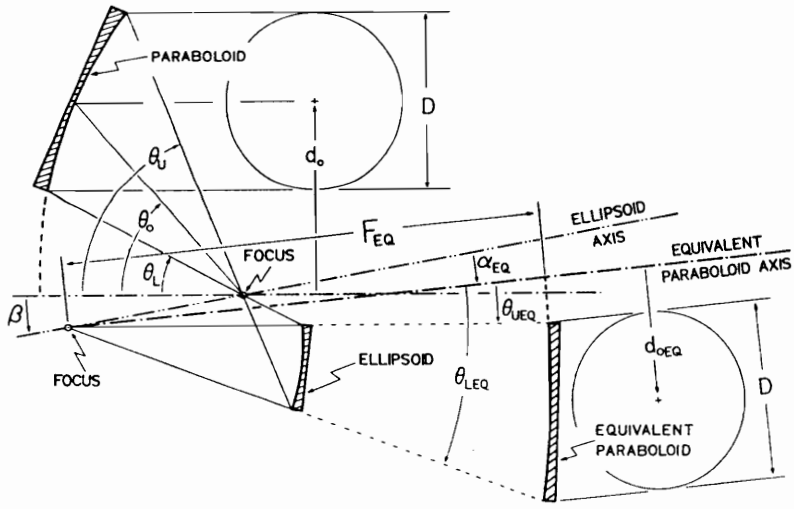

(b)

Figure 4.3-4. Equivalent paraboloid parameter definitions for the offset Cassegrain and Gregorian reflector configurations [12]. (a) Cassegrain. (b) Gregorian.

α such that the z_f-axis is colinear with the axis of the equivalent paraboloid parent reflector and is pointing towards the center of the subreflector, which is necessary for good illumination. The angles α and β are given by [12]:

$$tan\left(\frac{\beta}{2}\right) = \left(\frac{e-1}{e+1}\right)^2 tan\left(\frac{\beta-\theta_0}{2}\right) \tag{4.3-15}$$

and

$$tan\left(\frac{\alpha}{2}\right) = \left(\frac{e+1}{e-1}\right) tan\left(\frac{\beta}{2}\right). \tag{4.3-16}$$

For reflector configurations whose parameters are chosen according to (4.3-15) and (4.3-16) the equivalent parabola is axis-symmetric and its axis automatically coincides with the subreflector center. This leads to minimum spillover and cross-polarization levels [12]. Rusch et al. [12] performed performance calculations on both offset Cassegrain and Gregorian configurations in order to test the preceding equivalence theory. In both cases the parabolic reflector had a focal length of $F = 62.5\ \lambda$, an aperture diameter of $D = 100\ \lambda$ and an offset height of $d_0 = 75\ \lambda$ (see Fig. 4.3-5) [12]. The parent hyperboloid and ellipsoid had eccentricities e equal to 1.996 and 0.501, and interfocal distances $2c$ equal to 20.41 λ and 32.82 λ, respectively [12]. Both subreflectors had an x-axis projected length of 20 λ with their axes tilted by $\beta = 9^\circ$ and their feeds tilted by $|\alpha| = 26.64^\circ$ [12]. These values of β and α satisfy both (4.3-15) and (4.3-16). Both configurations had the same equivalent paraboloid with $F_{eq} = 179.13\ \lambda$ because both were designed using the same parabolic reflector, the same β angle and inverse subreflector eccentricities [12]. The feed used possessed a circular symmetric raised cosine pattern and provided an edge taper of -10 dB [12].

Typical principal plane patterns, computed using P.O./P.O., are shown in Figs. 4.3-5 to 4.3-7 [12]. The spherical coordinate system used for the radiation patterns is based on the x-y-z coordinate system shown in Fig. 4.3-3 [12]. Figure 4.3-5 shows patterns for the feed placed at the configuration focal point [12]. Subreflector diffraction causes the peak of the dual reflector patterns to be ~ 0.5 dB lower than the peak of the equivalent paraboloid pattern [12]. For the co-polarized patterns the sidelobe structures of the two patterns track fairly accurately to as low as 30 dB below the pattern peak, the agreement being

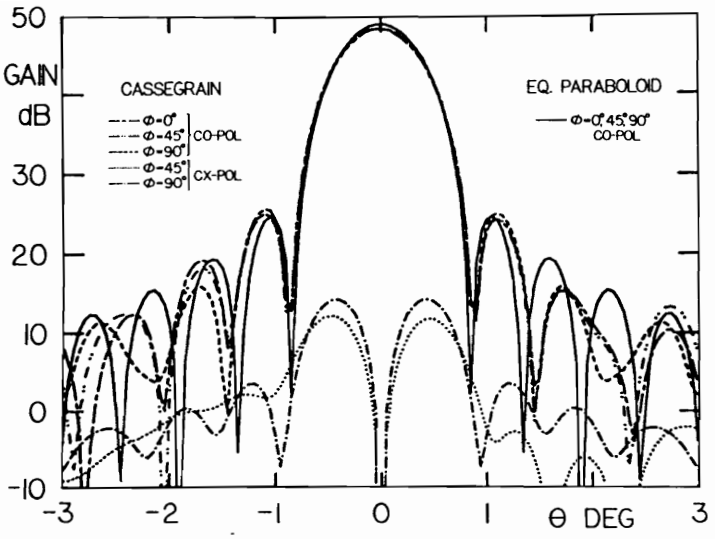

(a)

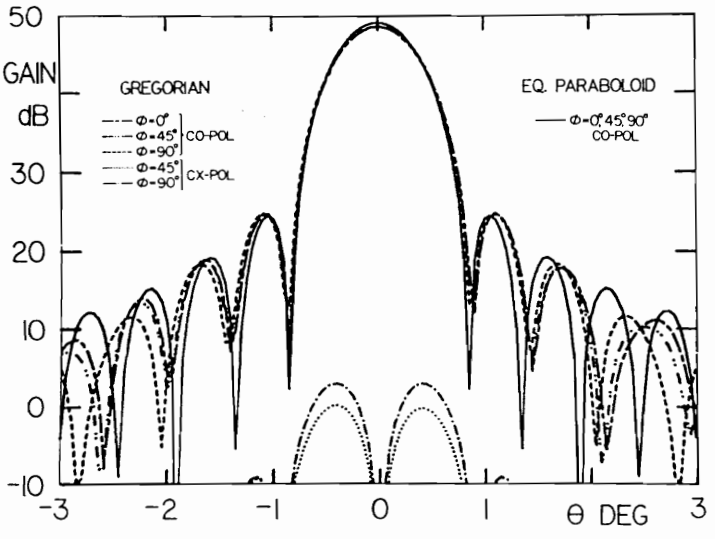

(b)

Figure 4.3-5. Comparison of P.O. radiation patterns for offset Cassegrain and Gregorian reflector configurations and their equivalent paraboloid [12]. (a) Boresight radiation patterns for the Cassegrain configuration and equivalent paraboloid. (b) Boresight radiation pattern for Gregorian configuration and equivalent paraboloid.

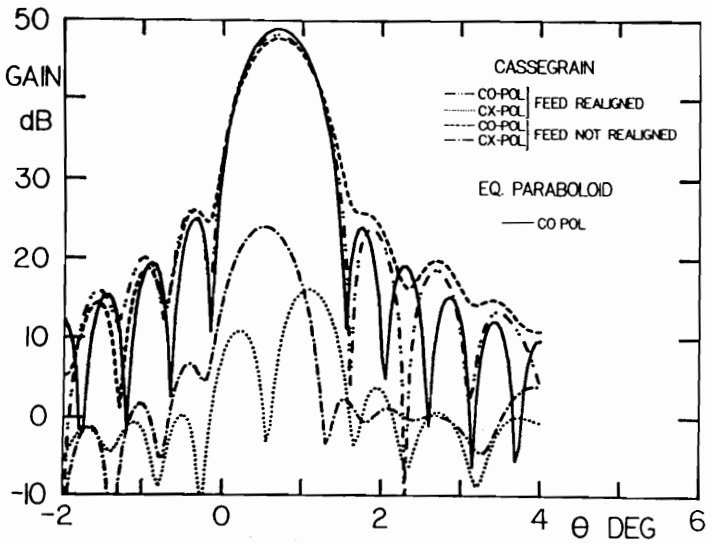

(a)

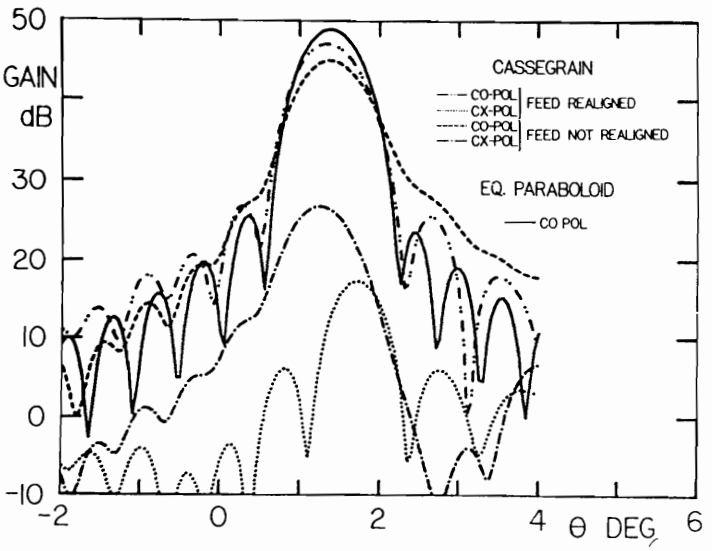

(b)

Figure 4.3-6. Comparison of P.O. radiation patterns for an offset Cassegrain reflector configuration and its equivalent paraboloid in the $\phi = 90^{\circ}$ plane with the feed displaced to effect beam scanning [12]. (a) Beam scanned by 1 HPBW. (b) Beam scanned by 2 HPBW.

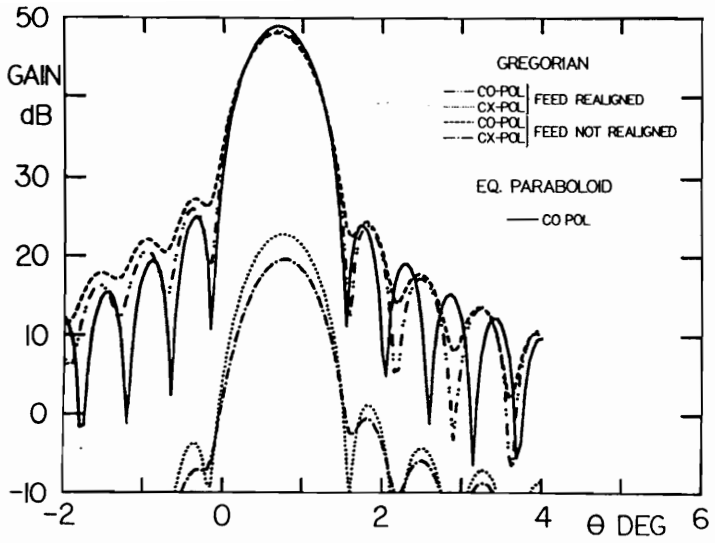

(a)

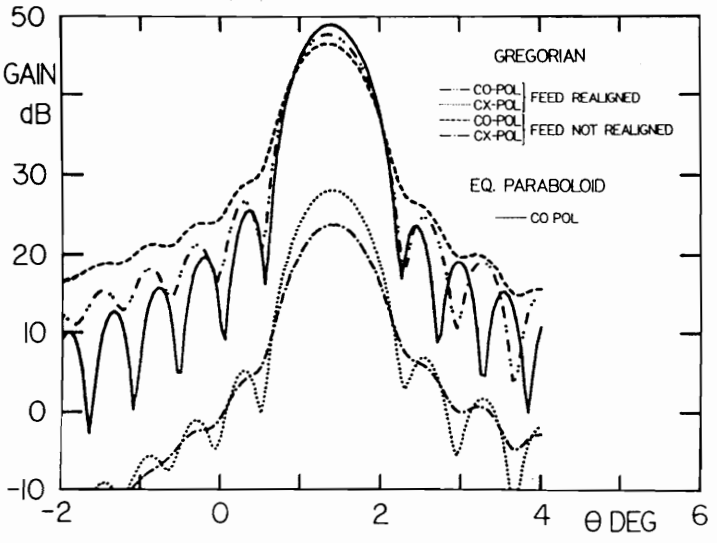

(b)

Figure 4.3-7. Comparison of P.O. radiation patterns for an offset Gregorian reflector configuration and its equivalent paraboloid in the $\phi = 90^\circ$ plane with the feed displaced to effect beam scanning [12]. (a) Beam scanned by 1 HPBW. (b) Beam scanned by 2 HPBW.

slightly better for the Gregorian configuration [12]. For cross-polarization, however, agreement is poor and the dual reflector configurations produce higher levels of cross-polarization due to subreflector diffraction effects, which are absent in the equivalent parabola geometry. The cross-polarization levels of the equivalent parabola is zero in both the $\phi = 0^\circ$ and $\phi = 90^\circ$ planes and -25 dB in the $\phi = 45^\circ$ plane and, therefore, is too small to appear in Fig. 4.3-5 [13].

Under scanned conditions, achieved by displacing the feed, agreement between the equivalent paraboloid and the dual reflector geometry deteriorates rapidly with increasing scan angle [12]. This is shown in Fig. 4.3-6 for the Cassegrain configuration and Fig. 4.3-7 for the Gregorian configuration [12]. In order to isolate spillover effects two sets of curves are computed: one with the feed boresight parallel to the xz-plane and another with the feed realigned to aim toward the point where the x_f-axis intercepts the subreflector [12]. Feed realignment is important in dual reflector configurations because of the narrow feed pattern and in both the Cassegrain and Gregorian cases scan performance was improved by feed realignment.

In all cases agreement between the equivalent paraboloid cross-polarization results and the dual reflector cross-polarization results were poor [12]. More importantly, there is significant difference between the equivalent paraboloid co-polarization results and the dual reflector co-polarization results at one half-power beamwidth (HPBW) of scan and gross differences at two HPBW of scan [12]. The authors note that this disagreement for the scanned case is expected since the equivalent paraboloid construct is only valid for focused feeds [12].

The failure of the equivalent paraboloid technique to accurately predict wide angle scan performance is highlighted in a study by Rahmat-Samii and Galindo-Israel [13]. Their study compared the equivalent paraboloid technique to a GTD/P.O. (geometric theory of diffraction on the subreflector physical optics surface current integration on the main reflector) analysis for an offset Cassegrain configuration [13]. The main reflector had the following dimensions (see Fig. 4.3-5) [13]: $D = 100\ \lambda$, $d_0 = 70\ \lambda$ and $f = 96\ \lambda$. The subreflector had diameter $D_s = 14.11\ \lambda$ and magnification $M = 1.5$, where M is related to the eccentricity e by

$$M = \frac{e+1}{e-1}. \tag{4.3-17}$$

Gain loss as a function of the number of half-power beamwidths scanned is shown in Fig. 4.3-8 [13]. The plots in Fig. 4.3-8 compare the characteristics of the Cassegrain, the equivalent paraboloid and the main reflector by itself. The plots show that the equivalent paraboloid gives good results to approximately 1.5 HPBW of scan but for wider scan angles the performance of the dual reflector is closer to that of the single main reflector.

Krichevsky and Difonzo [14,15] studied optimum feed locations for beam scanning in the plane of symmetry with offset Cassegrain and Gregorian antennas. Their results indicate that the optimum feed locations for Cassegrain configurations are located along a hyperbolic curve while the optimum feed locations for Gregorian configurations are located along an elliptic curve [14,15].

4.3.2 Beam Scanning by Subreflector Motion

Kitsuregawa [16] studied beam scanning through the use of a moving subreflector and a stationary feed for an offset Cassegrain configuration. The geometry used is shown in Fig. 4.3-9 [16]. The optimum displacement of the subreflector was determined by minimizing the difference between the actual subreflector and an ideal subreflector which is shaped and positioned such that the beam is scanned in the desired direction.

With Kitsuregawa's method comparison between actual and ideal subreflectors is performed at N discrete locations [16]. Position vectors from the feed to the actual subreflector without displacement are designated by S_i ($i = 1,2,\ldots,N$), position vectors to the actual subreflector with displacement are designated by S_i' and position vectors to the ideal subreflector are designated by $\bar{S}_i$ [16]. When the rotation of the subreflector is represented by the matrix A and the displacement by vector $\boldsymbol{d}$, S_i' is given by [16]

$$S_i' = A \cdot S_i + \boldsymbol{d} \tag{4.3-18}$$

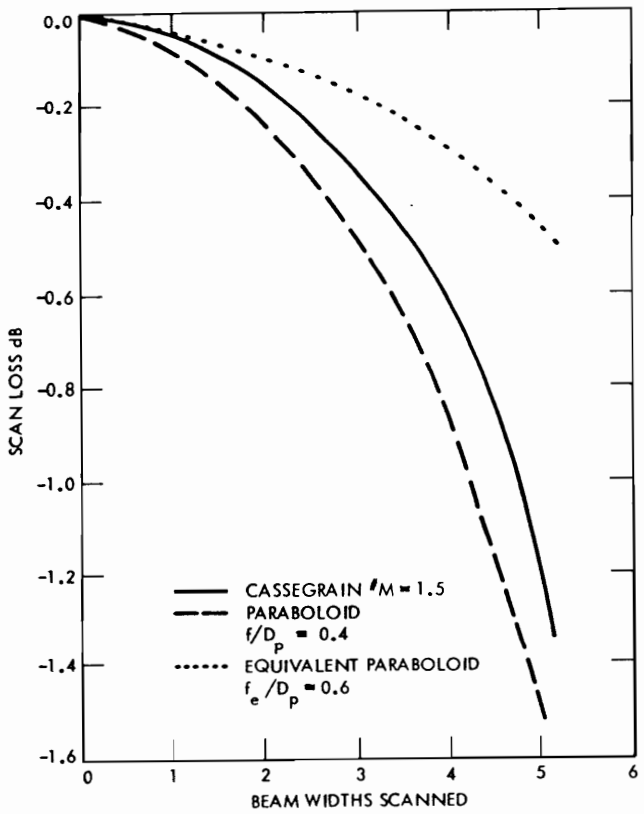

Figure 4.3-8. Scan loss comparison for a Cassegrain configuration with $M = 1.5$ and $D = 100\ \lambda$, its main reflector with $F/D_p = 0.4$ and its equivalent paraboloid with $F_e/D_e = 0.6$ [13]. Scanning is accomplished by feed displacement [13].

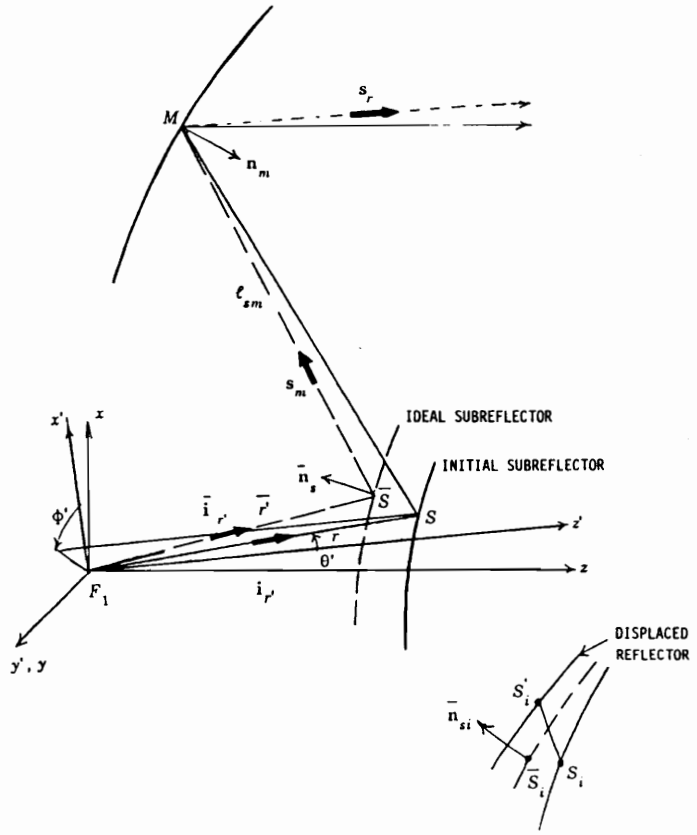

Figure 4.3-9. Geometry used by Kitsuregawa [16] for beam scanning with subreflector motion. Optimum subreflector displacement is found by minimizing the difference between points on the initial subreflector, S_i, and points the ideal subreflector corresponding to a desired scan direction, $\overline{S}_i$.

and the squared error is given by

$$I = \sum_{i=1}^{N} [(S_i' - \bar{S}_i) \cdot \hat{n}_{si}]^2 \tag{4.3-19}$$

where $\hat{n}_{si}$ is the subreflector normal unit vector at the point designated by $\bar{S}_i$ [16]. When the beam is scanned in the xz-plane, as shown in Fig. 4.3-10, $\bar{\bar{A}}$ and $\bar{d}$ are represented as follows:

$$\bar{\bar{A}} = \begin{bmatrix} \cos\theta_x & 0 & \sin\theta_x \\ 0 & 1 & 0 \\ -\sin\theta_x & 0 & \cos\theta_x \end{bmatrix} \tag{4.3-20}$$

$$\bar{d} = d_x \hat{i}_x + d_z \hat{i}_z. \tag{4.3-21}$$

The equations used to determine θ_x and $\bar{d}$ for least squared error are given by [17]

$$\frac{\partial I}{\partial \theta_x} = 0, \quad \frac{\partial I}{\partial d_x} = 0, \quad \frac{\partial I}{\partial d_z} = 0 \tag{4.3-22}$$

Figure 4.3-10(a) shows the subreflector displacement parameters θ_x, d_x and d_z for beam scan angles between -0.5° and 0.5° corresponding to a typical offset Cassegrain configuration with a 4.2 m main reflector aperture [16]. Fig. 4.3-10(b) shows absolute gain at 20 GHz as a function of scan angle for both linear subreflector displacement and the least squared error subreflector displacement [16]. Scanning performance obtained with the least squared error subreflector motions show considerable improvement.

4.3.3 The Dual Parabolic Reflector Configuration

In Sec. 3.3 the double Fourier transform technique is discussed. With this technique an array feed is placed in the focal plane and a sampled spatial Fourier transform is performed electronically by use of a Butler matrix. With a dual

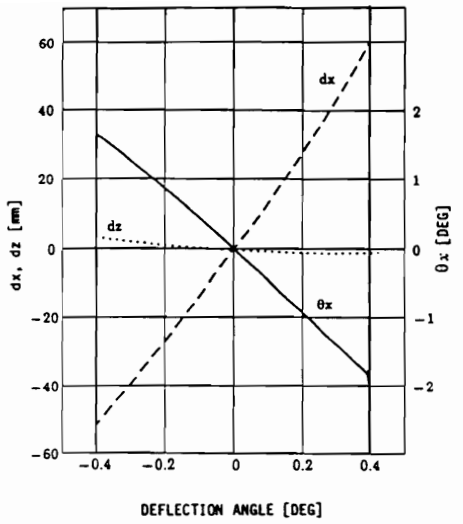

(a)

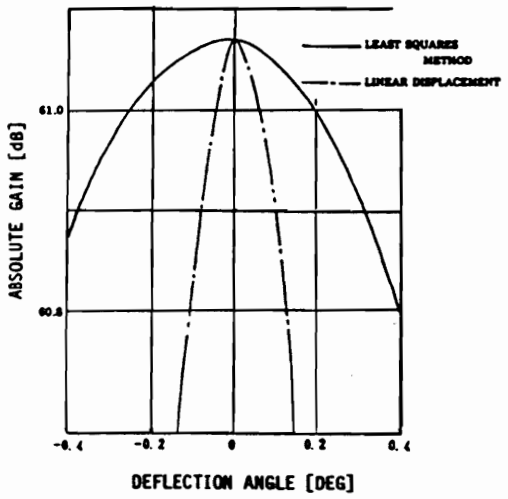

(b)

Figure 4.3-10. Examples of characteristics of Cassegrain configuration with beam scanning accomplished by subreflector motion [16]. (a) Subreflector displacement parameters [16]. (b) Gain reduction versus scan (deflection) angle obtained for a 4.2 m main reflector at 20 GHz [16]. Dashed line: results for linear subreflector motion. Solid line: results for least squared error motion.

parabolic reflector configuration a parabolic subreflector is used to optically obtain the Fourier transform of the focal plane field distribution. This is accomplished by placing the focal point of the parabolic subreflector at the same location as the focal point of the parabolic main reflector as shown in Fig. 4.3-11 [17]. The operation of the reflector configuration can be explained in terms of conjugate points. By definition, conjugate elements in an optical configuration have the property that the rays originating from a point of one element are transformed by the optical configuration into rays which pass through a corresponding point of the other element [17]. Two such corresponding points are called conjugate points [17]. For the dual parabolic reflector configuration the main reflector aperture plane is designated by Σ_0 and the feed array plane is designated by Σ_1 as shown in Fig. 4.3-11. On Σ_1 the center of illumination is determined by the ray which corresponds to the center point C_0 of the paraboloid and, therefore, the center of the array C_1 should be placed on this ray. If the points C_0 and and C_1 are conjugate points, as is approximately true for the dual parabolic configuration, then all rays incident on the main reflector at C_0, regardless of incidence angle, will be reflected to the center of the array at C_1. This is shown in Fig. 4.3-11 for two rays which subtend an angle of $\delta\theta_0$ [17]. The conjugate relationship, therefore, allows for a stationary array feed and insures a high level of illumination for all scan angles. In addition, if Σ_0 and Σ_1 are two planes orthogonal to the central ray through points C_0 and C_1 respectively, then Σ_0 and Σ_1 are approximately conjugate planes in the vicinity of C_0 and C_1 and the field E_1 on Σ_1 is the image of the field E_0 on Σ_0. For an array feed placed on Σ_1, the resultant radiation characteristics can be predicted with reasonable accuracy by modeling the entire array feed reflector configuration by a large image array located at Σ_0. The element positions in the image array are a magnified image of the element positions in the feed array with the relative phase and amplitude excitations preserved (as predicted by the above geometrical optics theory). The element patterns in the image array are equivalent to the corresponding element patterns in the feed array after being transformed by the optics. The diameter of the image array D_0 is related to the diameter of the feed array D_1 by the magnification factor M [17]:

$$M = \frac{F_0}{F_1} = \frac{D_0}{D_1} \tag{4.3-23}$$

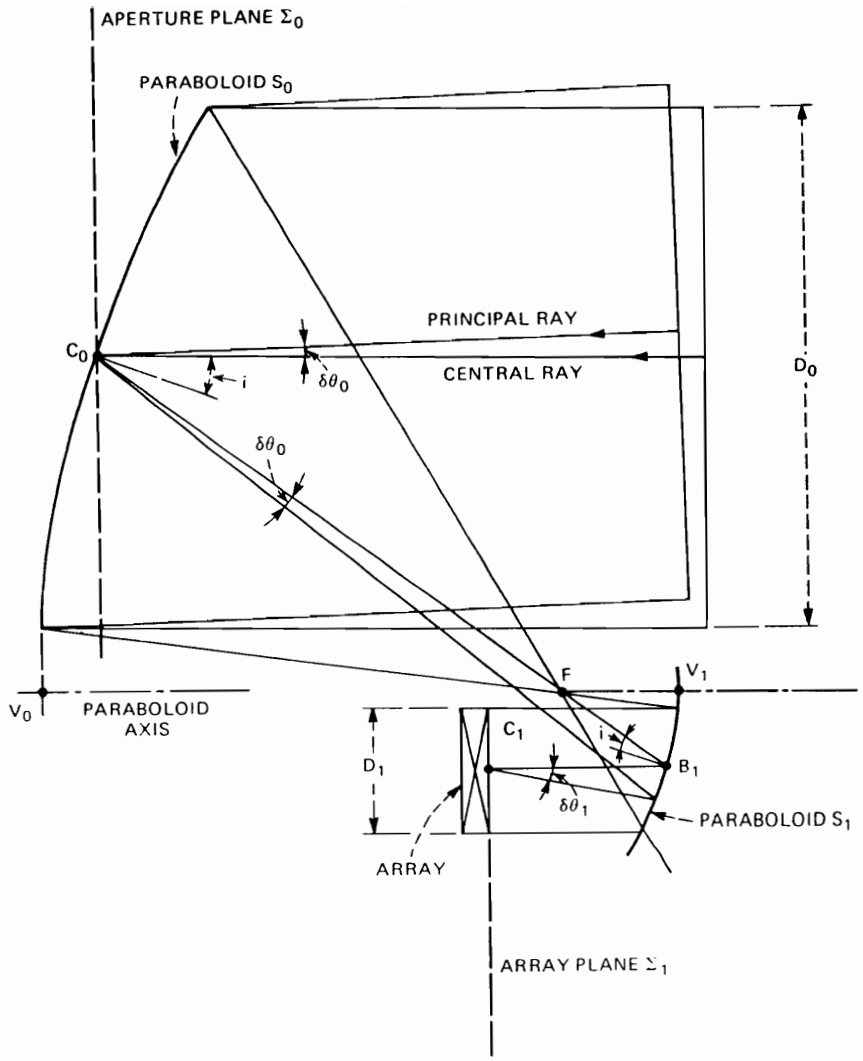

Figure 4.3-11. A Gregorian arrangement of two confocal paraboloids magnifying a small feed array [17]. The main reflector and the array are approximately conjugate elements.

where the focal length of the main reflector is F_0 and the focal length of the subreflector is F_1. The magnification factor can be chosen to be much greater than unity so that the feed array can be much smaller than the main reflector [17].

In Fig. 4.3-11 the array is relatively close to the subreflector which is a disadvantage for some applications. In the example presented by Dragone and Gans [17] a greater distance was desired in order to place a frequency diplexer grid between the array feed and the subreflector. The distance between the array and the subreflector was, therefore, increased by placing a hyperbolic reflector between the two parabolic surfaces as shown in Fig. 4.3-12 [17]. In this case the focal point of the parabolic subreflector is placed on the second focus of the hyperboloid. It is noted that the use of a diverging element between the two parabolic reflectors increases the distance that the focal fields move during scan and, therefore, necessitates a larger parabolic subreflector to prevent spillover.

The reflector configuration shown in Fig. 4.3-12 was designed for use as a hypothetical communication satellite in geosynchronous orbit at $105^\circ W$ longitude [17]. The antenna uses two feed arrays separated by a quasi-optical diplexer to transmit at 12 GHz and receive at 14 GHz [17]. The configuration is designed for a field of view of 3° elevation and 6° azimuth, which approximately correspond to the continental United States, and the corresponding dimensions are shown in the figure [17]. Because the plane of the array and the aperture plane are only approximately conjugate planes there is appreciable variation in illumination over the array aperture during beam scanning which results in gain loss. It is assumed that the spacing of the array elements is very small so that any desired phase distribution over Σ_1 can be produced by the array excitation. Under this assumption, if g^2 denotes the power distribution on Σ_1 due to the array excitation and f^2 denotes the power incident on Σ_1 do to a plane wave incident on the main reflector aperture, then the aperture efficiency ϵ_{ap} can be calculated by (see Sec. 3.1)

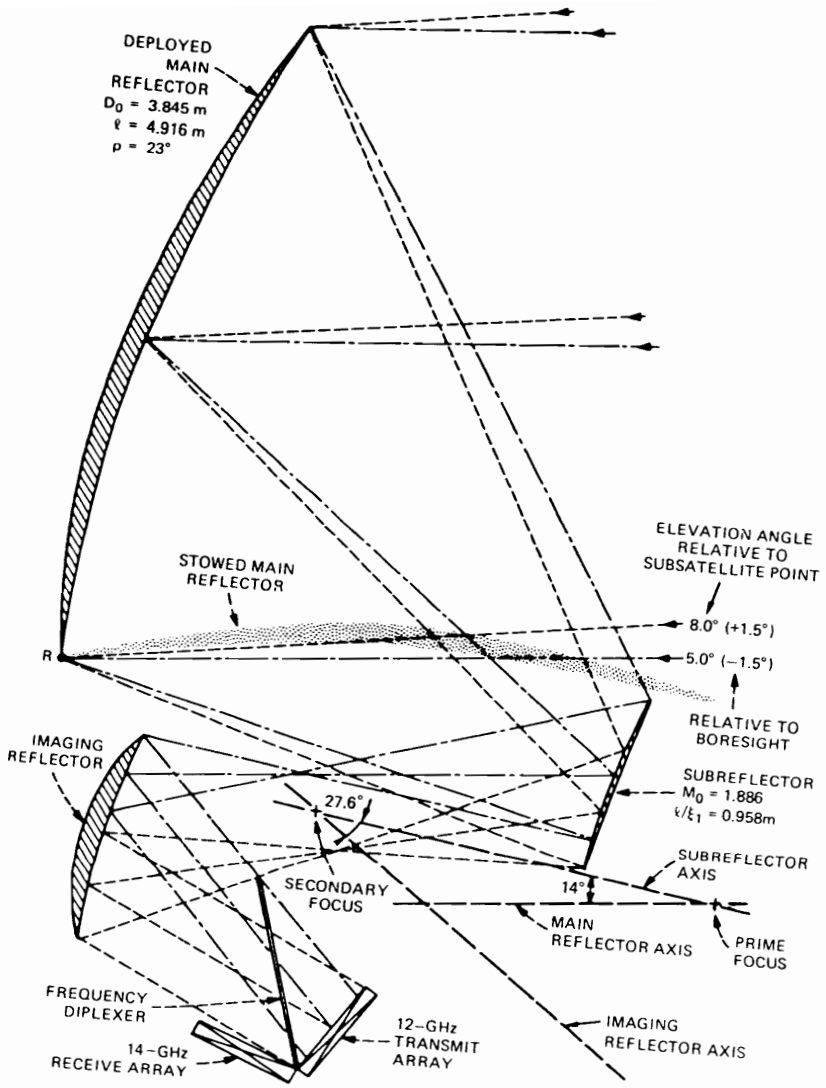

Figure 4.3-12. Imaging arrangement of three reflectors [17]. The subreflector is added to the arrangement of Fig. 4.3-11 to allow space for the frequency diplexer to allow the use of two feed arrays [17].

$$\epsilon_{ap} = \frac{\left(\int\int_{-\infty}^{\infty} fg \, dx \, dy \right)^2}{\int\int_{-\infty}^{\infty} f^2 \, dx \, dy \int\int_{-\infty}^{\infty} g^2 \, dx \, dy} \tag{4.3-24}$$

where the integrations are performed over the plane designated by Σ_1. Figure 4.3-13 shows the geometric optics array illuminations and the corresponding losses in gain given by (4.3-24) for uniform array excitation [17]. Also shown are the losses for a tapered excitation of -10 dB at the edge of the array [17]. Two cases, A and B, are shown in Fig. 4.3-13 [17]. In case A the array is centered at C_1 with diameter given by D_0/M [17]. For this case the scan loss is zero for boresight operation ($\delta\theta_0 = 0$), but becomes relatively high at the edge of the field of view due to spillover past the array feed. In case B the scan loss is minimized at the edge of the field of view by increasing the array size and slightly offsetting the array center. All losses for the 10 dB edge taper in Fig. 4.3-13 are normalized with respect to a -0.45 dB taper loss as calculated by (4.3-24) for case A and boresight operation ($\delta\theta_0 = 0$) with a 10 dB edge taper [17]. Contours of scan loss for case B and a 10 dB edge taper are shown in Fig. 4.3-14 [17]. The positive values for some scan directions are due to the -0.45 dB normalization.

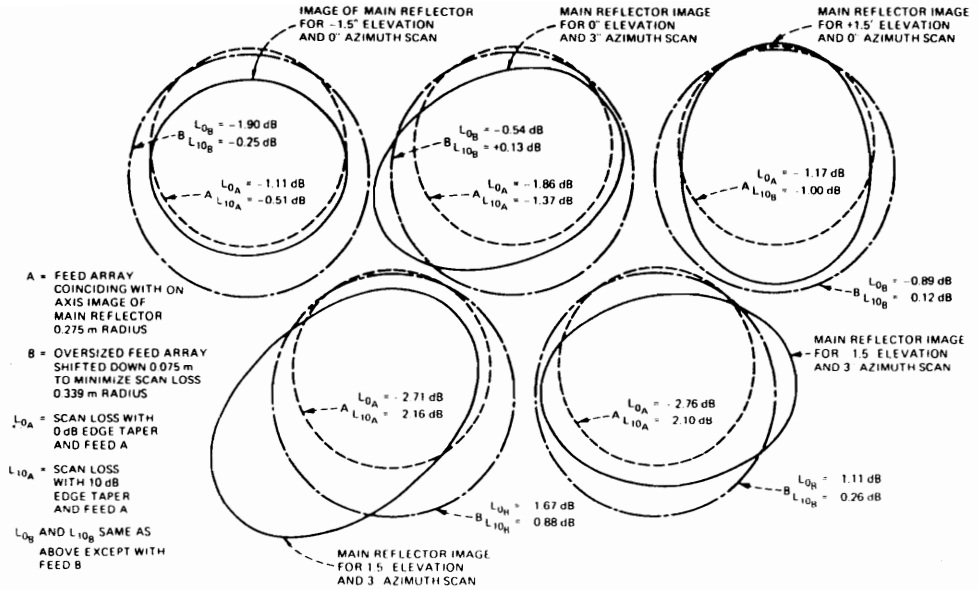

Figure 4.3-13. Vignetting at the array plane during beam scanning for the reflector configuration shown in Fig. 4.3-12 [17]. In case A the array is centered at C_1 and the diameter is given by D_0/M such that there is no spillover for boresight operation [17]. In case B the array has been enlarged and offset to minimize spillover at the scan limits [17]. All losses for the 10 dB taper are normalized to -0.45 dB, which is the value calculated by (4.3-24) for case A and boresight operation ($\delta\theta_0 = 0°$) with a 10 dB edge taper [17].

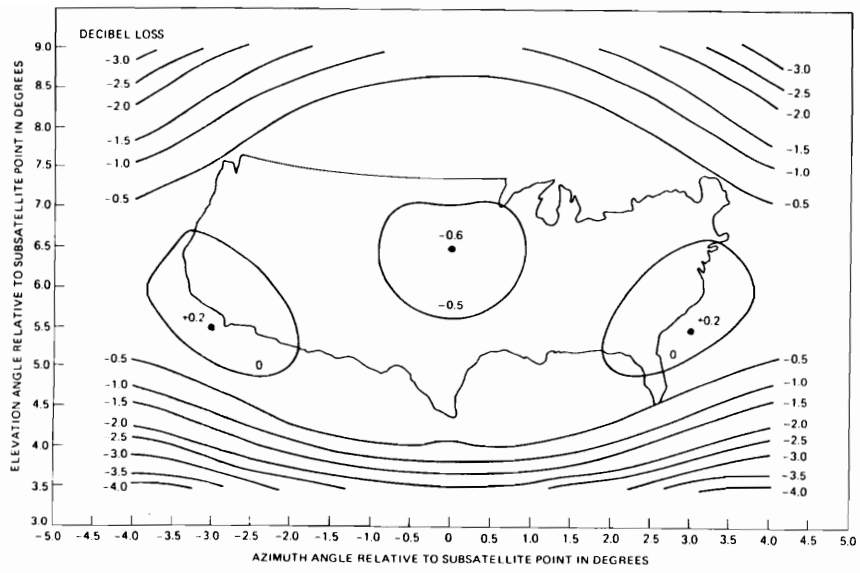

Figure 4.3-14. Contours of scan calculated for the oversized array case B and a 10 dB edge taper [17]. The positive values for some scan directions are due to a -0.45 dB normalization, which is the value calculated by (4.3-24) for case A and boresight operation ($\delta\theta_0 = 0°$) with a 10 dB edge taper [17].

4.4 References

1. J. Ruze, "Lateral-Feed Displacement in a Paraboloid," *IEEE Trans. on Ant. and Prop.*, vol. 13, no. 5, pp. 660-665, September 1965.

2. R. F. Harrington, *Time-Harmonic Electromagnetic Fields*, McGraw-Hill, Inc.: New York, 1961.

3. W. V. T. Rusch and A. C. Ludwig, "Determination of the Maximum Scan -Gain Contours of a Beam-Scanning Paraboloid and Their Relation to the Petzval Surface," *IEEE Trans. on Ant. and Prop.*, vol. 21, no. 2, pp. 141-147, March 1973.

4. Y. T. Lo and S.W. Lee, *Antenna Handbook*, Van Nostrand Reinhold Co.: New York, 1981.

5. A. V. Mrstik, "Scan Limits of Off-Axis Fed Parabolic Reflectors," *IEEE Trans. on Ant. and Prop.*, vol. 27, no. 5, pp. 647-651, September 1979.

6. S. J. Blank and W. A. Imbraile, "Array Feed Synthesis for Correction of Reflector Distortion and Vernier Beamstearing," *IEEE on Trans. Ant. and Prop.*, vol. 36, no. 10, pp. 1351-1358, October 1988.

7. A. W. Rudge and M. J. Withers, "New Technique for Beam Steering with Fixed Parabolic Reflectors," *Proc. IEE*, vol. 118, no. 7, July 1971.

8. C. C. Hung and R. Mittra, "Secondary Pattern and Focal Region Distribution of Reflector Antennas under Wide-Angle Scanning," *IEEE Trans. on Ant. and Prop.*, vol. 31, no. 5, pp. 756-763, September 1983.

9. P. T. Lam and S. W. Lee, "Directivity Optimization of a Reflector Antenna with Cluster Feeds: A Closed-Form Solution," *IEEE Trans. on Ant. and Prop.*, vol. 33, no. 11, pp. 1163-1174, November 1985.

10. P.T. Lam and S. W. Lee, "Correction to Directivity Optimization of a Reflector Antenna with Cluster Feeds: a Closed-Form Solution," *IEEE Trans. on Ant. and Prop.*, vol. 34, no. 12, pp. 1173, December 1986.

11. P. W. Hannan, "Microwave Antennas Derived from the Cassegrain Telescope," *IRE Trans. on Ant. and Prop.*, pp. 140-153, March 1961.

12. W. V. T. Rusch, A. Prata, Y. Rahmat-Samii and R. A. Shore, "Derivation and Application of the Equivalent Paraboloid for Classical Offset Classical and Gregorian Antennas," *IEEE Trans. on Ant. and Prop.*, vol. 38, no. 8, pp. 1141-1149, August 1990.

13. Y. Rahmat-Samii and V. Galindo-Israel, "Scan Performance of Dual Offset Reflector Antennas for Satellite Communications," *Radio Science*, vol. 16, no. 6, pp. 1093-1099, November-December 1981.

14. V. Krichevsky and D. F. Difonzo, "Beam-Scanning in the Offset Gregorian Antenna," *Comsat Tech. Review*, vol. 12, no. 2, pp. 251-269, Fall 1982.

15. V. Krichevsky and D. F. Difonzo, "Optimum Feed Locus for Beam Scanning in the Symmetry Plane of Offset Cassegrain Antennas: Two-Dimensional Case," *Comsat Tech. Review*, vol. 11, no. 1, pp. 131-157, Spring 1981.

16. T. Kitsuregawa, *Advanced Technology in Satellite Communication Antennas*, Artech House: Boston, 1990.

17. C. Dragone and M. J. Gans, "Imaging Reflector Arrangements to Form a Scanning Beam Using a Small Array," *Bell System Tech. Journal*, vol. 58, no. 2, pp. 501-515, February 1979.

Chapter 5

Shaped Reflector Configurations

Beam scanning characteristics of the parabolic reflector and classical Cassegrain and Gregorian reflector configurations were presented in Chapter 4. Increased design flexibility and the ability to tailor the reflector configuration for specific applications is possible by using more complex shaped reflector surfaces. This chapter introduces shaping techniques and presents examples of specific shaped reflector configurations designed for improved beam scanning characteristics.

The most efficient computational approach for shaped reflector synthesis is geometrical optics (G.O.), which uses rays to represent the flow of energy through the reflector system. In addition to being fast G.O. has the advantage of yielding frequency independent solutions for the reflector surfaces. For electrically small reflectors, however, diffraction effects become important and G.O. can not be used [21]. In the following only electrically large reflectors are considered and, therefore, only G.O. synthesis techniques are presented.

The reflector configurations discussed in Secs. 5.1-5.6 improve beam scanning performance by increasing the scan range for which a "good" focus is achieved. These configurations, which are frequently referred to as imaging systems, can employ feed motion to scan a single beam or can use several feeds to produce multiple simultaneous beams. The reflector configurations discussed in Secs. 5.7-5.8 require motion of the feed and one or more subreflectors to achieve beam scanning and are not appropriate for producing multiple simultaneous beams; however, these configurations are capable of achieving much

higher gain than is possible with the imaging systems.

5.1 The Prime Focus Spherical Reflector

The unique beam scanning properties of the spherical reflector can best be described by considering a prime focus spherical reflector in the transmit mode. The secondary beam produced by the configuration can be scanned by moving the feed along a spherical "focal" surface. The spherical center of the focal surface is coincident with the spherical center of the main reflector (see Fig. 5.1-1) [1]. As the feed is moved the feed pointing angle is changed so that the feed boresight direction is maintained normal to the focal surface. For each feed position a different portion of the spherical reflector is illuminated and the secondary beam direction is equal to the direction of the surface normal at the center of the illuminated portion. If spillover is neglected, the phase and amplitude distribution of the illuminated portion will remain unchanged for all feed positions and corresponding scan directions. Therefore, the performance of the spherical reflector is independent of scan angle. This property makes spherical reflectors very attractive for wide scanning applications.

A disadvantage of the prime focus spherical reflector is the associated spherical aberration. The amount of phase departure from that of a plane wave is a function of the aperture diameter and the radius of the reflector surface [1]. The functional relationship can be established through the use of geometrical optics. A diagram of a spherical reflector is shown in Fig. 5.1-1. This particular reflector is also referred to as a hemispherical reflector because it constitutes half of a total sphere. The spherical center is located at point C and the radius is R. Rays $\overline{FB}$ and $\overline{BA}$ are arbitrary incident and reflected rays originating at point F and intercepting the aperture plane at point A, which is a radial distance r from the z-axis. The focal length f is equal to the length of ray $\overline{OF}$. For the range of variables $0 \leq r/R \leq 0.6$ and $0.45 \leq f/R \leq 0.5$, the approximation can be made that reflected ray $\overline{BA}$ is parallel to the z-axis [1]. Under this condition, the total path length from the focal point F to the aperture plane point A is given by [1]

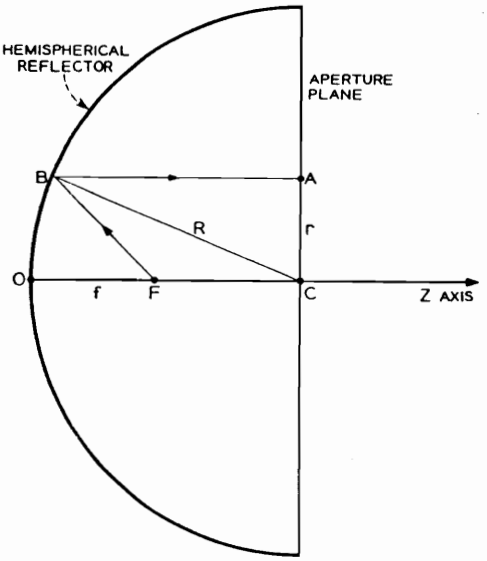

Figure 5.1-1. Spherical (hemispherical) reflector geometry [1].

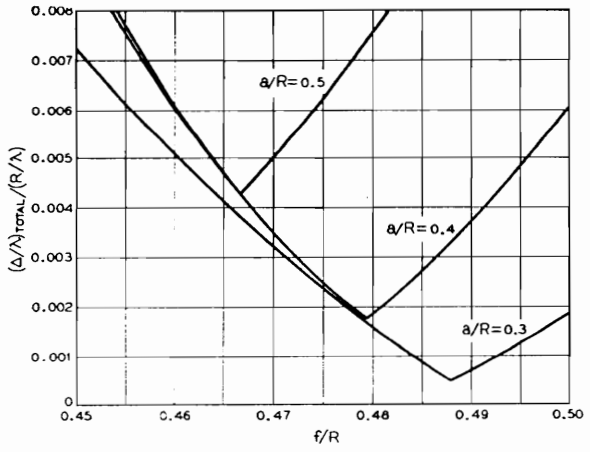

Figure 5.1-2. Total pathlength error for a spherical reflector of radius R versus normalized focal length f/R for several values of normalized aperture radii a/R [1].

$$|\overline{FB}| + |\overline{BA}| = d = \sqrt{R^2 - r^2} + \sqrt{r^2 + [\sqrt{R^2 - r^2} - (R - f)]^2}. \qquad (5.1\text{-}1)$$

The pathlength difference between an axial ray $\overline{FOC}$ and a non-axial ray $\overline{FBA}$ is given by [1]

$$\Delta = R + f - d. \qquad (5.1\text{-}2)$$

Therefore, using (5.1-1) and (5.1-2), the pathlength error in wavelengths is [1]

$$\Delta/\lambda = (R/\lambda)(2 - m - s - \sqrt{1 + m^2 - 2ms}) \qquad (5.1\text{-}3)$$

where $m = 1 - f/R$ and $s = \sqrt{1 - (r/R)^2}$.

When considering pathlength error over a given aperture a useful parameter is the total pathlength error $(\Delta/\lambda)_{total}$, which is defined as the difference between the maximum positive and maximum negative pathlength errors [1]. In Fig. 5.1-2 the total pathlength error for a spherical reflector is plotted as a function of the focal length f for different aperture radii a [1]. All parameters in Fig. 5.1-2 have been normalized with respect to the radius of the spherical reflector R. The optimum focal length for each aperture is determined by the minimum of the corresponding curve [1]. The optimum focal lengths found from Fig. 5.1-2 are only valid for uniformly illuminated apertures because implicit in (5.1-3) is the assumption that all rays have equal weighting.

For the case of a uniformly illuminated aperture the total pathlength error is least when the pathlength error at the edge of the aperture is zero [1]. Thus, equating (5.1-3) to zero and solving for f, the optimum focal length for a uniformly illuminated aperture of radius a is found to be [1]

$$f_{op} = \frac{1}{4}(R + \sqrt{R^2 - a^2}). \qquad (5.1\text{-}4)$$

Experimental evidence indicates that for tapered aperture distributions the optimum focal length is somewhat longer than this result [1]. If the aperture radius a is small compared to the radius of the sphere R, then (5.1-4) yields the

commonly used approximation for the optimum focal length, $f_{op} \simeq R/2$.

For a uniformly illuminated aperture the relationship between the maximum permissible aperture size and the total allowable pathlength error is given by [1]

$$\left(\frac{a}{R}\right)^4_{max} = \frac{14.7(\Delta/\lambda)_{total}}{(R/\lambda)} . \tag{5.1-5}$$

For example, if the total pathlength error is limited to $(\Delta/\lambda)_{total} = 1/16$ at 11.2 GHz for a spherical reflector with $R = 5$ feet, then $R/\lambda = 56.896$ and the maximal permissible illuminated diameter is $2a = 3.56$ feet.

Li [1] presented experimental results for a hemispherical reflector with a 10 foot aperture diameter ($R = 5$ feet). Measurements were performed at 11.2 GHz and the illuminated diameter of the reflector, as defined by the 10 dB beamwidth of the feed, was $2a = 3.56$ feet such that the total pathlength error was limited to $(\Delta/\lambda)_{total} = 1/16$ as calculated above. The resultant measured secondary pattern had a 3 dB beamwidth of 1.76°, a relative sidelobe level of -20 dB and an absolute gain of 39.4 dB [1]. The total useful scan range was 140°, however, it is noted that this scan range corresponds to a reflector which is very under illuminated. The aperture area efficiency, as defined by (6.7-26), is given by

$$\eta_a = \frac{a^2}{R^2} = 0.25, \tag{5.1-6}$$

therefore, only 25 % of the aperture area is used for any given scan direction.

5.2 The Parabolic Torus Reflector

The parabolic torus reflector is useful for applications requiring beam scanning in only one plane or in a conical path. For planar scanning the parabolic torus is generated by rotating a parabola of focal length F about axis $\overline{CG}$ which is perpendicular to the axis of the parabola as shown in Fig. 5.2-1.

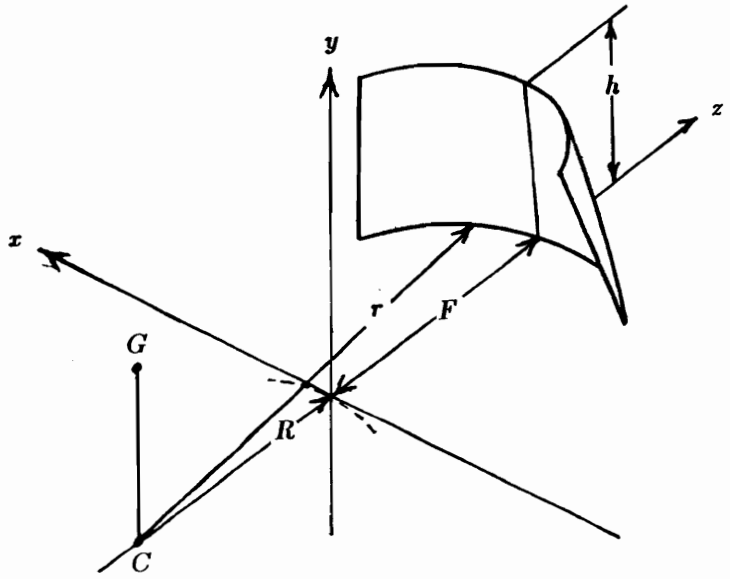

Figure 5.2-1. Geometry of the parabolic torus reflector.

The radius of the circular cross-section of the torus in the xz-plane is given by r. A general equation describing the reflector surface is given by (5.2-1). The resultant reflector roughly combines the focusing quality of a paraboloid with the wide scanning characteristics of a sphere [2]. The focal region of a planar scanning parabolic torus is an arc with radius R and center of curvature located at C. Beam scanning is accomplished by moving a single feed along the focal arc or using multiple feeds to create several simultaneous beams. The diameter of the illuminated portion of the reflector is approximately equal to the reflector height h shown in Fig. 5.2-1. For a given illumination and focal length F non-linear optimization can be used to find the value of R which minimizes aperture plane phase errors. However, in most cases it is adequate to make the focal arc coincident with the focus of the parabolic cross-section as shown in fig. 5.2-1. The F/D value of the illuminated portion is usually made equal to unity or larger in order to control spherical aberrations [2].

An offset parabolic torus antenna designed to simultaneously track several satellites in geostationary orbit is shown in Fig. 5.2-2 [2]. The dimensions of this reflector are $F_p = 1.17$ m , $R = 1.33$ m and the radius of curvature of the circular cross-section in the xz-plane is $r = 2.5$ m [2]. The aperture dimensions are $1.35\text{ m} \times 2.5\text{ m}$ [2]. The reflector has a planar (azimuthal) field of view of $\pm 15^\circ$ in the xz-plane and is designed to produce a 0.8° beamwidth at 22 GHz [2]. The measured boresight gain was 47.4 dB and remained essentially constant over the 30° scan range [2]. By feed squinting the azimuthal field of view was increased by 5° in both the positive and negative directions with a measured 1.4 dB gain reduction over the extended azimuthal scan range [2].

For most applications scanning in a single plane is not adequate. Scanning orthogonal to the usual scan plane (elevation) can be accomplished by displacing the feed in the direction normal to the plane of the focal arc [2]. This method was used with the antenna shown in Fig. 5.2-2 to scan the beam from -5° to $+2^\circ$ in elevation with a measured gain deviation of 1 dB over the entire 7° scan range [2].

An application for which the parabolic torus is particularly well suited is earth observation from low earth orbit (LEO). For such applications the torus can be used to generate simultaneous spot beams along a swath which is

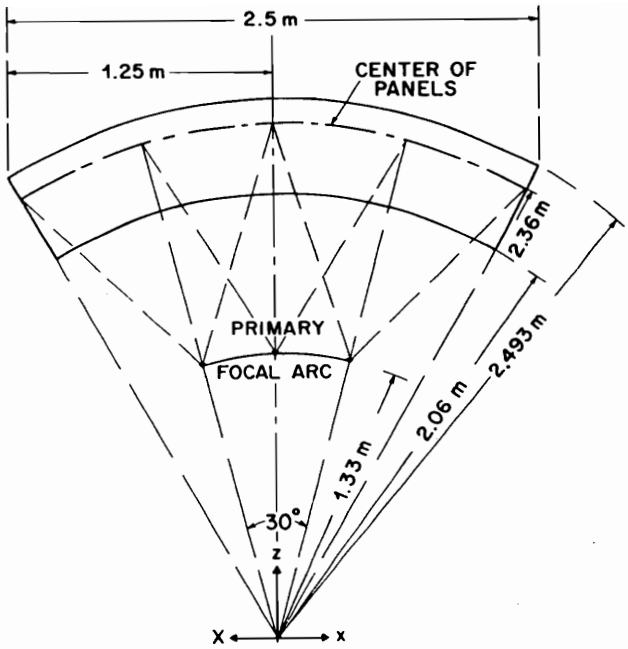

(a)

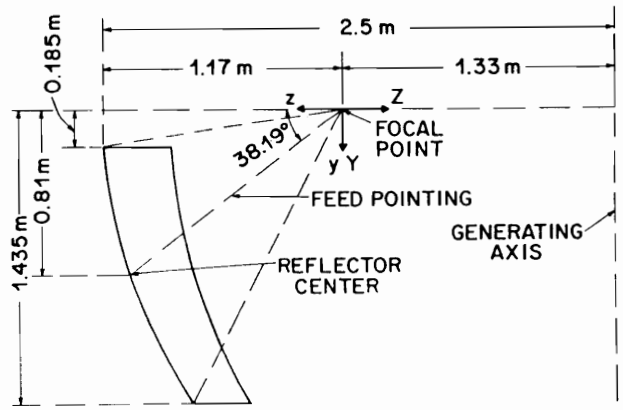

(b)

Figure 5.2-2. Top and side views of a parabolic torus reflector designed to track several satellites in geostationary orbit and produce an 0.8° beamwidth at 20 GHz [2]. (a) Top view. (b) Side view.

perpendicular to the direction of satellite travel. This type of scanning, which is referred to as "push broom", is shown in Fig. 5.2-3 [3]. General requirements for push broom scanning are a wide swath width and a constant incidence angle over the swath width. To maintain a constant incidence angle over the swath width conical scanning is required as shown in Fig. 5.2-3 [3]. To obtain a conical scanning torus the angle between the axis of the parent parabolic cross section and the rotation axis of the circular arc is made identical to the off-nadir angle β as shown in Fig. 5.2-4 [3]. Using the parameters shown in Fig. 5.2-4, a general expression for the position vector $\vec{P}$ from the focus point on the z-axis to points on the surface of the torus reflector is given by[3]:

$$\vec{P}(\theta,\psi) = R\,\widehat{C} + r\,\widehat{e} \tag{5.2-1}$$

where

$$\widehat{C} = sin\psi\;\widehat{y} - cos\psi\;\widehat{z} \tag{5.2-2}$$

$$\widehat{e} = cos(\beta-\theta)\;\widehat{x} + sin\;(\beta-\theta)\;\widehat{C} \tag{5.2-3}$$

$$r = \frac{2F}{(1+cos\theta)} \tag{5.2-4}$$

and

$F =$ focal length of parabolic cross section,
$R =$ radius of focal line arc,
$\beta =$ off-nadir angle ($\beta = 90^{\circ}$ for a planar scanning torus),
$\widehat{x}$, $\widehat{y}$, $\widehat{z}$ = unit vectors in the direction of the x, y and z-axis respectively.

In the above it has been assumed that the focal curve given by R is coincident with the focus of the parabolic cross-section. As with the planar scanning torus the optimum value of R is dependent on the focal length F and the size of the illuminated region.

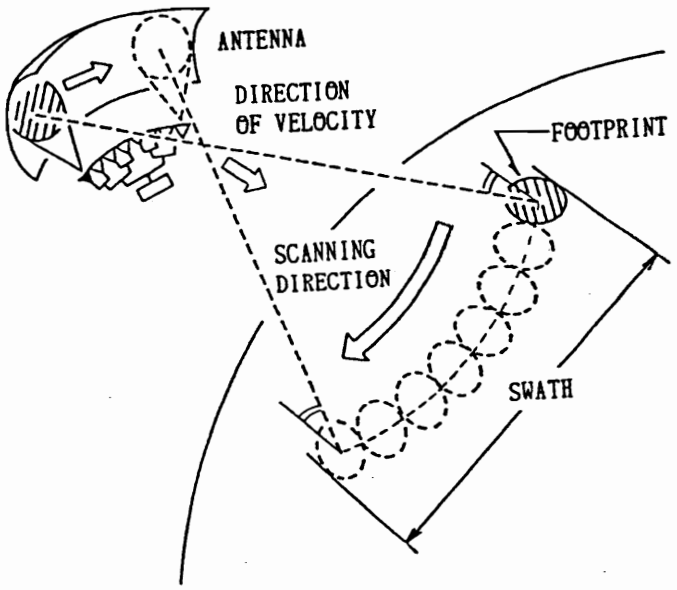

Figure 5.2-3. Push broom scanning using a conical parabolic torus reflector antenna to produce beams with constant incidence angles over the swath [3].

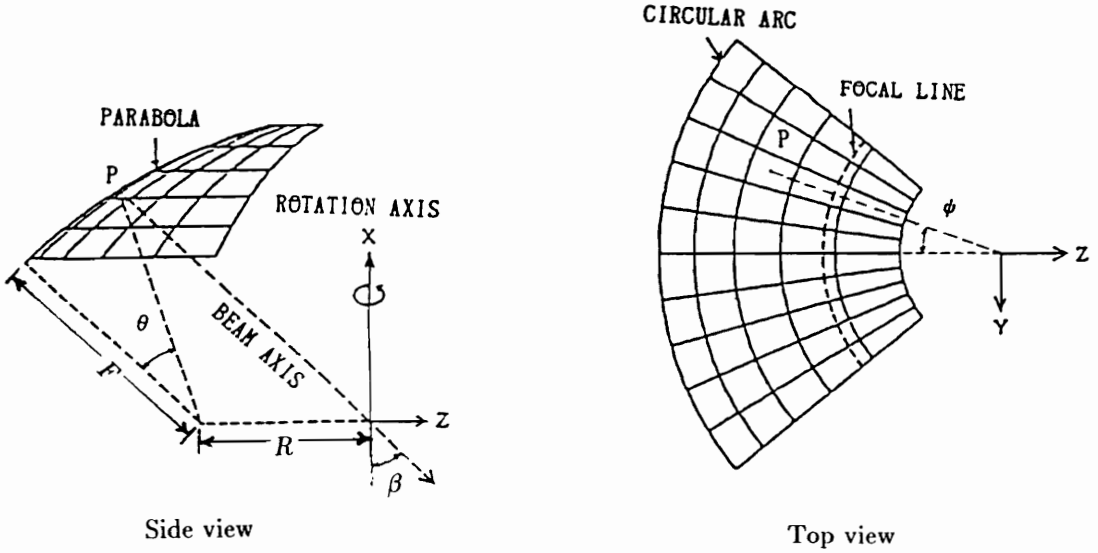

Side view

Top view

Figure 5.2-4. Geometry of a conical scanning parabolic torus reflector. The rotation axis is tilted by the off-nadir angle β with respect to the beam axis [3].

5.3 The High Aperture Efficiency Symmetric Reflector (HAESR)

The high aperture efficiency symmetric reflector is intended for applications requiring beam scanning in only one plane. Beam scanning is accomplished by feed motion along a focal curve or multiple feeds can be used to create several simultaneous beams [4]. For a maximum allowable aperture plane phase error the HAESR can achieve a much higher aperture illumination efficiency than possible with the parabolic torus and, therefore, a much smaller reflector can be used to achieve the same scan performance. The shape of the HAESR reflector surface is found in a two step process [4]. First, a fourth-order, even polynomial curve representing the reflector profile in the plane of scan is found using least squares to minimize scanned ray pathlength errors. Second, even polynomial terms in x and y which minimize astigmatism for both the unscanned and maximally scanned beams are added to form the three dimensional surfaces. The full design procedure is now outlined for a reflector designed to have a scan range of $\pm\alpha$ [4]. It is noted that the reflector configuration is symmetric about the zy-plane and, therefore, only the $+\alpha$ scan direction need be considered in the following design procedure.

The first step in the design procedure is to find the best scanning profile curve (the profile curve of a torus is circular). To initiate this step it is helpful to consider the ellipse shown in Fig. 5.3-1 [4]. The ellipse has foci at $(x,z) = (\pm c, 0)$ and a vertex point at $(0, -b)$. A ray starting at the focus point $(c,0)$ and reflecting at point $(0, -b)$ will pass through the second focus point at $(-c,0)$. This ray subtends angle $\alpha = tan^{-1}(c/b)$ with the z-axis. A tilted parabola can be defined which "best fits" the ellipse in the region about $(0, -b)$ as shown in Fig. 5.3-1 [4]. The tilted parabola has boresight direction α and is defined such that it passes through the vertex point $(0, -b)$ with the first derivative at $(0, -b)$ equal to zero $(dz/dx|_{(0,-b)} = 0)$ [4]. The preceding condition requires that the focal point of the tilted parabola (x_f, y_f) be located along the line between $(0, -b)$ and $(c,0)$. The tilted parabolic surface is given by [4]

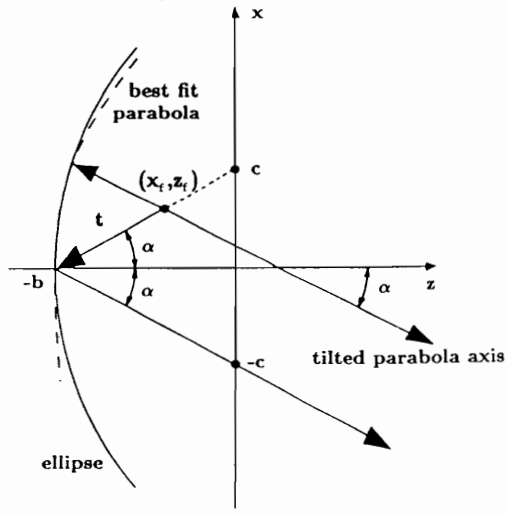

Figure 5.3-1. Ellipse and best fit tilted parabola used to initiate the design of the best scanning profile curve for the HAESR reflector [4].

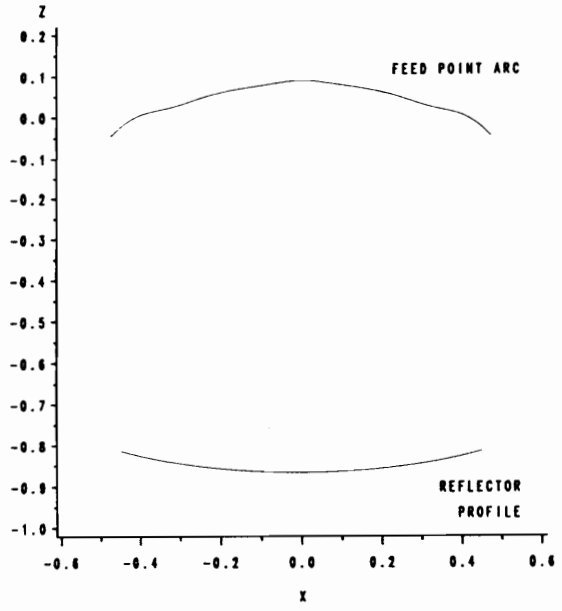

Figure 5.3-2. Scanning reflector profile curve and locus of optimum feed locations for the HAESR designed to scan $\pm 30^{\circ}$ [4].

$$z_p(x,y) = b(2t/c^2 - x/c - 1) - \sqrt{(2tb/c^2)^2(1 - cx/t) - (y/c)^2} \qquad (5.3\text{-}1)$$

where t is the distance of the focal point from the vertex point $(0, -b)$ along the line between $(0, -b)$ and $(c, 0)$.

Using the tilted parabola for the $+\alpha$ scan direction provides the basis for an improved profile based on the fourth-order even polynomial [4]

$$z_{so}(x) = -b + r_1 x^2 + r_2 x^4. \qquad (5.3\text{-}2)$$

The x^4 term represents a fourth-order correction to the untitled parabola given by the first two terms in (5.3-2). As long as the ratio r_1/r_2 is small, the difference near $x = 0$ between $z_{so}(x)$ and an untitled parabola with focus along the z-axis is small and, therefore, phase errors for beam pointing in the boresight direction are small [4]. Adding the x^4 term allows for a good fit between $z_{so}(x)$ and the tilted parabola $z_p(x,0)$ at points removed from $x = 0$ [4]. Thus, the profile curve $z_{so}(x)$ resembles an untitled parabola with focus on the z-axis for unscanned rays intersecting the curve near $x = 0$, and a tilted parabola with focus at (x_f, y_f) for scanned rays intersecting the curve at points removed from $x = 0$ [4]. The coefficients r_1 and r_2 are obtained by using the least squares method to minimize the difference between $z_{so}(x)$ and $z_p(x,0)$ over a specified range (or profile segment). An important aspect of the design is that different intervals or profile segments are used for different scan directions. Also, for any nonzero value of r_2 performance near the $z = 0$ axis is sacrificed in return for improved performance at the α scan limit [4].

It is desirable to maximize the length of the matching profile segment since this segment corresponds to the size of the usable portion of the reflector for scanned beams [4]. The size of the matching segment and the coefficients r_1 and r_2 are related to the focal length parameter t. As t is increased the reflector becomes flatter, the values of the coefficients decrease, and for a specified maximum allowable phase error the length of the matching segment can be increased. The size of the matching section and the value of the feed position parameter t are design parameters much like the F/D value for parabolic

reflectors [4]. These are selected by iterative reduction until the maximum error over the matching segment is less than a specified tolerance [4].

The second step in the design process is to extend the two-dimensional profile into a three-dimensional reflector surface. This is accomplished by adding terms of the form x^{2n} and y^{2n} to the profile of (5.3-2) resulting in the surface equation [4]

$$z_s(x,y) = z_{so}(x) + Py^2 + Qx^2y^2 + Ry^4 + Sx^4y^4. \tag{5.3-3}$$

The coefficients P, Q, R and S are found by matching to the ideal tilted paraboloid, however, for the three-dimensional case optimization is performed over a circular matching area instead of a profile segment [4]. The coefficients P, Q, R, S and the diameter of the matching area are related to the focal length parameter t. As t increases the reflector becomes flatter, the values of the coefficients decrease, and for a specified maximum allowable phase error the diameter of the matching area can be increased [4].

Rappaport [4] investigated the validity of the preceding design procedure by analyzing two example reflector configurations. The first configuration was designed to have a scan range of $\alpha = \pm 30^\circ$ and the second configuration was designed to have a scan range of $\alpha = \pm 8.5^\circ$. Performance of the configurations were evaluated using geometrical optics (G.O.) to obtain the aperture field distribution and the Fast Fourier Transform (FFT) to calculate the corresponding far field pattern [4].

A normalized (normalized by the focal length) profile of the reflector configuration designed to scan $\alpha = \pm 30^\circ$ is shown in Fig. 5.3-2 [4]. Also shown in Fig. 5.3-2 is the locus of feed positions corresponding to the $\pm 30^\circ$ scan range. The feed motion is more complicated than the circular feed path required for a parabolic torus. The illuminated region of the reflector has a diameter of 30 λ and the maximum phase error is limited to 8° ($\simeq 0.023\ \lambda$) [4]. The full profile of the reflector is 54 λ and the corresponding aperture area efficiency, as defined by (6.7-26), is $\eta_a \simeq 56$ % [4]. A torus reflector with similar scanning capabilities (8° maximum phase error) would have to be approximately 45 % larger and would have an aperture area efficiency of $\eta_a \simeq 39$ % [4].

Far-field patterns in the plane of scan are shown in Fig. 5.3-3. Figure 5.3-3(a) shows the radiation pattern for the 30° scan direction and Fig. 5.3-3(b) shows the radiation pattern for boresight operation. Also shown in Fig. 5.3-3 is the ideal pattern formed by a 30 λ diameter parabolic reflector. In Fig. 5.3-4 the performance of the HAESR and a parabolic reflector with the same focal length as the HAESR are compared over the 30° scan range [4]. For the unscanned beam the parabolic reflector has a peak gain that is 0.2 dB greater and a relative sidelobe level that is 2.5 dB lower than that produced by the HAESR [4]. However, for the 30° scan direction the beam produced by the parabolic reflector suffers a gain loss of 2 dB and a 9 dB increase in the relative sidelobe level while the characteristics of the beam produced by the HAESR remains relatively unchanged over the 30° scan range.

The effects on peak gain and relative sidelobe level caused by increasing the frequency with the HAESR are shown in Fig. 5.3-5 [4]. It is noted that while the peak gain remains relatively flat over the scan range for $D = 60\ \lambda$ and 90 λ, the effects of increased phase errors at the higher frequencies are evidenced by the decrease in peak gain. For $D = 60\ \lambda$ and 90 λ the peak gain produced by the HAESR is approximately 44 dB and 46 dB, respectively, while the peak gain produced by an ideal parabolic reflector at the two frequencies is 45.5 dB and 90 dB, respectively [4].

For the design of the $\alpha = \pm 8.5°$ reflector configuration the aperture area efficiency was maintained at $\eta_a = 49.2$ %; however, with the smaller scan range the maximum phase error was decreased to 7.56° ($\simeq 0.021\ \lambda$). The instantaneously illuminated aperture diameter is 500 λ and the $\pm 8.5°$ scan range corresponds to ± 68 beamwidths. The scan performance of this configuration is shown in Fig. 5.3-6 [4]. The peak gain of the unscanned beam is 1.2 dB below that produced by an ideal parabolic reflector and the relative sidelobe level is -13.9 dB [4]. For the 8.5° scanned beam the peak gain is only 0.4 dB below the peak gain produced by an ideal parabolic reflector and the relative sidelobe level is -11.6 dB [4].

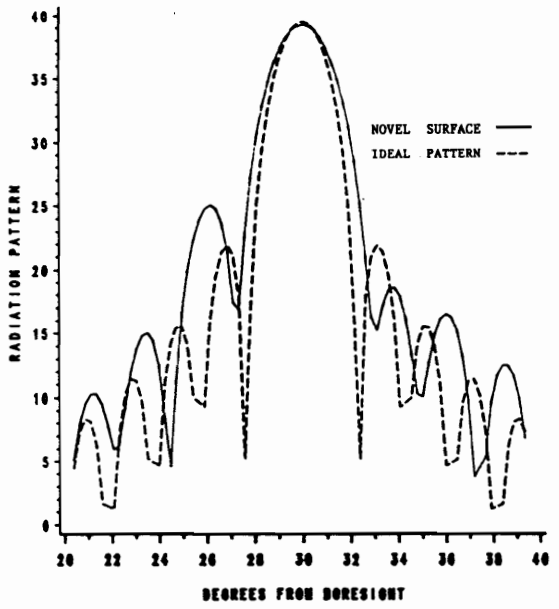

(a)

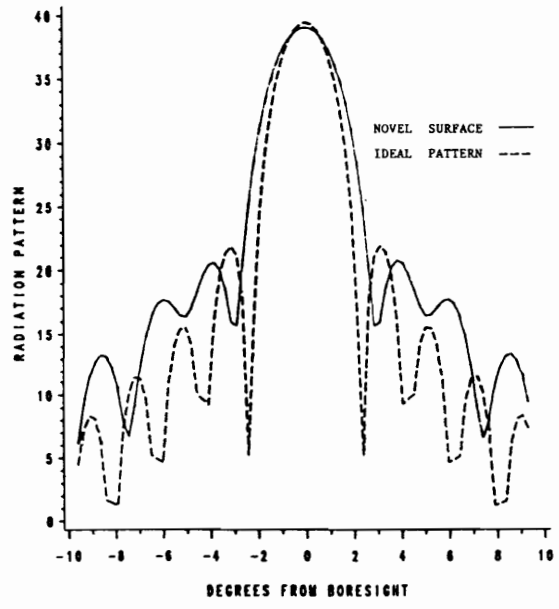

(b)

Figure 5.3-3. Radiation patterns produced by the HAESR reflector designed to scan $\pm 30^{\circ}$, and a 30 λ parabolic reflector with $F/D = 1$ [4]. (a) Radiation pattern through the plane of scan for the 30° scanned beam. HAESR reflector-solid; parabolic reflector-dashed. (b) Radiation pattern through the plane of scan for the unscanned beam. HAESR reflector-solid; Parabolic reflector-dashed.

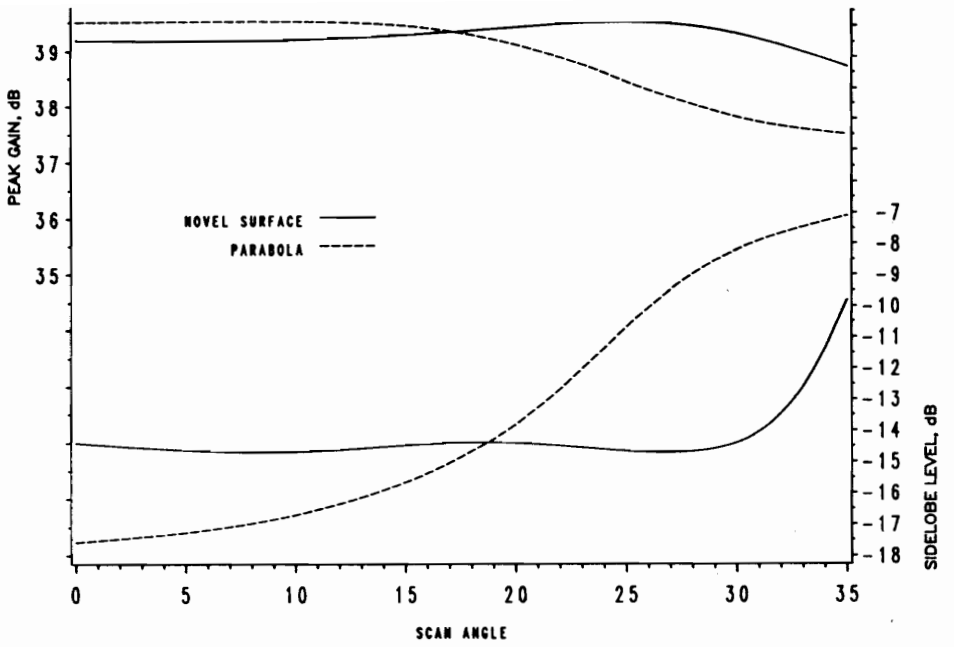

Figure 5.3-4. Peak gain and relative sidelobe level versus scan angle for the HAESR reflector designed to scan $\pm 30^{\circ}$, and a 30 λ diameter parabolic reflector with $F/D = 1$ [4]. HAESR reflector-solid; parabolic reflector-dashed.

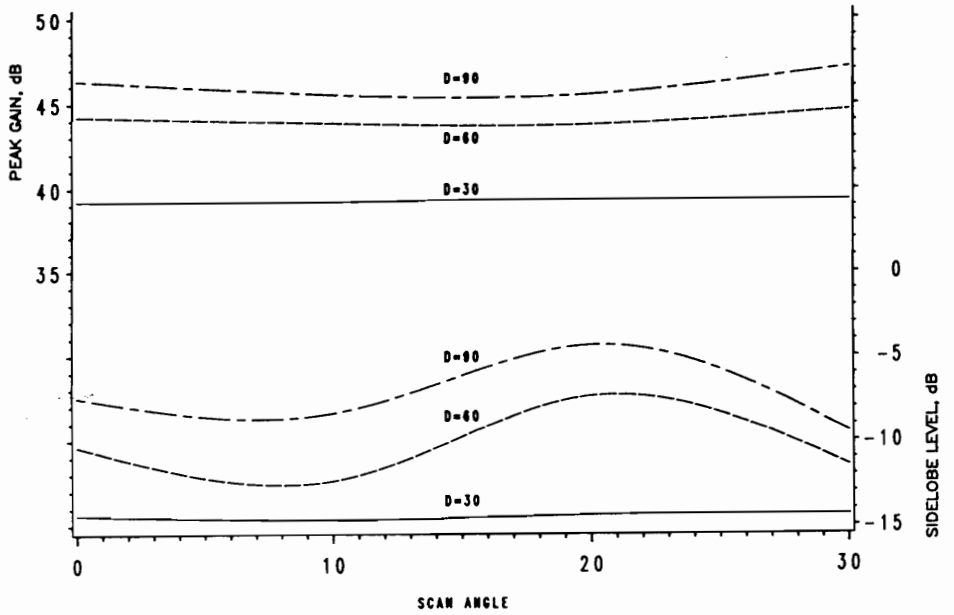

Figure 5.3-5. Peak gain and sidelobe level versus scan angle for the HAESR reflector designed to scan $\pm 30^{\circ}$ with an illuminated aperture diameter of 30 λ, 60 λ and 90 λ [4].

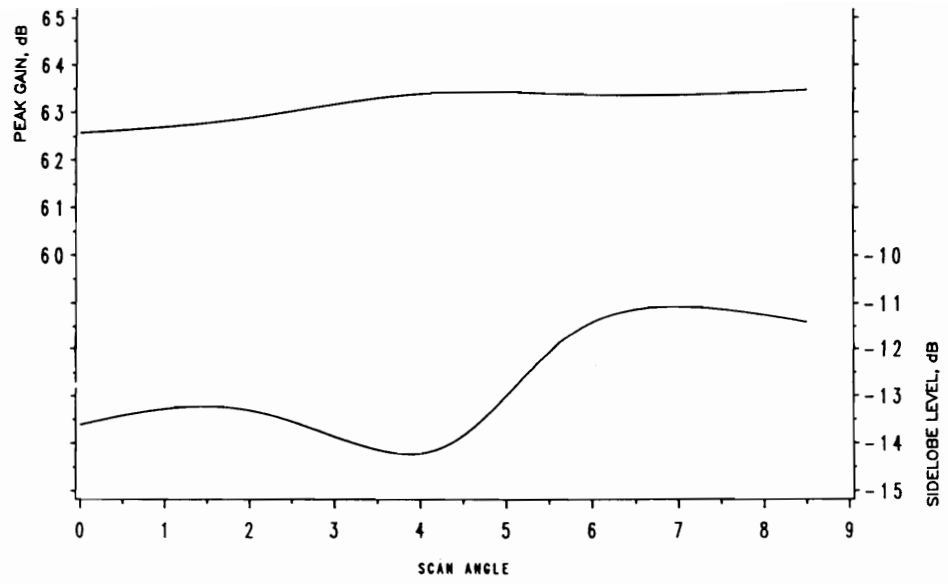

Figure 5.3-6. Peak gain and sidelobe level versus scan angle for the HAESR reflector designed to scan $\pm 8.5^{\circ}$ with an illuminated aperture diameter of 500 λ [2].

5.4 The Schwarzschild Reflector Configuration

The Schwarzschild reflector configuration is constructed of two shaped reflectors in a Cassegrain arrangement. The shape of the reflectors are defined such that as the feed is moved to the focal point from a displaced position the primary aberration coefficients in the perturbation eikonal of Schwarzschild (discussed in Chapter 2) go to zero with zero slope [5]. Therefore, for very small scan angles, the primary aberrations are vanishingly small and the beam scanning performance of the Schwarzschild configuration is enhanced compared to the classical Cassegrain reflector configuration.

White and DeSize [5] developed a method for obtaining a two-dimensional cylindrical Schwarzschild configuration. The geometry used is shown in Fig. 5.4-1 [5]. Figure 5.4-1(a) shows a cross-section of the reflector configuration and Fig. 5.4-1(b) shows an expanded view of the feed and aperture regions. Only half of the cross section is shown in these figures because the structure is rotationally symmetric about the x-axis. A ray parallel to the x-axis and separated from it by a distance H is reflected first by the main reflector and then by the subreflector. The angle between the final segment of the ray and the x-axis is α. The reflector system focuses incoming rays parallel to the x-axis to a point at the coordinate origin. If the source is displaced a small distance y normal to the x-axis, a new scanned plane wave should emerge from the system with a tilt angle θ relative to the original plane wave. Assuming the displacement y is small relative to the dimensions of the system, the change in the ray path length from the focal point to the aperture plane is given by [5]

$$\Delta p \simeq y \sin \alpha. \tag{5.4-1}$$

As shown in Fig. 5.4-1(a), the ray path length from the aperture to the emergent wave with tilt angle θ is given by [5]

$$\Delta p = H \tan \theta. \tag{5.4-2}$$

To ensure that all ray path lengths from the displaced focal point to the tilted

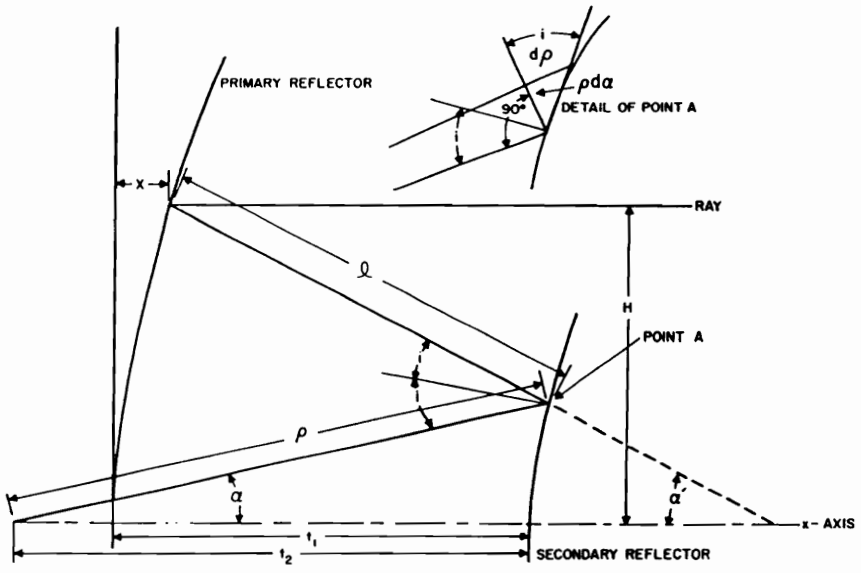

(a)

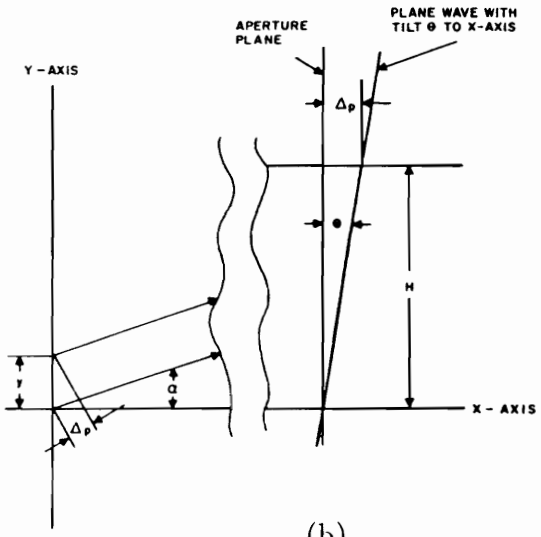

(b)

Figure 5.4-1. Geometry of the Schwarzschild reflector configuration [5]. (a) Cross-section of a generalized axis-symmetric Schwarzschild configuration. (b) Expanded view of the aperture plane and focal region of the Schwarzschild configuration.

plane wave are equal (corresponding to the phase error free condition for which all primary aberration coefficients are zero) (5.4-1) and (5.4-2) must be equal:

$$y \sin \alpha = H \tan \theta \tag{5.4-3}$$

or

$$\frac{H}{\sin \alpha} = \frac{y}{\tan \theta} = F \tag{5.4-4}$$

where F is a constant independent of H. Equation (5.4-4) is referred to as the Abbe' sine condition and is used in optical lens design [5].

White and DeSize [5] have obtained equations which satisfy (5.4-4) for the cross-sectional curves shown in Fig. 5.4-1. The subreflector is defined by $\rho(\alpha)$ which given by the following function [5]:

$$\frac{1}{\rho} = \frac{s}{t_1} + \frac{1}{t_2}\left(1 + \frac{S\kappa}{t_2}\right)^{\frac{F}{F - t_1}} (1 - S)^{-\frac{t_1}{F - t_1}} \tag{5.4-5}$$

where

$$s = \sin^2(\alpha/2). \tag{5.4-6}$$

The main reflector is defined by $x(H)$ which is given by the following [5]:

$$x = -t_2 + \frac{F^2}{t_1} s\,(1 - s) + t_2(1 - s)^{\frac{F}{F - t_1}} \left(1 - \frac{SF}{t_1}\right)^{\frac{F - 2t_1}{F - t_1}} \tag{5.4-7}$$

where

$$F = \frac{H}{\sin \alpha} = \frac{H}{2\sqrt{s\,(1 - s)}}. \tag{5.4-8}$$

Comparison of the equation for the parabola and the Taylor series expansion of (5.4-7) indicates that the two surfaces differ only by the presence of higher order terms (i.e. order 3 and greater). Therefore, it is possible to define a Schwarzschild reflector configuration and a classical Cassegrain configuration as

being "equivalent" if the main reflector surface curvatures on axis are the same to first order and the separation between main reflector and subreflector surfaces are the same [5]. For this case the constant F in (5.4-5) is equal to the focal length of the equivalent Cassegrain configuration [5].

White and DeSize [5] used geometrical optics to analyze the performance of several dual reflector configurations. Pathlength error as a function of aperture position for a Schwarzschild configuration and the equivalent classical Cassegrain configuration, both with a magnification of $m = 2$ and the feed located on the surface of the main reflector, are compared in Fig. 5.4-2 [5]. For this figure the aperture plane is parallel to the y-axis and is symmetric about the x-axis. Odd order (coma) aberrations cause the pathlength error curves to be anti-symmetric about the $y = 0$ axis while even order aberrations cause the pathlength error curves to be symmetric about the $y = 0$ axis. For both scan directions the Schwarzschild configuration shows a reduction in coma, as evidenced by the greater symmetry in the pathlength error curves, compared to the classical Cassegrain configuration. For the 5° scan case the improvement of the Schwarzschild configuration over the classical Cassegrain system is more pronounced than for the 10° scan case [5]. This result is expected because the design of the Schwarzschild configuration only ensures improved scan performance for small scan angles. White and DeSize [5] describe an over compensation method which decreases the amount of coma aberration over the scan range. Over compensation is obtained by calculating the amount by which the Schwarzschild main reflector deviates from a parabolic surface and then creating a new main reflector which increases this deviation by some percentage. The subreflector is then shaped such that phase errors are eliminated for boresight operation. For example, the reflector configuration is referred to as 100 % overcompensated if the main reflector doubles the deviation between the parabolic main reflector and the Schwarzschild main reflector. Pathlength error curves for a range of off-axis scan directions for a 100 % over compensated reflector configuration with magnification $m = 2$ are shown in Fig. 5.4-3 [5].

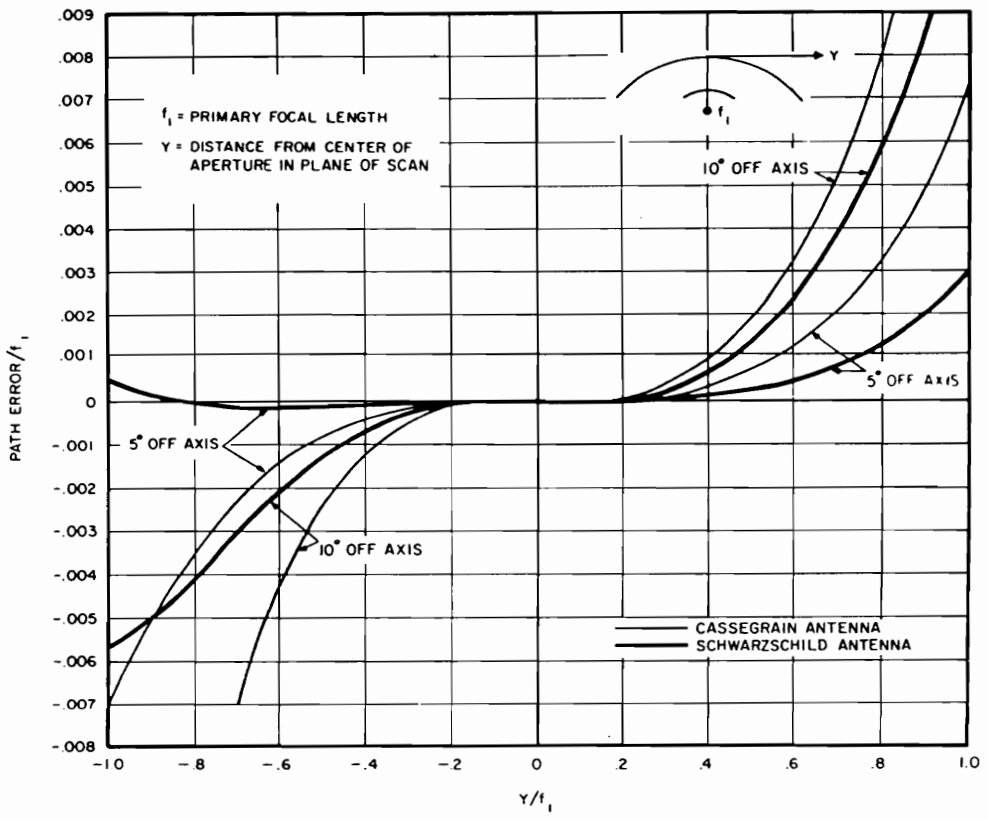

Figure 5.4-2. Path error curves in the aperture plane of a Schwarzschild reflector configuration and the equivalent classical Cassegrain configuration with magnification factor m = 2 [5].

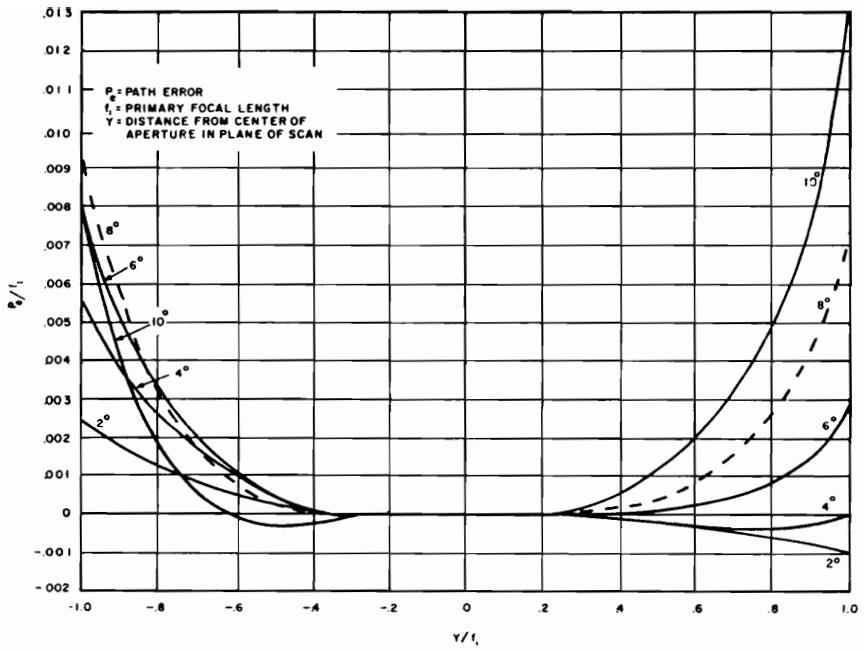

Figure 5.4-3. Path error curves in the aperture plane of a 100 % overcompensated reflector configuration with magnification factor m = 2 [5].

5.5 The Bifocal Reflector Configuration

With two shaped reflectors it is possible to create a reflector configuration with two perfect focal points corresponding to $\pm$ angular limits of scan. The impetus behind this design is the observation by Rao [6] that a bifocal dielectric lens has a wider angle scan capability than a dielectric lens with a single focus. Therefore, it is reasonable to assume that a bifocal reflector configuration will exhibit better beam scanning performance than a single focus reflector configuration.

Rao's [6] design technique for the bifocal reflector configuration involves obtaining a set of bifocal curves and then forming an axis-symmetric surface by revolving the curves about a central axis. A disadvantage of this design technique is that rotating the two dimensional curves to form a three dimensional structure spreads the two perfect focal points into an imperfect focal ring. Also, only axis-symmetric structures can be designed using this technique leading to aperture blockage. Despite these limitations theoretical analysis of a bifocal reflector configuration designed by this technique showed considerable scan improvement compared to an equivalent classical Cassegrain configuration [6]. A technique for obtaining a set of bifocal curves is presented later in this section. An example set of bifocal curves are shown in Fig. 5.5-1 where focal point $B(0,d)$ corresponds to the $-\alpha$ scan direction and focal point $A(0,d)$ corresponds to the $+\alpha$ scan direction [6].

A comparison performed by Rao [6] considered a bifocal configuration and a classical Cassegrain configuration for which the main reflector diameters were 6.48 m and the subreflector diameters where 1.25 m. The bifocal configuration had a focal ring corresponding to a 6° scan direction. Figure 5.5-2(a) shows the calculated secondary patterns for the bifocal configuration and those calculated for the classical Cassegrain configuration at 4 GHz over a scan range of 0° to 6° [6]. The variation in gain is 1.5 dB for the bifocal configuration versus 5.8 dB for the classical Cassegrain configuration, and the variation in half-power beamwidth is 0.8°-0.9° for the bifocal configuration versus 0.8°-1.5° for the classical Cassegrain configuration. The sidelobes are lower for the bifocal configuration except for patterns which are close to boresight. Boresight gain for the bifocal configuration

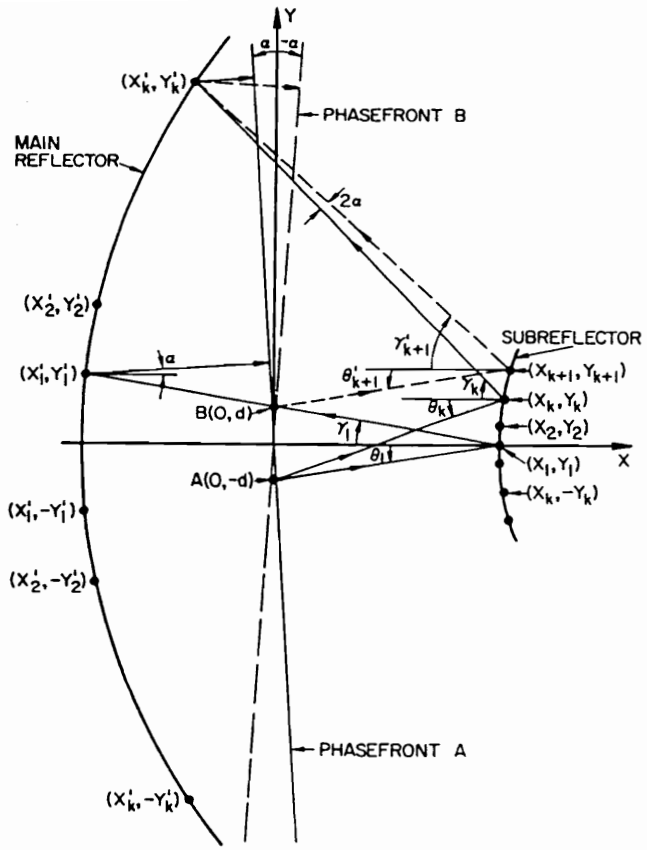

Figure 5.5-1. Cross-section of the axis-symmetric bifocal dual reflector configuration designed by Rao [6].

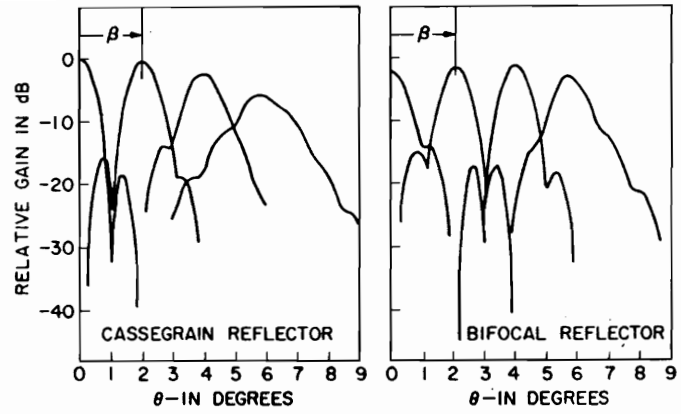

(a)

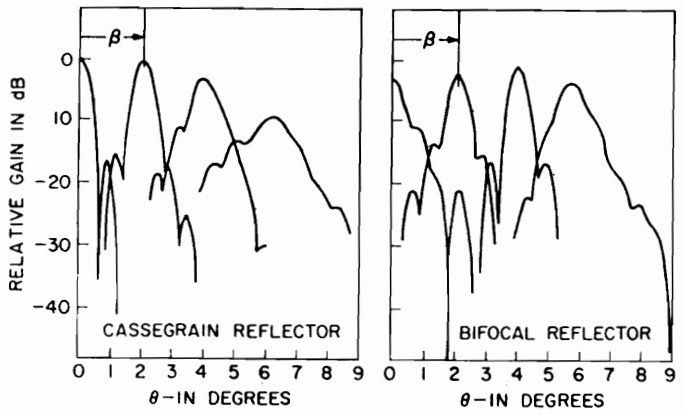

(b)

Figure 5.5-2. Calculated pattern versus scan direction θ for the axis-symmetric bifocal dual reflector [6]. (a) 4 GHz results. (b) 6 GHz results.

is several dB lower than that for the classical Cassegrain configuration. Figure 5.5-2(b) shows the calculated secondary patterns for the same example at a frequency of 6 GHz [6]. In this case the variation in gain over the scan range is 2 dB for the bifocal configuration versus 9.3 dB for the classical Cassegrain configuration, and the variation in half-power beamwidth is 0.6°-0.7° for the bifocal configuration versus 0.6°-1.2° for the classical Cassegrain configuration.

Rappaport [7] extended Rao's [6] technique by developing a method for generating three dimensional bifocal reflector surfaces with two perfect focal points. An advantage of this method is that it facilitates the design of offset configurations leading to reduced aperture blockage. A disadvantage is that improved scan capabilities are only obtained in the plane containing the two focal points as opposed to a conical region corresponding to the focal ring in Rao's technique. Rappaport's design procedure can be explained with reference to Fig. 5.5-3 [7]. Angle α specifies the scan direction and is measured counterclockwise from the x-axis in the xz-plane. Focal point F_1 corresponds to the $+\alpha$ scan direction and focal point F_2 corresponds to the $-\alpha$ scan direction. To eliminate phase error all path lengths from F_1 to the $+\alpha$ scanned aperture plane must be equal, and likewise for F_2 and the $-\alpha$ scanned aperture plane. The aperture center parameter C is the x-coordinate of the intersection line of the two scanned aperture planes. Adjusting C has the effect of moving the relative positions of the two aperture planes. Therefore, setting the path length from each focal point to their respective aperture planes to be equal to a constant L, and varying C, has the same effect as fixing the position of the aperture planes and using two different path length parameters (L_1 for one focus and L_2 for the other) which are varied independently of each other.

To initiate the design procedure a set of bifocal curves must first be obtained. To perform this step the following parameter values are specified: the scan angle α (the total beam scanning capability of the reflector is $\pm\alpha$); the focal point positions F_1 and F_2; the path length from the focal points to their respective aperture planes L; the aperture center C; an initial point on the subreflector S_1; and the subreflector normal at S_1, $\hat{n}_{S1}$.

Beginning with these initial parameters outgoing ray $\vec{R}_{1k}$ is traced from focal point F_1 to subreflector point S_k, where $k = 1$ for the initial subreflector

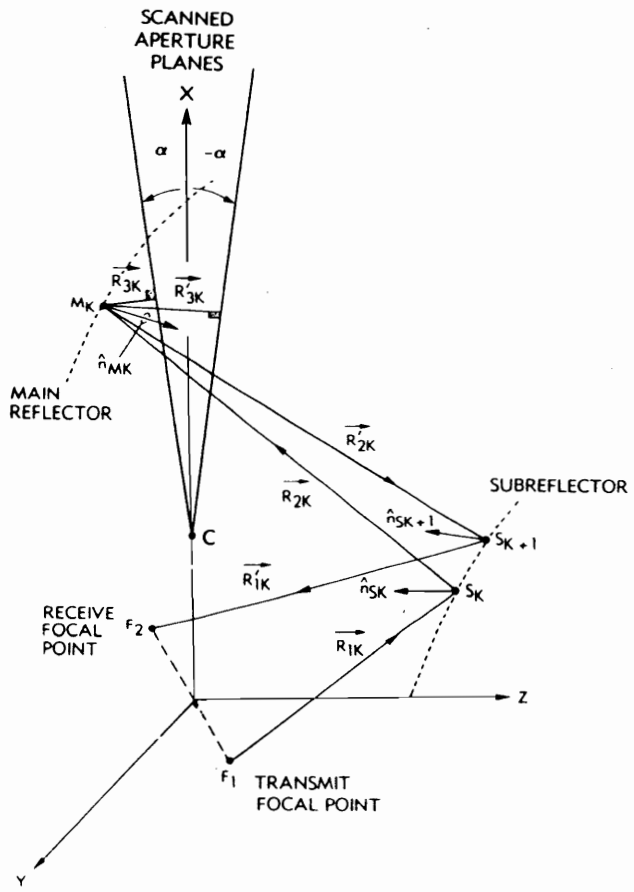

Figure 5.5-3. Geometry used for Rappaport's design procedure for the offset bifocal dual reflector antenna [7].

point. The normal at this point $\hat{n}_{Sk}$ is used to find the reflected ray $\vec{R}_{2k}$ such that Snell's law of reflection is satisfied. Using parameters α and C the position of the constant phase plane corresponding to the $+\alpha$ scan direction is found. Ray $\vec{R}_{3k}$ must be perpendicular to the constant phase plane and this property, along with the total pathlength L, is used to find the point on the main reflector M_k and the normal at this point $\hat{n}_{Mk}$ such that Snell's law of reflection is satisfied and

$$\vec{R}_{1k} + \vec{R}_{2k} + \vec{R}_{3k} = L. \tag{5.5-1}$$

Next, the system is considered in the receiving mode. The constant phase plane corresponding to the $-\alpha$ scan direction is found using α and C and the ray $\vec{R}'_{3k}$ is defined such that it is perpendicular to this plane and intersects the main reflector at point M_k. Using $\hat{n}_{Mk}$ and applying Snell's law of reflection reflected ray $\vec{R}'_{2k}$ corresponding to incident ray $\vec{R}'_{3k}$ is found. Finally, using $\vec{R}'_{2k}$, the position of the second focal point F_2 and the total path length L, a second point on the subreflector S_{k+1} and surface normal n_{Sk+1} are defined such that

$$\vec{R}'_{1k} + \vec{R}'_{2k} + \vec{R}'_{3k} = L \tag{5.5-2}$$

and Snell's law is satisfied on the subreflector. The entire process is repeated with a second ray $\vec{R}_{1k+1}$ which travels from F_1 to S_{k+1} and after several repetitions a locus of points and corresponding normals are found for both the main reflector and the subreflector. It is noted that with the above procedure there is no guarantee that the points and normals found for each reflector specify a continuous curve and hence a realizable solution. To ensure a continuous curve a cubic spline can be specified through the set of point corresponding to each reflector using the normal at the first and last points on each curve. If the normals at the rest of the points agree with those calculated by the cubic spline routine, it is assumed that a valid curve has been found [7].

Once a set of valid two dimensional curves are found the procedure is repeated to synthesize a three dimensional surface by choosing a new initial subreflector point which lies off of the plane of symmetry and performing a new

iterative generation, thus producing a second set of reflector curves [7]. A third set of curves is generated from a third subreflector point, and the process is repeated until the curves construct a surface. Although each curve in the process may be realizable, joining the curves to form a realizable surface presents the same problem as does joining the points with a curve. The sequence of initial subreflector points determines the relative positions of the reflector curves and hence the feasibility of joining them into a surface [7]. Therefore, a trial transverse polynomial $z = P(y)$ with $P(0) = 0$ is selected, which determines the shape of the subreflector in the third dimension [7]. The sequence of initial subreflector points and surface normals are given by [7]

$$s_{ij} = (x_0,\, \mathrm{i}\Delta y,\, z_0 + P(i\Delta y)) \tag{5.5-3 a}$$

$$\hat{n}s_{1i} = \frac{[ns_{1x},\ -(\frac{dP}{dy}|_{i\Delta y})ns_{1x},\ ns_{1z}]}{\sqrt{(ns_{1x})^2 + [(\frac{dP}{dy}|_{i\Delta y})^2 + 1]\ (ns_{1z})^2}} \tag{5.5-3 b}$$

where $(x_0, 0, z_0)$ and $(n_{s1x}, 0, n_{s1z})$ are the initial subreflector point and its normal, and $i\Delta y$ is an i^{th} increment in the y-direction. Optimizing the transverse polynomial and quantifying the effects of small variations has been identified as an area requiring future investigation [7]

Rappaport [7] used this algorithm to design and construct an offset bifocal reflector configuration with a scan capability of $\pm 8°$. To simplify construction it was desired to obtain a bifocal configuration for which a parabolic main reflector could be used. Therefore, to obtain a transverse polynomial a set of bifocal curves were found for which the main reflector approximated a paraboloid. Then, given the bifocal main reflector, the unscanned system focal point and the z-intercept of the subreflector, the closest classical Cassegrain configuration was found. The subreflector of the closest Cassegrain configuration was then used to obtain the transverse polynomial $P(y)$ [7].

The example bifocal configuration designed by Rappaport had a main reflector diameter of 130 λ, a subreflector diameter of 47.5 λ [7]. A comparison of calculated peak gain for the bifocal configuration, the most efficient Cassegrain

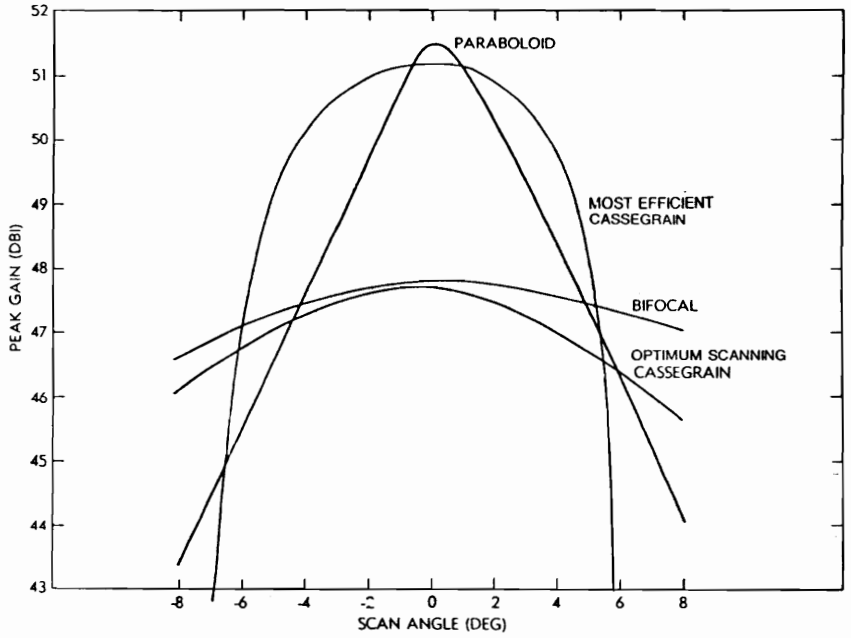

Figure 5.5-4. Comparison of calculated peak gain versus scan angle for an offset bifocal reflector configuration, an offset parabolic reflector, the most efficient classical Cassegrain configuration and the optimum scanning Cassegrain configuration [7]. Each constrained to fit within the same volume and have a 130 λ diameter aperture [7].

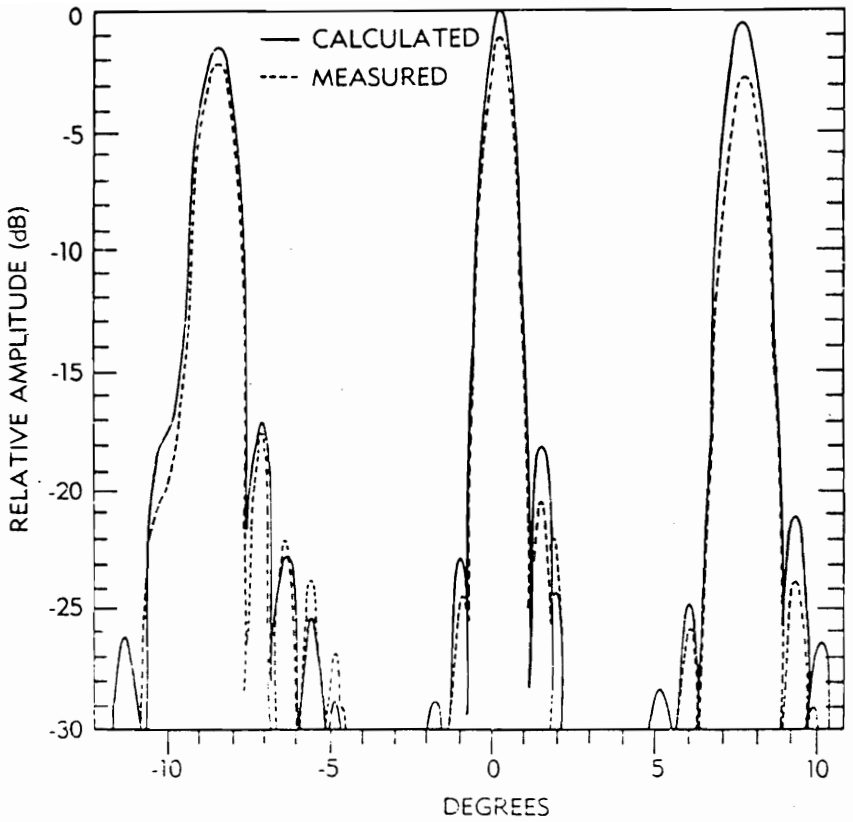

Figure 5.5-5. Comparison of calculated and experimental results for $-8°$, $0°$ and $+8°$ beam scan directions for an offset bifocal dual reflector with a 130 λ aperture [7].

configuration and the optimum scanning Cassegrain configuration (the optimum scanning Cassegrain is the classical Cassegrain from which the polynomial $P(y)$ was taken) are shown in Fig. 5.5-4. Each of these configurations are constrained to fit within the same volume and have a 130 λ aperture diameter [7].

Rappaport [7] constructed a model of the bifocal configuration for operation at 36 GHz. The main reflector was cut from a commercially available parabolic microwave reflector and the shaped subreflector was cut from high density styrofoam and coated with conducting paint [7]. The feed used was a conical Potter horn with a 9° flare angle and a 7 λ diameter aperture [7]. Measured versus calculated secondary patterns for scan angles of 8°, 0°, and $-8°$ are shown in Fig. 5.5-5 [7]. The bifocal configuration achieved a scan angle of $\pm 8°$ with a peak gain variation of only 3 dB and a first sidelobe level not exceeding 15 dB below the beam maximum, with no aperture blockage for any scan direction [7].

5.6 The Scan Optimized Dual Reflector Configuration

With a dual reflector configuration it is possible to create two perfect focal points corresponding to two distinct far-field scan directions, such configurations are discussed in Sec. 5.6. While it is not possible to create more than two perfect focal points with a dual reflector configuration, improvement over the scan performance possible with a bifocal configuration is possible by applying scan optimization [8]. With scan optimization the shapes of the main reflector and subreflector are "optimized" in the sense that aperture plane phase errors are minimized over the entire scan range. It is noted that the phase errors do not necessarily vanish in any given scan direction and, therefore, in general, no perfect focus point exists for the configuration.

Albertsen et al. [8] presented an optimization approach for which shape optimization is performed by an iterative procedure starting with an "initial"

guess classical Cassegrain configuration. Optimization is initiated by choosing a set of directions which span the scan range and optimizing performance for those directions. In each iteration the set of best feed positions for the given set of scan directions are calculated. For the set of feed positions the reflector surfaces are adjusted in a symmetrical way in order to reduce aberrations for the defined set of scan directions. The process is repeated until convergence to a "best" solution for the given set of scan directions. The procedure is more explicitly outlined in the following.

For the iteration procedure the surfaces are expanded in terms of cubic basis splines. Thus, the main reflector surface $f(x,y)$, is expanded in the series [8]:

$$f(x, y) = \sum_{i,j} c_{ij} B_i(x) B_j(y) \tag{5.6-1}$$

and the subreflector surface, $g(x, y)$, is expanded in the series

$$g(x, y) = \sum_{i,j} d_{ij} B_i(x) B_j(y) \tag{5.6-2}$$

where $B_i(x)$ and $B_j(y)$ are basis-spline functions and c_{ij} and d_{ij} are the expansion coefficients [8].

The reflector configuration is optimized using geometrical optics (G.O.). Rays are traced from the scanned aperture plane to the focal region. A point r_i in the focal region is found for each ray such that the pathlength from r_i to the aperture plane is the same for each ray. The feed position is defined as the mean value $\overline{u}$ of the points r_i and the variance is given by [8]

$$v = \sum_{i=1}^{N} \frac{1}{N} (r_i - \overline{u})^2. \tag{5.6-3}$$

The variance is used to obtain an estimate of the magnitude of phase aberration. For each iteration in the optimization procedure the optimum feed position for the given scan direction is calculated by obtaining the values of r_i which minimize the variance given by (5.6-3) [8]. Optimization of the reflector surfaces is then performed by a numerical Levenberg-Marquardt algorithm for

minimization of a sum of squares of nonlinear functions [8]. In this case the sum of squares to be minimized is given by (5.6-3) and the variables are the c_{ij} and d_{ij} coefficients of (5.6-1) and (5.6-2) [8].

Albertsen et al. [8] presented several reflector configuration examples. For the starting point an offset classical Cassegrain configuration was used. A cross-section of the initial reflector configuration in the plane of symmetry is shown in Fig. 5.6-1. The subreflector is a plane and the main reflector is a parabola for which $F/D = 1.5$. The diameter of the main reflector is $D = 300\ \lambda$ and a 10 dB edge taper was used. Two types of scanning were considered [8]: a planar scan range of $\pm 7^\circ$ orthogonal to the plane of symmetry; and a 3.5° conical scan. If the plane of symmetry is defined to be the xz-plane, then the planar scan range is defined by $\phi = 90^\circ$, $\theta = 0^\circ$-7° and $\phi = 270^\circ$, $\theta = 0^\circ$-7°, and the conical scan range is defined by $\phi = 0^\circ$-360°, $\theta = 0^\circ$-3.5°.

For planar scan two examples were considered [8]. For the first example scan optimization was performed for the following two scan directions to form a bifocal configuration: $\phi = 90^\circ$, $\theta = 7^\circ$; and $\phi = 270^\circ$, $\theta = 7^\circ$. For the second example scan optimization was performed for the following five directions to create a more uniform distribution of phase aberrations through out the scan range: $\phi = \pm 90^\circ$, $\theta = 0^\circ$, 3.5° and 7°. For the conical scan case scan optimization was performed for the following nine scan directions [8]: $\theta = 0^\circ$, and $\theta = 3.5^\circ$, $\phi = 0^\circ$, $\pm 45^\circ$, $\pm 90^\circ$, $\pm 135^\circ$ and 180°.

The maximum gain of the three shaped configurations and the non-shaped classical Cassegrain configuration are presented on Table 5.6-1 [8]. The results for the planar $\pm 7^\circ$ scan range will be considered first.

The non-shaped configuration has a peak gain of 58.51 dB for boresight operation and suffers a gain loss of 11.98 dB over the $\pm 7^\circ$ scan range. The bifocal configuration has a peak gain of 58.38 dB in the $\theta = 7^\circ$, $\phi = \pm 90^\circ$ scan directions corresponding to the perfect focal points and suffers a 3.05 dB gain loss over the $\pm 7^\circ$ scan range. The configuration optimized for the five scan directions has a peak gain of 58.31 dB in the boresight direction and suffers a gain loss of only 0.16 dB over the $\pm\ 7^\circ$ scan range. It is evident that the configuration optimized for the five scan directions achieves by far the best scan

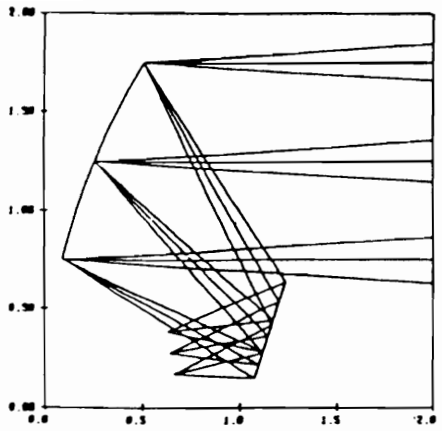

Figure 5.6-1. Cross-section of the initial reflector configuration used to obtain the scan optimized dual reflector configuration [8]. The aperture diameter is $D/\lambda = 300$ and $F/D = 1.5$ [8].

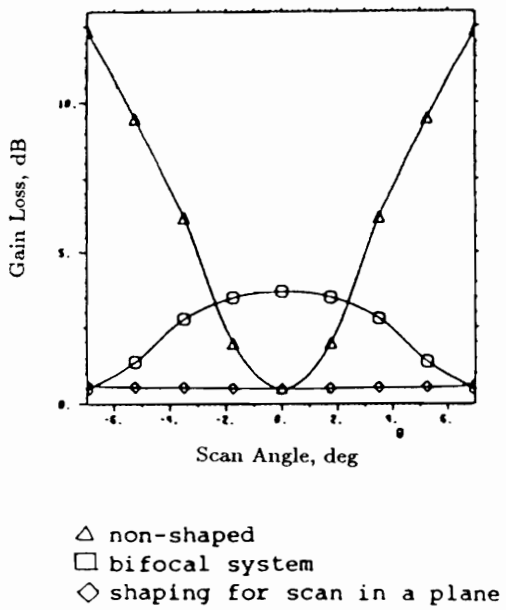

Figure 5.6-2. Gain loss versus scan angle calculated for: a non-shaped classical Cassegrain configuration-triangle; a bifocal configuration-square; and a configuration shaped for scanning in five directions-diamond [8].

performance while sacrificing only 0.2 dB of gain loss in the boresight direction compared to the classical Cassegrain configuration.

Table 5.6-1

Maximum Gain vs Scan Direction for Various Reflector Types [8]

Scan Direction θ	ϕ	Classical Cassegrain	Bifocal	Optimized for Five Directions	Optimized for Nine Directions
0.00°	0°	58.51	55.33	58.31	57.37
1.75°	90°	57.01	55.51	58.29	
3.50°	90°	52.82	56.19	58.24	57.58
5.25°	90°	49.48	57.57	58.21	
7.00°	90°	46.53	58.38	58.15	
3.50°	0°	52.05			56.50
3.50°	180°	53.65			56.40

The $\pm 7^{\circ}$ planar scan results on Table 5.6-1 are plotted in Fig. 5.6-2 in the form of gain loss versus scan angle [8]. For this plot gain loss is taken with respect to a uniformly illuminated 300 λ aperture for which the gain is 59.48 dB.

Results for the 3.5° conical scan case are also presented in Table 5.6-1 [8]. The non-shaped configuration has a peak gain of 58.51 dB in the boresight direction and suffers a gain loss of 6.46 dB over the conical scan range. The configuration optimized for nine scan directions has a peak gain of 57.58 dB in the $\phi = 90^{\circ}$, $\theta = 45^{\circ}$ scan direction and suffers a gain loss of 1.18 dB over the conical scan range. While the results for the conical scan configuration were not as impressive as those for the planar scan configurations, a 5.28 dB gain improvement was obtained with only a 0.93 dB loss in peak gain.

5.7 The Gregorian Corrected Spherical Reflector Configuration

To conserve space and keep required motions to a minimum, it is desirable to limit the F/D ratios of mechanically scanned microwave systems to approximately 0.5 or less [9]. If a spherical reflector has an F/D ratio of 0.5 and the total pathlength error over the aperture is limited to $\lambda/16$, then the maximum size of the illuminated aperture is restricted to 58.8 λ, as calculated by (5.1-5) assuming $D = a$ and $F = R/2$. Therefore, for systems with F/D ratios that are 0.5 or less and aperture diameters that are 58.8 λ or greater, some method of spherical aberration correction is needed if satisfactory antenna gain and beam shape are to be maintained.

The simplest method for correcting spherical aberration is with a single correcting subreflector as described by Holt and Bouche [9]. Positioned in a Gregorian configuration, the correcting subreflector is able to completely compensate for the spherical aberration caused be the spherical main reflector [9]. The secondary beam is scanned by moving the correcting subreflector and feed as a unit along a spherical surface [9]. A diagram of a spherical main reflector and correcting subreflector is shown in Fig. 5.7-1(a) [9]. If the spherical reflector subtends a cone of full angle 2β and the illuminated portion of the spherical reflector, due to rays reflected from the subreflector, subtends a cone of full angle 2α, both measurements made with respect to the center of curvature of the sphere (see Fig. 5.7-1), then the system scanning capability is a cone of full angle $2(\beta - \alpha)$. Scan angles greater than $2(\beta - \alpha)$ result in main reflector spillover as based on geometrical optics.

A parabolic surface reflects incident parallel rays to a single caustic point (focus point) and subreflectors can be placed either before or after the caustic point to create a Cassegrain or a Gregorian configuration, respectively. The situation is more complicated for a spherical reflector. Rather than a caustic point incident parallel rays are reflected to form a caustic region. The envelope of the caustic region is called the caustic surface and is specified by x_c and y_c which are given by [9]

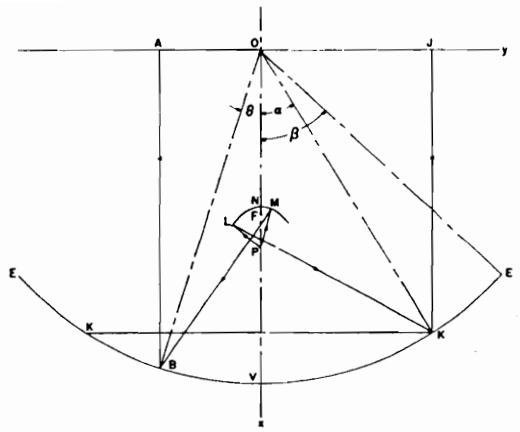

(a)

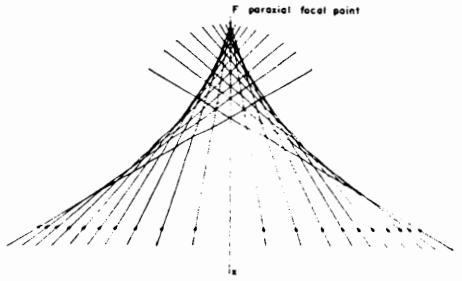

(b)

Figure 5.7-1. Spherical reflector with correcting secondary reflector [9]. (a) geometry of the configuration[9]. F = paraxial focus, V = reflector vertex, EE = reflector aperture, AOJ = reflector wavefront, $2(\beta - \alpha)$ = total scan angle, P = corrector focus, N = corrector vertex, KK = corrected aperture. (b) Ray trace of the caustic region for a plane wave reflected from a spherical surface.

$$x_c = \frac{R(3\ cos\theta - cos3\theta)}{4} \tag{5.7-1a}$$

$$y_c = \frac{R(3\ sin\ \theta - sin3\theta)}{4}. \tag{5.7-1b}$$

A ray trace of the caustic region is shown in Fig. 5.7-1(b) [9]. The darkened boundary of the cone shaped caustic surface is clearly seen in this figure. Energy density is high within the caustic surface and maximum near the paraxial focal point F located half way between the center of curvature for the spherical reflector O and the reflector vertex [9]. Inside the caustic region two or more reflected rays pass through each point while outside this region only one ray passes through each point. In general, each point on the subreflector surface can only correct for the pathlength error of a single ray, therefore, the correcting subreflector must be located outside of the caustic region [9].

Closed form expressions for correcting subreflector surfaces can be obtained by requiring that all rays traced from the feed to the aperture plane (located at O) have equal path lengths [9]

$$\overline{AB} + \overline{BM} + \overline{MP} = \overline{OV} + \overline{VN} + \overline{NP}. \tag{5.7-2}$$

Holt and Bouche [9] derived the equations for the correcting subreflector surface using a normalized configuration with the main reflector defined as a section of a sphere of unit radius. For this configuration, points on the reflector surfaces are defined as follows [9]:

$(c, s) = (\cos\theta, sin\theta)$: x, y coordinates of points on the spherical main reflector surface.

(u, v): x, y coordinates of points on the correcting subreflector surface.

(n, o): x, y coordinates of the vertex N of the correcting subreflector.

(p, o): x, y coordinates of the feed position P.

With these coordinates the location of the paraxial focus F becomes (1/2, 0) and (5.7-2) can be rewritten [9]

$$cos\theta + [(u-c)^2 + (v-s)^2]^{1/2} + [(u-p)^2 + v^2]^{1/2} = 2 - 2n + p. \tag{5.7-3}$$

Calculation of the slope of ray $\overline{BM}$ yields [9]

$$tan 2\theta = \frac{v-s}{u-c}. \tag{5.7-4}$$

Simultaneous solution of (5.7-3) and (5.7-4) for the coordinates (u, v) of points on the subreflector surface yields [9]

$$u = \frac{c - [c^2 - 4(1-n) - (1-p^2) + (2+p-2n)^2](2c^2-1)}{4(pc^2 - c - n + 1)} \tag{5.7-5}$$

and

$$v = \pm \frac{(2cu-1)s}{2c^2-1} \tag{5.7-6}$$

where n $\leq 1/2$ and $p \geq 1/2$.

A cross section of the caustic region and four specific examples of correcting subreflectors are plotted in Fig. 5.7-2 [9]. The angles noted on the subreflectors indicate the corresponding angular dimension of the illuminated portion of the main reflector, α (see Fig. 5.7-1) [9]. For teardroped shaped reflectors A B and C the points where the reflector intercepts the caustic surface determines the geometrical limits of usable corrector surface [9]. Subreflector D is located inside the caustic surface and therefore is not a valid solution. For a given feed position $p \geq 1/2$ and a given angular aperture illumination 2α, the corrector with minimum diameter and, therefore, the subreflector which causes the least amount of aperture blockage, is obtained by placing the corrector vertex at the paraxial focal point, $F = (1/2, 0)$ (surface B in Fig. 5.7-2) [9]. It is noted that for this case the caustic surface intersects the subreflector surface which leads to diffraction effects [18].

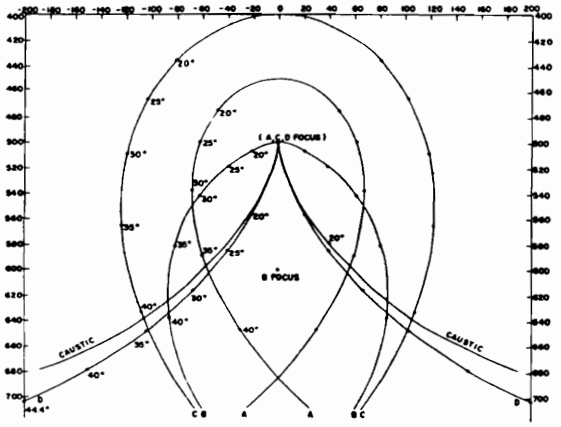

Curve	Corrector	
	Vertex n	Focus p
A	0.45	0.5
B	0.5	0.6
C	0.40	0.5
D	0.5	0.5

Figure 5.7-2. Cross section of Gregorian corrector shapes and there relation to the caustic surface formed by rays reflected from a spherical reflector surface [9].

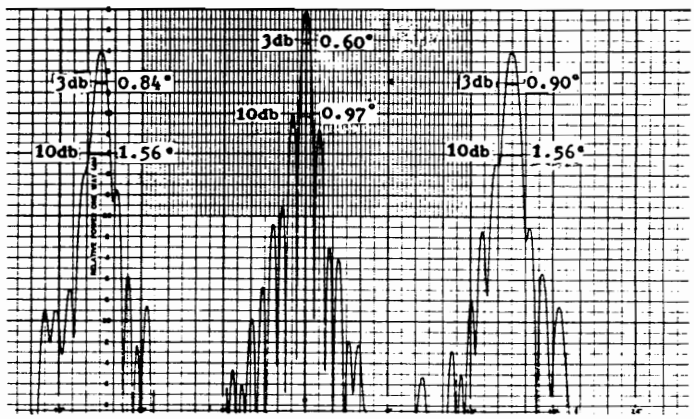

Figure 5.7-3. Measured H-plane patterns for a 10 foot spherical reflector ($n = 0.5, p = 0.6$) fed by a correcting reflector and horn combination at 9.34 GHz [9]. The scan range shown in $\pm 15°$ [9].

Holt and Bouche [9] presented experimental results for a spherical reflector with both a radius of curvature and an aperture diameter of 10 feet corresponding to a 60° cap from a complete sphere [9]. To keep the correcting subreflector as small as possible the subreflector vertex was placed at the paraxial focus point, $n = 0.5$. The feed was placed at a point 1 foot from the paraxial focus corresponding to $p = 0.6$. For this reflector configuration the correcting subreflector surface, as obtained from (5.7.5), is given by the following [9]:

$$x_s = 120\ u = 120\left[\frac{c - (c^2 - 2c + 1.6)(2c^2 - 1)}{4\ (0.6\ c^2 - c) + 2}\right] \text{inches} \tag{5.7-7}$$

and

$$y_s = \pm 120\ v = 120\left[\frac{(2uc - 1)s}{2c^2 - 1}\right] \text{inches.} \tag{5.7-8}$$

The feed/subreflector illumination pattern had a conical angle of $2\alpha = 60°$ such that the entire surface of the main reflector was illuminated [9]. Therefore, $\alpha = \theta$ (see Fig. 5.7-1) and in (5.7-7) and (5.7-8)

$$-30° \leq \theta \leq 30°. \tag{5.7-9}$$

For the marginal ray $\theta = \alpha = 30°$, (5.7-8) yields $y = Rv_{max} = 7.5$ inches and, hence, the diameter of the correcting subreflector is 15 inches (12.5 % of the main reflector diameter). Aperture blockage due to the correcting subreflector is approximately 1.5 % of the area of the main reflector aperture. Any amount of beam scanning results in main reflector spillover and a corresponding decrease in gain and beamwidth because the main reflector is fully illuminated for boresight operation.

Experimental results at 9.44 GHz, corresponding to a 96 λ aperture, showed a beamwidth of 0.59° and a first sidelobe level in the range of -11 dB to -12 dB. Typical H-plane patterns over the $\pm 15°$ scan range are shown in Fig. 5.7-3 [9]. Over the scan range the side lobe levels remain constant and the beamwidth increases. The increase in beamwidth, which results in an

approximate 4 dB gain loss at the scan limit, is due to the effective decrease in the size of the illuminated aperture due to main reflector spillover. At 24 GHz, corresponding to a 245 λ aperture, the measured beamwidth was 0.22° and the first sidelobe level was again in the range of -11 dB to -12 dB [9].

High sidelobe levels are associated with the Gregorian corrected spherical reflector configuration because the subreflector geometry required to correct for spherical aberrations causes a high inverse illumination taper across the main reflector aperture [9]. A more desirable illumination taper can be obtained by introducing a second subreflector as is discussed in the next section.

5.7.1 Method for Increasing Aperture Efficiency

With the Gregorian corrected spherical reflector it is possible to increase main reflector illumination efficiency by oversizing the correcting subreflector and illuminating a different portion of the subreflector for different scan directions. Figure 5.7-4(a) shows a cross-section of the traditional scanning scenario for a spherical reflector with a correcting subreflector. The feed and subreflector move together as a fixed unit. The main reflector is oversized to allow for $\pm$ 5° of scan with no spillover, as defined by the edge rays, and to have a 30 m illuminated region on the main reflector. The resultant main reflector physical diameter is 36 m. Figure 5.7-4(b) shows the method for increasing main reflector illumination efficiency. The subreflector motion is identical to that shown in Figure 5.7-4(a), however, during scan the feed is tilted to illuminate a slightly different portion of the subreflector such that the same portion of the main reflector is illuminated for all scan directions. Increased blockage due to the larger subreflector could be eliminated by using an offset configuration. A disadvantage of this concept is the increased complexity associated with independent motion between the subreflector and feed horn.

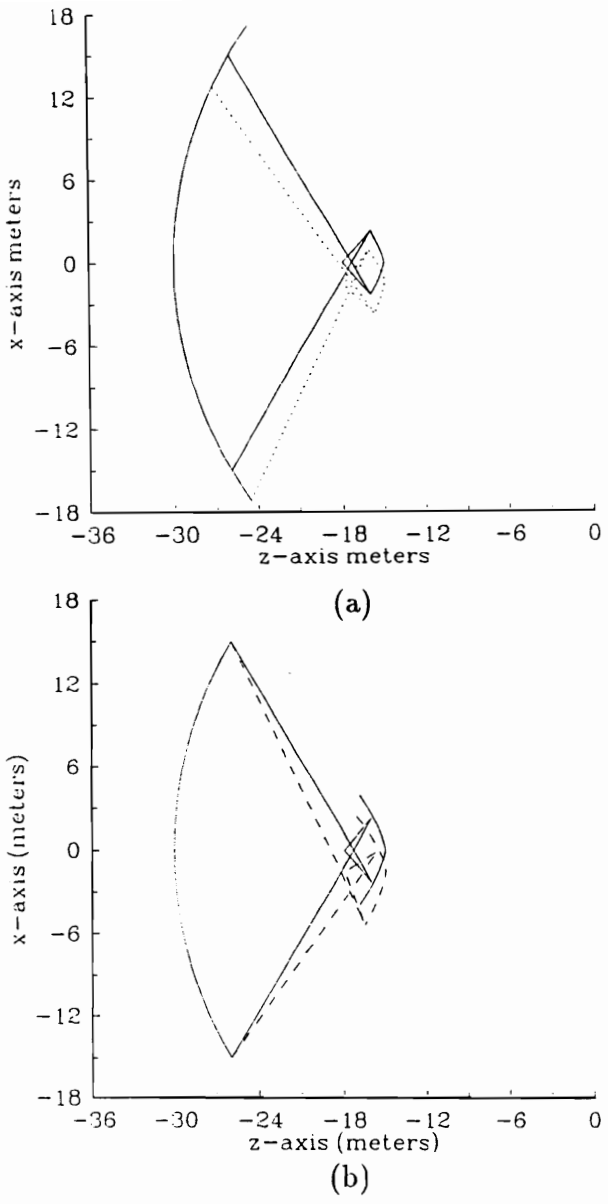

Figure 5.7-4. Comparison of scanning scenarios for a 25 m spherical reflector with a Gregorian corrector over a scan range of $\pm 5^{\circ}$. The solid line indicates feed and subreflector positions for boresight operation and the dashed line indicates feed and subreflector positions for the 5° scan direction. (a) Conventional scanning scenario with oversized main reflector to prevent spillover. (b) Scanning scenario with oversized subreflector and relative motion between the feed and subreflector such that the same region of the main reflector is illuminated for each scan direction.

5.8 The Dual Corrected Spherical Reflector Configuration

A spherical main reflector with a single correcting subreflector was introduced in Sec. 5.7. The single subreflector was able to correct the spherical aberrations caused by the main reflector; however, the corrector caused an inverse illumination taper in the aperture of the main reflector leading to an unacceptably high side lobe level [9]. Mittra and Galindo-Israel [10] have shown that with a reflector system consisting of two shaped reflectors it is possible to control both the phase and amplitude distribution in the aperture of the larger reflector. Therefore, two shaped subreflectors can be used as a feed system for a spherical main reflector to provide control of both phase and amplitude in the aperture of the main reflector. For such three reflector configurations the subreflector which is optically closest to the main reflector is called the secondary reflector and the reflector which is optically closest to the feed horn is called the tertiary reflector. Also, for consistency, the the term primary reflector is applied to the main reflector. With two correcting subreflectors beam scanning is achieved by moving the feed and the two correcting subreflectors as a rigid unit along a spherical surface. As with the single corrector discussed in Sec. 5.7, the aperture efficiency can be improved by oversizing the subreflectors and rotating the feed relative to the subreflectors to illuminate the same portion of the primary reflector for all scan directions.

The origins of dual reflector shaping to achieve control of both amplitude and phase can be traced to Kinber [11] in 1962 and Galindo [12] and Green [13] in 1963. The goal of these early works was to obtain dual reflector configurations with both high aperture efficiency and low spillover for radio astronomy. The objective of dual shaped reflector synthesis can be described with the help of Fig. 5.8-1 [10]. The bundle of rays radiated from the feed is the G.O. representation of the feed pattern in both phase and amplitude [10]. The output bundle of rays corresponding to a specific feed pattern after two reflections is required to have [10]: (i) a prescribed phase front; (ii) a prescribed energy density distribution; and (iii) a prescribed periphery.

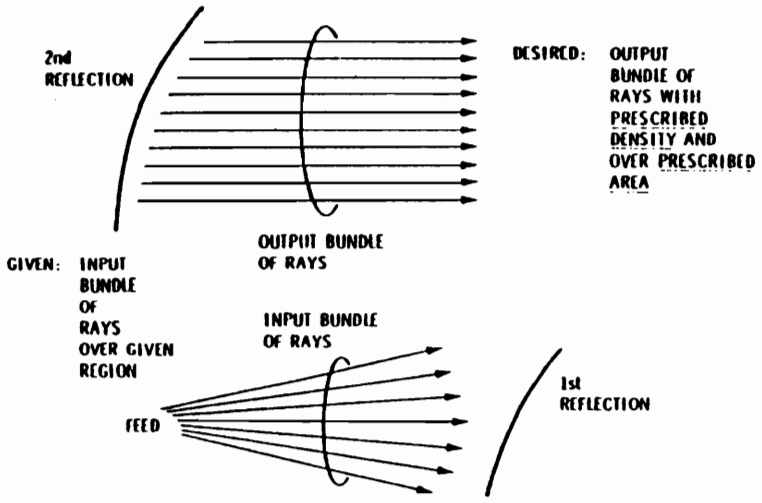

Figure 5.8-1. Geometrical optics representation of the problem to be solved by dual reflector synthesis [10].

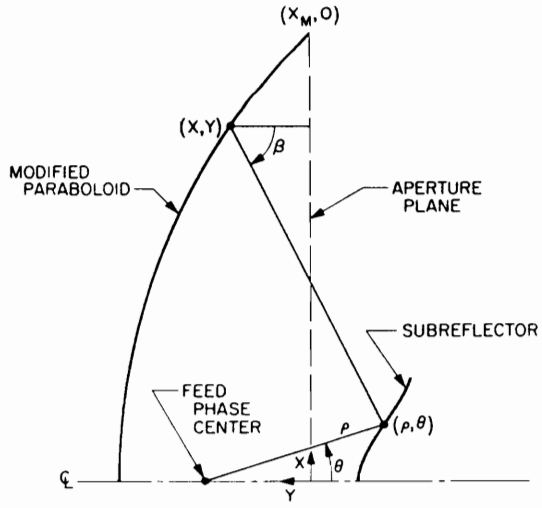

Figure 5.8-2. Geometry of a dual shaped reflector configuration [21].

A non-mathematical approach was taken by Green who observed that for a two reflector configuration of high magnification (a large ratio of main reflector to subreflector diameter) the distribution of energy in the main reflector aperture is largely controlled by the subreflector curvature while the phase distribution is largely controlled by the main reflector curvature [13]. For prime focus parabolic reflectors a $csc^4(\theta/2)$ feed power pattern results in a (maximum-gain) uniform amplitude aperture distribution; therefore, Green took a given feed pattern and designed a circularly symmetric subreflector which radiated a $csc^4(\theta/2)$ power pattern [13]. The subreflector designed by Green did not radiate a spherical wave front. To compensate for the nonspherical incident phase front, Green perturbed the shape of the main reflector making it non-parabolic [13]. He found that this perturbation had only a small effect on the aperture energy distribution. He thus obtained an aberration free phase front and a very good approximation to a uniform amplitude distribution [13]. It has been noted that it is difficult to show whether further iterations in perturbing the shape of the secondary reflector and primary reflector would converge to an exact solution [13].

For rotationally symmetric (axis-symmetric) reflector configurations a set of differential equations can be obtained which yield an exact solution for the shapes of both the main reflector and the subreflector corresponding to a desired aperture phase and amplitude distribution. This is referred to as the differential approach [11,12].

5.8.1 The Differential Equation Approach

The differential equation approach was introduced by Kinber [11] and Galindo-Israel [12]. Referring to Fig. 5.8-2, the following principles of geometrical optics are used to develop a set of coupled differential equations [21]:

1. Snell's law: at each reflector the incident and reflected rays and the surface normal are coplanar and the angle of incidence equals the angle of reflector [21]. Hence,

$$\frac{1}{\rho}\frac{d\rho}{d\theta} = tan\left[\frac{(\theta+\beta)}{2}\right] \tag{5.8-1 a}$$

$$\frac{dy}{dx} = -tan\left[\frac{\beta}{2}\right] \tag{5.8-1 b}$$

2. Conservation of Energy: energy flow along each differential tube of rays remains constant, even when the tube undergoes reflection [21]. Hence,

$$I(x)\ x\ dx = F(\theta)\ sin\theta\ d\theta \tag{5.8-2}$$

where $F(\theta)$ is the axially symmetric distribution of power radiated by the primary feed and $I(x)$ is the power distribution in the main reflector aperture.

3. Theorem of Malus: ray directions are normal to the constant-phase surfaces and this condition is maintained after any number of reflections [21].

Rearranging the above three simultaneous differential equations in the unknowns ρ, θ and y yields the following set of ordinary, nonlinear simultaneous equations which can be solved to achieve an exact solution for the reflector surfaces [21]:

$$\frac{d\rho}{dx} = \rho\frac{d\theta}{dx}\,tan\left[\frac{\theta+\beta}{2}\right] \tag{5.8-3}$$

$$\frac{d\theta}{dx} = \frac{x\ I(x)}{sin\ \theta F(\theta)} \tag{5.8-4}$$

$$\frac{dy}{dx} = -tan\,\frac{\beta}{2}. \tag{5.8-5}$$

A complete description of the synthesis procedure is found in [12].

If the offset reflector problem is formulated by the same method as that

employed for the axis-symmetric problem, there results a set of partial, instead of ordinary, nonlinear simultaneous equations which must be solved [10,14,15]. The existence of a solution to these differential equations requires that they form a total differential [10]. Galindo and Mittra [14] showed that in many cases the equations form a nearly total differential. Hence, in order to obtain a solution one or more of the three requirements must be relaxed [10]. For example a solution can be obtained for a pair of reflectors which satisfy the aperture power constraint (ii) and the periphery constraint (iii) but do not fully satisfy the phase constraint (i). The main reflector can then be reshaped to eliminate residual aperture plane phase errors; however, this compromises constraints (ii) and (iii) [15].

5.8.2 The Iterative Approach

Iterative techniques have been developed to solve the problem of synthesizing offset dual shaped reflector systems [16,17]. With these techniques the synthesis problem is reduced to solving a set of linear equations by locally expanding the reflector surfaces in terms of smooth surface functions. As with solutions based on differential equations, iterative techniques only guarantee convergence to physically realizable reflector surfaces for axis-symmetric configurations; however, an advantage of iterative techniques is that the solution is easier to control. For example, in order to obtain a nearly exact solution for offset configurations, the iterative technique developed by Kildal [18] incorporates a floating mapping procedure which automatically relaxes the aperture plane power distribution constraint until a solution which satisfies the phase constraint and "best satisfies" the aperture plane power constraint is achieved [18]. Kildal's [18] method has been used to design a pair of offset dual correcting subreflectors for the 305 m spherical reflector antenna at the Arecibo observatory. A diagram of the primary reflector, correcting subreflectors, feed and sample rays is shown in Fig. 5.8-3 [18]. The reflectors are offset to eliminate blockage due to the tertiary reflector. The feed has a theoretical $cos^n(\theta/2)$ pattern and n is adjusted to give a -18.19 dB illumination taper at the edge of the tertiary reflector, which corresponds to $\theta \simeq 30°$. The correcting subreflectors

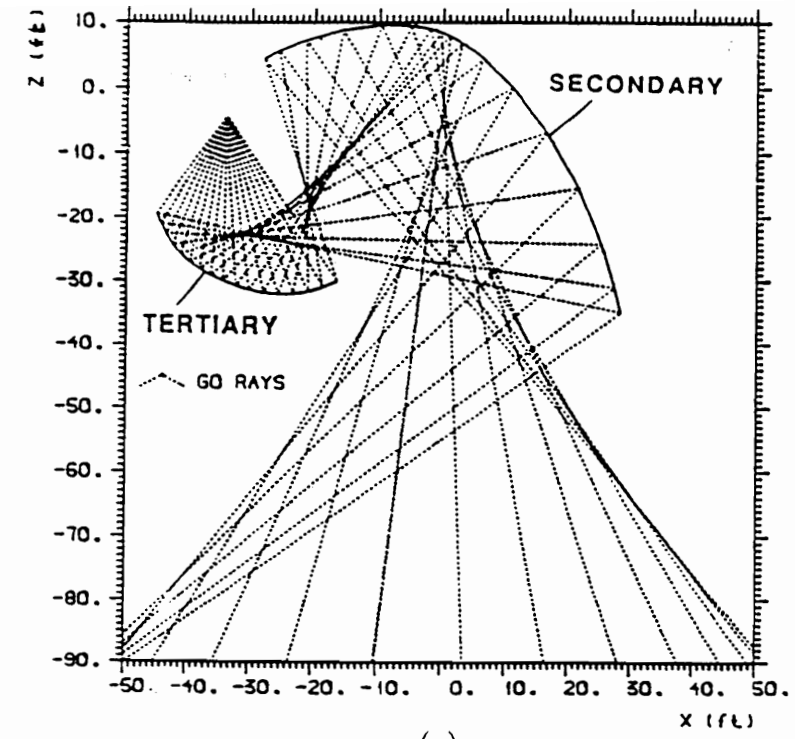

(a)

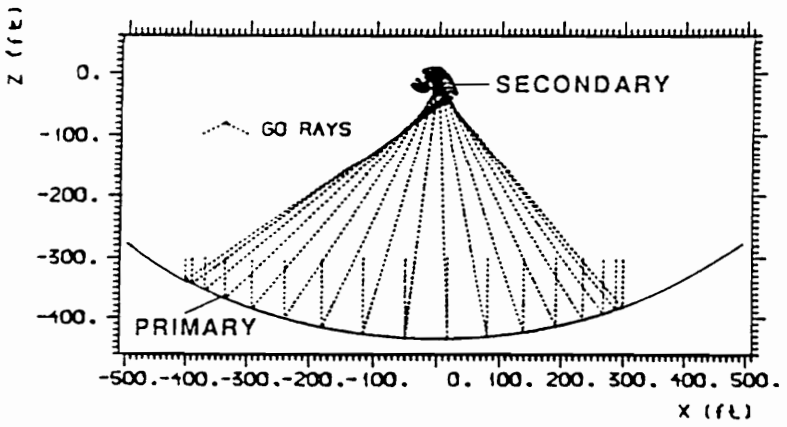

(b)

Figure 5.8-3. Cross-section of the spherical primary reflector and Gregorian dual-reflector feed proposed for use on Arecibo [18]. (a) Detail of the dual reflector feed. (b) Complete tri-reflector configuration.

are designed to produce a primary aperture edge taper of -6 dB.

The aperture plane field distribution calculated using G.O. is shown in Fig. 5.8-4(a) and the aperture plane field distribution calculated using P.O. at 1 GHz is shown in Fig. 5.8-4(b) [18]. There is good agreement between the G.O. and P.O. calculated fields; however, the P.O. field has a finite slope at the G.O. boundaries and the P.O. field has a dip at the center of the aperture. The slope is an expected result of edge diffraction [18]. The dip, which is more pronounced at low frequencies and is not at the center of the illuminated aperture, has been shown to be a diffraction effect associated with the paraxial focus (i.e. the cusp of the caustic surface) and is referred to as cusp diffraction [18]. Cusp diffraction represents a general physical limitation which occurs when a reflector surface is located too close to a cusp as is the case with the secondary reflector shown in Fig. 5.8-3 [18]. Cusp diffraction can be reduced by moving the secondary reflector surface further away from the paraxial focus, however, this results in a larger subreflector surface and more aperture blockage. Kildal [18] notes that the size of the illuminated portion of the primary reflector can be increased without increasing spillover by making the illuminated aperture elliptical with the largest cross section orthogonal to the plane of beam scanning; however, the corresponding radiation pattern will assume a slightly elliptical cross section.

5.8.3 The Optimization Approach

A third method for generating shaped dual reflecting surfaces is to make use of nonlinear computer optimization techniques [17,19]. An advantage of this approach is that it is easy to implement for offset configurations while other approaches require extensive manipulation to ensure convergence to a best solution [15,16].

A good example of the optimization approach is the technique used by Watanabe [19] to design a pair of shaped subreflectors to be used with a spherical primary reflector. With Watanabe's technique the shapes of the correcting subreflectors are determined such that the following two conditions are satisfied [19]:

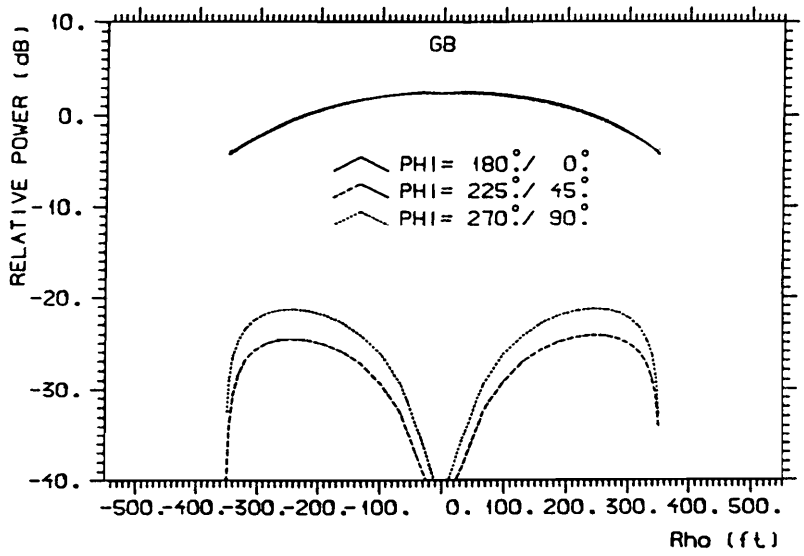

(a)

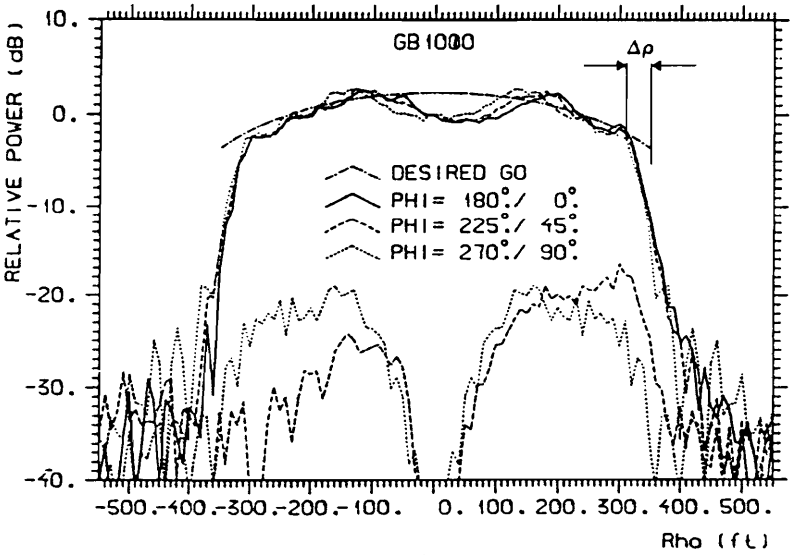

(b)

Figure 5.8-4. Co- (solid curve) and Cross- (dashed curve) polarized aperture fields for the tri-reflector configuration shown in Fig. 5.8-2 [18]. (a) Obtained by geometrical optics. (b) Obtained by physical optics integration.

a. No phase aberrations are present in the aperture of the primary reflector.

b. The difference between the desired aperture intensity distribution and the intensity distribution obtained by shaping the correcting subreflectors is minimized.

The reflector configuration considered by Watanabe [19] is shown in Fig. 5.8-5. With Watanabe's [19] notation the primary reflector, secondary reflector and tertiary reflector are referred to as the main reflector, sub-reflector and aux-reflector, respectively. Watanabe's approach begins with an initial guess for the specified feed pattern $I_f(\theta)$ and the shape of the aux-reflector, which is represented in spherical coordinates by $r = f(\theta, \phi)$ [19]. With this starting point the following procedure is performed [19]:

(1) For the given aux-reflector function f the shape of the secondary reflector which satisfies the aberration free requirement (a) is obtained.

(2) For the given tertiary reflector and secondary reflector, the intensity distribution in the aperture plane $I(\rho_a, \phi_a)$ is calculated based on the feed pattern $I_f(\theta)$.

(3) The difference between the calculated aperture plane energy distribution and the desired aperture plane energy distribution $I_d(\rho_a, \phi_a)$ is used to obtain the error

$$\epsilon = \iint\limits_{aperture} |I(\rho_a, \phi_a) - I_d(\rho_a, \phi_a)|^2 \, ds. \tag{5.8-6}$$

Using the above three steps the shapes of the subreflectors satisfying requirements (a) and (b) are obtained by solving the variational problem of

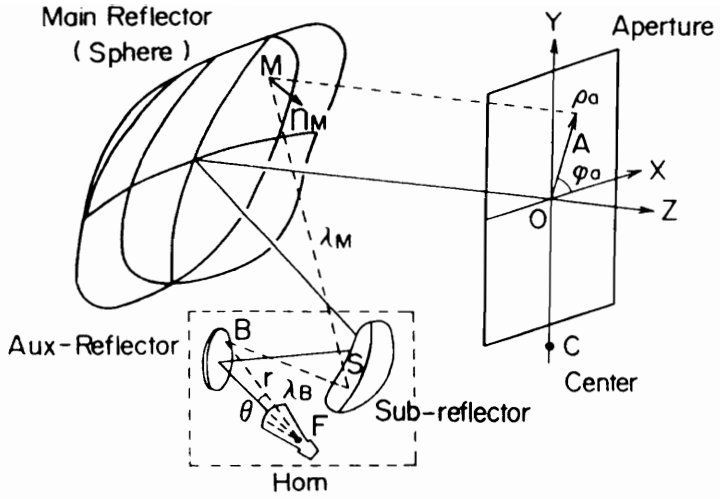

Figure 5.8-5. Offset spherical reflector with two correcting subreflectors designed by Watanabe [19].

finding the stationary function f which minimizes the functional ϵ represented by procedures (1), (2) and (3) [19]. The variational problem is converted into an optimization problem by expanding f into a series and solving for the coefficients using non-linear optimization techniques [19].

In order to evaluate the validity of this design technique, Watanabe [19] designed two sets of correcting subreflectors to be used with the same spherical primary reflector to create two desired aperture distributions. The two resulting reflector configurations are referred to as the #1-antenna and the #2-antenna. The #1-antenna is designed for low sidelobe characteristics while the #2-antenna is designed for high gain. The difference between the two desired aperture distributions causes a difference in gain of 0.9 dB [19].

For both antennas the radius of the spherical primary reflector is $R_0 = 3.954$ m and the major and minor axes of the elliptical primary reflector aperture are 2.8 m $\times$ 1.9 m [19]. The diameter of the instantaneously illuminated area of the primary reflector is $2\rho_0 = 1.765$ m and the corresponding aperture area efficiency as calculated by (6.7-26) is $\eta_a = 58.56$ %. The scan range before primary reflector spillover, in terms of G.O., is 16° azimuth and 2° elevation [19].

For both the #1-antenna and the #2-antenna the size of the sub-reflector is approximately 0.36 m $\times$ 0.24 m and the size of the aux-reflector is approximately 0.23 m $\times$ 0.22 m [19]. The feed used was a dual mode conical horn with diameter 0.108 m giving a -25 dB edge illumination on the tertiary reflector for both the #1-antenna and #2-antenna [19].

Both the #1-antenna and the #2-antenna were constructed and the radiation characteristics were measured. The 34 GHz gain measurements, as a function of beam steering angle, are shown on Table 5.8-1. For these results η indicates the beam scan angle in the azimuth plane while ζ indicates the beam scan angle in the elevation plane. The maximum gain reduction over the scan range of $|\eta| \leq 8°$ (60 beamwidths) and $|\zeta| \leq 2°$ (15 beamwidths) is 0.4 dB for the #1 antenna and 0.6 dB for the #2-antenna [19].

Table 5.8-1
Gain Measured at 34 GHz for the #1-Antenna and #2-Antenna
for Various Azimuth (η) and Elevation (ζ) Scan Angles [19]

η (deg)	ζ (deg)	#1-Antenna gain (dB)	#2-Antenna gain (dB)
0	-2	55.7	56.4
0	0	55.9	56.6
0	2	55.9	56.6
8	-2	55.5	56.0
8	0	55.7	56.2
8	2	55.7	56.3

Figure 5.8-6 shows measured azimuthal plane far-field radiation patterns for both the #1-antenna and the #2-antenna [19]. The dotted lines indicate cross polarization patterns and the dot-dash lines indicate null tracking patterns. In both cases the null depth is approximately -40 dB [19].

With the three reflector configuration shown in Fig. 5.8-5 beam scanning is achieved by moving the feed and two correcting subreflectors as a unit along a spherical surface. To allow beam scanning with a stationary feed Watanabe [20] designed a three reflector beam waveguide. A diagram of this configuration is shown in Fig. 5.8-7 [20]. While this configuration allows for a stationary feed it requires motion of all five subreflectors. A concept for mechanically realizing the required subreflector motions is shown in Fig. 5.8-8 [20].

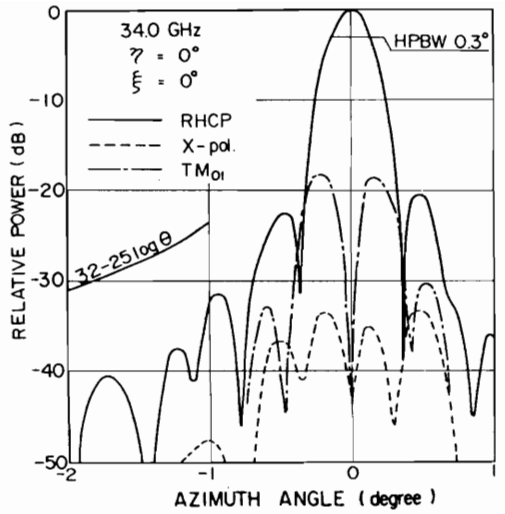

(a)

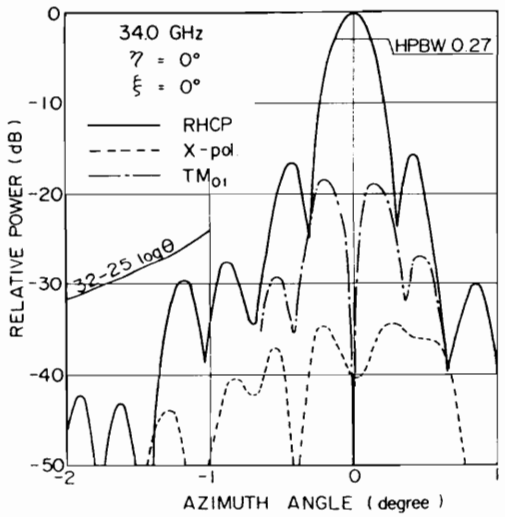

(b)

Figure 5.8-6. Measured radiation patterns for two tri-reflector configurations designed by Watanabe [19]. The measurements are made at 34 GHz and both configurations have illuminated primary reflector aperture diameters of 1.765 m [19]. (a) Results for #1-antenna. (b) Results for #2-antenna.

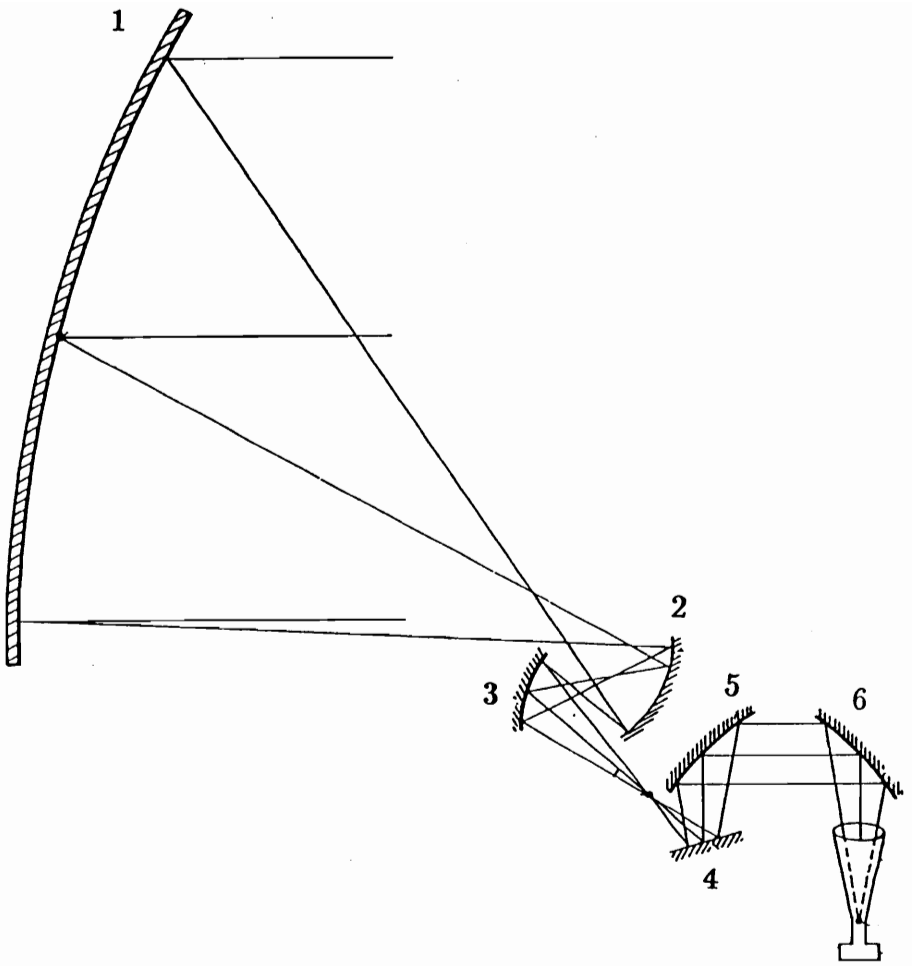

Figure 5.8-7. Cross section of Watanabe's [20] beam waveguide feed (reflectors 4, 5 and 6) used in conjunction with the spherical primary reflector and two correcting subreflectors (reflectors 2 and 3).

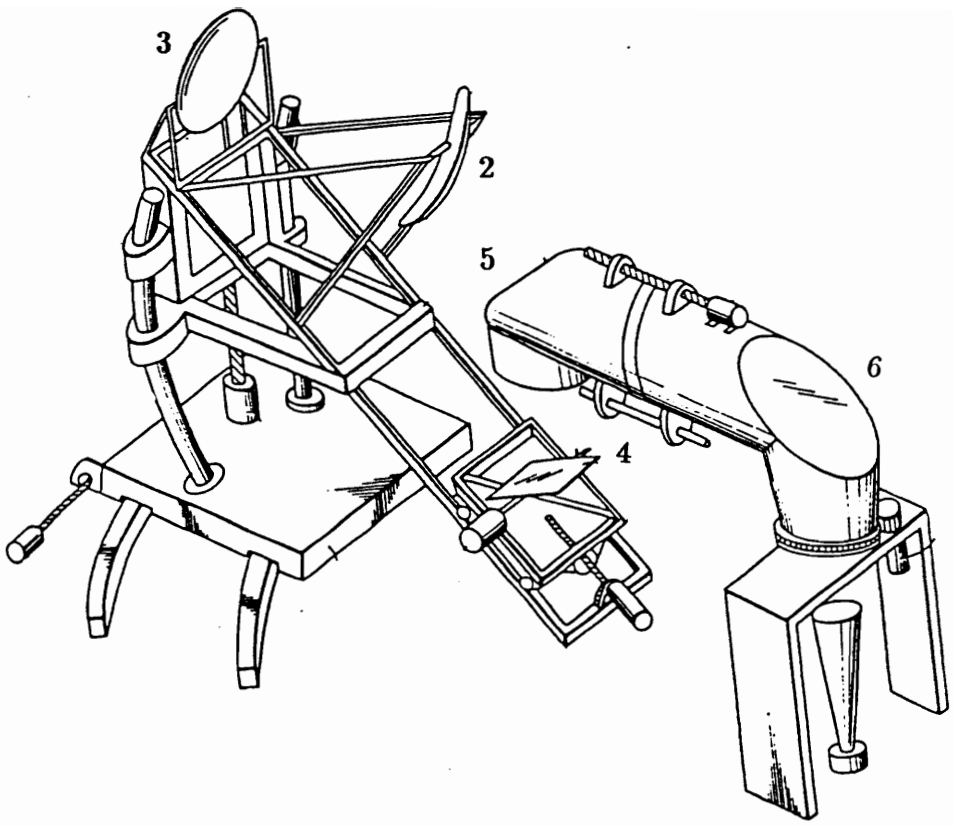

Figure 5.8-8. Watanabe's [20] design for mechanically realizing the motions required for the five subreflector beam waveguide shown in Fig. 5.8-7.

5.9 Summary of Shaped Reflector Configurations

This section presents a summary of the shaped reflector configurations discussed in this chapter. Because each configuration offers a large amount of performance flexibility, depending on the particular design, the approach used here is to qualitatively compare the reflector configurations using Table 5.9-1.

Table 5.9-1
Qualitative Comparison of Reflector Configuration Performance

Reflector Configuration	Scan Range (deg)	Scan Range (BW)	Scan Mechanism
Prime Focus Spherical Reflector	Large	Small	Feed motion or multiple feeds
Prime Focus Parabolic Torus Reflector	Large *	Medium	Feed motion or multiple feeds
High Aperture Efficiency Symmetric Reflector (HAESR)	Large †	Medium	Feed motion or multiple feeds
Schwarzschild Reflector	Medium	Small	Feed motion or multiple feeds
Bifocal Dual Reflector	Medium	Medium	Feed motion or multiple feeds
Scan Optimized Dual Reflector	Medium	Medium	Feed motion or multiple feeds
Gregorian Corrected Spherical Reflector	Large	Large	Motion of feed and subreflector as a rigid unit
Dual Corrected Spherical Reflector	Large	Large	Motion of feed and two subreflectors as a rigid unit

* Beam scanning is limited to a single plane or a conical path.

† Beam scanning is limited to a single plane.

‡ Has very high sidelobes due to inverse aperture illumination taper.

5.10 References

1 T. Li, "A Study of Spherical Reflectors as Wide-Angle Scanning Antennas," *IRE Trans. on Ant. and Prop.*, vol. 7, no. 3, pp. 223-226, July 1959.

2. T. Chu and P. P. Iannone, "Radiation Properties of a Parabolic Torus Reflector," *IEEE Trans. on Ant. and Prop.*, vol. 37, no. 7, pp. 865-874, July 1989.

3. H. Nakaguro, T. Noguchi, T. Ebisui, T. Imatani, T. Katagi, Y. Ito, K. Tachi and Y. Sato, "Development of Conical Scanning Torus Antenna for Advanced Microwave Scanning Radiometer," *Proc. of ISAP*'89, pp. 651-654.

4. C. M. Rappaport and W. P. Craig, "High Aperture Efficiency Symmetric Reflector Antennas with up to 60° Field of View," *IEEE Trans. on Ant. and Prop.*, vol. 39, no. 3, pp. 336-344, March 1991.

5. W. D. White and L. K. DeSize, "Scanning Characteristics of Two-Reflector Antenna Systems," *IRE Int. Conf. Record*, Pt. 1, pp. 44-70, 1962.

6. B. L. J. Rao, "Bifocal Dual Reflector Antenna," *IEEE Trans. on Ant. and Prop.*, vol. 22, no. 5, pp. 711-714, September 1974.

7. C. M. Rappaport, "An Offset Bifocal Reflector Antenna Design for Wide -Angle Beam Scanning," *IEEE Trans. on Ant. and Prop.*, vol. AP-32, no. 11, pp. 1196-1204, November 1984.

8. N. C. Albertsen, K. Pontoppidan and S. B. Serensen, "Shapping of Dual Reflector Antennas for Improvement of Scan Performance," *IEEE Ant. and Prop. Society Inter. Symp. Digest*, pp. 357-360, June 1985.

9. F. S. Holt and E. L. Bouche, "A Gregorian Corrector for Spherical Reflectors," *IEEE Trans. on Ant. and Prop.*, vol. 12, no. 1, pp. 44-47, January 1964.

10. R. Mittra and V. Galindo-Israel, "Shaped Dual Reflector Synthesis," *IEEE Ant. and Prop. Soc. News* , pp. 5-9, August 1980.

11. Y. Kinber, "On Two Reflector Antennas," *Radio Eng. Electron Physics*, vol. 6, June 1962.

12. V. Galindo, "Design of Dual Reflector Antennas with Arbitrary Phase and Amplitude Distribution," *IEEE Trans. on Ant. and Prop.*, vol. 12 , no. 4, pp. 403-408, July 1964.

13. K. A. Green, "Modified Cassegrain Antennas for Arbitrary Aperture Illumination," *IEEE Trans. on Ant. and Prop.*, vol. 11, no. 5, pp. 589-590, September 1963.

14. R. Mittra and V. Galindo, "Some Fundamental Questions Related to the Problem of Dual Reflector Synthesis," *Proceedings of the National Radio Science Meeting*, Boulder, Co., January 1978.

15. V. Galindo-Israel, R. Mittra and A. Cha, "Aperture Amplitude and Phase Control of Offset Dual Reflectors," *IEEE Transactions on Ant. and Prop.*,vol. 27, no. 2, pp. 154-164, March 1979.

16. P. Kildal, "Synthesis of Multireflector Antennas by Kinematic and Dynamic Ray Tracing," *IEEE Trans. on Ant. and Prop.*, vol. 38, no. 10, pp. 1600-1606, October 1990.

17. T. Lee, W. D. Burnside and R. C. Rudduck, *A New Approach for Shaping of Dual-Reflector Antennas*, ElectroScience Laboratory, Ohio State University, December 1987.

18. P. Kildal, L. Baker and T. Hagfors, "Development of a Dual-Reflector Feed for the Arecibo Radio Telescope: An Overview," *IEEE Ant. and Prop. Magazine*, vol. 33, no. 5, October 1991.

19. F. Watanabe and Y. Mizugutch, "An Offset Spherical Tri-Reflector Antenna," *Trans of the IECE of Japan*, vol. E 66, no. 2, pp. 108-115, February 1983.

20. F. Watanabe, *United States Patent*, pat no. 4,516,128, May 1985.

21. W. V. T. Rusch and P. D. Potter, *Analysis of Reflector Antennas*, Academic Press, Inc.: New York, 1970.

Chapter 6

The Conjugate Tri-Reflector Antenna

In this chapter a tri-reflector antenna configuration is introduced which accomplishes beam scanning by motion of a small tertiary reflector. The proposed reflector configuration is referred to as the conjugate tri-reflector for reasons which will be made apparent in Sec. 6.2. The conjugate tri-reflector was initially developed for passive remote sensing from geostationary orbit, however, it is not limited to this application. Important attributes of the reflector configuration are high gain and beam scanning over a range of several degrees in all directions with minimum reflector motion, no feed motion and high primary aperture utilization for all scan directions. In the following principles of conjugate tri-reflector operation and a detailed design procedure are presented. Also presented are techniques for obtaining optimum tertiary reflector motions and evaluating beam scanning performance.

6.1 Design Constraints and Reflector Configuration Selection

The design of a high gain reflector configuration for passive remote sensing and suitable for use with a geostationary platform involves a number of unique design constraints. These are now outlined:

Elimination of Feed Motion: The feed and associated electronics, which must be moved with the feed in order to maintain radiometric calibration, constitute a dense package. This is particularly true for multiple frequency applications where several feeds are required and for array feeds which may be used to provide phase error compensation as discussed in Chapter 3. Therefore, it is desirable to have a stationary feed to reduce power consumption and decrease vibration and inertial torque which can effect beam pointing of other instruments sharing the platform. Also, a stationary feed increases reliability in that flexible cables do not have to be used.

Small Feed Array Size: A feed array is useful in that it allows for compensation of both systematic phase errors due to beam scanning and phase errors due to mechanical limitations in reflector construction. A large feed array, however, increases power consumption and reduces radiometric sensitivity. Therefore, it is important to keep systematic and mechanical phase errors to a minimum in order maintain a small feed array size.

Simple Reflector Motion: To reduce mechanical complexity and increase reliability it is desirable to keep reflector motions as simple as possible. Also, the large primary reflector should be kept stationary and motion should be restricted to the smaller subreflectors in order to keep inertial torque as small as possible.

High Primary Aperture Utilization: Approximately the same portion of the primary reflector should be illuminated for all scan directions so that the reflector does not have to be oversized and can be kept as small as possible.

There are several existing reflector configurations which partially meet the above design constraints and show promise for geostationary applications. All of these configurations provide for a stationary feed and primary reflector. Watanabe [1] introduced a configuration consisting of a spherical primary reflector and five subreflectors (see Sec. 5.8). Two of the subreflectors are used to correct for spherical aberration and provide a desired mapping between the

feed pattern and the primary aperture amplitude distribution. The remaining three subreflectors form a beam waveguide which permit beam scanning with a stationary feed. Watanabe's [1] configuration provides for wide angle scanning with virtually no scan induced phase errors; however, it suffers from low primary aperture utilization and requires complicated motions involving all five subreflectors.

Kitsuregawa [2] demonstrated beam scanning with a classical Cassegrain reflector configuration using a stationary feed and a moving subreflector (see Sec. 4.3). However, this configuration requires large, complicated motions of the subreflector and is limited to very small scan ranges due to scan induced phase errors.

Electronic beam scanning with no reflector or feed motion has been demonstrated using array-fed dual reflector configurations consisting of a parabolic primary reflector and either a parabolic [3] or an elliptic [4] secondary reflector (see Sec. 4.3). With these configurations the reflectors are used to produce a magnified image of the feed array in the aperture of the primary reflector. These configurations exhibit moderately high primary aperture utilization and lend themselves to applications requiring multiple simultaneous beams or rapid electronic beam scanning. However, for high gain applications they require large feed arrays.

The conjugate tri-reflector configuration was developed to specifically address the design constraints outlined above. The configuration consists of a parabolic primary reflector, an elliptical secondary reflector and a shaped tertiary reflector. Beam scanning is achieved entirely by motion of the relatively small tertiary reflector. This configuration accomplishes beam scanning of several degrees in all directions with minimum reflector motion, no feed motion and high primary aperture utilization for all scan directions. A limitation of the conjugate tri-reflector is that phase errors are incurred as a result of beam scanning. Scan induced phase errors are dependent on the specific tri-reflector configuration considered and on the degree of tertiary reflector motion complexity allowed. Such factors are considered in Chapter 7. The principles of conjugate tri-reflector operation are now discussed.

6.2 Principles of Operation

Operation of the conjugate tri-reflector is similar to that of the array-fed dual reflector configurations described by Dragone [3] and Skahill [4]; however, with the conjugate tri-reflector the array feed has been replaced by a movable tertiary reflector. A diagram of the reflector configuration is shown in Fig. 6.2-1. The parent primary reflector is a parabola of revolution with focal point located at F_1. The tertiary reflector has a non-analytic shape and is synthesized according to the algorithm discussed in the following section. The system focal point is located at F. The essential element is the elliptical secondary reflector. The parent secondary reflector is formed by rotating an ellipse with foci at F_2 and F_2' about the axis formed by the line passing through these two points. For this reflector points F_2 and F_2' are conjugate points and any ray passing through one point will be reflected by the elliptical surface and intercept the other point [3]. If the point F_2 is placed on the primary reflector surface and the point F_2' is placed on the surface of the tertiary reflector, then the primary reflector and the tertiary reflector will be conjugate elements in the vicinity of points F_2 and F_2', respectively [3]. It is this conjugate relationship which gives rise to the name conjugate tri-reflector. Any ray striking the primary reflector at point F_2, regardless of incidence angle, will be reflected to the point F_2' on the tertiary reflector surface. This behavior can be understood by considering two cases of incoming plane waves, one along the z-axis and one arriving at angle θ. This is shown in Fig. 6.2-1 with incident rays $\vec{R}_1$ and $\vec{R}_1'$. Ray $\vec{R}_1$ is parallel to the z-axis and ray $\vec{R}_1'$ represents a scan of angle θ with respect to the z-axis. After reflection from the primary and secondary reflector surfaces, corresponding rays $\vec{R}_3$ and $\vec{R}_3'$ intersect the tertiary reflector at point F_2' giving rise to reflected rays $\vec{R}_4$ and $\vec{R}_4'$. If the initial tertiary reflector position is such that reflected ray $\vec{R}_4$ intersects the feed point F, then reflected ray $\vec{R}_4'$ can be made to pass through the point F by rotating the tertiary reflector by angle α about point F_2' where α is given by

$$\alpha = \frac{1}{2}\, cos^{-1}(\hat{R}_3 \cdot \hat{R}_3'). \tag{6.2-1}$$

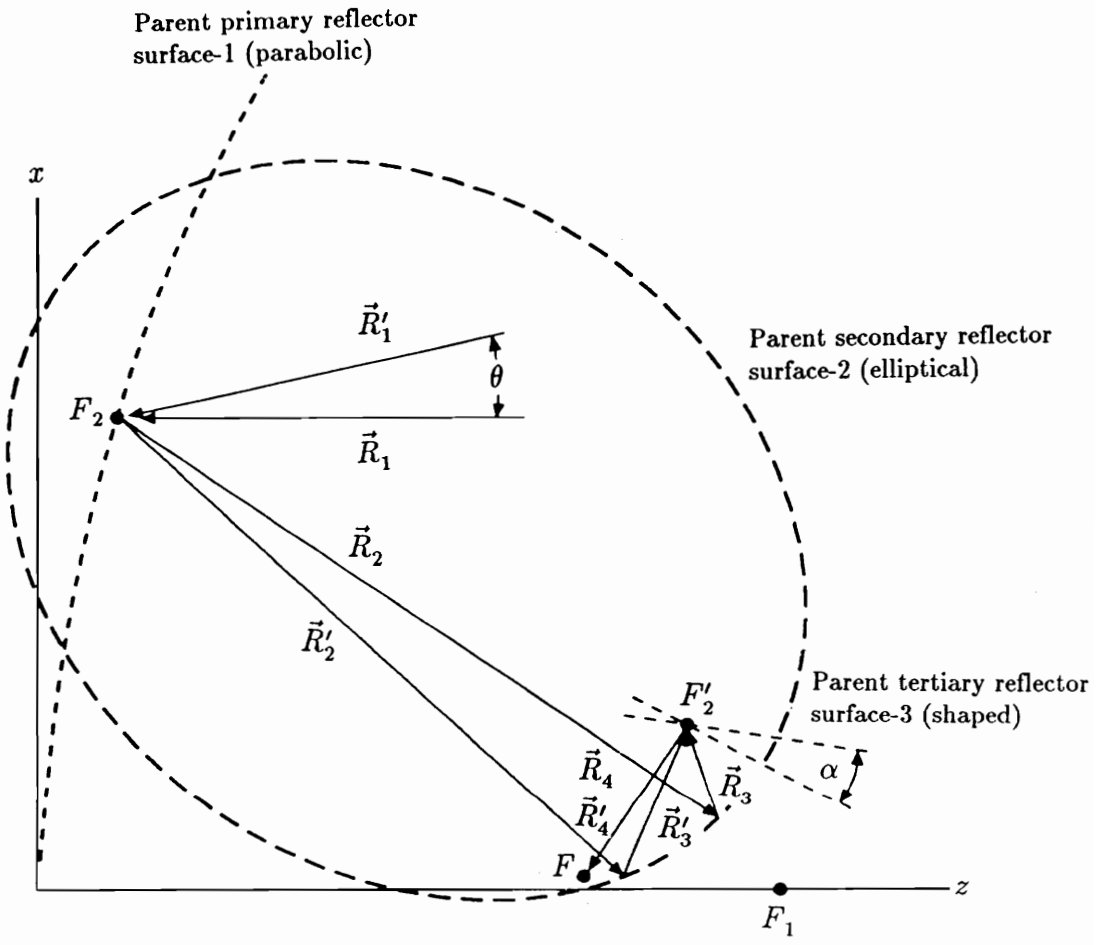

Figure 6.2-1. Basic elements of the conjugate tri-reflector antenna configuration. Ray paths are shown for incident rays $\vec{R}_1$ and $\vec{R}'_1$ which strike the parent primary reflector at point F_2. Unprimed (primed) rays correspond to a scan angle of 0° (θ).

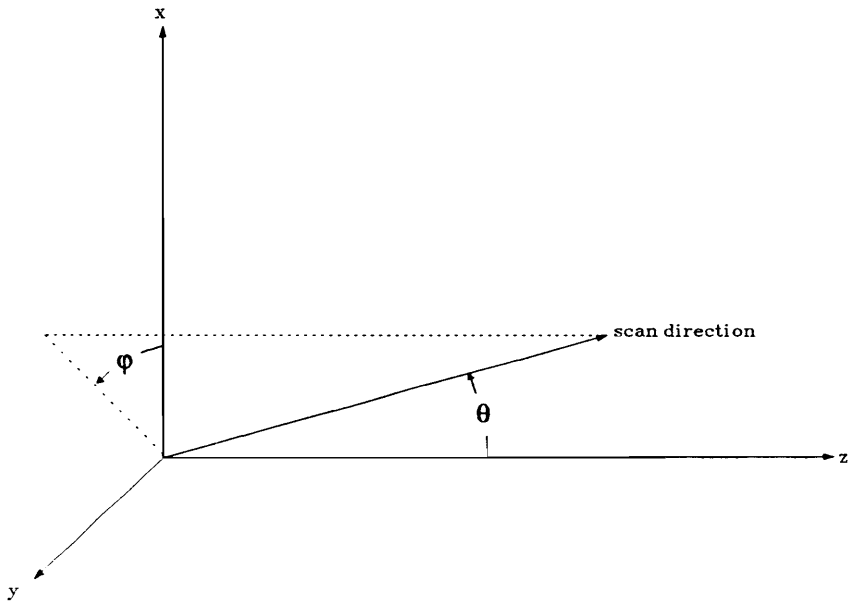

Figure 6.2-2. Definition of scan direction angles θ and ϕ.

If the reflector configuration is considered to be transmitting instead of receiving, then by reciprocity the ray reflected at point F_2 can be made to scan through angle θ by rotating the tertiary reflector by angle α about the point F_2'. The same is approximately true for rays which intersect the primary reflector in the neighborhood of F_2. If F_2 is placed at the center of the primary reflector aperture, then these scanned rays correspond to the region of maximum energy density and, therefore, the beam produced by the reflector configuration can be scanned by rotating the tertiary reflector about point F_2'. This does not mean that rotation about F_2' results in the best scan performance in terms of minimizing aperture plane phase errors; however, it is expected that the optimum tertiary reflector motions will not require the center of the tertiary reflector to move far from the point F_2' and, hence, reflector motion will be reduced.

The previous discussion was confined to scanning within the plane of symmetry (xz-plane); however, the same arguments hold true for beam scanning out of the plane of symmetry. In the following scanning in θ and ϕ, which are shown in Fig. 6.2-2, results in a conical coverage region. For this case the tertiary reflector must be allowed at least two degrees of rotational freedom as discussed in Sec. 6.4.

6.3 Synthesis Procedure

Geometrical optics (G.O.) is used for conjugate tri-reflector synthesis. The parameters necessary for synthesis are illustrated in Fig. 6.3-1 and are summarized on Table 6.3-1. The aperture plane passes through point P_s and is rotated about this point for any desired synthesis scan direction (θ_s, ϕ_s). For purposes of clarity Fig. 6.3-1 is a cross-sectional view and ϕ_s is not shown. The parent primary reflector is a paraboloid of revolution with vertex at the coordinate origin and focal point F_1 located along the z-axis. The projected aperture of the primary reflector is circular with center at x_c and diameter d. The parent secondary reflector is an ellipse with one focal point F_2 located on

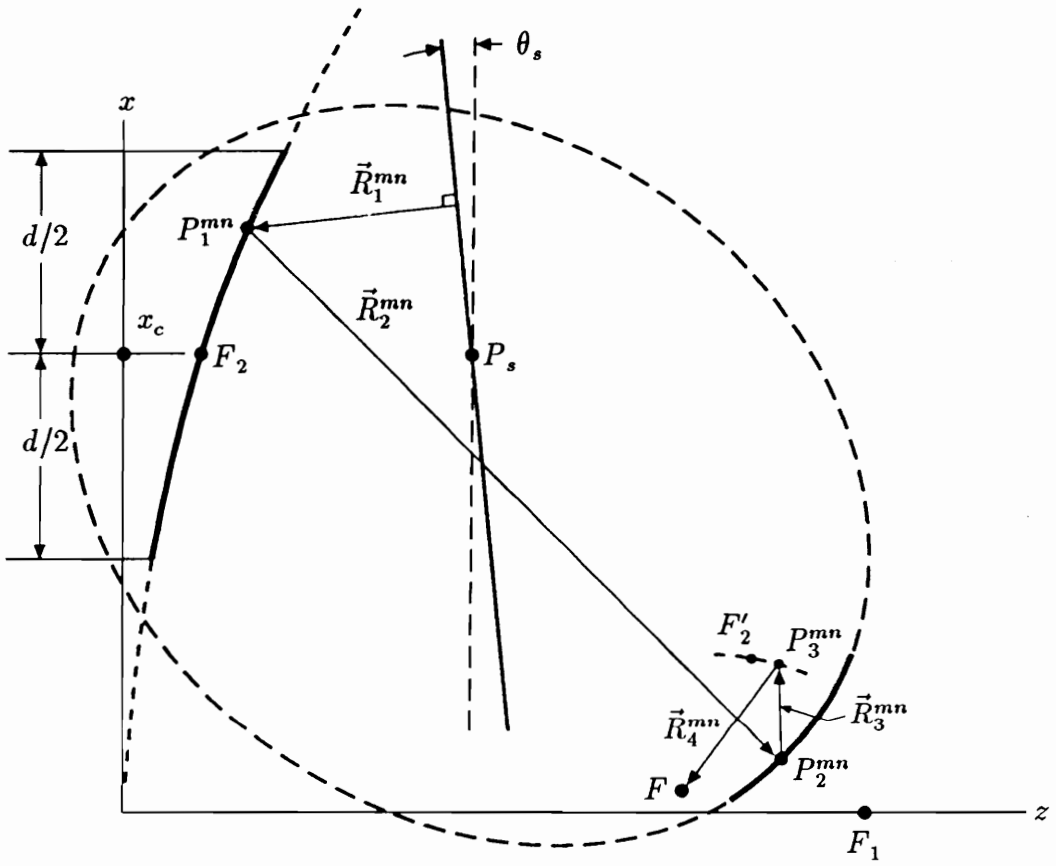

Figure 6.3-1. Geometry (in cross-section) of the conjugate tri-reflector antenna configuration depicting synthesis parameters. Superscript indicates the mn^{th} point joined by a common ray path.

the primary reflector surface and the other focal point F_2' located on the tertiary reflector surface. By the definition of an ellipse, the distance between F_2 and F_2' for any ray which intercepts the secondary reflector surface is equal to a constant which is designated by e_r. The feed is located at the point F.

Table 6.3-1

Conjugate Tri-reflector Synthesis Input Parameters

Symbol	Definition
P_s	The point about which the aperture plane rotates.
(θ_s, ϕ_s)	The synthesis scan direction.
F_1	The focal point of the parabolic primary reflector.
x_c	The x-coordinate of the center of the primary reflector.
d	Projected diameter of the primary reflector.
F_2, F_2'	The two foci of the elliptical secondary reflector.
e_r	The distance from F_2 to F_2' for any ray which intercepts the secondary reflector surface.
F	The desired feed location.

The synthesis parameters on Table 6.3-1 are sufficient to specify the aperture plane corresponding to a synthesis scan direction (θ_s, ϕ_s), the primary reflector and the parent secondary reflector. Therefore, beginning with these three surfaces, rays are traced from the aperture plane to the feed point F. For each ray path Snell's law of reflection is enforced at the primary and secondary reflector surfaces and a tertiary reflector point is calculated such that all ray paths traced from the aperture plane to F have equal pathlengths. The pathlength is obtained by the additional constraint that the tertiary reflector surface pass through the secondary reflector focal point F_2'. The result is a locus of points which define the tertiary reflector surface. With this procedure the aperture plane can be specified for any desired scan direction and for each scan

direction a unique tertiary reflector surface is obtained. It is noted that for each scan direction a slightly different portion of the parent secondary reflector is illuminated. By calculating the illuminated portion of the parent secondary reflector for a number of limiting scan directions the perimeter of the reflector can be approximated such that there is no spillover (in terms of G.O.) for the specified scan range.

A detailed description of the synthesis procedure is presented in the following three steps.

Step 1

In the first step a set of points which define the surface of the primary reflector are chosen. The choice of position and number of primary reflector points is arbitrary; however, there should be enough points to adequately describe the reflector surface and they should be evenly spaced. A useful method for generating primary reflector points has been developed for this application. With this method the set of points is designated by

$$\{P_1^{mn}\}, \qquad \begin{matrix} m = 0,\ldots, M \\ n = 1,\ldots, N(m) \end{matrix} \tag{6.3-1}$$

and the x, y and z-coordinates of each point are given by P_{1x}^{mn}, P_{1y}^{mn} and P_{1z}^{mn} where the coordinate system is shown in Fig. 6.3-1. The surface of the parabolic primary reflector is given by the equation

$$z = g_1(x,y) = \frac{x^2 + y^2}{4\, f_1} \tag{6.3-2}$$

where f_1 is the focal length of the parabolic reflector. The mn^{th} point on the surface of the primary reflector is obtained by defining P_{1x}^{mn} and P_{1y}^{mn} and using (6.3-2) to calculate P_{1z}^{mn}. The location of points P_{1x}^{mn} and P_{1y}^{mn} are calculated using the xy-plane projection of the primary reflector surface. The projection is circular with diameter d and center coordinates $(x_c, 0, 0)$. The xy-coordinates of the primary reflector points are located on a set on M concentric rings which are

equally spaced over the projected aperture. Each ring is centered at $(x_c, 0, 0)$ and has radius

$$r_m = m\left(\frac{d}{2M}\right), \qquad m = 0,\ldots,M \tag{6.3-3}$$

and circumference

$$c_m = 2\pi r_m, \qquad m = 0,\ldots,M. \tag{6.3-4}$$

To obtain a set of points which are evenly spaced across the aperture the arc distance between adjacent points on each ring is set equal to the distance between rings, which is $d/(2M)$. If the angle subtended between adjacent points on the m^{th} ring is designated by ϕ_m, then

$$\frac{d}{2M} = \phi_m r_m = \phi_m m\left(\frac{d}{2M}\right) \tag{6.3-5}$$

where $\phi_m r_m$ is the approximate arc length between adjacent points. From (6.3-5) the subtended angle between adjacent points on the m^{th} ring is found to be

$$\phi_m = \frac{1}{m}, \qquad \text{for } m > 0. \tag{6.3-6}$$

The number of points located on the m^{th} ring is specified by $N(m)$ where

$$\begin{aligned} N(m) &= int\left(\frac{2\pi}{\phi_m}\right), && \text{for } m > 0 \\ N(m) &= 1, && \text{for } m = 0 \end{aligned} \tag{6.3-7}$$

and the right side of (6.3-7) is rounded to the nearest integer. The rectangular coordinates of each initial point are related to r_m and $N(m)$ by the following:

$$P_{1x}^{mn} = r_m \cos\left(\frac{n\,2\pi}{N(m)}\right), \qquad \begin{aligned} m &= 0,\ldots,M \\ n &= 1,\ldots,N(m) \end{aligned} \tag{6.3-8}$$

$$P_{1y}^{mn} = r_m \sin\left(\frac{n2\pi}{N(m)}\right), \qquad \begin{matrix} m = 0,..,M \\ n = 1,..,N(m). \end{matrix} \tag{6.3-9}$$

All examples presented in this work were synthesized using $M = 7$ which results in 171 surface points. An example of the set of initial points which results from using $M = 7$ is shown in Fig. 6.3-2.

For each initial point the surface normal is obtained by the equation

$$\hat{n}_1 = n_{1x}\,\hat{x} + n_{1y}\,\hat{y} + n_{1z}\,\hat{z} = \frac{-\partial g_1/\partial x\,\hat{x} - \partial g_1/\partial y\,\hat{y} + \hat{z}}{\sqrt{(\partial g_1/\partial x)^2 + (\partial g_1/\partial y)^2 + 1}} \tag{6.3-10}$$

where the signs on the right side of (6.3-10) correspond to the reflector geometry shown in Fig. 6.3-1.

Step 2

In this step rays are traced from the aperture plane to the surface of the parent secondary reflector to obtain the set of secondary reflector points $\{P_2^{mn}\}$. For a specified synthesis scan direction (θ_s, ϕ_s) the incident ray direction at the mn^{th} point on the primary reflector surface is given by

$$\begin{aligned} \hat{r}_1^{mn} &= r_{1x}^{mn}\,\hat{x} + r_{1y}^{mn}\,\hat{y} + r_{1z}^{mn}\,\hat{z} \\ &= -\sin\theta_s \cos\phi_s\,\hat{x} - \sin\theta_s \sin\phi_s\,\hat{y} - \cos\phi_s\,\hat{z}. \end{aligned} \tag{6.3-11}$$

Applying Snell's law the reflected ray direction is given by [5]

$$\hat{r}_2^{mn} = \hat{r}_1^{mn} - 2(\hat{n}_1^{mn} - \hat{r}_1^{mn})\hat{n}_1^{mn}. \tag{6.3-12}$$

The reflected ray direction can also be expressed explicitly in terms of the intersection point on the parent secondary reflector surface by

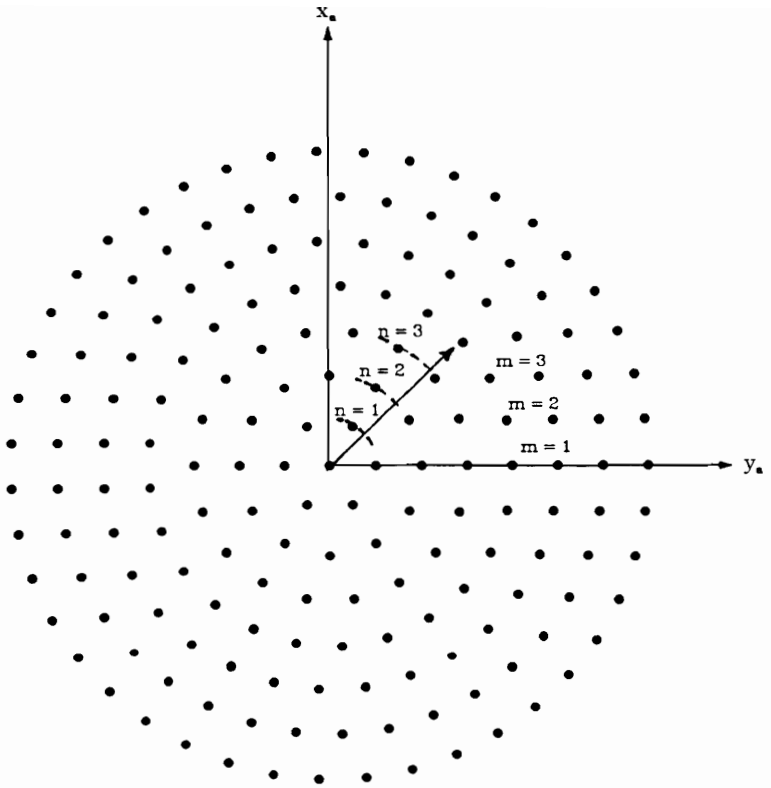

Figure 6.3-2. Example of the set of 171 primary reflector surface points synthesized by using $M = 7$.

$$\hat{r}_2^{mn} = \frac{(P_{2x}^{mn} - P_{1x}^{mn})\,\hat{x} + (P_{2y}^{mn} - P_{1y}^{mn})\,\hat{y} + (P_{2z}^{mn} - P_{1z}^{mn})\,\hat{z}}{\sqrt{(P_{2x}^{mn} - P_{1x}^{mn})^2 + (P_{2y}^{mn} - P_{1y}^{mn})^2 + (P_{2z}^{mn} - P_{1z}^{mn})^2}}. \tag{6.3-13}$$

Equating $\hat{x}$, $\hat{y}$ and $\hat{z}$ components of (6.3-12) and (6.3-13), together with a few algebraic manipulations, yields the following two equations:

$$P_{2y}^{mn} = K_1\,(P_{2x}^{mn} - P_{1x}^{mn}) + P_{1y}^{mn} \tag{6.3-14}$$

where

$$K_1 = \frac{r_{1y}^{mn} - 2\,(\hat{n}_1^{mn} \cdot \hat{r}_1^{mn})\,n_{1y}^{mn}}{r_{1x}^{mn} - 2\,(\hat{n}_1^{mn} \cdot \hat{r}_1^{mn})\,n_{1x}^{mn}}$$

and

$$P_{2z}^{mn} = L_1\,(P_{2x}^{mn} - P_{1x}^{mn}) + P_{1z}^{mn} \tag{6.3-15}$$

where

$$L_1 = \frac{r_{1z}^{mn} - 2\,(\hat{n}_1^{mn} \cdot \hat{r}_1^{mn})\,n_{1z}^{mn}}{r_{1x}^{mn} - 2\,(\hat{n}_1^{mn} \cdot \hat{r}_1^{mn})\,n_{1x}^{mn}}.$$

Equations (6.3-14) and (6.3-15) represent two independent equations for the three unknowns P_{2x}^{mn}, P_{2y}^{mn} and P_{2z}^{mn}. A third independent equation can be obtained from the following equation for the elliptical surface of the parent secondary reflector:

$$x = g_2(y,z) = \tag{6.3-16}$$

$$\frac{-(G + Dy + Ez) \pm \sqrt{(G + Dy + Ez)^2 - 4A(By^2 + Cz^2 + Fyz + Hy + Iz + J)}}{2\,A}$$

where

$$A = 1 - a^2 \qquad F = -2bc$$
$$B = 1 - b^2 \qquad G = -2(ad + F'_{2x})$$
$$C = 1 - c^2 \qquad H = -2(bd + F'_{2y})$$
$$D = -2ab \qquad I = -2(cd + F'_{2z})$$
$$E = -2ac \qquad J = F'^2_{2x} + F'^2_{2y} + F'^2_{2z} - d^2$$

and

$$a = \frac{F_{2x} - F'_{2x}}{e_r} \qquad c = \frac{F_{2z} - F'_{2z}}{e_r}$$

$$b = \frac{F_{2y} - F'_{2y}}{e_r}$$

$$d = \frac{(F'^2_{2x} + F'^2_{2y} + F'^2_{2z} - F^2_{2x} - F^2_{2y} - F^2_{2z})}{2\, e_r} + \frac{e_r}{2}.$$

The sign preceding the radical on the right side of (6.3-16) is dependent on the geometry of the configuration considered and is negative for the geometry shown in Fig. 6.3-1. Substitution of (6.3-14) and (6.3-15) into (6.3-16) leads to the desired equation:

$$P^{mn}_{2x} = \frac{-B_2 \pm \sqrt{B_2 - 4A_2C_2}}{2A_2} \tag{6.3-17}$$

where

$$A_2 = (2A + DK_1 + EL_1)^2 - (DK_1 + EL_1)^2 + 4A(K_1^2B + L_1^2C + FK_1L_1)$$
$$B_2 = 4A(G + D\alpha + E\beta + 2BK_1\alpha + 2CL_1\beta +$$
$$\quad F(K_1\beta + L_1\alpha) + K_1H + L_1I)$$
$$C_2 = 4A(B\alpha^2 + C\beta^2 + F\alpha\beta + H\alpha + I\beta + J)$$

and

$$\alpha = -K_1P^{mn}_{1x} + P^{mn}_{1y}$$
$$\beta = -L_1P^{mn}_{1x} + P^{mn}_{1z}.$$

In (6.3-17) $A, B, C, D, E, F, G, H, I, J$ and K are defined in (6.3-16) and K_1 and L_1 are defined in (6.3-14) and (6.3-15). The sign preceding the radical on the right side of (6.3-17) is dependent on the geometry of the configuration considered and is negative for the geometry shown in Fig. 6.3-1. Once P_{2x}^{mn} is found, P_{2y}^{mn} and P_{2z}^{mn} can be obtained directly from (6.3-14) and (6.3-15).

The surface normal at each secondary reflector point is obtained from the following equation:

$$\hat{n}_2 = n_{2x}\,\hat{x} + n_{2y}\,\hat{y} + n_{2z}\,\hat{z} = \frac{\hat{x} + \partial g_2/\partial y\;\hat{y} - \partial g_2/\partial z\;\hat{z}}{\sqrt{1 + (\partial g_2/\partial y)^2 + (\partial g_2/\partial z)^2}}. \tag{6.3-18}$$

where the signs on the right side of (6.3-18) correspond to the illuminated portion of the parent secondary reflector shown in Fig. 6.3-1.

Step 3

The final step of the synthesis procedure renders the set of points $\{P_3^{mn}\}$ which define the tertiary reflector surface and the corresponding set of surface normals $\{\hat{n}_3^{mn}\}$. Applying Snell's law the direction of the ray reflected from the mn^{th} point on the surface of the secondary reflector is given by [5]

$$\hat{r}_3^{mn} = \hat{r}_2^{mn} - 2\,(\hat{n}_2^{mn} \cdot \hat{r}_2^{mn})\,\hat{n}_2^{mn} \tag{6.3-19}$$

where $\hat{r}_2^{mn}$ is given by (6.3-13). The reflected ray direction can also be expressed explicitly in terms of the intersection point on the tertiary reflector surface by

$$\hat{r}_3^{mn} = \frac{(P_{3x}^{mn} - P_{2x}^{mn})\,\hat{x} + (P_{3y}^{mn} - P_{2y}^{mn})\,\hat{y} + (P_{3z}^{mn} - P_{2z}^{mn})\,\hat{z}}{\sqrt{(P_{3x}^{mn} - P_{2x}^{mn})^2 + (P_{3y}^{mn} - P_{2y}^{mn})^2 + (P_{3z}^{mn} - P_{2z}^{mn})^2}}. \tag{6.3-20}$$

Equating $\hat{x}$, $\hat{y}$ and $\hat{z}$ components of (6.3-19) and (6.3-20), together with a few algebraic manipulations, yields the following two equations:

Equating the left side of (6.3-23) and the right side of (6.3-28), and rearranging terms, leads to the equation:

$$|\vec{R}_3^{mn}| + |\vec{R}_4^{mn}| = |\vec{R}_1'| + e_r + |\vec{R}_4'| - |\vec{R}_1^{mn}| - |\vec{R}_2^{mn}| \tag{6.3-31}$$

$$= l_{34}^m(\theta_s, \phi_s, P_s, e_r, F_2, F_2', P_1^{mn}, P_2^{mn}).$$

It is noted that all arguments of the length function l_{34}^m are known and that (6.3-24), (6.3-25), (6.3-29) and (6.3-30) can be used to calculate the value of l_{34}^m. Substitution of (6.3-21) and (6.3-22) into the two terms on the left side of (6.3-31), and rearranging terms, leads to the following equation for the z-coordinate of the mn^{th} point on the tertiary reflector surface

$$P_{3z}^{mn} = \tag{6.3-32}$$

$$\Big\{(l_{34}^{mn})^2 + 2P_{2z}^{mn}\Big(l_{34}^{mn}\sqrt{1+(K_2)^2+(L_2)^2} + K_2(P_{2x}^{mn} - F_x) + L_2(P_{2y}^{mn} - F_y)\Big)$$

$$-(P_{2x}^{mn} - F_x)^2 - (P_{2y}^{mn} - F_y)^2 + (P_{2x}^{mn})^2 - (F_z)^2\Big\} \div$$

$$2\Big\{l_{34}^{mn}\sqrt{1+(K_2)^2+(L_2)^2} + K_2(P_{2x}^{mn} - F_x) + L_2(P_{2y} - F_y) + P_{2z}^{mn} - F_z\Big\}$$

where K_2 and L_2 are defined in (6.3-21) and (6.3-22). Once P_{3z}^{mn} is found, P_{3x}^{mn} and P_{3y}^{mn} can be obtained directly from (6.3-21) and (6.3-22).

The surface normals $\{\hat{n}_3^{mn}\}$ corresponding to the set of tertiary reflector surface points $\{P_3^{mn}\}$ are obtained directly from Snell's law of reflection [5]:

$$\hat{r}_4^{mn} = \hat{r}_3^{mn} - 2(\hat{n}_3^{mn} \cdot \hat{r}_3^{mn})\ \hat{n}_3^{mn}. \tag{6.3-33}$$

The following three independent equations arise from the $\hat{x}$, $\hat{y}$ and $\hat{z}$ components of (6.3-33):

$$r_{4x}^{mn} - r_{3x}^{mn} = -2(\hat{n}_3^{mn} \cdot \hat{r}_3^{mn})\ n_{3x}^{mn} \tag{6.3-34}$$

$$r_{4y}^{mn} - r_{3y}^{mn} = -2(\hat{n}_3^{mn} \cdot \hat{r}_3^{mn})\, n_{3y}^{mn} \tag{6.3-35}$$

$$r_{4z}^{mn} - r_{3z}^{mn} = -2(\hat{n}_3^{mn} \cdot \hat{r}_3^{mn})\, n_{3z}^{mn} \tag{6.3-36}$$

Division of (6.3-36) by (6.3-34) leads to

$$n_{3z}^{mn} = M_2\, n_{3x}^{mn} \tag{6.3-37}$$

where

$$M_2 = \frac{r_{4z}^{mn} - r_{3z}^{mn}}{r_{4x}^{mn} - r_{3x}^{mn}}.$$

Division of (6.3-35) by (6.3-34) leads to

$$n_{3y}^{mn} = N_2\, n_{3x}^{mn} \tag{6.3-38}$$

where

$$N_2 = \frac{r_{4y}^{mn} - r_{3y}^{mn}}{r_{4x}^{mn} - r_{3x}^{mn}}.$$

Substitution of (6.3-37) and (6.3-38) into (6.3-33) yields

$$n_{3x}^{mn} = \pm \sqrt{\frac{r_{3x}^{mn} - r_{4x}^{mn}}{2\,(r_{3x}^{mn} + N_2 r_{3y}^{mn} + M_2 r_{3z}^{mn})}} \tag{6.3-39}$$

and n_{3z}^{mn} and n_{3y}^{mn} can be obtained directly from (6.3-37) and (6.3-38). The sign preceding the radical on the right side of (6.3-39) is dependent on the geometry of the configuration considered and is negative for the geometry shown in Fig. 6.3-1.

6.4 Definition of Tertiary Reflector Motion Parameters $(\alpha, \beta, \vec{T})$

Beam scanning with the conjugate tri-reflector is accomplished entirely by tertiary reflector motion. The tertiary reflector is allowed two rotational degrees of freedom specified by angles α and β and three translational degrees of freedom specified by the vector $\vec{T}$. Tertiary reflector motion is preformed by first rotating the tertiary reflector about the point P_r shown in Fig. 6.4-1(a) and then linearly translating the reflector. Tertiary reflector rotation is discussed first.

6.4.1 Tertiary Reflector Rotation

Tertiary reflector rotation is performed with respect to the local ijk-coordinate system shown in Fig. 6.4-1(a). The xyz-coordinate system shown in Fig. 6.4-1(a) is identical to the coordinate system used in Fig. 6.3-1. The origin of the ijk-coordinate system is located at the point P_r and the axis directions are specified by the unit vectors $\hat{i}$, $\hat{j}$ and $\hat{k}$. The direction of the k-axis is colinear with the direction of the tertiary reflector surface normal at the point F_2'. Therefore, in the xyz-coordinate system, $\hat{k}$ is given by

$$\hat{k} = k_x\,\hat{x} + k_y\,\hat{y} + k_z\,\hat{z} = n_{3x}'\,\hat{x} + n_{3y}'\,\hat{y} + n_{3z}'\,\hat{z} \tag{6.4-1}$$

where $\hat{n}_3'$ is the tertiary reflector surface normal at the point F_2'. The angle subtended by $\hat{k}$ and the $\hat{z}$ is given by

$$\theta_{kz} = cos^{-1}(k_z) \tag{6.4-2}$$

and the angle subtended by the projection of $\hat{k}$ onto the xy-plane and $\hat{x}$ is given by

$$\phi_{kx} = tan^{-1}(k_y/k_x). \tag{6.4-3}$$

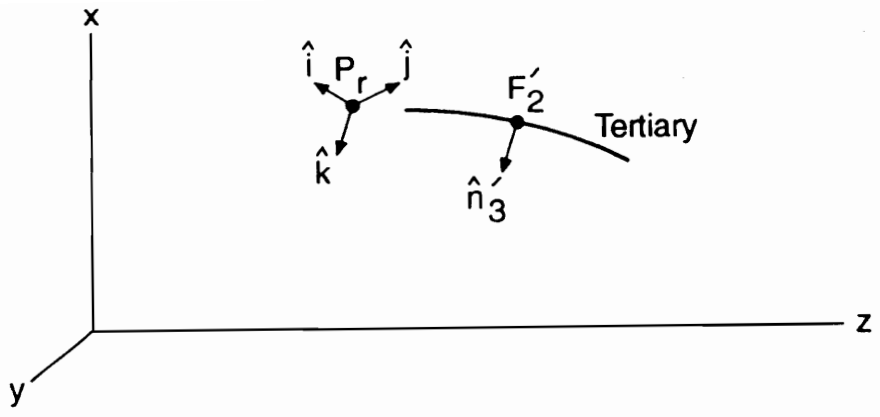

(a)

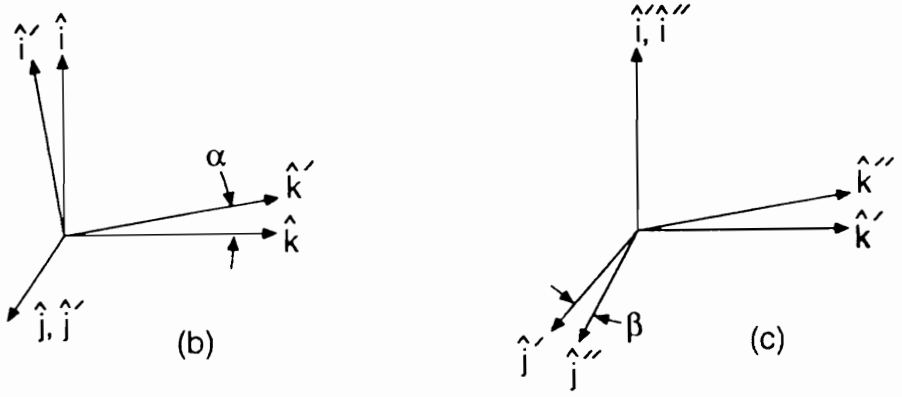

Figure 6.4-1. Definition of tertiary reflector coordinate system. (a) Location of the tertiary reflector coordinate system with respect to the (x, y, z) antenna coordinate system. (b) Tertiary reflector rotation about the j-axis by angle α. The tertiary reflector remains fixed with respect to the $i'j'k'$-axes. (c) Tertiary reflector rotation bout the i' axis by angle β. The tertiary reflector remains fixed with respect to the $i''j''k''$-axes.

Angles θ_{kz} and ϕ_{kx} are used to define $\hat{i}$ and $\hat{j}$ as follows:

$$\hat{i} = (cos\theta_{kz}\ cos\phi_{kx})\ \hat{x} + (cos\theta_{kz}\ sin\phi_{kx})\ \hat{y} - (sin\theta_{kz})\ \hat{z} \tag{6.4-4}$$

$$= i_x\ \hat{x} + i_y\ \hat{y} + i_z\ \hat{z}$$

and

$$\hat{j} = -(sin\phi_{kx})\ \hat{x} + (cos\phi_{kx})\ \hat{y} + 0\ \hat{z} \tag{6.4-5}$$

$$= j_x\ \hat{x} + j_y\ \hat{y} + j_z\ \hat{z}.$$

Tertiary reflector rotation is performed in two steps. In the first step the tertiary reflector is rotated about the j-axis by angle α. This is shown in Fig. 6.4-1(b) where the tertiary reflector remains fixed with respect to the $i'j'k'$-coordinate system. In the second step the tertiary reflector is rotated about the i'-axis by angle β. This is shown in Fig. 6.4-1(c) where in this case the tertiary reflector remains fixed with respect to the $i''j''k''$-coordinate system. The set of tertiary reflector points after rotational transformation $\{P_{3r}^{mn}\}$ are related to the corresponding points before transformation $\{P_3^{mn}\}$ by the following:

$$\begin{bmatrix} P_{3rx}^{mn} \\ P_{3ry}^{mn} \\ P_{3rz}^{mn} \end{bmatrix} = \overline{\overline{A}}^{-1}\ \overline{\overline{R}}\ \overline{\overline{A}} \begin{bmatrix} P_{3x}^{mn} - P_{rx} \\ P_{3y}^{mn} - P_{ry} \\ P_{3z}^{mn} - P_{rz} \end{bmatrix} + \begin{bmatrix} P_{rx} \\ P_{ry} \\ P_{rz} \end{bmatrix} \tag{6.4-6}$$

where

$$\overline{\overline{A}} = \begin{bmatrix} i_x & i_y & i_z \\ j_x & j_y & j_z \\ k_x & k_y & k_z \end{bmatrix} \tag{6.4-7}$$

and

$$\overline{\overline{R}} = \begin{bmatrix} \cos\alpha & \sin\alpha \sin\beta & \sin\alpha \cos\beta \\ 0 & \cos\beta & -\sin\beta \\ -\sin\alpha & \cos\alpha \sin\beta & \cos\alpha \cos\beta \end{bmatrix}. \tag{6.4-8}$$

The set of reflector surface normals $\{\hat{n}_{3r}^{mn}\}$ corresponding to the transformed set of tertiary reflector surface points $\{P_{3r}^{mn}\}$ are obtained from $\{\hat{n}_{3}^{mn}\}$ by the following:

$$\begin{bmatrix} n_{3rx}^{mn} \\ n_{3ry}^{mn} \\ n_{3rz}^{mn} \end{bmatrix} = \overline{\overline{A}}^{-1} \, \overline{\overline{R}} \, \overline{\overline{A}} \begin{bmatrix} n_{3x}^{mn} \\ n_{3y}^{mn} \\ n_{3z}^{mn} \end{bmatrix} \tag{6.4-9}$$

where $\overline{\overline{A}}$ and $\overline{\overline{R}}$ are given by (6.4-8) and (6.4-9).

6.4.2 Tertiary Reflector Translation

Tertiary reflector translation is performed in the xyz-coordinate system shown in Fig. 6.4-1(a). Each point on the tertiary reflector surface is translated by the vector $\vec{T}$ where

$$\vec{T} = T_x \, \hat{x} + T_y \, \hat{y} + T_z \, \hat{z}. \tag{6.4-10}$$

The set of tertiary reflector points after linear transformation $\{P_{3rt}^{mn}\}$ are related to the corresponding set of points before transformation $\{P_{3r}^{mn}\}$ by the following:

$$\begin{bmatrix} P_{3rtx}^{mn} \\ P_{3rty}^{mn} \\ P_{3rtz}^{mn} \end{bmatrix} = \begin{bmatrix} P_{3rx}^{mn} \\ P_{3ry}^{mn} \\ P_{3rz}^{mn} \end{bmatrix} + \begin{bmatrix} T_x \\ T_y \\ T_z \end{bmatrix}. \tag{6.4-11}$$

Tertiary reflector translation has no effect on the direction of the surface normals; therefore, $\{\hat{n}_{3rt}^{mn}\} = \{\hat{n}_{3r}^{mn}\}$.

6.5 Transmit Ray Path Calculation

Geometrical optics (G.O.) is useful in the preliminary stages of reflector configuration investigation because G.O. is fast and, therefore, allows a large number of candidate configurations to be considered before moving to more accurate, but numerically more intensive, analysis methods. In the following the procedure used for calculating a set of G.O. transmit rays from the feed to the primary reflector aperture plane is presented.

A typical transmit ray path is shown in Fig. 6.5-1(a) where the aperture plane corresponds to the (θ, ϕ) scan direction. The method used to calculate the transmit ray paths is identical to the approach used in Sec. 6.3. The ray paths calculated correspond to the set of rays which intersect the tertiary reflector surface points $\{P_{3rt}^{mn}\}$, where the rt subscript is used to indicate that the motion transformations described in Sec. 6.4 have been performed on the tertiary reflector. Corresponding intersection points are found on the parent primary and secondary reflector surfaces and the aperture plane. It is noted that no surface interpolations are performed during transmit ray path calculation. By avoiding surface interpolations transmit ray paths can be calculated accurately and rapidly and, therefore, used efficiently within an iterative routine to find the optimum tertiary reflector motions corresponding to a given scan direction. Transmit ray paths are calculated in the following three steps.

Step 1: Ray Tracing From the Feed to the Secondary Reflector Surface

In this step a set of rays are traced from the feed to the set of tertiary reflector surface points $\{P_{3rt}^{mn}\}$ and from the tertiary reflector surface to the surface of the parent secondary reflector to obtain the set of secondary reflector surface points $\{P_{2rt}^{mn}\}$. The incident ray direction at the mn^{th} point on the surface of the tertiary reflector is given by

$$\widehat{r}_{3rt}^{mn} = \frac{(P_{3rtx}^{mn} - F_x)\,\widehat{x} + (P_{3rty}^{mn} - F_y)\,\widehat{y} + (P_{3rtz}^{mn} - F_z)\,\widehat{z}}{\sqrt{(P_{3rtx}^{mn} - F_x)^2 + (P_{3rty}^{mn} - F_y)^2 + (P_{3rtz}^{mn} - F_z)^2}}. \tag{6.5-1}$$

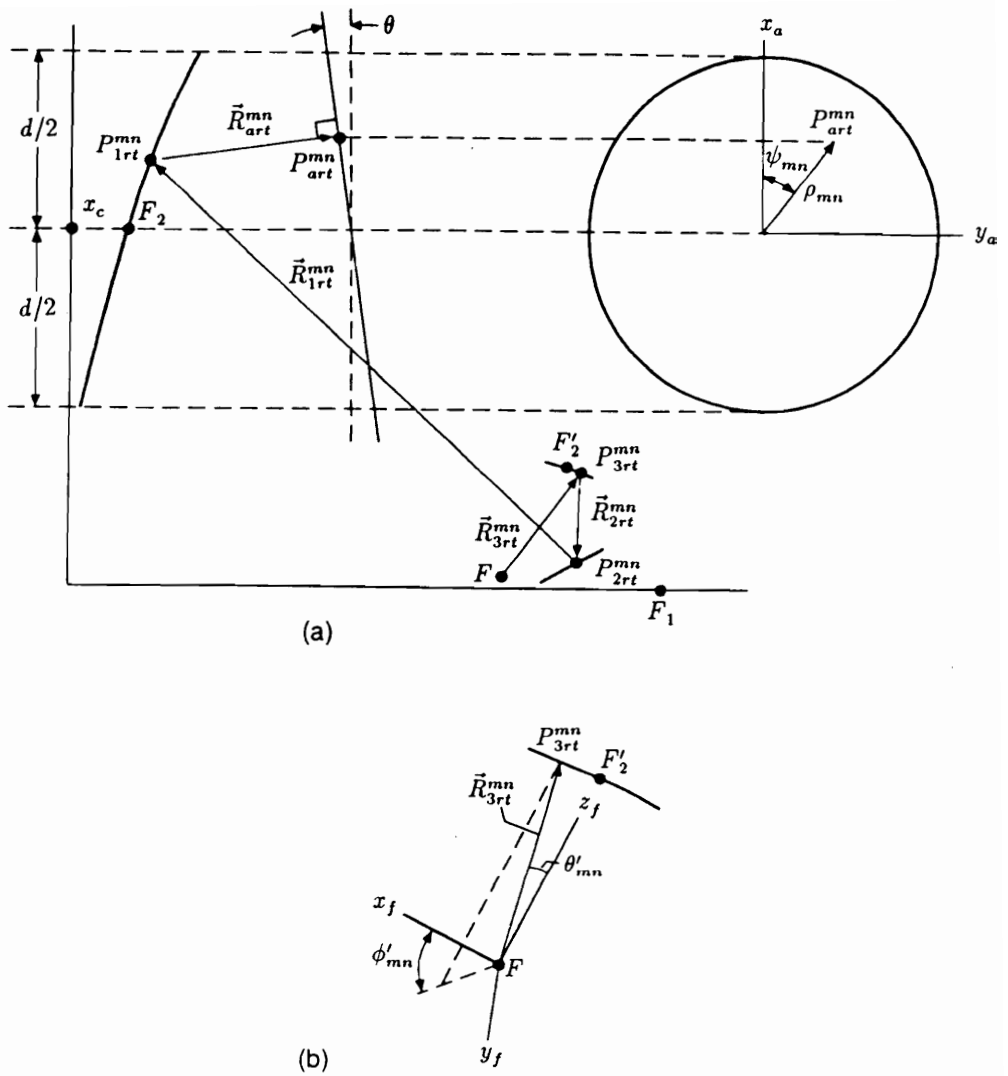

Figure 6.5-1. Transmit ray tracing diagrams. (a) Diagram of the conjugate tri-reflector antenna configuration (in cross-section) showing major components and important parameters for transmit ray tracing analysis. Also shown is the aperture plane coordinate system. (b) Diagram of the feed coordinate system.

Applying Snell's law the reflected ray direction is given by [5]

$$\hat{r}_{2rt}^{mn} = \hat{r}_{3rt}^{mn} - 2\,(\hat{n}_{3rt}^{mn} \cdot \hat{r}_{3rt}^{mn})\,\hat{n}_{3rt}^{mn}. \tag{6.5-2}$$

The reflected ray direction can also be expressed explicitly in terms of the intersection point on the surface of the secondary reflector by

$$\hat{r}_{2rt}^{mn} = \frac{(P_{2rtx}^{mn} - P_{3rtx}^{mn})\,\hat{x} + (P_{2rty}^{mn} - P_{3rty}^{mn})\,\hat{y} + (P_{2rtz}^{mn} - P_{3rtz}^{mn})\,\hat{z}}{\sqrt{(P_{2rtx}^{mn} - P_{3rtx}^{mn})^2 + (P_{2rty}^{mn} - P_{3rty}^{mn})^2 + (P_{2rtz}^{mn} - P_{3rtz}^{mn})^2}}. \tag{6.5-3}$$

Equating $\hat{x}$, $\hat{y}$ and $\hat{z}$ components of (6.5-2) and (6.5-3) results in the following three equations

$$r_{3rtx}^{mn} - 2(\hat{n}_{3rt}^{mn} \cdot \hat{r}_{3rt}^{mn}) n_{3rtx}^{mn} = \frac{(P_{2rtx}^{mn} - P_{3rtx}^{mn})}{\sqrt{(P_{2rtx}^{mn} - P_{3rtx}^{mn})^2 + (P_{2rty}^{mn} - P_{3rty}^{mn})^2 + (P_{2rtz}^{mn} - P_{3rtz}^{mn})^2}} \tag{6.5-4}$$

$$r_{3rty}^{mn} - 2(\hat{n}_{3rt}^{mn} \cdot \hat{r}_{3rt}^{mn}) n_{3rty}^{mn} = \frac{(P_{2rty}^{mn} - P_{3rty}^{mn})}{\sqrt{(P_{2rtx}^{mn} - P_{3rtx}^{mn})^2 + (P_{2rty}^{mn} - P_{3rty}^{mn})^2 + (P_{2rtz}^{mn} - P_{3rtz}^{mn})^2}} \tag{6.5-5}$$

$$r_{3rtz}^{mn} - 2(\hat{n}_{3rt}^{mn} \cdot \hat{r}_{3rt}^{mn}) n_{3rtz}^{mn} = \frac{(P_{2rtz}^{mn} - P_{3rtz}^{mn})}{\sqrt{(P_{2rtx}^{mn} - P_{3rtx}^{mn})^2 + (P_{2rty}^{mn} - P_{3rty}^{mn})^2 + (P_{2rtz}^{mn} - P_{3rtz}^{mn})^2}}. \tag{6.5-6}$$

Division of (6.5-5) by (6.5-4) yields

$$P_{2rty}^{mn} = K_3(P_{2rtx}^{mn} - P_{3rtx}^{mn}) + P_{3rty}^{mn} \tag{6.5-7}$$

where

$$K_3 = \frac{r_{3rty}^{mn} - 2(\hat{n}_{3rt}^{mn} \cdot \hat{r}_{3rt}^{mn}) n_{3rty}^{mn}}{r_{3rtx}^{mn} - 2(\hat{n}_{3rt}^{mn} \cdot \hat{r}_{3rt}^{mn}) n_{3rtx}^{mn}}.$$

Division of (6.5-6) by (6.5-4) yields

$$P_{2rtz}^{mn} = L_3(P_{2rtx}^{mn} - P_{3rtx}^{mn}) + P_{3rtz}^{mn} \tag{6.5-8}$$

where

$$L_3 = \frac{r_{3rtz}^{mn} - 2(\hat{n}_{3rt}^{mn} \cdot \hat{r}_{3rt}^{mn}) n_{3rtz}^{mn}}{r_{3rtx}^{mn} - 2(\hat{n}_{3rt}^{mn} \cdot \hat{r}_{3rt}^{mn}) n_{3rtx}^{mn}}.$$

Equations (6.5-7) and (6.5-8) represent two independent equations for the three unknowns P_{2rtx}^{mn}, P_{2rty}^{mn} and P_{2rtz}^{mn}. A third independent equation can be obtained from the equation for the secondary reflector's elliptical parent, (6.3-16). Substitution of (6.5-7) and (6.5-8) into (6.3-16) gives the desired equation

$$P_{2rtx}^{mn} = \frac{-B_2 \pm \sqrt{B_2 - 4A_2C_2}}{2A_2} \tag{6.5-9}$$

where

$$A_2 = (2A + DK_3 + EL_3)^2 - (DK_3 + EL_3)^2 + 4A(K_3^2B + L_3^2C + FK_3L_3)$$
$$B_2 = 4A(G + D\alpha + E\beta + 2BK_3\alpha + 2CL_3\beta + F(K_3\beta + L_3\alpha) + K_3H + L_3I)$$
$$C_2 = 4A(B\alpha^2 + C\beta^2 + F\alpha\beta + H\alpha + I\beta + J)$$

and

$$\alpha = -K_3\, P_{3rtx}^{mn} + P_{3rty}^{mn}$$
$$\beta = -L_3\, P_{3rtx}^{mn} + P_{3rtz}^{mn}$$

where A,B,C,D,E,F,G,H,I and J are given by (6.3-16) and K_3 and L_3 are given

by (6.5-7) and (6.5-8). The sign preceding the radical on the right side of (6.5-9) is dependent on the geometry of the configuration considered and is negative for the geometry shown in Fig. 6.5-1(a). Once P_{2rtx}^{mn} is found from (6.5-9), P_{2yrt}^{mn} and P_{2zrt}^{mn} are found from (6.5-7) and (6.5-8) and $\hat{n}_{2rt}^{mn}$ is obtained from (6.3-18).

Step 2: Ray Tracing From the Secondary Reflector Surface to the Primary Reflector Surface

The ray tracing approach described in Step 1 is repeated to find the set of parent primary reflector surface points $\{P_{1rt}^{mn}\}$ which correspond to the set of secondary reflector surface points $\{P_{2rt}^{mn}\}$. The incident ray direction $\hat{r}_{2rt}^{mn}$ at the mn^{th} point on the surface of the secondary reflector is given by (6.5-3). Applying Snell's law the corresponding reflected ray direction is given by [5]

$$\hat{r}_{1rt}^{mn} = \hat{r}_{2rt}^{mn} - 2(\hat{n}_{2rt}^{mn} \cdot \hat{r}_{2rt}^{mn})\hat{n}_{2rt}^{mn}. \tag{6.5-10}$$

The reflected ray direction can also be expressed explicitly in terms of the intersection point on the surface of the primary reflector by

$$\hat{r}_{1rt}^{mn} = \frac{(P_{1rtx}^{mn} - P_{2rtx}^{mn})\,\hat{x} + (P_{1rty}^{mn} - P_{2rty}^{mn})\,\hat{y} + (P_{1rtz}^{mn} - P_{2rtz}^{mn})\,\hat{z}}{\sqrt{(P_{1rtx}^{mn} - P_{2rtx}^{mn})^2 + (P_{1rty}^{mn} - P_{2rty}^{mn})^2 + (P_{1rtz}^{mn} - P_{2rtz}^{mn})^2}}. \tag{6.5-11}$$

Equating $\hat{x}$, $\hat{y}$ and $\hat{z}$ components of (6.5-10) and (6.5-11) results in the following three equations:

$$r_{2rtx}^{mn} - 2(\hat{n}_{2rt}^{mn} \cdot \hat{r}_{2rt}^{mn})n_{2rtx}^{mn}$$

$$= \frac{(P_{1rtx}^{mn} - P_{2rtx}^{mn})}{\sqrt{(P_{1rtx}^{mn} - P_{2rtx}^{mn})^2 + (P_{1rty}^{mn} - P_{2rty}^{mn})^2 + (P_{1rtz}^{mn} - P_{2rtz}^{mn})^2}} \tag{6.5-12}$$

$$r_{2rty}^{mn} - 2(\hat{n}_{2rt}^{mn} \cdot \hat{r}_{2rt}^{mn}) n_{2rty}^{mn}$$

$$= \frac{(P_{1rty}^{mn} - P_{2rty}^{mn})}{\sqrt{(P_{1rtx}^{mn} - P_{2rtx}^{mn})^2 + (P_{1rty}^{mn} - P_{2rty}^{mn})^2 + (P_{1rtz}^{mn} - P_{2rtz}^{mn})^2}} \tag{6.5-13}$$

$$r_{2rtz}^{mn} - 2(\hat{n}_{2rt}^{mn} \cdot \hat{r}_{2rt}^{mn}) n_{2rtz}^{mn}$$

$$= \frac{(P_{1rtz}^{mn} - P_{2rtz}^{mn})}{\sqrt{(P_{1rtx}^{mn} - P_{2rtx}^{mn})^2 + (P_{1rty}^{mn} - P_{2rty}^{mn})^2 + (P_{1rtz}^{mn} - P_{2rtz}^{mn})^2}}. \tag{6.5-14}$$

Division of (6.5-12) by (6.5-14) leads to

$$P_{1rtx}^{mn} = K_2(P_{1rtz}^{mn} - P_{2rtz}^{mn}) + P_{2rtx}^{mn} \tag{6.5-15}$$

where

$$K_2 = \frac{r_{2rtx}^{mn} - 2(\hat{n}_{2rt}^{mn} \cdot \hat{r}_{2rt}^{mn}) n_{2rtx}^{mn}}{r_{2rtz}^{mn} - 2(\hat{n}_{2rt}^{mn} \cdot \hat{r}_{2rt}^{mn}) n_{2rtz}^{mn}}.$$

Division of (6.5-13) by (6.5-14) leads to

$$P_{1rty}^{mn} = L_2(P_{1rtz}^{mn} - P_{2rtz}^{mn}) + P_{2rty}^{mn} \tag{6.5-16}$$

where

$$L_2 = \frac{r_{2rty}^{mn} - 2(\hat{n}_{2rt}^{mn} \cdot \hat{r}_{2rt}^{mn}) n_{2rty}^{mn}}{r_{2rtz}^{mn} - 2(\hat{n}_{2rt}^{mn} \cdot \hat{r}_{2rt}^{mn}) n_{2rtz}^{mn}}.$$

Equations (6.5-15) and (6.5-16) represent two independent equations for the three unknowns P_{1rtx}^{mn}, P_{1rty}^{mn} and P_{1rtz}^{mn}. A third independent equation can be obtained from the equation for the primary reflector's parabolic parent, (6.3-2). Substitution of (6.5-15) and (6.5-16) into (6.3-2) gives the desired equation

$$P_{1rtz}^{mn} = \frac{-B_1 \pm \sqrt{B_1 - 4A_1C_1}}{2A_1}. \tag{6.5-17}$$

where

$$\begin{aligned} A_1 &= K_2^2 + L_2^2 \\ B_1 &= 2\,K_2\,P_{2rtx}^{mn} + 2\,L_2\,P_{2rty}^{mn} - 2\,K_2^2\,P_{2rtz}^{mn} - 2\,L_2^2\,P_{2rtz}^{mn} - 4f_1 \\ C_1 &= K_2^2\,(P_{2rtz}^{mn})^2 + L_2^2\,(P_{2rtz}^{mn})^2 - 2\,K_2\,P_{2rtx}^{mn}\,P_{2rtz}^{mn} - 2\,L_2\,P_{2rty}^{mn}\,P_{2rtz}^{mn} + \\ &\quad (P_{2rtx}^{mn})^2 + (P_{2rty}^{mn})^2 \end{aligned}$$

and K_2 and L_2 are given by (6.5-15) and (6.5-16). The sign preceding the radical on the right side of (6.5-17) is dependent on the geometry of the configuration considered and is negative for the geometry shown in Fig. 6.5-1(a). Once P_{1rtz}^{mn} is found from (6.5-17), P_{1rtx}^{mn} and P_{1rty}^{mn} are found from (6.5-15) and (6.5-16) and $\hat{n}_{1rt}^{mn}$ is obtained from (6.3-10).

Step 3: Ray Tracing From the Primary Reflector Surface to the Aperture Plane

The ray tracing approach is repeated once more to find the set of aperture plane points $\{P_{art}^{mn}\}$ which correspond to the set of primary reflector surface points $\{P_{1rt}^{mn}\}$. The incident ray direction $\hat{r}_{1rt}^{mn}$ at the mn^{th} point on the surface of the primary reflector is given by (6.5-11). Applying Snell's law the corresponding reflected ray direction is given by [5]

$$\hat{r}_{art}^{mn} = \hat{r}_{1rt}^{mn} - 2(\hat{n}_{1rt}^{mn} \cdot \hat{r}_{1rt}^{mn})\hat{n}_{1rt}^{nm}. \tag{6.5-18}$$

The reflected ray direction can also be expressed explicitly in terms of the intersection point on the surface of the primary reflector by

$$\hat{r}_{art}^{mn} = \frac{(P_{artx}^{mn} - P_{1rtx}^{mn})\,\hat{x} + (P_{arty}^{mn} - P_{1rty}^{mn})\,\hat{y} + (P_{artz}^{mn} - P_{1rtz}^{mn})\,\hat{z}}{\sqrt{(P_{artx}^{mn} - P_{1rtx}^{mn})^2 + (P_{arty}^{mn} - P_{1rty}^{mn})^2 + (P_{artz}^{mn} - P_{1rtz}^{mn})^2}}. \tag{6.5-19}$$

Equating $\hat{x}$, $\hat{y}$ and $\hat{z}$ components of (6.5-18) and (6.5-19) results in the following three equations

$$r_{1rtx}^{mn} - 2(\hat{n}_{1rt}^{mn} \cdot \hat{r}_{1rt}^{mn}) n_{1rtx}^{mn}$$

$$= \frac{(P_{artx}^{mn} - P_{1rtx}^{mn})}{\sqrt{(P_{artx}^{mn} - P_{1rtx}^{mn})^2 + (P_{arty}^{mn} - P_{1rty}^{mn})^2 + (P_{artz}^{mn} - P_{1rtz}^{mn})^2}} \tag{6.5-20}$$

$$r_{1rty}^{mn} - 2(\hat{n}_{1rt}^{mn} \cdot \hat{r}_{1rt}^{mn}) n_{1rty}^{mn}$$

$$= \frac{(P_{arty}^{mn} - P_{1rty}^{mn})}{\sqrt{(P_{artx}^{mn} - P_{1rtx}^{mn})^2 + (P_{arty}^{mn} - P_{1rty}^{mn})^2 + (P_{artz}^{mn} - P_{1rtz}^{mn})^2}} \tag{6.5-21}$$

$$r_{1rtz}^{mn} - 2(\hat{n}_{1rt}^{mn} \cdot \hat{r}_{1rt}^{mn}) n_{1rtz}^{mn}$$

$$= \frac{(P_{artz}^{mn} - P_{1rtz}^{mn})}{\sqrt{(P_{artx}^{mn} - P_{1rtx}^{mn})^2 + (P_{arty}^{mn} - P_{1rty}^{mn})^2 + (P_{artz}^{mn} - P_{1rtz}^{mn})^2}}. \tag{6.5-22}$$

Division of (6.5-20) by (6.5-22) leads to

$$P_{artx}^{mn} = K_1 (P_{artz}^{mn} - P_{1rtz}^{mn}) + P_{1rtx}^{mn} \tag{6.5-23}$$

where

$$K_1 = \frac{r_{1rtx}^{mn} - 2(\hat{n}_{1rt}^{mn} \cdot \hat{r}_{1rt}^{mn}) n_{1rtx}^{mn}}{r_{1rtz}^{mn} - 2(\hat{n}_{1rt}^{mn} \cdot \hat{r}_{1rt}^{mn}) n_{1rtz}^{mn}}.$$

Division of (6.5-21) by (6.5-22) leads to

$$P_{arty}^{mn} = L_1 (P_{artz}^{mn} - P_{1rtz}^{mn}) + P_{1rty}^{mn} \tag{6.5-24}$$

where

$$L_1 = \frac{r_{1rty}^{mn} - 2(\hat{n}_{1rt}^{mn} \cdot \hat{r}_{1rt}^{mn}) n_{1rty}^{mn}}{r_{1rtz}^{mn} - 2(\hat{n}_{1rt}^{mn} \cdot \hat{r}_{1rt}^{mn}) n_{1rtz}^{mn}}.$$

Equations (6.5-23) and (6.5-24) represent two independent equations for the three unknowns P_{artx}^{mn}, P_{arty}^{mn} and P_{artz}^{mn}. A third independent equation is obtained from the following equation for the aperture plane:

$$z = P_{sz} + (P_{sx} - x)\ tan\theta\ cos\phi + (P_{sy} - y)\ tan\theta\ sin\phi \tag{6.5-25}$$

where θ and ϕ are the polar angles of the designated scan direction. Substitution of (6.5-23) and (6.5-24) into (6.5-25) gives the desired equation

$$P_{artz}^{mn} = \{P_{sz} + (P_{sx} + K_1\ P_{1rtz}^{mn} - P_{1rtx}^{mn})\ tan\theta\ cos\phi + \tag{6.5-26}$$

$$(P_{sy} + L_1 P_{1rtz}^{mn} - P_{1rty}^{mn})\ tan\theta\ sin\phi\} \div$$

$$(1 + K_1\ tan\theta\ cos\phi + L_1\ tan\theta\ sin\phi)$$

where K_1 and L_1 are given by (6.5-23) and (6.5-24). Once P_{azrt}^{mn} is found from (6.5-26), P_{artx}^{mn} and P_{arty}^{mn} are found from (6.5-23) and (6.5-24).

A useful parameter is the length of the mn^{th} ray path from the feed to the aperture plane. This parameter is given by the following:

$$\begin{aligned} l_{mn} = {} & \sqrt{(P_{3rtx}^{mn} - F_x)^2 + (P_{3rty}^{mn} - F_y)^2 + (P_{3rtz}^{mn} - F_z)^2} \\ & + \sqrt{(P_{2rtx}^{mn} - P_{3rtx}^{mn})^2 + (P_{2rty}^{mn} - P_{3rty}^{mn})^2 + (P_{2rtz}^{mn} - P_{3rtz}^{mn})^2} \\ & + \sqrt{(P_{1rtx}^{mn} - P_{2rtx}^{mn})^2 + (P_{1rty}^{mn} - P_{2rty}^{mn})^2 + (P_{1rtz}^{mn} - P_{2rtz}^{mn})^2} \\ & + \sqrt{(P_{artx}^{mn} - P_{1rtx}^{mn})^2 + (P_{arty}^{mn} - P_{1rty}^{mn})^2 + (P_{artz}^{mn} - P_{1rtz}^{mn})^2}. \end{aligned} \tag{6.5-27}$$

6.5.1 Definition of Aperture Plane and Feed Coordinate Systems

It is useful to define both an aperture plane and a feed coordinate system. The aperture plane coordinate system is shown in Fig. 6.5-1(a). This is a two dimensional coordinate system located on the aperture plane which is defined by (6.5-25). The center of the aperture plane coordinate system is located at the intersection point between the aperture plane and the transmit ray for $m = 0$ and $n = 1$, $(P^{01}_{axrt}, P^{01}_{ayrt}, P^{01}_{azrt})$. Transmit ray intersection points are located on the aperture plane by cylindrical coordinates ρ_{mn} and ψ_{mn} which are given by

$$\psi_{mn} = tan^{-1}\left(\frac{\sqrt{(P^{mn}_{ayrt} - P^{01}_{ayrt})^2 + (P^{mn}_{azrt} - P^{01}_{azrt})^2 sin^2\phi}}{\sqrt{(P^{mn}_{axrt} - P^{01}_{axrt})^2 + (P^{mn}_{azrt} - P^{01}_{azrt})^2 cos^2\phi}}\right) \tag{6.5-28}$$

and

$$\rho_{mn} = \sqrt{(P^{mn}_{axrt} - P^{01}_{axrt})^2 + (P^{mn}_{ayrt} - P^{01}_{ayrt})^2 + (P^{mn}_{azrt} - P^{01}_{azrt})^2}. \tag{6.5-29}$$

The feed coordinate system is shown in Fig. 6.5-1(b). The axes directions of the feed coordinate system are given by $\hat{x}_f$, $\hat{y}_f$ and $\hat{z}_f$. The origin of the feed coordinate system is located at the focal point F and $\hat{z}_f$ is taken as the direction of the ray between the focal point and the central tertiary reflector point P^{01}_{3rt}. In the xyz-coordinate system shown in Fig. 6.5-1(a) the direction of $\hat{z}_f$ is given by

$$\begin{aligned}\hat{z}_f &= z_{fx}\,\hat{x} + z_{fy}\,\hat{y} + z_{fz}\,\hat{z} \qquad (6.5\text{-}30)\\ &= \frac{(P^{01}_{3rtx} - F_x)\,\hat{x} + (P^{01}_{3rty} - F_y)\,\hat{y} + (P^{01}_{3rtz} - F_z)\,\hat{z}}{\sqrt{(P^{01}_{3rtx} - F_x)^2 + (P^{01}_{3rty} - F_y)^2 + (P^{01}_{3rtz} - F_z)^2}}\end{aligned}$$

where F_x, F_y and F_z are the x, y and z-coordinates of the focal point F. The angle subtended between $\hat{z}_f$ and $\hat{z}$ is given by

$$\theta_f = cos^{-1}(z_{fz}) \tag{6.5-31}$$

and the angle subtended between the projection of $\hat{z}_f$ onto the xy-plane and $\hat{x}$ is given by

$$\phi_f = tan^{-1}\left(\frac{z_{fy}}{z_{fx}}\right). \tag{6.5-32}$$

Angles θ_f and ϕ_f are used to obtain unite vectors $\hat{x}_f$ and $\hat{y}_f$ as follows:

$$\begin{aligned}\hat{x}_f &= x_{fx}\,\hat{x} + x_{fy}\,\hat{y} + x_{fz}\,\hat{z} \\ &= (cos\theta_f\, cos\phi_f)\,\hat{x} + (cos\theta_f\, sin\phi_f)\,\hat{y} - (sin\theta_f)\,\hat{z}\end{aligned} \tag{6.5-33}$$

and

$$\begin{aligned}\hat{y}_f &= y_{fx}\,\hat{x} + y_{fy}\,\hat{y} + y_{fz}\,\hat{z} \\ &= -(sin\phi_f)\,\hat{x} + (cos\phi_f)\,\hat{y} + 0\,\hat{z}.\end{aligned} \tag{6.5-34}$$

In the feed coordinate system the direction of mn^{th} ray $\hat{r}_{3rt}^{mn}$ is specified by the polar angles θ'_{mn} and ϕ'_{mn} which are given by

$$\theta'_{mn} = cos^{-1}(\hat{r}_{3rt}^{mn} \cdot \hat{z}_f) \tag{6.5-35}$$

and

$$\phi'_{mn} = tan^{-1}\left(\frac{\hat{r}_{3rt}^{mn} \cdot \hat{y}_f}{\hat{r}_{3rt}^{mn} \cdot \hat{x}_f}\right). \tag{6.5-36}$$

6.6 Tertiary Reflector Motion Optimization

Once a locus of transmit ray paths from the feed to the aperture plane are known, several functions can be defined such that the function minimum corresponds to the optimum values of α, β and $\vec{T}$ for a specified tertiary reflector

rotation point P_r and scan direction (θ,ϕ). One function which could be used is the *rms* pathlength deviation $\Delta L_{ave}(\alpha,\beta,\vec{T},\theta,\phi)$. This is a natural function to use since it is related to the *rms* aperture plane phase error by

$$\overline{\delta} = \frac{2\pi}{\lambda}\,\Delta L_{ave} \tag{6.6-1}$$

and, therefore, minimizing ΔL_{ave} minimizes aperture plane *rms* phase errors. It was found by trial and error, however, that the function ΔL_{ave} leads to poor convergence properties for α, β and $\vec{T}$ and a better function to use is the *rms* pointing error given by

$$\overline{\xi}(\alpha,\beta,\vec{T},\theta,\phi) = \sum_{m=0}^{M}\sum_{n=1}^{N(m)} \left(W_1(\rho_{mn})\,|\hat{r}_{art}^{mn}\times\hat{r}_d(\theta,\phi)|\right)^2 \tag{6.6-2}$$

where $\hat{r}_{art}^{mn}$ is the direction of the mn^{th} transmit ray at the aperture plane, $\hat{r}_d(\theta,\phi)$ is the desired scan direction given by

$$\hat{r}_d(\theta,\phi) = sin\theta\ cos\phi\ \hat{x} + sin\theta\ sin\phi\ \hat{y} + cos\theta\ \hat{z} \tag{6.6-3}$$

and $W_1(\rho_{mn})$ is a weighting factor corresponding to an approximate aperture amplitude distribution. In the examples presented in Chapter 7 the weighting factor is taken to be a parabolic taper on a pedestal with a 16 dB edge taper as given by the following equation [6]:

$$W_1(\rho_{mn}) = C + (1-C)\left[1-\left(\frac{2\rho_{mn}}{d}\right)^2\right] \tag{6.6-4}$$

where $C = 0.0158$, d is the diameter of the primary reflector and ρ_{mn} is given by (6.5-29).

In most cases it is desirable to constrain the amount of allowable tertiary reflector linear translation. This is easily accomplished by adding a weighting function to $\overline{\xi}(\alpha,\beta,\vec{T},\theta,\phi)$ such that the resultant value increases when the translational motion exceeds the desired maximum. The weighting function $W_c(T_{max},\vec{T})$ used for this purpose has the following form:

$$W_c(T_{max},\vec{T}) = 0, \quad \text{for} \quad T_{max} \leq \sqrt{T_x^2 + T_y^2 + T_z^2} \tag{6.6-7a}$$

and

$$W_c(T_{max},\vec{T}) = C\left(T_{max} - \sqrt{T_x^2 + T_y^2 + T_z^2}\right), \tag{6.6-7b}$$

$$\text{for} \quad T_{max} \geq \sqrt{T_x^2 + T_y^2 + T_z^2}$$

where T_{max} is the maximum allowable translational movement and C is an arbitrarily large constant.

For a specified scan direction (θ,ϕ) any one of a number of nonlinear optimization schemes can be used to find the values of α, β and $\vec{T}$ which minimize the sum $\overline{\xi} + W_c$. In the examples presented in Chapter 7 Powell's method [8] is used because it has the advantage of not requiring calculation of the gradient.

6.7 Geometrical Optics (G.O.) Performance Evaluation

For a given scan direction (θ,ϕ) and set of optimum values for the tertiary reflector motion parameters α, β and $\vec{T}$, G.O. is used to calculate the following two useful performance parameters: the normalized primary aperture diameter d/λ [3] such that gain loss due to scan induced phase errors does not exceed a specified threshold; and the primary reflector area efficiency η_a. Primary reflector area efficiency is useful as a measure of how efficiently the primary reflector is utilized for any given scan direction. The normalized aperture diameter d/λ is useful because electrical size is the limiting quantity and for a given primary reflector aperture diameter d the maximum frequency of operation (for a specified maximum gain loss) can be inferred. Calculation of

this parameter requires knowledge of the mapping function between the feed pattern and the resulting primary aperture amplitude distribution. Calculation of the feed-to-aperture mapping function is now discussed.

6.7.1 Feed-to-Aperture Mapping Function

The mapping function between the feed radiation pattern and the primary aperture electric-field amplitude distribution is obtained from the locus of transmit rays. If it is assumed that there is no spillover in the reflector configuration, then conservation of energy dictates that the power input by the feed be equal to the power exiting the primary aperture. This is expressed by the following relation:

$$\int_0^{2\pi}\int_0^{d/2} |\vec{E}_a|^2(\rho,\psi)\ \rho\, d\rho\, d\psi = \int_0^{2\pi}\int_0^{\theta'_M} |\vec{E}_F|^2(\theta',\phi')\ sin\theta'\ d\theta'\ d\phi' \tag{6.7-1}$$

where d is the diameter of the primary reflector, $\vec{E}_a(\rho,\psi)$ is the aperture plane electric field distribution, θ'_M is the maximum angle subtended by the tertiary reflector as viewed from the feed point F and $\vec{E}_F(\theta',\phi')$ is the feed radiation pattern. Equation (6.7-1) can be written in the following differential form by introducing the Jacobian functions $J_1(\rho,\psi/m,n)$ and $J_2(\theta',\phi'/m,n)$:

$$\begin{aligned} &|\vec{E}_a(\rho_{mn},\psi_{mn})|^2\ \rho_{mn}\ J_1(\rho_{mn},\psi_{mn}/m,n) \\ &= |\vec{E}_F(\theta'_{mn},\phi'_{mn})|^2\ sin\,\theta'_{mn}\ J_2(\theta'_{mn},\phi'_{mn}/m,n) \end{aligned} \tag{6.7-2}$$

where ψ_{mn}, ρ_{mn}, θ'_{mn} and ϕ'_{mn} are calculated by (6.5-28), (6.5-29), (6.5-35) and (6.5-36) and are shown in Fig. 6.5-1. The Jacobians J_1 and J_2 used in (6.7-2) are approximated using finite differences as follows:

$$J_1(\rho_{mn},\psi_{mn}/m,n) = \left(\frac{\partial\rho_{mn}}{\partial m}\right)\left(\frac{\partial\psi_{mn}}{\partial n}\right) - \left(\frac{\partial\rho_{mn}}{\partial n}\right)\left(\frac{\partial\psi_{mn}}{\partial m}\right) \tag{6.7-3}$$

where

$$\frac{\partial \rho_{mn}}{\partial m} \simeq \rho_{m+1,n} - \rho_{mn}, \qquad \frac{\partial \psi_{mn}}{\partial m} \simeq \psi_{m+1,n} - \psi_{mn}$$

$$\frac{\partial \rho_{mn}}{\partial n} \simeq \rho_{m,n+1} - \rho_{mn}, \qquad \frac{\partial \psi_{mn}}{\partial n} \simeq \psi_{m,n+1} - \psi_{mn}$$

and

$$J_2(\theta'_{mn}, \phi'_{mn}/m, n) = \left(\frac{\partial \theta'_{mn}}{\partial m}\right)\left(\frac{\partial \phi'_{mn}}{\partial n}\right) - \left(\frac{\partial \theta'_{mn}}{\partial n}\right)\left(\frac{\partial \phi'_{mn}}{\partial m}\right) \tag{6.7-4}$$

where

$$\frac{\partial \theta'_{mn}}{\partial m} \simeq \theta'_{m+1,n} - \theta'_{mn}, \qquad \frac{\partial \phi'_{mn}}{\partial m} \simeq \phi'_{m+1,n} - \phi'_{mn}$$

$$\frac{\partial \theta'_{mn}}{\partial n} \simeq \theta'_{m,n+1} - \theta'_{mn}, \qquad \frac{\partial \phi'_{mn}}{\partial n} \simeq \phi'_{m,n+1} - \phi'_{mn}.$$

Rearranging terms in (6.7-4) leads to the following equation for the aperture plane electric field amplitude distribution in terms of the radiated feed pattern:

$$|\vec{E}_a(\psi_{mn}, \rho_{mn})| \simeq \sqrt{\frac{|\vec{E}_F(\theta'_{mn}, \phi'_{mn})|^2 \, sin\,\theta'_{mn} \, J_2(\theta'_{mn}, \phi'_{mn}/m, n)}{\rho_{mn} \, J_1(\rho_{mn}, \psi_{mn}/m, n)}}. \tag{6.7-5}$$

6.7.2 Normalized Primary Aperture Diameter d/λ

The tolerance theory developed by Ruze [7] is used to approximate the normalized primary aperture diameter d/λ such that gain loss due to scan induced phase errors does not exceed a specified threshold. For any aperture plane phase error distribution $\delta(x,y)$ the directivity of the reflector system is given by [7]

$$D = \frac{4\pi}{\lambda^2} \frac{\left| \int_{-\infty}^{\infty} \int_{-\infty}^{\infty} \vec{E}_a(x,y)\, e^{j\delta(x,y)}\, dx\, dy \right|^2}{\int_{-\infty}^{\infty} \int_{-\infty}^{\infty} |\vec{E}_a(x,y)|^2\, e^{j\delta(x,y)}\, dx\, dy} \tag{6.7-6}$$

where the integrals are evaluated over the primary aperture plane. If it is assumed that the phase and polarization of $\vec{E}_a(x,y)$ are constant across the aperture plane then (6.7-6) can be rewritten as [7]

$$D = \frac{4\pi}{\lambda^2} \frac{\left[\int_{-\infty}^{\infty} \int_{-\infty}^{\infty} |\vec{E}_a(x,y)|\, e^{j\delta(x,y)}\, dx\, dy \right]^2}{\int_{-\infty}^{\infty} \int_{-\infty}^{\infty} |\vec{E}_a(x,y)|^2\, e^{j\delta(x,y)}\, dx\, dy}. \tag{6.7-7}$$

If $\delta(x,y)$ is small the exponential can be expanded in a power series and the ratio of directivity with phase errors D to directivity with no phase errors D_0 can be written

$$\frac{D}{D_0} \simeq 1 - \overline{\delta^2} + (\overline{\delta})^2 \tag{6.7-8}$$

where

$$\overline{\delta^2} = \frac{\int_{-\infty}^{\infty} \int_{-\infty}^{\infty} |\vec{E}_a(x,y)|\, \delta^2(x,y)\, dx\, dy}{\int_{-\infty}^{\infty} \int_{-\infty}^{\infty} |\vec{E}_a(x,y)|\, dx\, dy}$$

$$\simeq \frac{\sum_{i=0}^{N} \sum_{j=0}^{N} |\vec{E}_a(x_j,y_i)|\, \delta^2(x_j,y_i)}{\sum_{i=0}^{N} \sum_{j=0}^{N} |\vec{E}_a(x_j,y_i)|} \tag{6.7-9}$$

and

$$\bar{\delta} = \frac{\int_{-\infty}^{\infty}\int_{-\infty}^{\infty} |\vec{E}_a(x,y)|\, \delta(x,y)\, dx\, dy}{\int_{-\infty}^{\infty}\int_{-\infty}^{\infty} |\vec{E}_a(x,y)|\, dx\, dy}$$

$$\simeq \frac{\sum_{i=0}^{N}\sum_{j=0}^{N} |\vec{E}_a(x_j,y_i)|\, \delta(x_j,y_i)}{\sum_{i=0}^{N}\sum_{j=0}^{N} |\vec{E}_a(x_j,y_i)|}, \tag{6.7-10}$$

where it assumed that points x_j and y_i are equally spaced in a rectangular grid across the aperture plane. The aperture field distribution $|\vec{E}_a(x_j,y_i)|$ is obtained from $|\vec{E}_a(\psi_{mn},\rho_{mn})|$, which is given by (6.7-5) by polynomial interpolation. The phase error $\delta(x_i,y_j)$ is related to the pathlength from the feed to the aperture plane for the ij^{th} ray, denoted by l_{ij}, by the equation

$$\delta(x_i, y_j) = \frac{2\pi}{\lambda}\,(l_{ij} - l_{ave}) \tag{6.7-11}$$

where l_{ij} is obtained from l_{mn}, which is given by (6.5-27), using polynomial interpolation.

The average pathlength l_{ave} can be defined such that $\bar{\delta} = 0$ by substituting (6.7-11) into (6.7-10) and setting the resulting equation equal to zero. The average pathlength thus obtained is

$$l_{ave} = \sum_{i=0}^{N}\sum_{j=0}^{N} W_{ij}\, l_{ij} \tag{6.7-12}$$

where the normalized weighting factor W_{ij} is given by

$$W_{ij} = \frac{|\vec{E}_a(x_i,y_j)|}{\sum_{i=0}^{N}\sum_{j=0}^{N} |\vec{E}_a(x_i,y_j)|}. \tag{6.7-13}$$

The ratio of directivity with phase errors D to the directivity with no phase

errors D_o can then be written

$$\frac{D}{D_0} = 1 - \overline{\delta^2} = 1 - \left(\frac{2\pi}{\lambda}\right)^2 \sum_{i=0}^{N} \sum_{j=0}^{N} W_{ij}(l_{ij} - l_{ave})^2 \tag{6.7-14}$$

where $\overline{\delta^2}$ is obtained by substitution of (6.7-11) and (6.7-13) into (6.7-9). Multiplying both sides of (6.7-14) by the primary reflector diameter d and rearranging terms leads to the following equation which relates the maximum normalized reflector diameter d/λ to the maximum allowable gain loss due to phase errors D/D_0:

$$(d/\lambda)_m \simeq \left\{ \frac{1 - D/D_0}{\left(\frac{2\pi}{d}\right)^2 \sum_{i=0}^{N} \sum_{j=0}^{N} W_{ij}(l_{ij} - l_{ave})^2} \right\}^2. \tag{6.7-15}$$

It is noted that significant variation in diameter of the illuminated portion of the parent primary reflector can result from beam scanning. To account for this effect the following value is used to approximate the diameter of the illuminated portion of the primary reflector in (6.7-15):

$$d \simeq \frac{2}{N(M)} \sum_{n=1}^{N(M)} \rho_{Mn} \tag{6.7-16}$$

where ρ_{mn} is given by (6.5-29).

6.7.3 Primary Reflector Area Efficiency η_a

The primary reflector area efficiency is a useful parameter because it indicates how efficiently the primary reflector aperture is utilized for any given scan direction. The definition of area efficiency is now derived.

The xy-plane shown in Fig. 6.7-1 represents the aperture plane of an antenna. The region enclosed by the curve $I_f(x,y)$ represents the portion of the aperture plane which is illuminated by a feed. The illumination over this region is given by $\vec{E}_a(x,\mathrm{y})$ which assumes zero values outside of this boundary. $I_f(x,y)$ is indicated by a dashed line in Fig. 6.7-1 and the area enclosed by this curve is

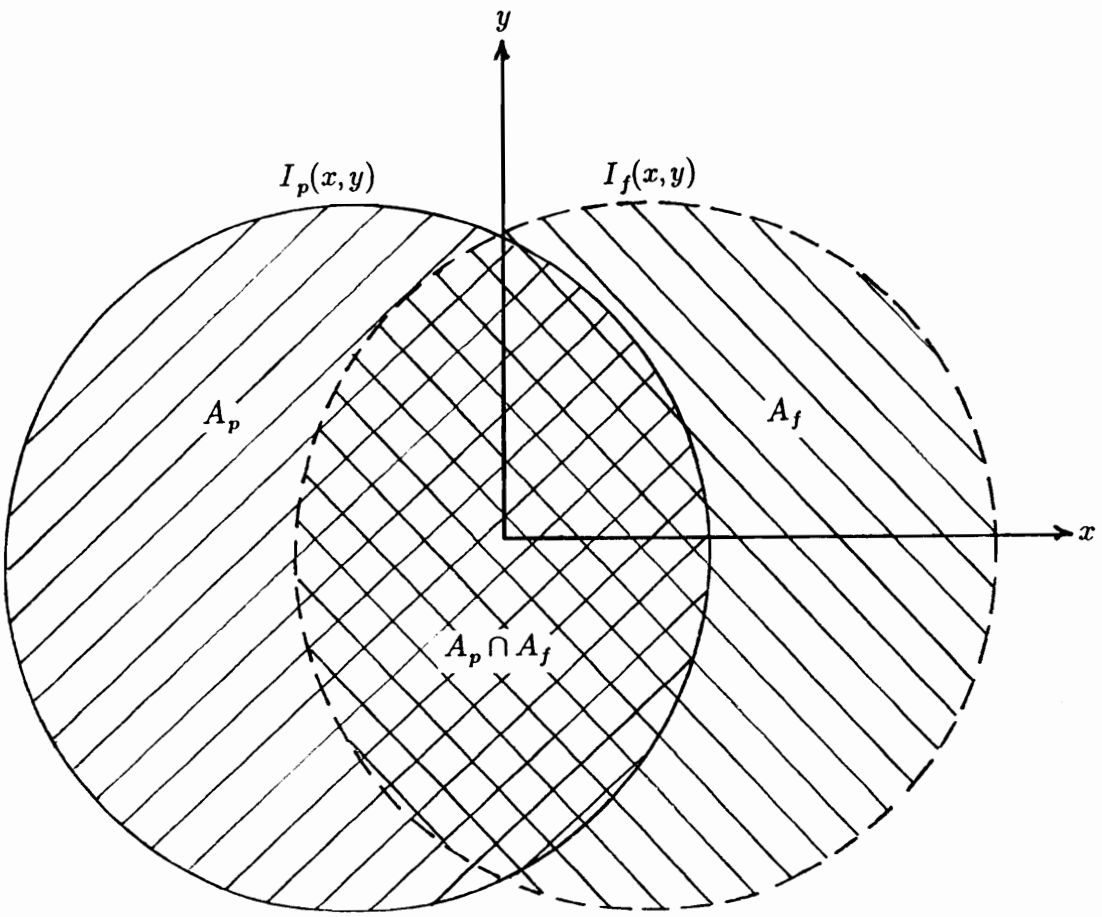

Figure 6.7-1. Aperture plane of a reflector antenna. The region enclosed by curve $I_f(x,y)$ represents the portion of the aperture plane which is illuminated by a feed. $I_f(x,y)$ is indicated by a dashed line and the area enclosed by this curve is designated by A_f. The region enclosed by the curve $I_p(x,y)$ represents the physical antenna aperture. $I_p(x,y)$ is indicated by a solid line and the area enclosed by this curve is designated by A_p. Only the area given by the intersection of A_p and A_f gives rise to forward radiation.

designated by A_f. The region enclosed by the curve $I_p(x,y)$ represents the physical antenna aperture which, if illuminated, gives rise to forward radiation. $I_p(x,y)$ is indicated by a solid line in Fig. 6.7-1 and the area enclosed by this curve is designated by A_p. The curve $I_p(x,y)$ can represent either the boundary of an iris or the rim of a reflector for which the portion of $\vec{E}_a(x,y)$ which falls outside of $I_p(x,y)$ represents either scattered radiation or spillover, respectively. In either case only the area given by the intersection of A_p and A_f gives rise to forward radiation. This "used" area is designated by

$$A_u = A_p \cap A_f \tag{6.7-17}$$

By definition the directivity of the system described above is given by [6]

$$D = \frac{4\pi}{\lambda^2} \frac{\left| \iint\limits_{A_u} \vec{E}_a(x,y)\, dx\, dy \right|^2}{\iint\limits_{A_u} |\vec{E}_a(x,y)|^2\, dx\, dy}. \tag{6.7-18}$$

Gain is related to directivity by [6]

$$\mathrm{G} = eD \tag{6.7-19}$$

where the radiation efficiency e is defined as the ratio of the power radiated in the forward direction P_r to the total power input by the source P_{in} [6]

$$e = \frac{P_r}{P_{in}}. \tag{6.7-20}$$

If it is assumed that ohmic losses and subreflector spillover are negligible, then

$$e \simeq \frac{\iint\limits_{A_u} |\vec{E}_a(x,y)|^2\, dx\, dy}{\iint\limits_{A_f} |\vec{E}_a(x,y)|^2\, dx\, dy} \tag{6.7-21}$$

and from (6.7-18), (6.7-19) and (6.7-21) the gain is given by

$$G \simeq \frac{4\pi}{\lambda^2} \frac{\left| \int\int_{A_u} \vec{E}_a(x,y)\, dx\, dy \right|^2}{\int\int_{A_f} |\vec{E}_a(x,y)|^2\, dx\, dy}. \tag{6.7-22}$$

By definition gain is also given by [6]

$$G = \epsilon_{ap}\, A_p\, \frac{4\pi}{\lambda^2} \tag{6.7-23}$$

where ϵ_{ap} is the aperture efficiency and A_p is the physical aperture area. Equating (6.7-22) and (6.7-23) leads to the following equation for aperture efficiency

$$\epsilon_{ap} \simeq \frac{\left| \int\int_{A_u} \vec{E}_a(x,y)\, dx\, dy \right|^2}{A_p \int\int_{A_f} |\vec{E}_a(x,y)|^2\, dx\, dy}. \tag{6.7-24}$$

It is noted that (6.7-24) gives the aperture efficiency corresponding to the direction of highest gain while the equations defined in Sec. 3.1 give the aperture efficiency with respect to a specified direction defined by a second antenna. If it is assumed that an idealized feed is used such that $\vec{E}_a(x,y)$ has both uniform amplitude and phase over A_f, then a "normalized" aperture efficiency or "area efficiency" can be defined as

$$\eta_a \simeq \frac{(A_u)^2}{A_p A_f} = \frac{(A_p \cap A_f)^2}{A_p A_f}. \tag{6.7-25}$$

If there is no spillover at the primary reflector and the only loss of gain is due to under illumination, then (6.7-25) reduces to

$$\eta_a \simeq \frac{A_f}{A_p}. \tag{6.7-26}$$

It is noted that some authors mistakenly refer to (6.7-26) as aperture efficiency, however, this is clearly not the case due to the simplifying assumptions used.

In the following chapter aperture area efficiency given by (6.7-25) is used as a figure-of-merit to evaluate primary aperture illumination as a function of scan direction. The use of area efficiency is preferable to aperture efficiency because area efficiency is independent of the feed pattern used. For the conjugate tri-reflector the set of G.O. transmit rays which intersect the edge of the tertiary reflector are used to obtain the G.O. edge of illumination at the parent primary reflector. The illuminated portion of the primary aperture $I_f(x,y)$ is approximated by the xy-plane projection of the G.O. edge of illumination at the parent primary reflector, which is given by the following set of points:

$$\{P_{1rtx}^{Mn}, P_{1rty}^{Mn}\}, \qquad n = 1,\ldots,n(M) \tag{6.7-27}$$

where $\{P_{1rt}^{mn}\}$ is given by (6.5-17). The physical aperture $I_p(x,y)$, defined by d and x_c in Sec. 6.3, is approximated by following the set of points:

$$\{P_{1x}^{Mn}, P_{1y}^{Mn}\}, \qquad n = 1,\ldots,n(M) \tag{6.7-28}$$

where $\{P_1^{mn}\}$ is given by (6.3-1). It is noted that (6.7-27) and (6.7-28) assume that rays reflected at the primary reflector are approximately parallel to the z-axis shown in Fig. 6.5-1(a). A plot similar to Fig. 6.7-1 is obtained by plotting the points given by (6.7-27) and (6.7-28) together on the same graph. Such plots are said to depict aperture plane vignetting [3]. Plots of aperture plane vignetting are useful because they depict in a qualitative manner both spillover and under illumination at the primary aperture plane.

6.8 References

1. F. Watanabe and Y. Mizugutch, "An Offset Spherical Tri-Reflector Antenna," *Trans of the IECE of Japan*, vol. E 66, no. 2, pp. 108-115, February 1983.

2. T. Kitsuregawa, *Advanced Technology in Satellite Communication Antennas*, Artech House: Boston, 1990.

3. C. Dragone and M. J. Gans, "Imaging Reflector Arrangements to Form a Scanning Beam Using a Small Array," *Bell System Tech. Journal*, vol. 58, no. 2, pp. 501-515, February 1979.

4. G. Skahill, "A Dual Reflector Antenna Scans Many Beamwidths Without Loss of Gain, Resolution, or Sidelobe Level," *Microwave Journal*, pp. 129-139, March 1988.

5. M. Born and E. Wolf, *Principles of Optics*, The Macmillan Company: New York, 1964.

6. W. Stutzman and G. Thiele, *Antenna Theory and Design*, John Wiley & Sons, Inc.: New York, 1981.

7. J. Ruze, "Antenna Tolerance Theory," *Proc IEEE*, vol. 54, pp. 633-640, April 1966.

8. W. Press, B. Flannery, S. Teukolsky and W. Vetterling, *Numerical Recipes the Art of Scientific Computing*, Cambridge University Press, Inc.: New York, 1986.

Chapter 7

Conjugate Tri-reflector G.O. Performance Results

The conjugate tri-reflector antenna configuration is comprised of a parabolic primary reflector, an elliptic secondary reflector and a shaped tertiary reflector. These three elements can be arranged to form three distinct types of realizable tri-reflector configurations which are referred to as: Cassegrain I; Gregorian; and Cassegrain II. In this chapter the electrical and mechanical characteristics of representative cases of these three reflector configurations are compared. Also included in the comparison is an offset prime focus parabolic reflector with beam scanning accomplished by feed translation. In all cases comparison is performed over an elliptical scan range that subtends $\pm 2.5^\circ$ in the xz-plane and $\pm 5^\circ$ in the yz-plane.

Electrical performance evaluations are obtained using the geometrical optics (G.O.) methods developed in Chapter 6. The specific scan directions considered are (see Fig. 6.3-2):

$$\begin{aligned}
&\phi = 0.0^\circ, \quad \theta = 0.1^\circ\text{- } 2.5^\circ \\
&\phi = 45.0^\circ, \quad \theta = 0.1^\circ\text{- } 3.1^\circ \\
&\phi = 90.0^\circ, \quad \theta = 0.1^\circ\text{- } 5.0^\circ \\
&\phi = 135.0^\circ, \quad \theta = 0.1^\circ\text{- } 3.1^\circ \\
&\phi = 180.0^\circ, \quad \theta = 0.1^\circ\text{- } 2.5^\circ
\end{aligned} \tag{7-1}$$

where for each value of ϕ ten equal increments of θ are used with the first and last value of θ indicated in (7-1). It is unnecessary to consider $\phi = 225^\circ$, 270° and 315° because the configurations are symmetrical about the xz-plane. As discussed in Chapter 6, for each scan direction tertiary reflector motion parameter values α, β and $\vec{T}$ are obtained by numerical optimization and the normalized aperture diameter d/λ and the aperture area efficiency η_a are calculated. The normalized aperture diameter is calculated subject to 1 dB gain loss due to scan induced phase errors. Therefore, $D/D_0 = 0.7943$ in (6.7-15). The feed pattern used is

$$\vec{E}_F(\theta') = cos^q \theta' \tag{7-3}$$

where θ' is defined with respect to the feed coordinate system as shown in Fig. 6.5-1(b). The value of q is chosen such that

$$20 \times \log\left(cos^q\, \theta'_{ave}\right) = -15 \text{ dB} \tag{7-4}$$

where θ'_{ave} is the average half angle subtended by the tertiary reflector as viewed from the feed with the tertiary reflector positioned for boresight operation.

7.1 The Cassegrain I Configuration

The cross-section of an example Cassegrain I configuration is shown in Fig. 7.1-1. This configuration is referred to as Cassegrain because the secondary reflector surface is placed between the primary reflector surface and the primary reflector focal point F_1. Also shown in Fig. 7.1-1 are ray paths for rays striking the top, center and bottom of the primary reflector for scan angles of $\phi = 0^\circ$ and $\theta = 2.5^\circ$, 0° and -2.5°. To create Fig. 7.1-1 a separate tertiary reflector was synthesized for each scan direction using the procedure described in Sec. 6.3. Different line types have been used to indicate the portion of the secondary reflector illuminated for each scan direction. The synthesis parameter values

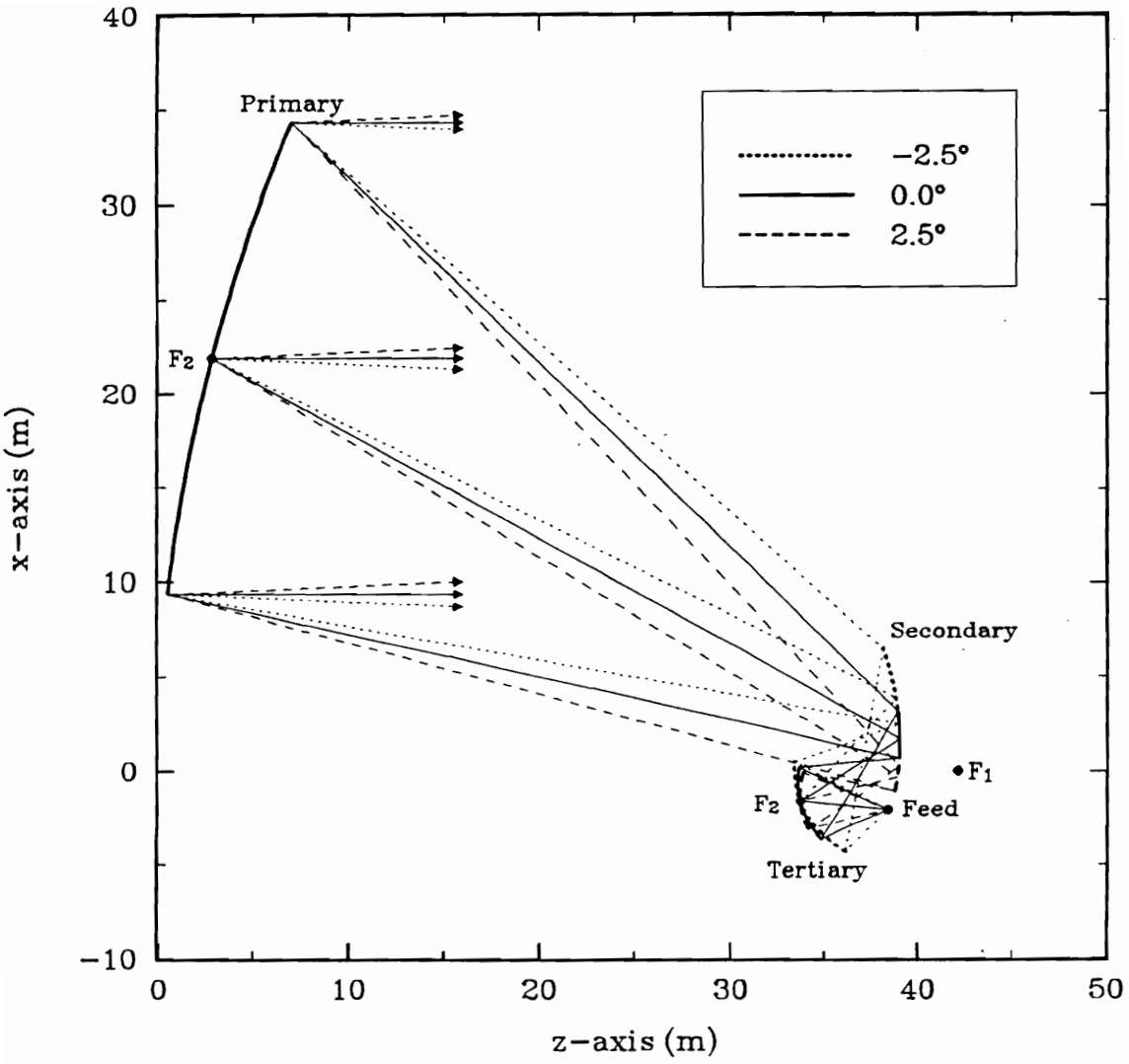

Figure 7.1-1. Cross-section of an example Cassegrain I tri-reflector configuration. Ray paths are shown for rays striking the top, center and bottom of the primary reflector for scan angles of $\phi = 0^{\circ}$ and $\theta = 2.5^{\circ}$, 0° and -2.5°.

used are shown on Table 7.1-1. These parameters are defined on Table 6.3-1 and shown in Fig. 6.3-1.

Table 7.1-1
Synthesis Parameter Values used for
Cassegrain I Configuration Synthesis

Parameter	Value (m)
P_s	(21.87, 0.0, 2.83)†
F_1	(0.0, 0.0, 42.19)†
x_c	21.87
d	25.0
F_2	(21.87, 0.0, 2.83)†
F_2'	(-1.56, 0.0, 33.75)†
e_r	47.72
F	(-2.03, 0.0, 38.44)†

† indicates values in xyz-coordinate system

Front and side views of the Cassegrain I configuration are shown in Fig. 7.1-2. The tertiary reflector shown in this figure was synthesized with $\theta_s = 0.0^\circ$ and $\phi_s = 0.0^\circ$. The primary reflector has an offset height of $H = 9.375$ m (see Fig. 4.1-9) and an F/D value of 1.69. The xy-plane projected area of the primary reflector is $A_p = 490.9$ m^2. The secondary reflector is oversized such that there is no spillover for the scan range defined by (7-1). The secondary reflector rim is an ellipse with a major axis of $2a_2 = 11.54$ m and a minor axis of $2b_2 = 6.16$ m. The projected aperture area of the secondary reflector, as approximated by $A_s \simeq \pi a_2 b_2$, is 55.8 m^2, which is 11.36 % of the primary aperture area. The tertiary reflector rim is an ellipse with a major axis of $2a_3 = 4.03$ m and a minor axis of $2b_3 = 3.78$ m. The projected aperture area of the tertiary reflector, as approximated by $A_t \simeq \pi a_3 b_3$, is 11.96 m^2, which is 2.4 %

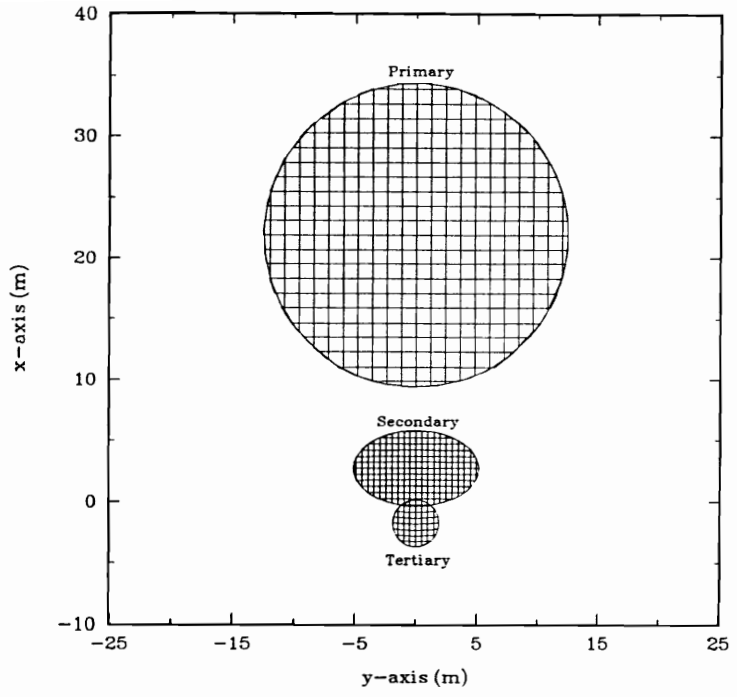

(a)

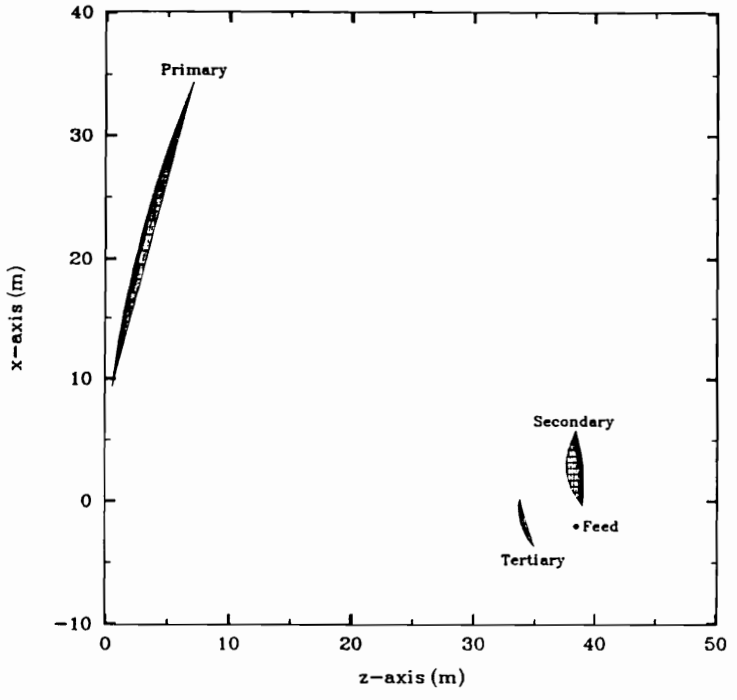

(b)

Figure 7.1-2. Front (a) and side (b) views of the Cassegrain I configuration. The secondary reflector is oversized to allow for beam scanning over an elliptical scan range which subtends $\pm 2.5^{\circ}$ in the xz-plane and $\pm 5^{\circ}$ in the yz-plane (see Fig. 6.2-2).

of the primary aperture area. The overall length of the reflector configuration as measured along the z-axis is 39 m and the overall height as measured along the x-axis is 38 m. For boresight operation the average half angle subtended by the tertiary reflector as viewed from the feed is $\theta'_{ave} = 24.48^{\circ}$ for which (7-3) yields $q = 18.33$. If it is assumed that the feed is a pyramidal horn, then the feed aperture size d_f can be approximated by [1]

$$d_f/\lambda \simeq \sqrt{\frac{q+0.5}{1.39}}. \tag{7.1-1}$$

For $q = 18.33$ (7.1-1) yields $d_f \simeq 3.68\ \lambda$.

In the following section the scan performance of the the conjugate tri-reflector shown in Fig. 7.1-2 is investigated using the G.O. techniques developed in Chapter 6. Beam scanning is accomplished entirely by tertiary reflector motion which is constrained to two degrees of rotational freedom about point F'_2. It is noted that the tertiary reflector was synthesized with $\theta_s = 0.0^{\circ}$ and $\phi_s = 0.0^{\circ}$ and, therefore, the aperture is only free of phase errors for boresight operation along the z-axis.

7.1.1 Scan Performance for Two Degrees of Rotational Freedom About Point F'_2

Scan performance was calculated with the tertiary reflector constrained to two degrees of rotational freedom. Motion optimization was performed with $P_r = F'_2$ and $T_{max} = 0$ as discussed in Chapter 6. Calculated values for motion parameters α and β are plotted versus scan angle θ for the five values of ϕ indicated in (7.1) in Figs. 7.1-3 - 7.1-7. The corresponding values of the normalized aperture diameter d/λ and primary reflector area efficiency η_a are plotted versus θ in Figs. 7.1-8 and 7.1-9. The results of the above performance calculations for the limiting scan directions in (7-1) are summarized on Table 7.1-2.

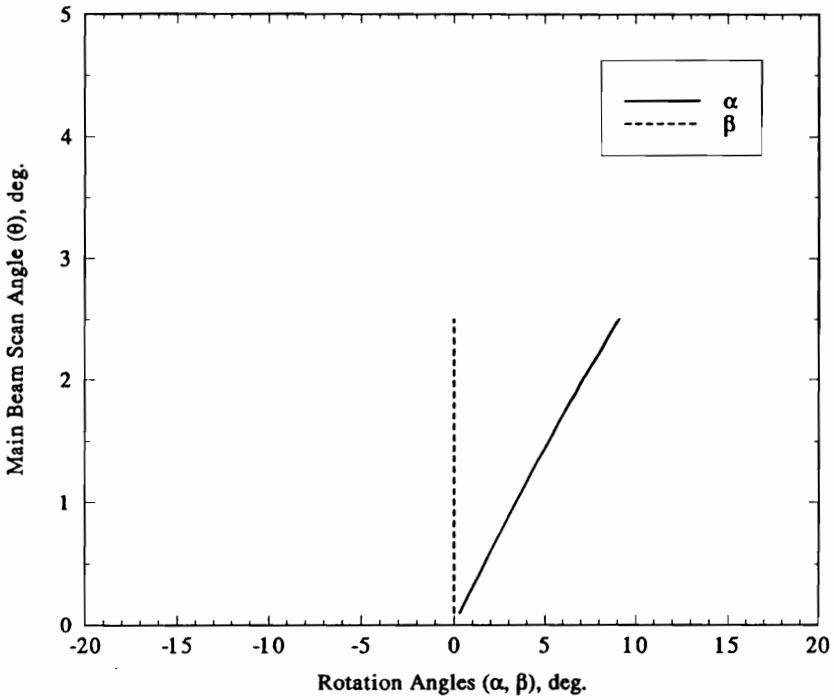

Figure 7.1-3. Cassegrain I configuration tertiary reflector rotation angles α and β used to scan the main beam over the range $\theta = 0.1°$-$2.5°$ with $\phi = 0.0°$.

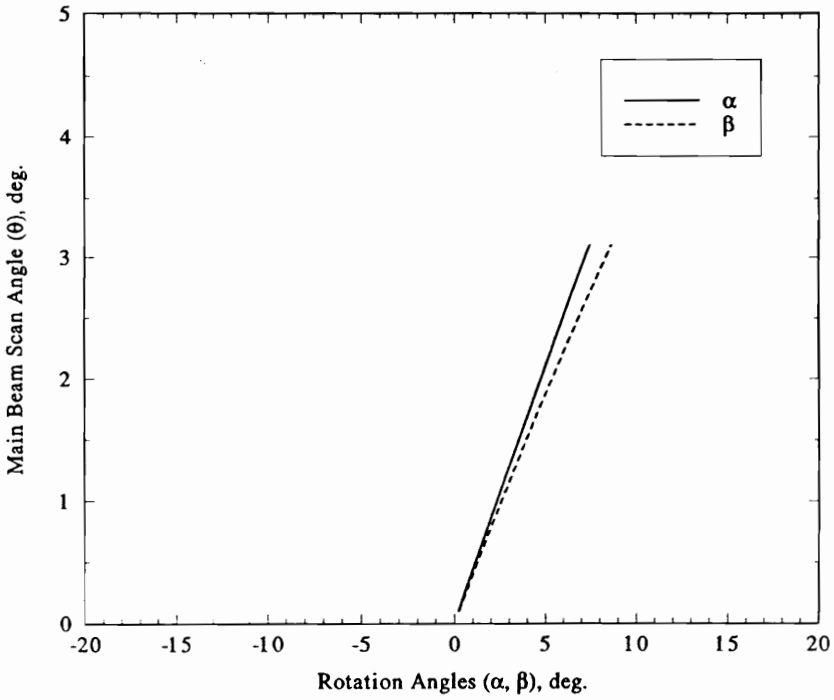

Figure 7.1-4. Cassegrain I configuration tertiary reflector rotation angles α and β used to scan the main beam over the range $\theta = 0.1°$-$3.1°$ with $\phi = 45.0°$.

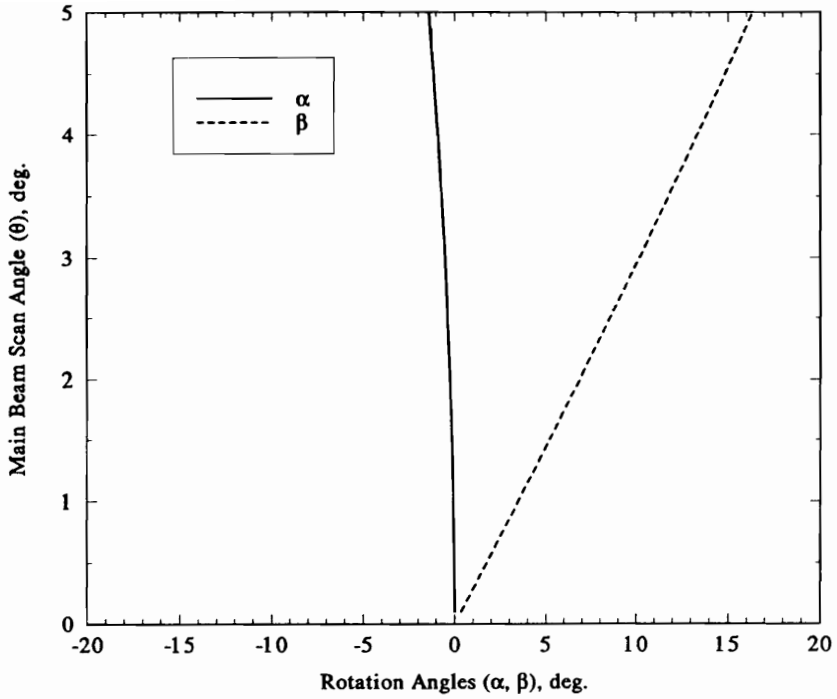

Figure 7.1-5. Cassegrain I configuration tertiary reflector rotation angles α and β used to scan the main beam over the range $\theta = 0.1°$-$5.0°$ with $\phi = 90.0°$.

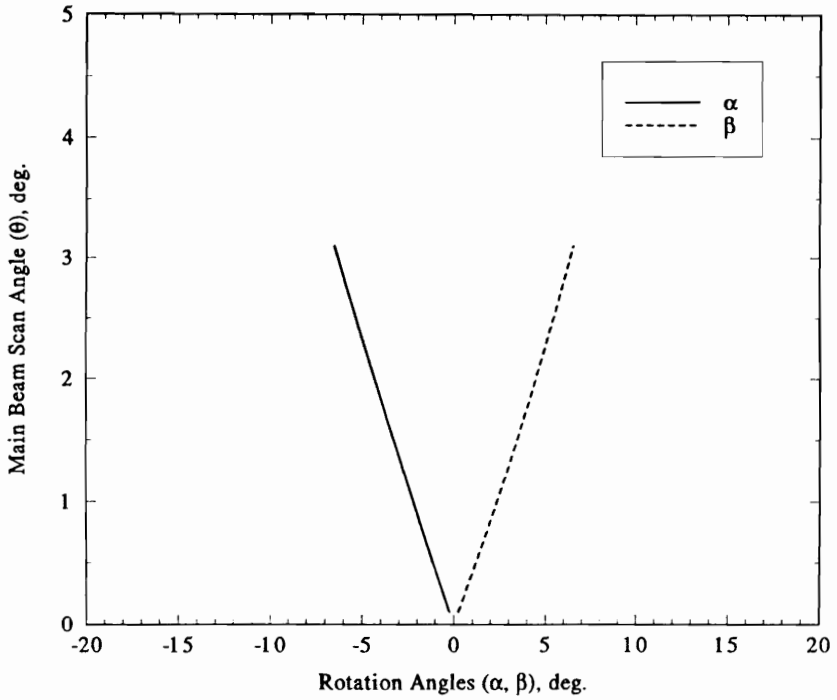

Figure 7.1-6. Cassegrain I configuration tertiary reflector rotation angles α and β used to scan the main beam over the range $\theta = 0.1°$-$3.1°$ with $\phi = 135.0°$.

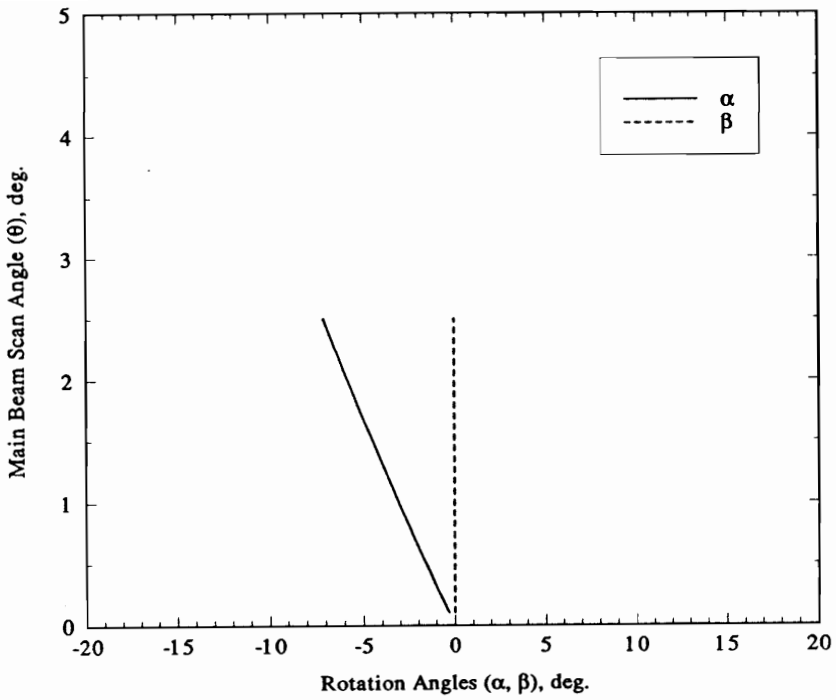

Figure 7.1-7. Cassegrain I configuration tertiary reflector rotation angles α and β used to scan the main beam over the range $\theta = 0.1°$-$2.5°$ with $\phi = 180.0°$.

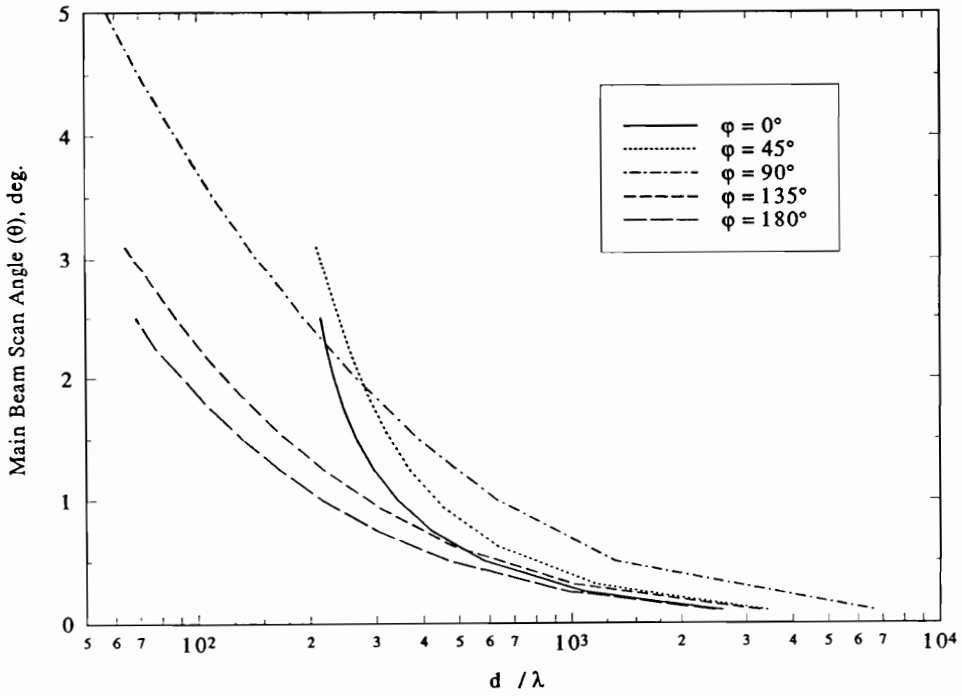

Figure 7.1-8. Normalized aperture diameter d/λ for the Cassegrain I configuration subject to 1 dB maximum gain loss due to scan induced phase errors. Tertiary reflector motion is constrained to two degrees of rotational freedom about the point $P_r = F_2'$. The scan range is given by (7-1).

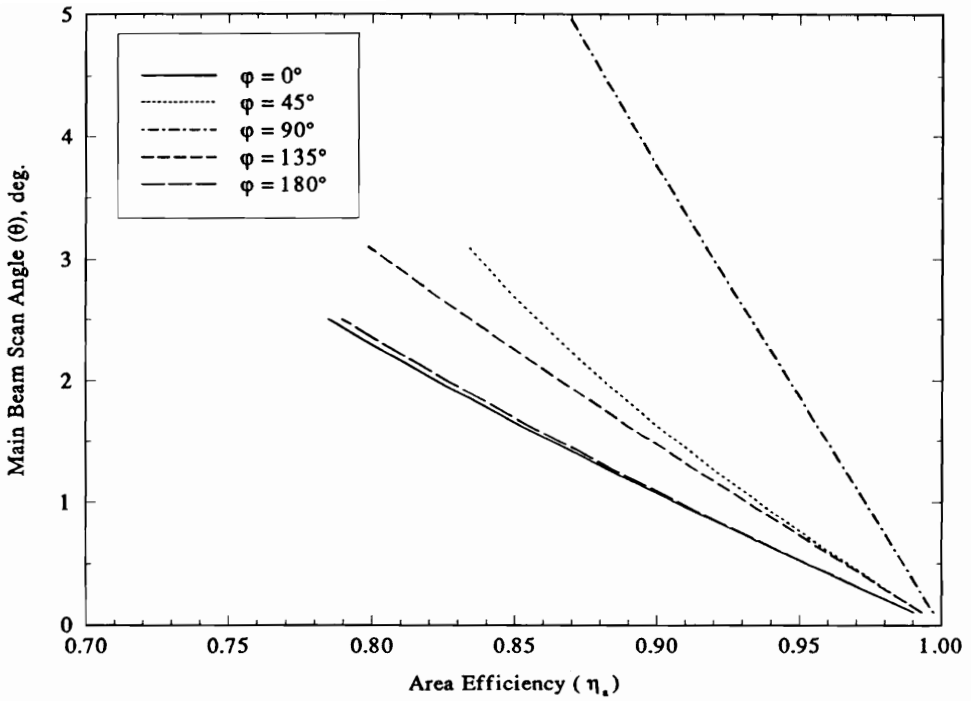

Figure 7.1-9. Primary aperture area efficiency η_a for the Cassegrain I configuration. Tertiary reflector motion is constrained to two degrees of rotational freedom about the point $P_r = F_2'$. The scan range is given by (7-1).

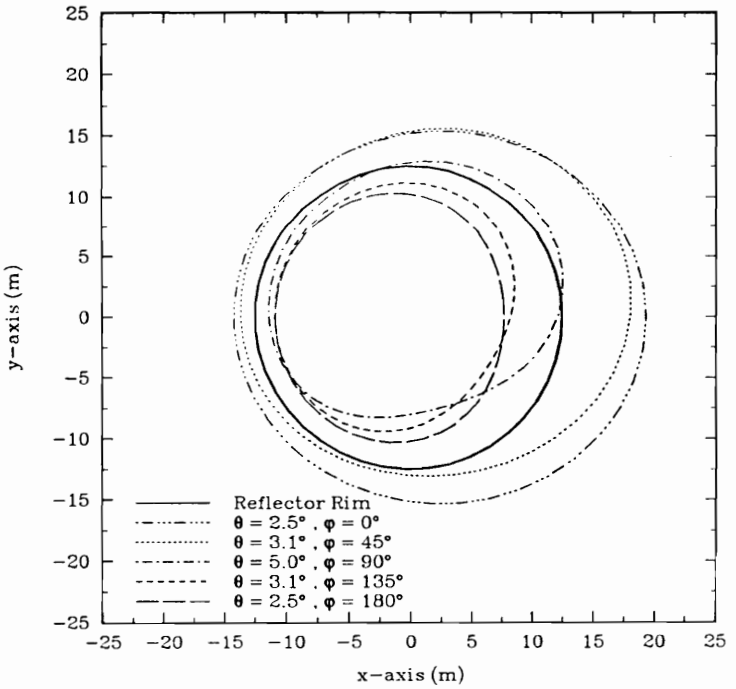

Figure 7.1-10. Primary aperture plane vignetting for the Cassegrain I configuration for the limiting scan directions in (7-1) and tertiary reflector motion constrained to two degrees of rotational freedom about point $P_r = F_2'$.

Table 7.1-2

Cassegrain I Performance Results

Two Degrees of Tertiary Reflector Motion (α, β)

$P_r = F_2'$, $T_{max} = 0$

ϕ (deg)	θ (deg)	α (deg)	β (deg)	d/λ	η_a
0	2.5	9.08	0.0	213	0.78
45	3.1	7.45	8.63	208	0.84
90	5.0	-1.41	16.33	57	0.87
135	3.1	-6.53	6.52	64	0.80
180	2.5	-7.11	0.0	68	0.79

The highest frequency for which this configuration can operate over the entire scan range with less than 1 dB of gain loss due to scan induced phase errors is that for which $d/\lambda = 57$. For the 25 m aperture this corresponds to a maximum operating frequency of $f_M = 0.68$ GHz. Figure 7.1-10 shows vignetting at the primary aperture plane for the limiting scan directions. It is noted that this configuration suffers from a large amount of vignetting leading to poor aperture utilization. This conclusion is also evident by the low values calculated for the aperture area efficiency η_a.

7.2 The Gregorian Configuration

The cross-section of an example Gregorian configuration is shown in Fig. 7.2-1. This configuration is referred to as Gregorian because the primary reflector focal point F_1 is placed between the primary and secondary reflector surfaces. Also shown in Fig. 7.2-1 are ray paths for rays striking the top, center and bottom of the primary reflector for scan angles of $\phi = 0^\circ$ and $\theta = 2.5^\circ$, 0° and -2.5°. To create Fig. 7.2-1 a separate tertiary reflector was synthesized for each scan direction using the procedure described in Sec. 6.3. Different line types have been used to indicate the portion of the secondary reflector illuminated for each scan direction. The synthesis parameter values used are shown on Table 7.2-1. These parameters are defined on Table 6.3-1 and shown in Fig. 6.3-1.

Table 7.2-1
Synthesis Parameter Values used for
Gregorian Configuration Synthesis

Parameter	Value (m)
P_s	(21.87, 0.0, 2.83) †
F_1	(0.0, 0.0, 42.19) †
x_c	21.87
d	25.0
F_2	(21.87, 0.0, 2.83) †
F_2'	(4.69, 0.0, 43.75) †
e_r	54.80
F	(-3.12, 0.0, 40.62) †

† indicates values in xyz-coordinate system

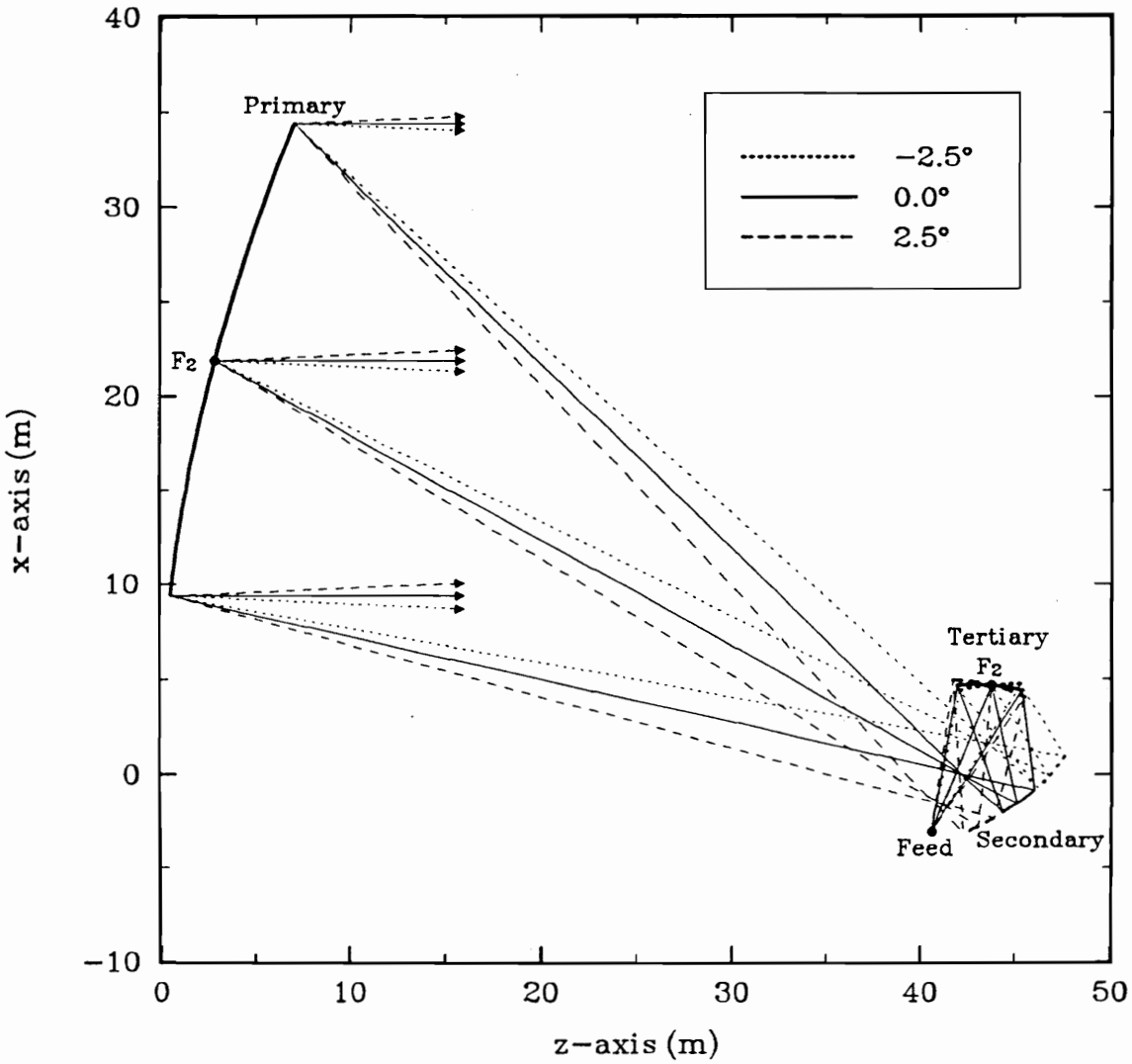

Figure 7.2-1. Cross-section of an example Gregorian tri-reflector configuration. Ray paths are shown for rays striking the top, center and bottom of the primary reflector for scan angles of $\phi = 0^{\circ}$ and $\theta = 2.5^{\circ}$, 0° and -2.5°.

Front and side views of the Gregorian configuration are shown in Fig. 7.2-2. The tertiary reflector shown in this figure was synthesized with $\theta_s = 0.0^\circ$ and $\phi_s = 0.0^\circ$. The primary reflector has an offset height of $H = 9.375$ m (see Fig. 4.1-9) and an F/D value of 1.69. The xy-plane projected area of the primary reflector is $A_p = 490.9$ m^2. The secondary reflector is oversized such that there is no spillover for the scan range defined by (7-1). The secondary reflector rim is an ellipse with a major axis of $2a_2 = 9.95$ m and a minor axis of $2b_2 = 6.74$ m. The projected aperture area of the secondary reflector, as approximated by $A_s \simeq \pi a_2 b_2$, is 52.7 m^2, which is 10.73 % of the primary aperture area. The tertiary reflector rim is an ellipse with a major axis of $2a_3 = 3.40$ m and a minor axis of $2b_3 = 3.28$ m. The projected aperture area of the tertiary reflector, as approximated by $A_t \simeq \pi a_3 b_3$, is 8.75 m^2, which is 1.78 % of the primary aperture area. The overall length of the reflector configuration as measured along the z-axis is 48 m and the overall height as measured along the x-axis is 38 m. For boresight operation the average half angle subtended by the tertiary reflector as viewed from the feed is $\theta'_{ave} = 11.22^\circ$ for which (7-3) yields $q = 89.49$. For a pyramidal horn (7.1-1) yields an aperture dimension of $d_f \simeq 8.04\ \lambda$.

In the following sections the scan performance of the the conjugate tri-reflector shown in Fig. 7.2-2 is investigated using the G.O. techniques developed in Chapter 6. Beam scanning is accomplished entirely by tertiary reflector motion. Two cases of tertiary reflector motion are considered. In the first case motion is constrained to two degrees of rotational freedom about point F'_2 and in the second case two degrees of rotational freedom and three degrees of translational freedom are allowed. These cases are presented in Secs. 7.2.1 and 7.2.2, respectively. It is noted that the tertiary reflector was synthesized with $\theta_s = 0.0^\circ$ and $\phi_s = 0.0^\circ$ and, therefore, the aperture is only free of phase errors for boresight operation along the z-axis.

7.2.1 Scan Performance for Two Degrees of Rotational Freedom About Point F'_2

Scan performance was calculated with the tertiary reflector constrained to

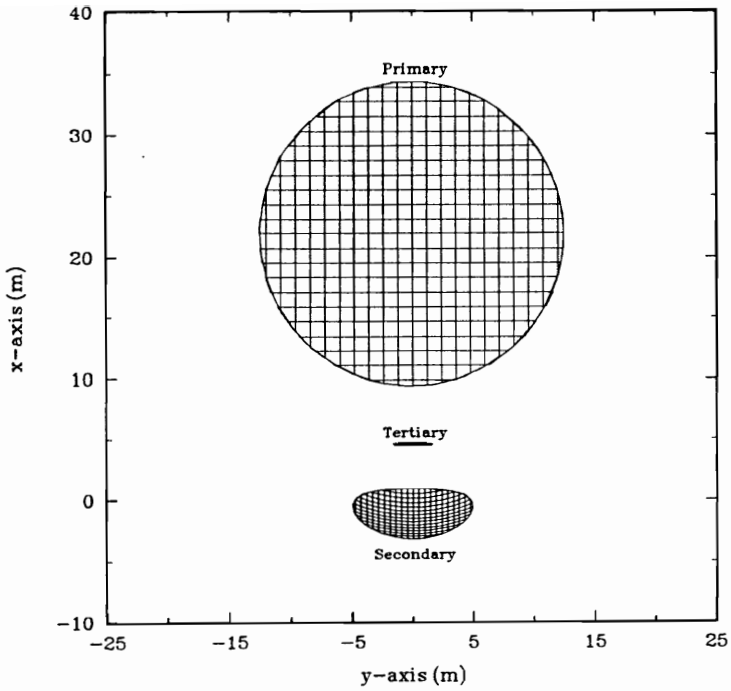

(a)

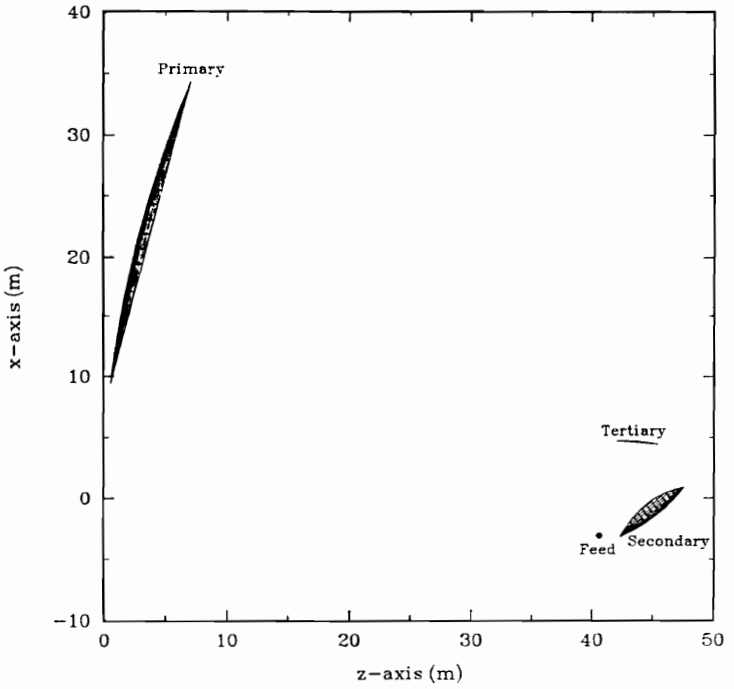

(b)

Figure 7.2-2. Front (a) and side (b) views of the Gregorian configuration. The secondary reflector is oversized to allow for beam scanning over an elliptical scan range which subtends $\pm 2.5^{\circ}$ in the xz-plane and $\pm 5^{\circ}$ in the yz-plane (see Fig. 6.2-2)

two degrees of rotational freedom. Motion optimization was performed with $P_r = F_2'$ and $T_{max} = 0$ as discussed in Chapter 6. Calculated values for motion parameters α and β are plotted versus scan angle θ for the five values of ϕ indicated in (7.1) in Figs. 7.2-3 - 7.2-7. The corresponding values of the normalized aperture diameter d/λ and primary reflector area efficiency η_a are plotted versus θ in Figs. 7.2-8 and 7.2-9. The results of the above performance calculations for the limiting scan directions in (7-1) are summarized on Table 7.2-2.

Table 7.2-2

Gregorian Performance Results

Two Degrees of Tertiary Reflector Motion (α, β)

$P_r = F_2'$, $T_{max} = 0$

ϕ (deg)	θ (deg)	α (deg)	β (deg)	d/λ	η_a
0	2.5	8.65	0.0	170	0.85
45	3.1	8.41	-7.04	170	0.84
90	5.0	4.86	-1.89	246	0.87
135	3.1	-7.62	-1.03	270	0.94
180	2.5	-10.22	0.0	207	0.90

The highest frequency for which this configuration can operate over the entire scan range with less than 1 dB of gain loss due to scan induced phase errors is that for which $d/\lambda = 170$. For the 25 m aperture this corresponds to a maximum operating frequency of $f_M = 2.04$ GHz. Figure 7.2-10 shows vignetting at the primary aperture plane for the limiting scan directions. Considerable reduction in vignetting is observed compared to the results obtained for the Cassegrain I configuration.

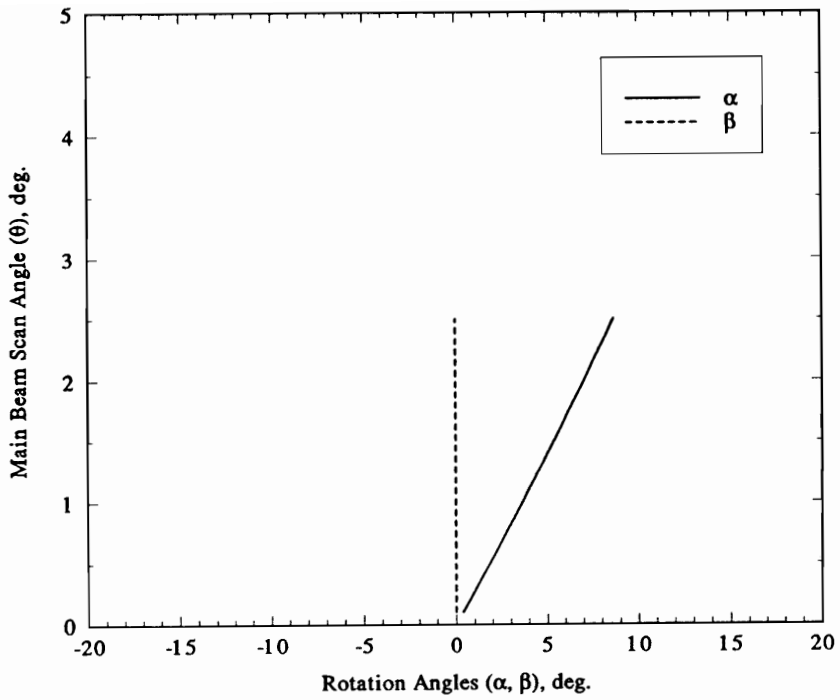

Figure 7.2-3. Gregorian configuration tertiary reflector rotation angles α and β used to scan the main beam over the range $\theta = 0.1°$-$2.5°$ with $\phi = 0.0°$.

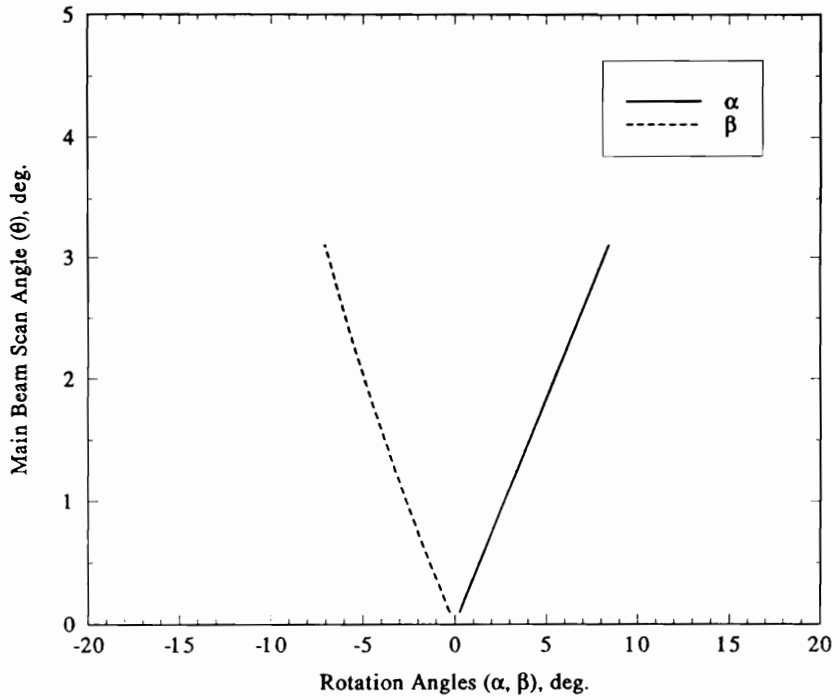

Figure 7.2-4. Gregorian configuration tertiary reflector rotation angles α and β used to scan the main beam over the range $\theta = 0.1°$-$3.1°$ with $\phi = 45.0°$.

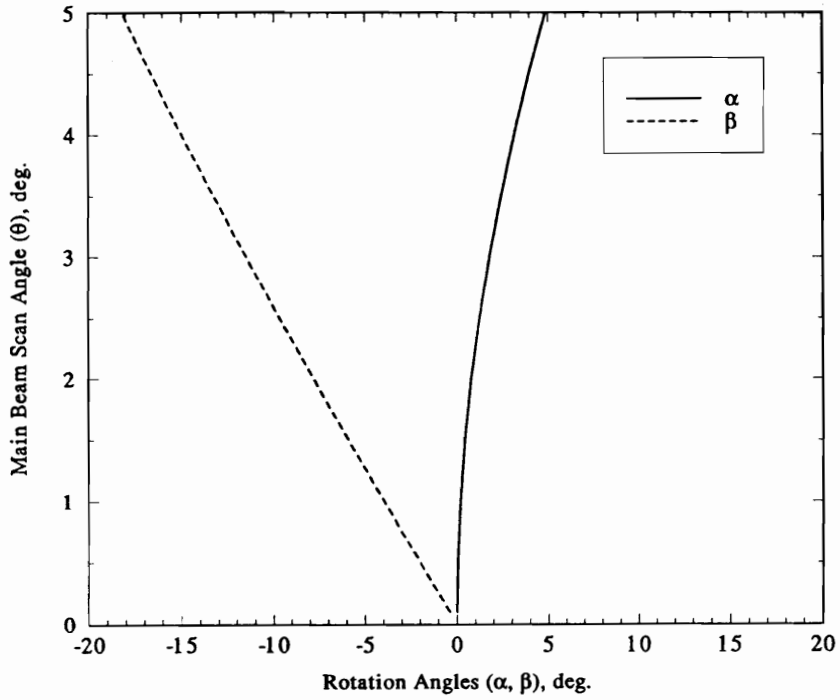

Figure 7.2-5. Gregorian configuration tertiary reflector rotation angles α and β used to scan the main beam over the range $\theta = 0.1°$-$5.0°$ with $\phi = 90.0°$.

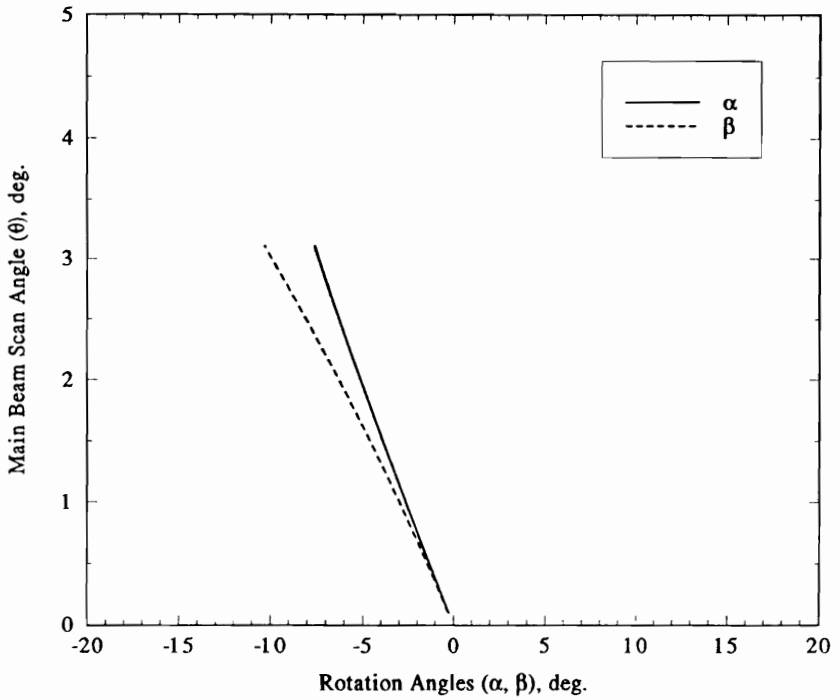

Figure 7.2-6. Gregorian configuration tertiary reflector rotation angles α and β used to scan the main beam over the range $\theta = 0.1°$-$3.1°$ with $\phi = 135.0°$.

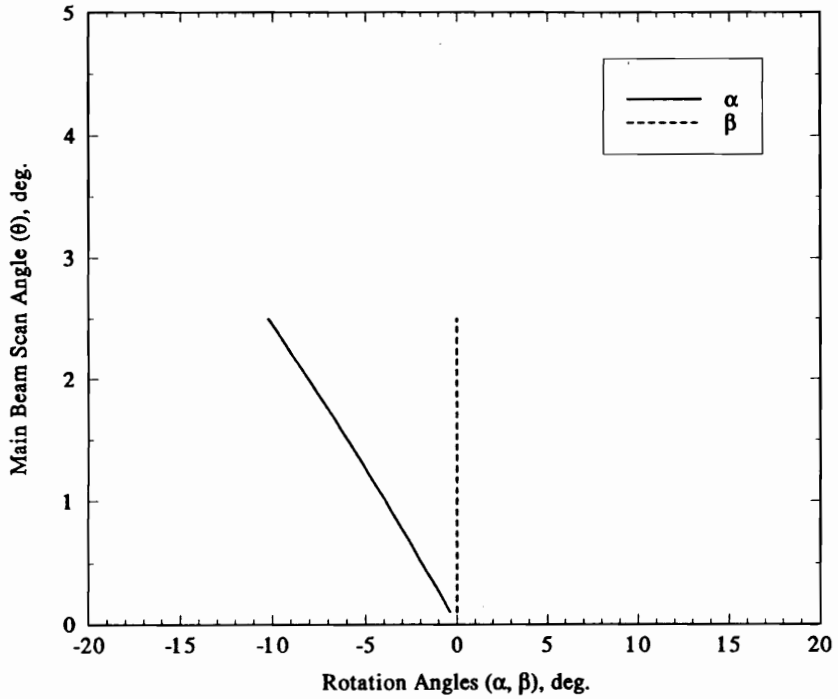

Figure 7.2-7. Gregorian configuration tertiary reflector rotation angles α and β used to scan the main beam over the range $\theta = 0.1°$-$2.5°$ with $\phi = 180.0°$.

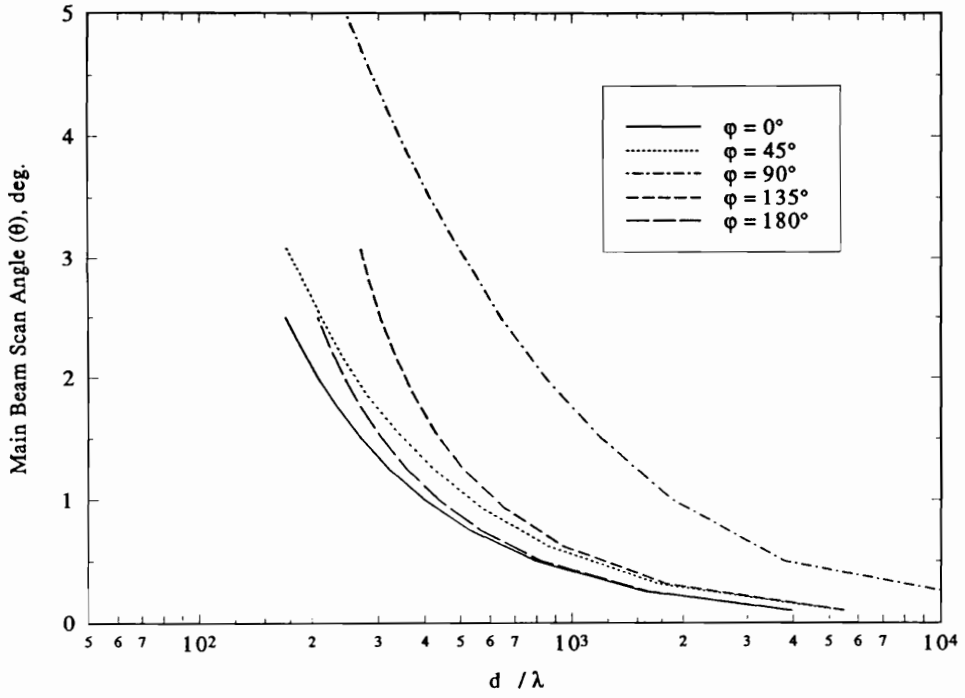

Figure 7.2-8. Normalized aperture diameter d/λ for the Gregorian configuration subject to 1 dB maximum gain loss due to scan induced phase errors. Tertiary reflector motion is constrained to two degrees of rotational freedom about the point $P_r = F_2'$. The scan range is given by (7-1).

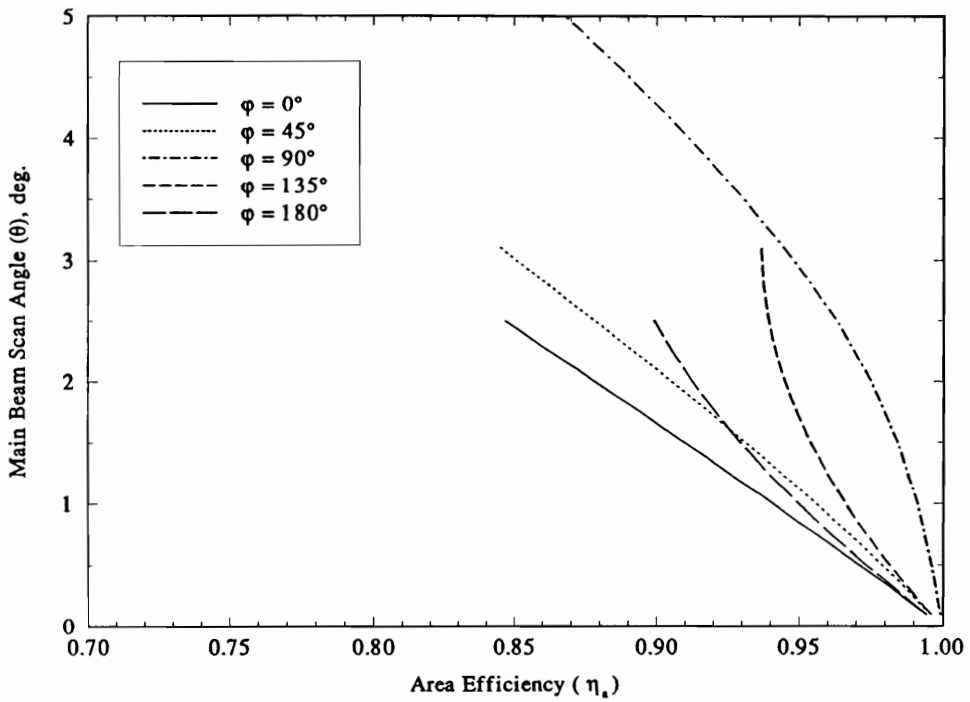

Figure 7.2-9. Primary aperture area efficiency η_a for the Gregorian configuration. Tertiary reflector motion is constrained to two degrees of rotational freedom about the point $P_r = F_2'$. The scan range is given by (7-1).

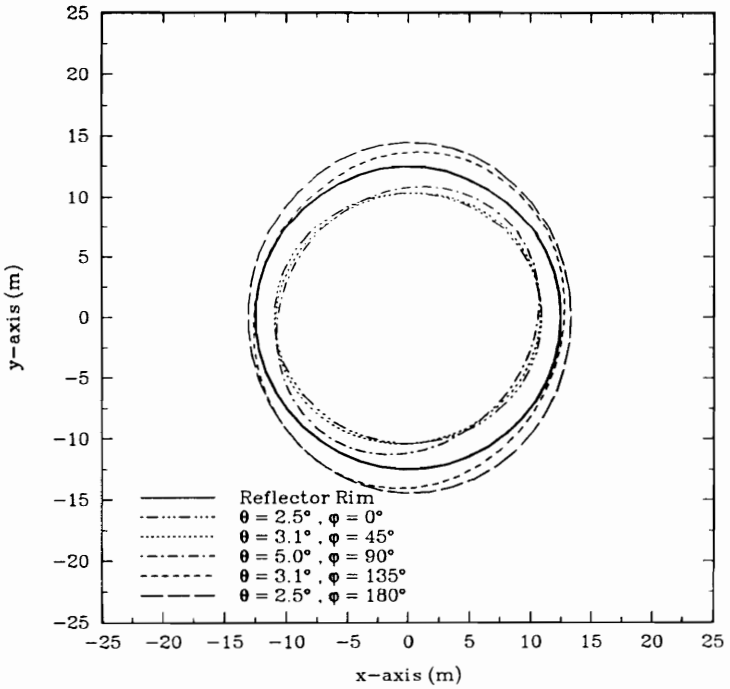

Figure 7.2-10. Primary aperture plane vignetting for the Gregorian configuration for the limiting scan directions in (7-1) and tertiary reflector motion constrained to two degrees of rotational freedom about point $P_r = F_2'$.

7.2.2 Scan Performance for Two Degrees of Rotational Freedom and Three Degrees of Translational Freedom

Scan performance was calculated with the tertiary reflector allowed two degrees of rotational freedom and three degrees of translation freedom with the maximum linear translation constrained to 0.25 m. Motion optimization was performed with $P_r = F_2'$ and $T_{max} = 0.25$ m as discussed in Chapter 6. Calculated values for motion parameters α, β, and $\vec{T}$ are plotted versus scan angle θ for the five values of ϕ indicated in (7.1) in Figs. 7.2-11 - 7.2-15. The corresponding values of the normalized aperture diameter d/λ and primary reflector area efficiency η_a are plotted versus θ in Figs. 7.2-16 and 7.2-17. The results of the above performance calculations for the limiting scan directions in (7-1) are summarized on Table 7.2-3.

Table 7.2-3

Gregorian Performance Results

Five Degrees of Tertiary Reflector Motion $(\alpha, \beta, \vec{T})$

$P_r = F_2'$, $T_{max} = 0.25$

ϕ (deg)	θ (deg)	α (deg)	β (deg)	T_x (m)	T_y (m)	T_z (m)	d/λ	η_a
0	2.5	8.51	0.0	0.247	0.0	0.037	211	0.83
45	3.1	8.08	-6.87	0.25	0.0	0.0	215	0.83
90	5.0	4.61	-17.74	0.25	0.0	0.0	350	0.85
135	3.1	-8.80	-10.45	-0.04	0.015	-0.247	322	0.88
180	2.5	-10.14	0.0	0.25	0.0	0.0	248	0.88

The highest frequency for which this configuration can operate over the entire scan range with less than 1 dB of gain loss due to scan induced phase errors is that for which $d/\lambda = 211$. For the 25 m aperture this corresponds to a maximum operating frequency of $f_M = 2.53$ GHz. Figure 7.2-18 shows vignetting at the primary aperture plane for the limiting scan directions. A small increase in vignetting is observed as a result of allowing tertiary reflector translation.

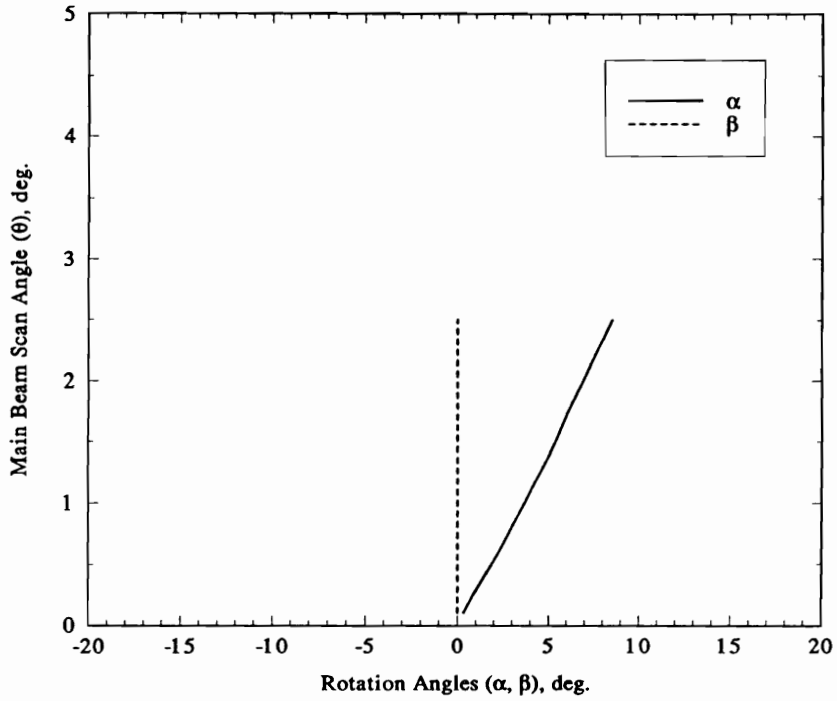

(a)

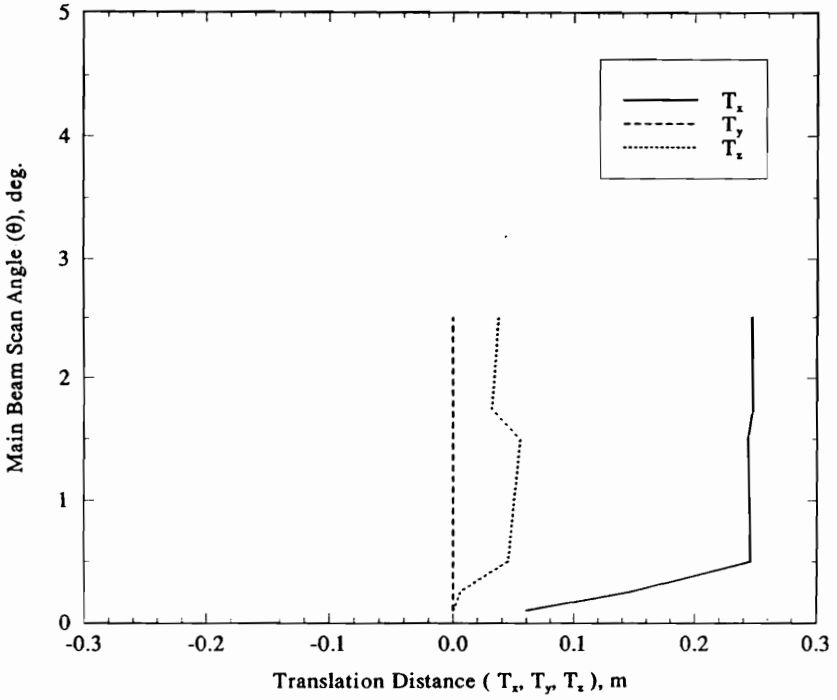

(b)

Figure 7.2-11. Gregorian configuration tertiary reflector rotation angles α and β and translation distances T_x, T_y and T_z used to scan the main beam over the range $\theta = 0.1°$-$2.5°$ with $\phi = 0.0°$. (a) Rotation angles. (b) Translation distances.

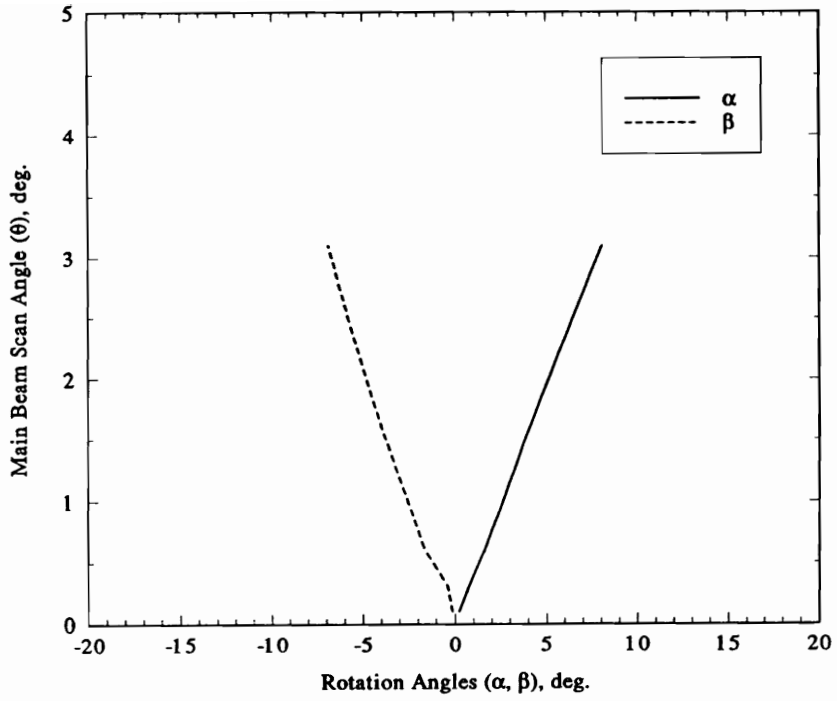

(a)

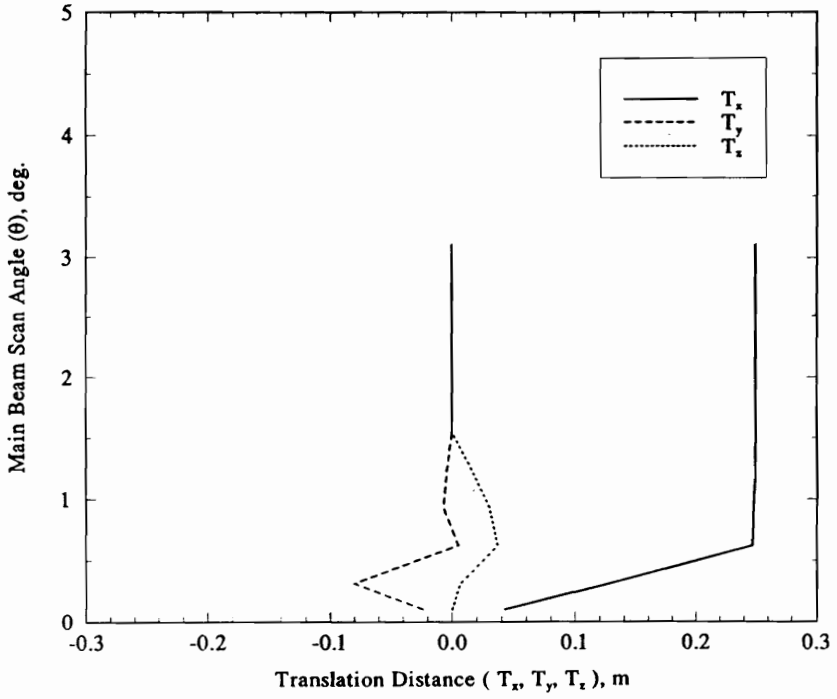

(b)

Figure 7.2-12. Gregorian configuration tertiary reflector rotation angles α and β and translation distances T_x, T_y and T_z used to scan the main beam over the range $\theta = 0.1°$-$3.1°$ with $\phi = 45.0°$. (a) Rotation angles. (b) Translation distances.

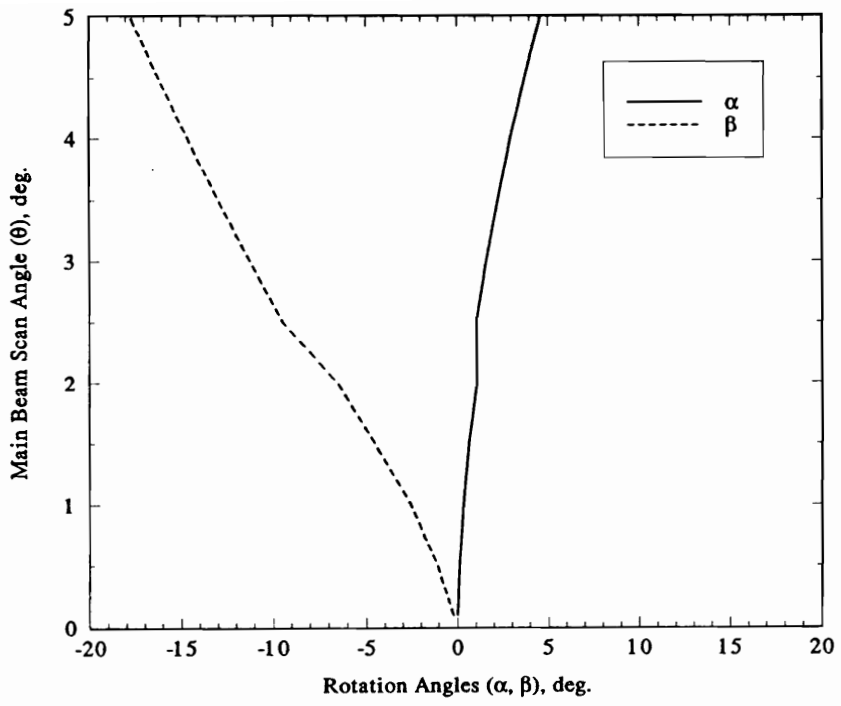

(a)

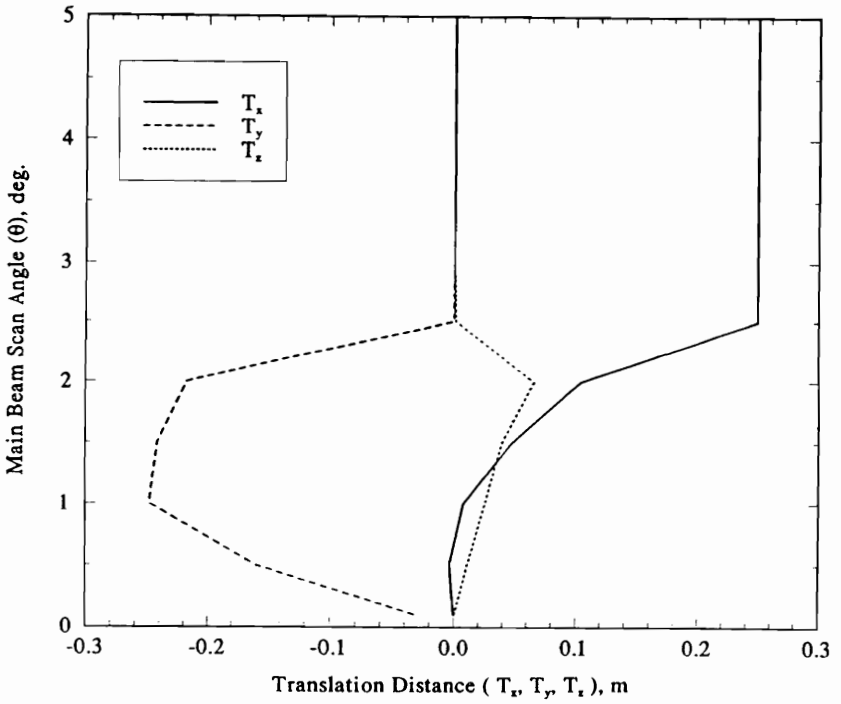

(b)

Figure 7.2-13. Gregorian configuration tertiary reflector rotation angles α and β and translation distances T_x, T_y and T_z used to scan the main beam over the range $\theta = 0.1°$-$5.0°$ with $\phi = 90.0°$. (a) Rotation angles. (b) Translation distances.

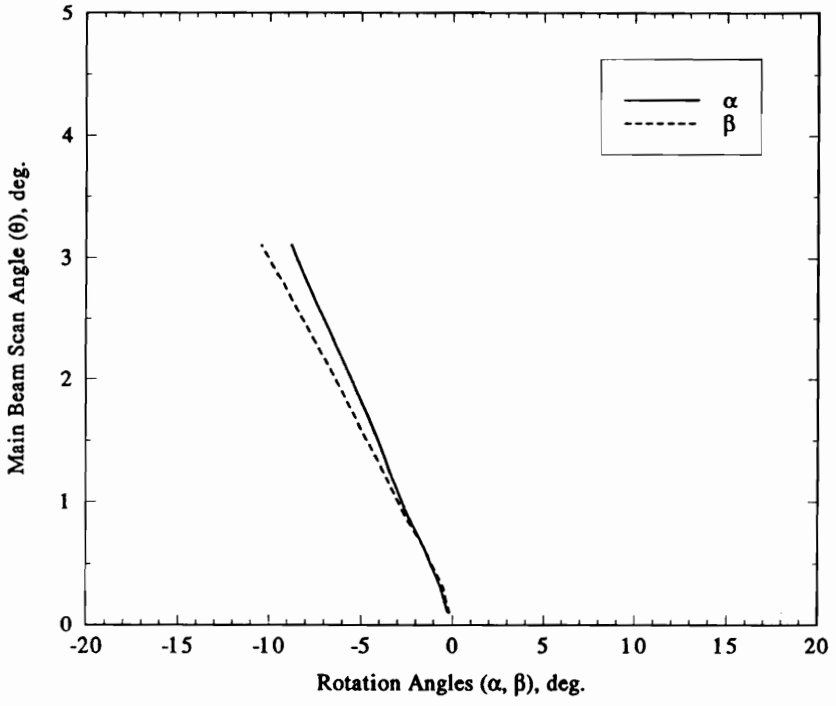

(a)

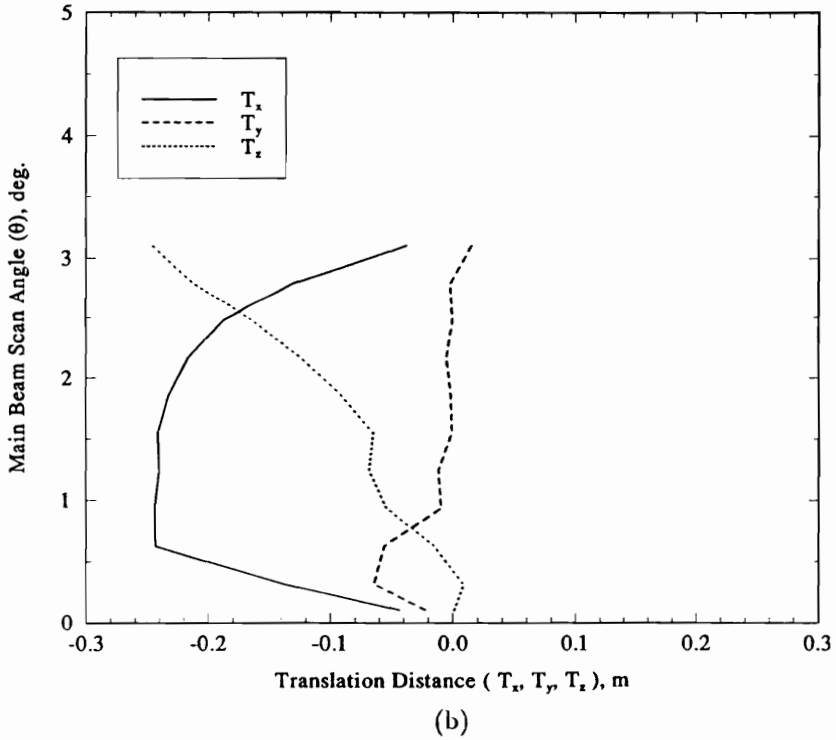

(b)

Figure 7.2-14. Gregorian configuration tertiary reflector rotation angles α and β and translation distances T_x, T_y and T_z used to scan the main beam over the range $\theta = 0.1°$-$3.1°$ with $\phi = 135.0°$. (a) Rotation angles. (b) Translation distances.

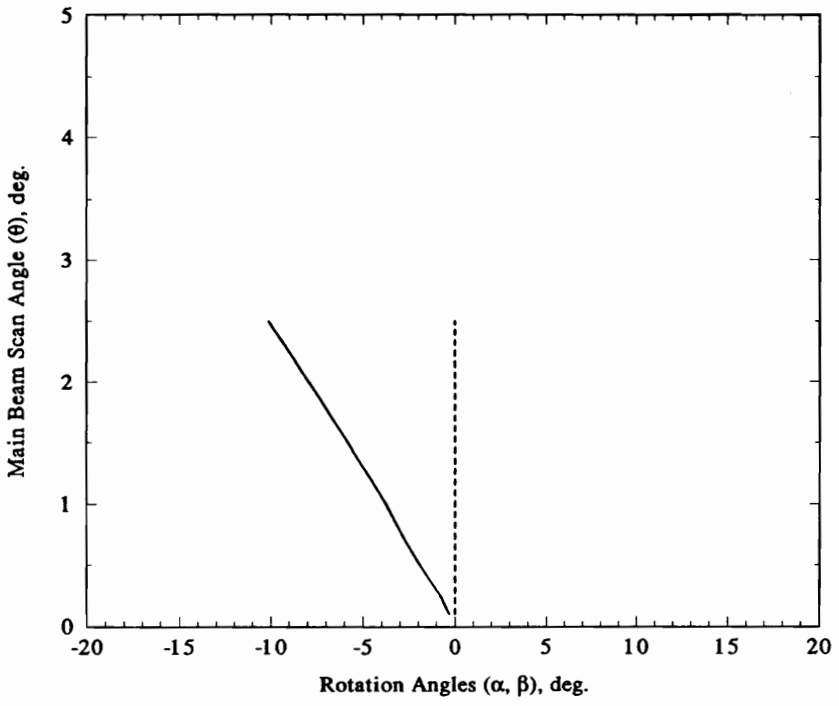

(a)

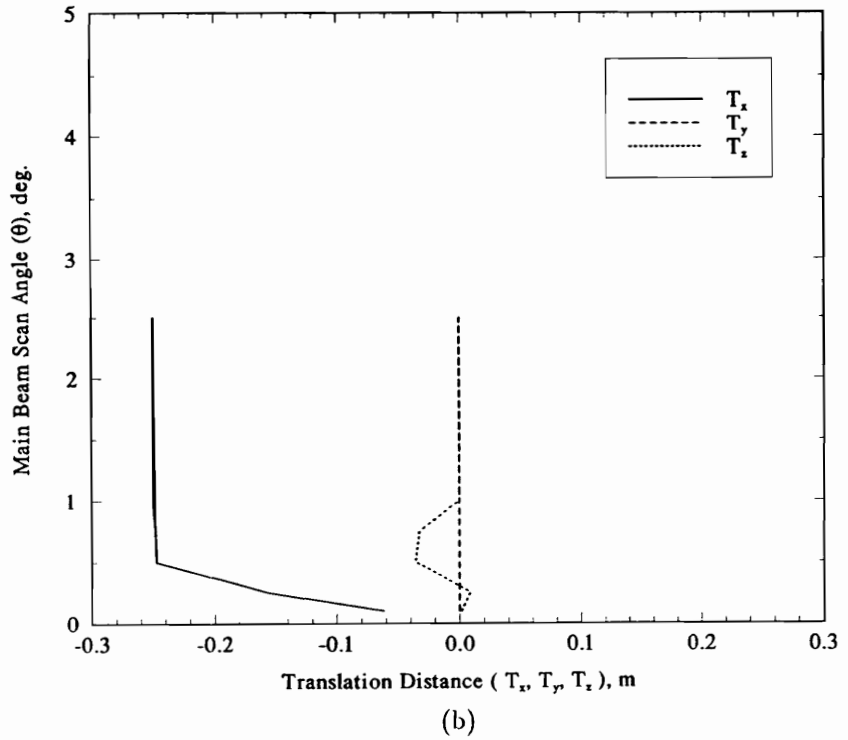

(b)

Figure 7.2-15. Gregorian configuration tertiary reflector rotation angles α and β and translation distances T_x, T_y and T_z used to scan the main beam over the range $\theta = 0.1°$-$2.5°$ with $\phi = 180.0°$. (a) Rotation angles. (b) Translation distances.

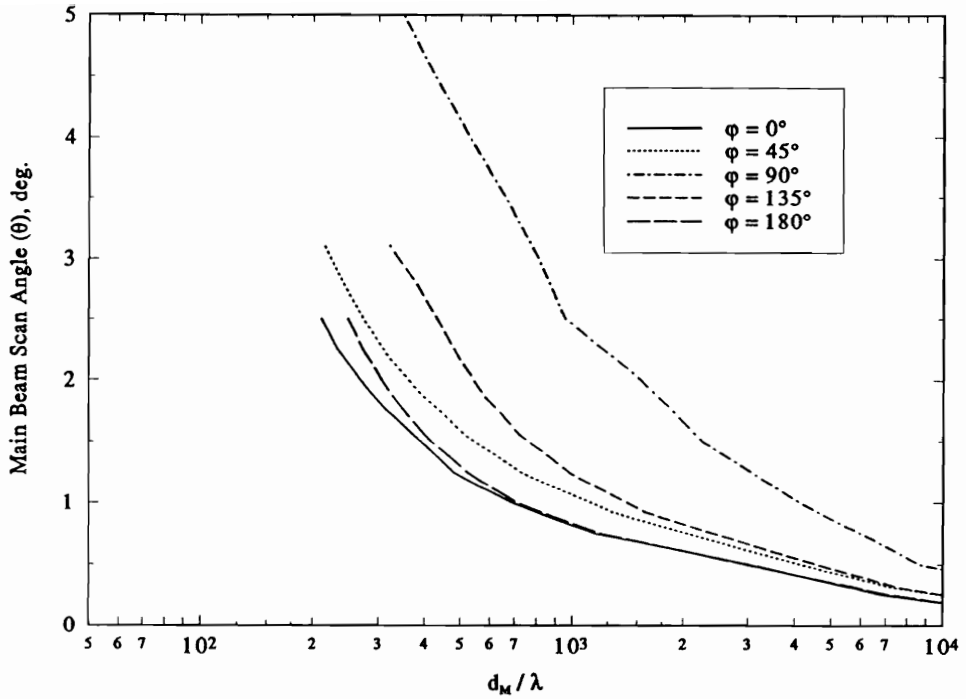

Figure 7.2-16 Normalized aperture diameter d/λ for the Gregorian configuration subject to 1 dB maximum gain loss due to scan induced phase errors. Tertiary reflector motion is allowed two degrees of rotational freedom and three degrees of translational freedom. The scan range is given by (7-1).

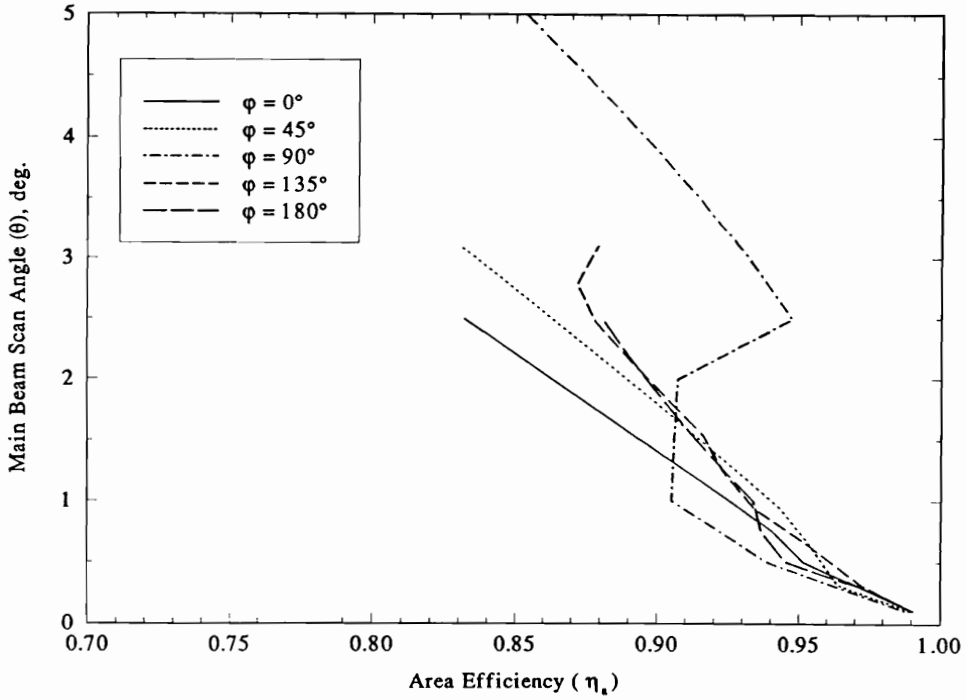

Figure 7.2-17. Primary aperture area efficiency η_a for the Gregorian configuration. Tertiary reflector motion is allowed two degrees of rotational freedom and three degrees of translational freedom. The scan range is given by (7-1).

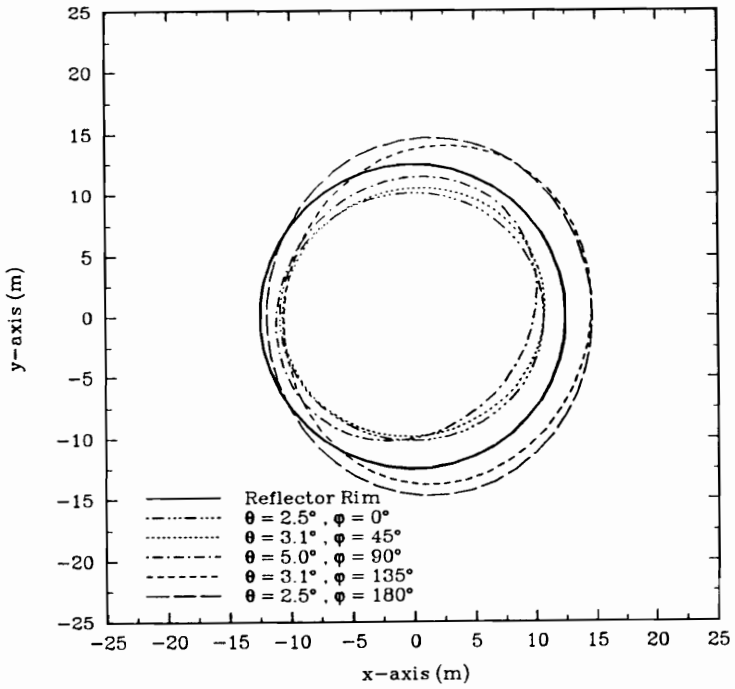

Figure 7.2-18. Primary aperture plane vignetting for the Gregorian configuration for the limiting scan directions in (7-1) and tertiary reflector motion allowed two degrees of rotational freedom and three degrees of translational freedom.

7.3 The Cassegrain II Configuration

The cross-section of an example Cassegrain II configuration is shown in Fig. 7.3-1. This configuration is referred to as Cassegrain because the secondary reflector surface is placed between the primary reflector surface and the primary reflector focal point F_1. Also shown in Fig. 7.3-1 are ray paths for rays striking the top, center and bottom of the primary reflector for scan angles of $\phi = 0^\circ$ and $\theta = 2.5^\circ$, 0° and -2.5°. To create Fig. 7.3-1 a separate tertiary reflector was synthesized for each scan direction using the procedure described in Sec. 6.3. Different line types have been used to indicate the portion of the secondary reflector illuminated for each scan direction. The synthesis parameter values used are shown on Table 7.3-1. These parameters are defined on Table 6.3-1 and shown in Fig. 6.3-1.

Table 7.3-1
Synthesis Parameter Values used for
Cassegrain II Configuration Synthesis

Parameter	Value (m)
P_s	$(28.12, 0.0, 4.69)$ †
F_1	$(0.0, 0.0, 42.19)$ †
x_c	28.12
d	25.0
F_2	$(28.12, 0.0, 4.69)$ †
F_2'	$(9.37, 0.0, 39.37)$ †
e_r	51.52
F	$(0.625, 0.0, 35.0)$ †

† indicates values in xyz-coordinate system

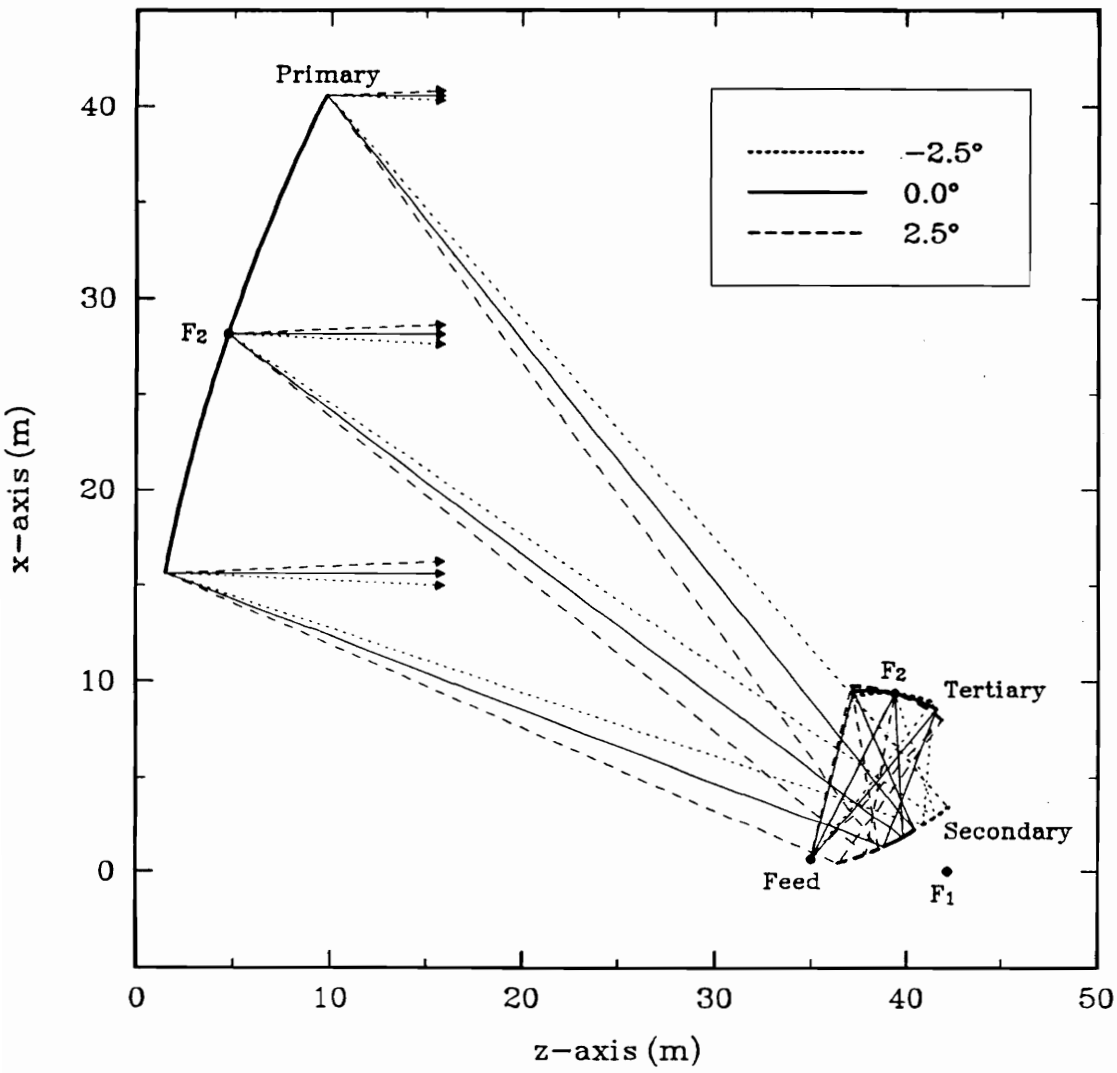

Figure 7.3-1. Cross-section of an example Cassegrain II tri-reflector configuration. Ray paths are shown for rays striking the top, center and bottom of the primary reflector for scan angles of $\phi = 0°$ and $\theta = 2.5°$, $0°$ and $-2.5°$.

Front and side views of the Cassegrain II configuration are shown in Fig. 7.3-2. The tertiary reflector shown in this figure was synthesized with $\theta_s = 0.0^\circ$ and $\phi_s = 0.0^\circ$. The primary reflector has an offset height of $H = 15.625$ m (see Fig. 4.1-9) and an F/D value of 1.69. The xy-plane projected area of the primary reflector is $A_p = 490.9$ m^2. The secondary reflector is oversized such that there is no spillover for the scan range defined by (7-1). The secondary reflector rim is an ellipse with a major axis of $2a_2 = 9.87$ m and a minor axis of $2b_2 = 6.52$ m. The projected aperture area of the secondary reflector, as approximated by $A_s \simeq \pi a_2 b_2$, is 50.58 m^2, which is 10.3 % of the primary aperture area. The tertiary reflector rim is an ellipse with a major axis of $2a_3 = 4.52$ m and a minor axis of $2b_3 = 4.30$ m. The projected aperture area of the tertiary reflector, as approximated by $A_t \simeq \pi a_3 b_3$, is 15.24 m^2, which is 3.1 % of the primary aperture area. The overall length of the reflector configuration as measured along the z-axis is 42.5 m and the overall height as measured along the x-axis is 40.6 m. For boresight operation the average half angle subtended by the tertiary reflector as viewed from the feed is $\theta'_{ave} = 12.94^\circ$ for which (7-3) yields $q = 67.13$. For a pyramidal horn (7.1-1) yields an aperture dimension of $d_f \simeq 6.97\ \lambda$.

In the following sections the scan performance of the the Cassegrain II conjugate tri-reflector shown in Fig. 7.3-2 is investigated using the G.O. techniques developed in Chapter 6. Beam scanning is accomplished entirely by tertiary reflector motion. Four cases of tertiary reflector motion are considered: two degrees of rotational freedom about point F'_2; two degrees of rotational freedom and three degrees of translational freedom; two degrees of rotational freedom and one degree of translational freedom; and two degrees of rotational freedom about an optimum rotation point. These cases are presented in Secs. 7.3.1, 7.3.2, 7.3.3 and 7.3.4, respectively. It is noted that the tertiary reflector was synthesized with $\theta_s = 0.0^\circ$ and $\phi_s = 0.0^\circ$ and, therefore, the aperture is only free of phase errors for boresight operation along the z-axis.

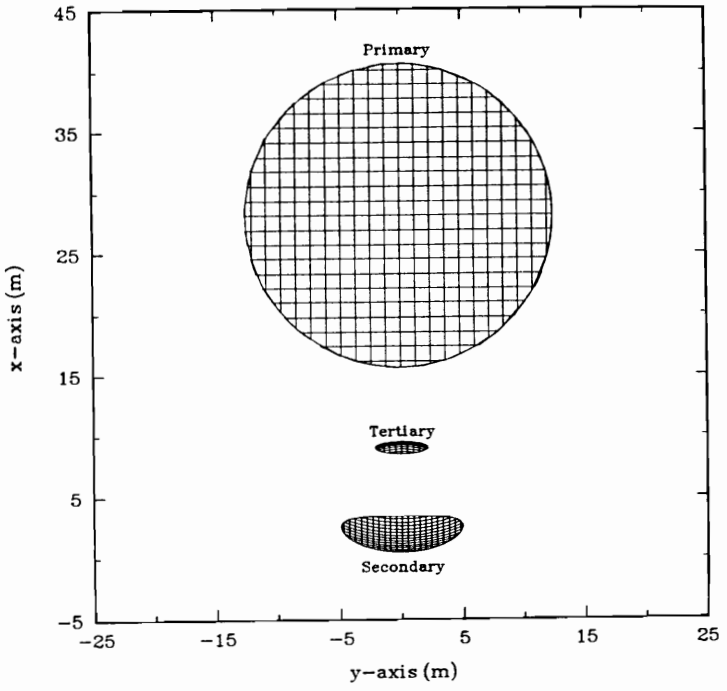

(a)

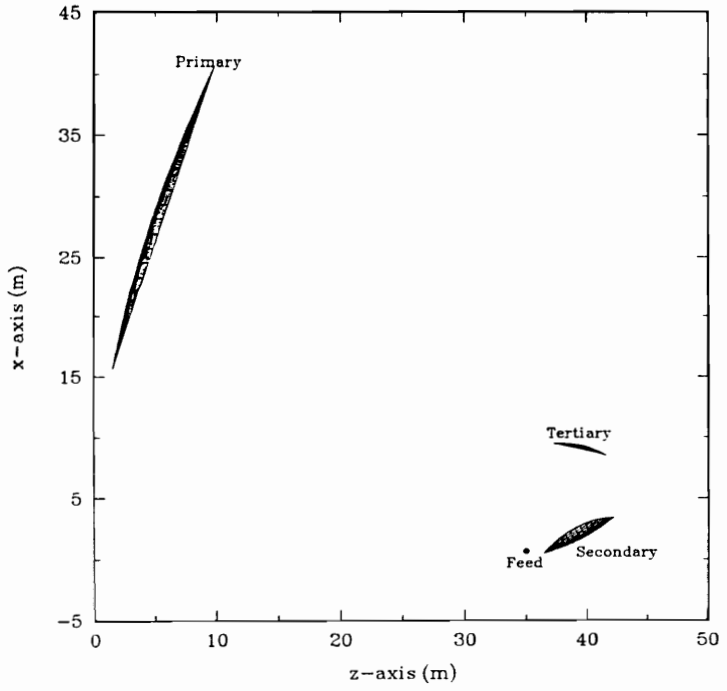

(b)

Figure 7.3-2. Front (a) and side (b) views of the Cassegrain II configuration. The secondary reflector is oversized to allow for beam scanning over an elliptical scan range which subtends $\pm 2.5^{\circ}$ in the xz-plane and $\pm 5^{\circ}$ in the yz-plane (see Fig. 6.2-2)

7.3.1 Scan Performance for Two Degrees of Rotational Freedom About Point F_2'

Scan performance was calculated with the tertiary reflector constrained to two degrees of rotational freedom. Motion optimization was performed with $P_r = F_2'$ and $T_{max} = 0$ as discussed in Chapter 6. Calculated values for motion parameters α and β are plotted versus scan angle θ for the five values of ϕ indicated in (7.1) in Figs. 7.3-3 - 7.3-7. The corresponding values of the normalized aperture diameter d/λ and primary reflector area efficiency η_a are plotted versus θ in Figs. 7.3-8 and 7.3-9. The results of the above performance calculations for the limiting scan directions in (7-1) are summarized on Table 7.3-2.

Table 7.3-2
Cassegrain II Performance Results
Two Degrees of Tertiary Reflector Motion (α, β)
$P_r = F_2'$, $T_{max} = 0$

ϕ (deg)	θ (deg)	α (deg)	β (deg)	d/λ	η_a
0	2.5	6.61	0.0	152	0.86
45	3.1	6.30	-5.59	159	0.87
90	5.0	2.88	-14.24	287	0.91
135	3.1	-5.97	-7.58	413	0.92
180	2.5	-7.68	0.0	344	0.89

The highest frequency for which this configuration can operate over the entire scan range with less than 1 dB of gain loss due to scan induced phase errors is that for which $d/\lambda = 152$. For the 25 m aperture this corresponds to a maximum operating frequency of $f_M = 1.82$ GHz. Figure 7.3-10 shows vignetting at the primary aperture plane for the limiting scan directions. Considerable reduction in vignetting is observed compared to the results obtained for the Cassegrain I and Gregorian configurations.

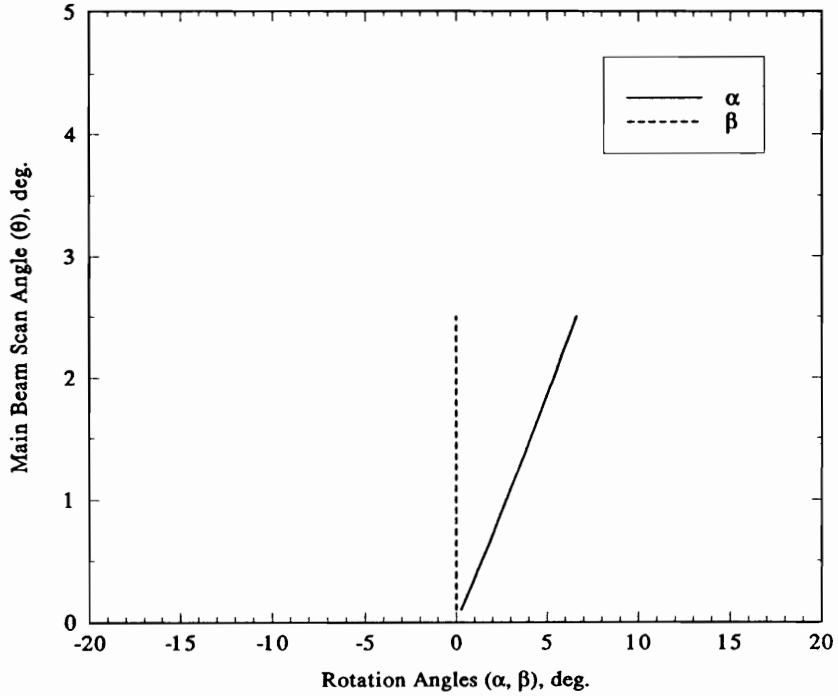

Figure 7.3-3. Cassegrain II configuration tertiary reflector rotation angles α and β used to scan the main beam over the range $\theta = 0.1°$-$2.5°$ with $\phi = 0.0°$.

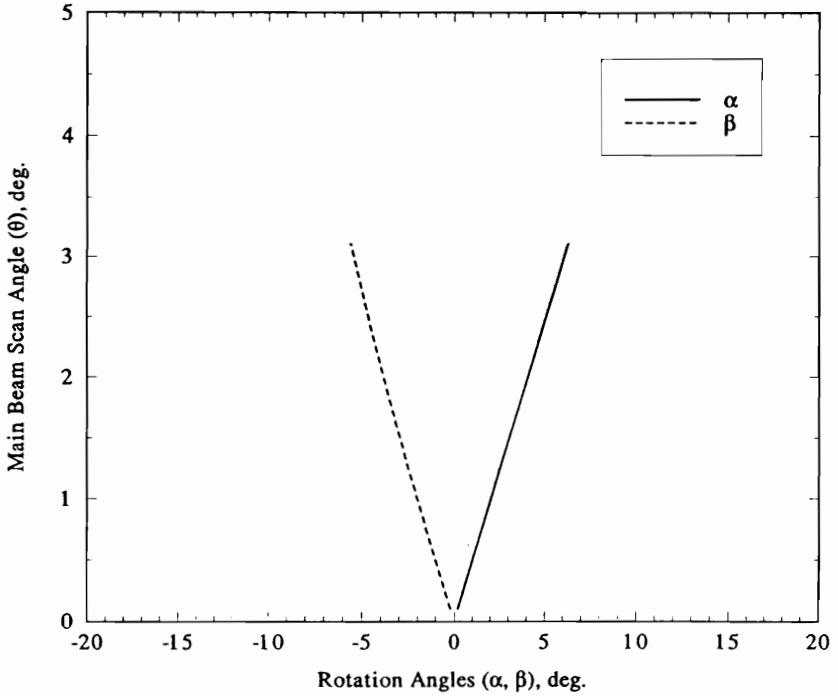

Figure 7.3-4. Cassegrain II configuration tertiary reflector rotation angles α and β used to scan the main beam over the range $\theta = 0.1°$-$3.1°$ with $\phi = 45.0°$.

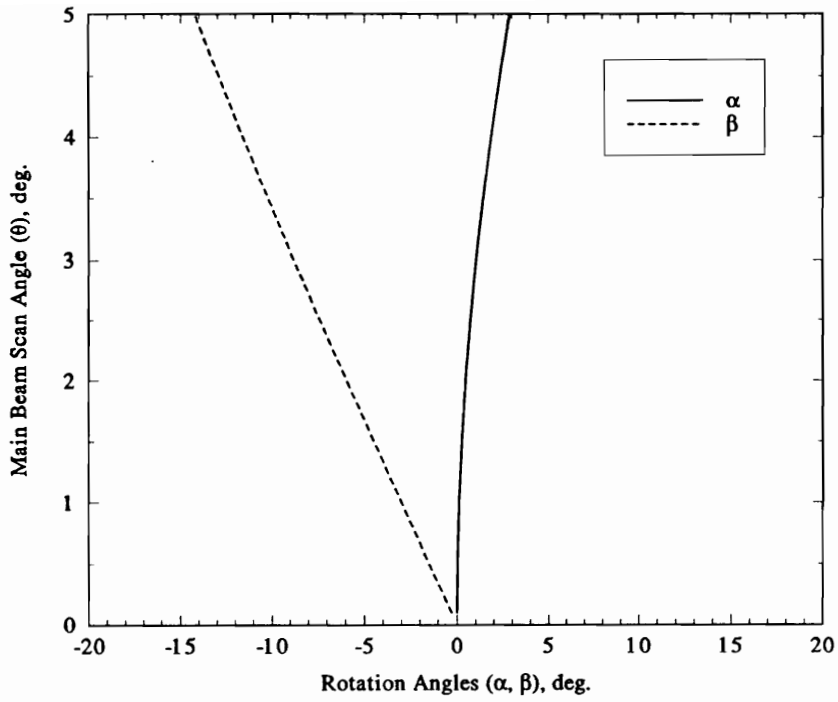

Figure 7.3-5. Cassegrain II configuration tertiary reflector rotation angles α and β used to scan the main beam over the range $\theta = 0.1°$-$5.0°$ with $\phi = 90.0°$.

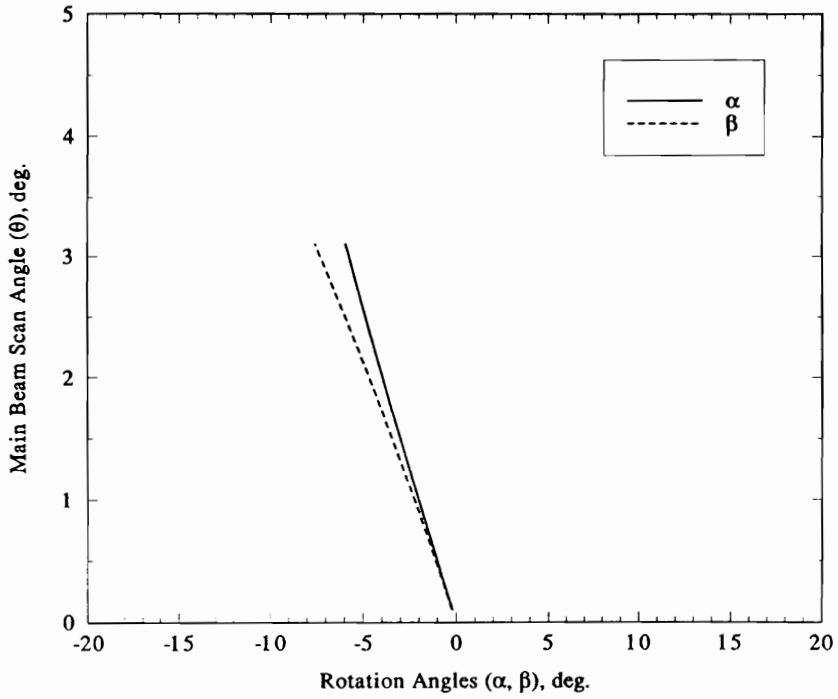

Figure 7.3-6. Cassegrain II configuration tertiary reflector rotation angles α and β used to scan the main beam over the range $\theta = 0.1°$-$3.1°$ with $\phi = 135.0°$.

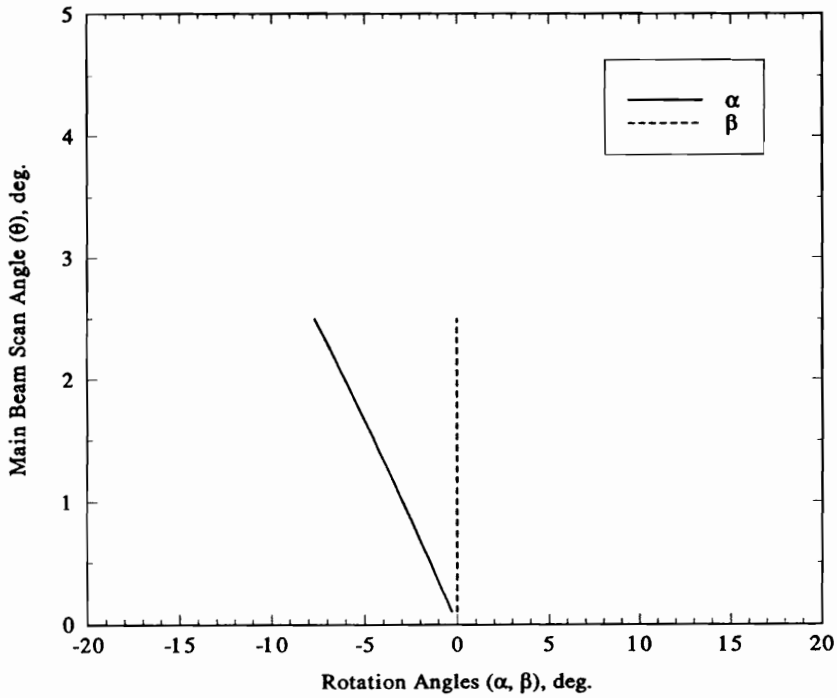

Figure 7.3-7. Cassegrain II configuration tertiary reflector rotation angles α and β used to scan the main beam over the range $\theta = 0.1°$-$2.5°$ with $\phi = 180.0°$.

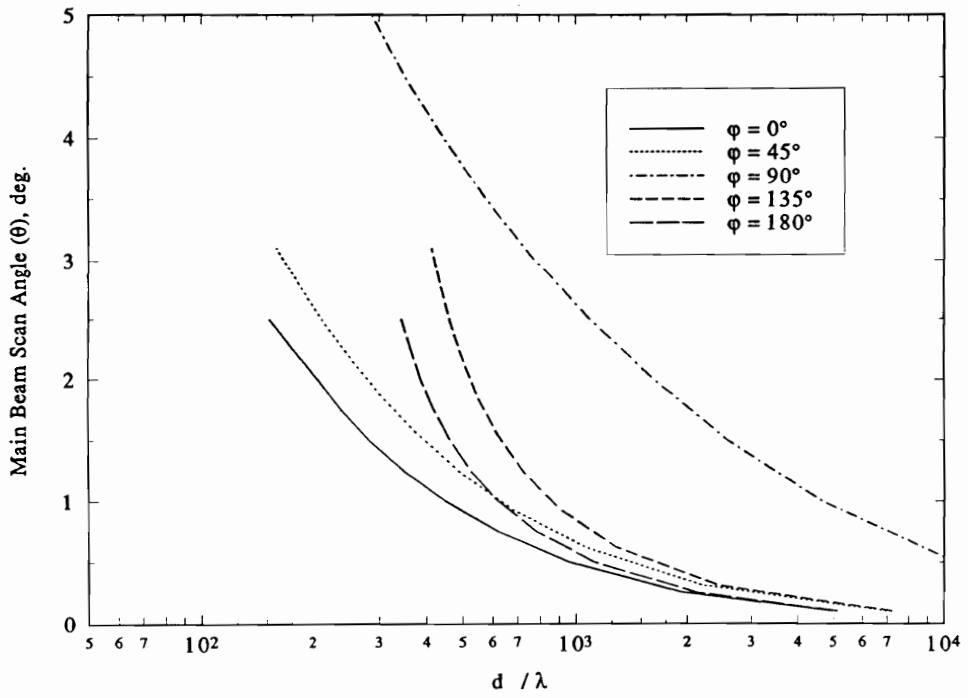

Figure 7.3-8. Normalized aperture diameter d/λ for the Cassegrain II configuration subject to 1 dB maximum gain loss due to scan induced phase errors. Tertiary reflector motion is constrained to two degrees of rotational freedom about the point $P_r = F_2'$. The scan range is given by (7-1).

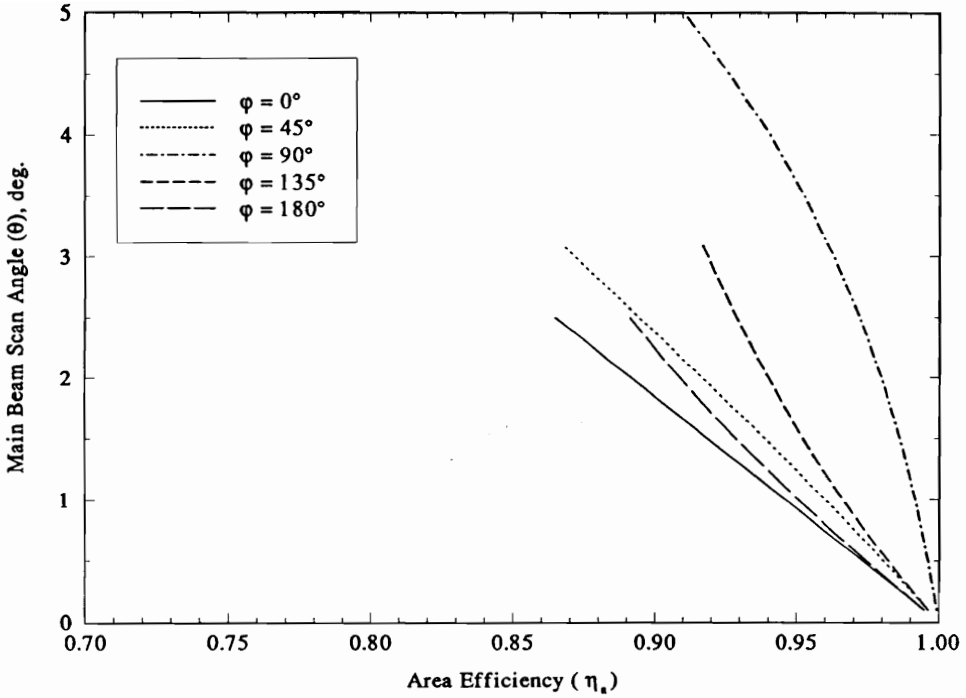

Figure 7.3-9. Primary aperture area efficiency η_a for the Cassegrain II configuration. Tertiary reflector motion is constrained to two degrees of rotational freedom about the point $P_r = F_2'$. The scan range is given by (7-1).

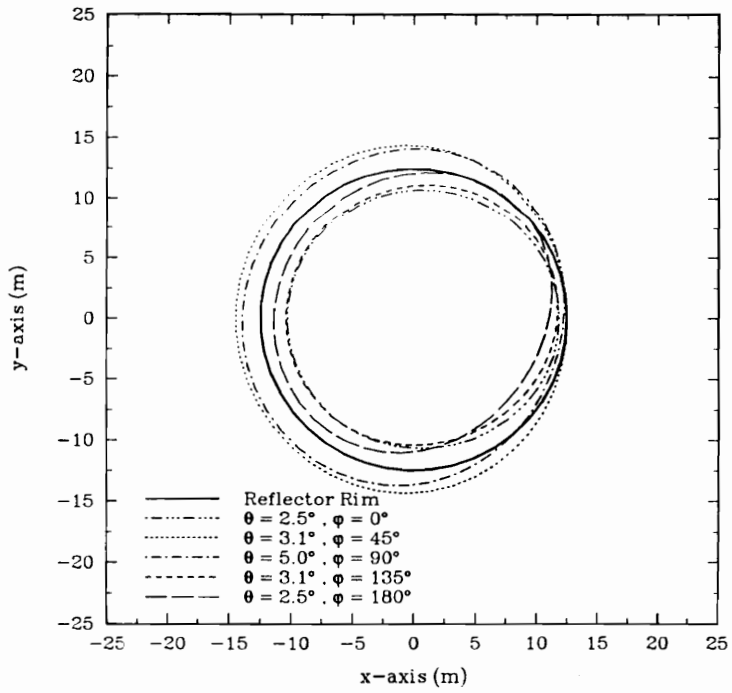

Figure 7.3-10. Primary aperture plane vignetting for the Cassegrain II configuration for the limiting scan directions in (7-1) and tertiary reflector motion constrained to two degrees of rotational freedom about point $P_r = F_2'$.

7.3.2 Scan Performance for Two Degrees of Rotational Freedom and Three Degrees of Translational Freedom

Scan performance was calculated with the tertiary reflector constrained to two degrees of rotational freedom and three degrees of translation freedom with the maximum linear translation constrained to 0.25 m. Motion optimization was performed with $P_r = F_2'$ and $T_{max} = 0.25$ m as discussed in Chapter 6. Calculated values for motion parameters α, β, and $\vec{T}$ are plotted versus scan angle θ for the five values of ϕ indicated in (7.1) in Figs. 7.3-11 - 7.3-15. The corresponding values of the normalized aperture diameter d/λ and primary reflector area efficiency η_a are plotted versus θ in Figs. 7.3-16 and 7.3-17. The results of the above performance calculations for the limiting scan directions in (7-1) are summarized on Table 7.3-3.

Table 7.3-3
Cassegrain II Performance Results
Five Degrees of Tertiary Reflector Motion $(\alpha, \beta, \vec{T})$
$P_r = F_2'$, $T_{max} = 0.25$

ϕ (deg)	θ (deg)	α (deg)	β (deg)	T_x (m)	T_y (m)	T_z (m)	d/λ	η_a
0	2.5	6.56	0.00	-0.23	0.00	-0.08	396	0.91
45	3.1	5.77	-5.63	-0.20	-0.03	-0.14	395	0.91
90	5.0	3.98	-13.86	-0.20	-0.11	0.09	1129	0.94
135	3.1	-6.10	-6.08	0.20	-0.14	-0.01	1779	0.90
180	2.5	-7.49	0.00	0.25	0.00	0.01	2708	0.91

The highest frequency for which this configuration can operate over the entire scan range with less than 1 dB of gain loss due to scan induced phase errors is that for which $d/\lambda = 396$. For the 25 m aperture this corresponds to a maximum operating frequency of $f_M = 4.75$ GHz. Figure 7.3-18 shows vignetting at the primary aperture plane for the limiting scan directions.

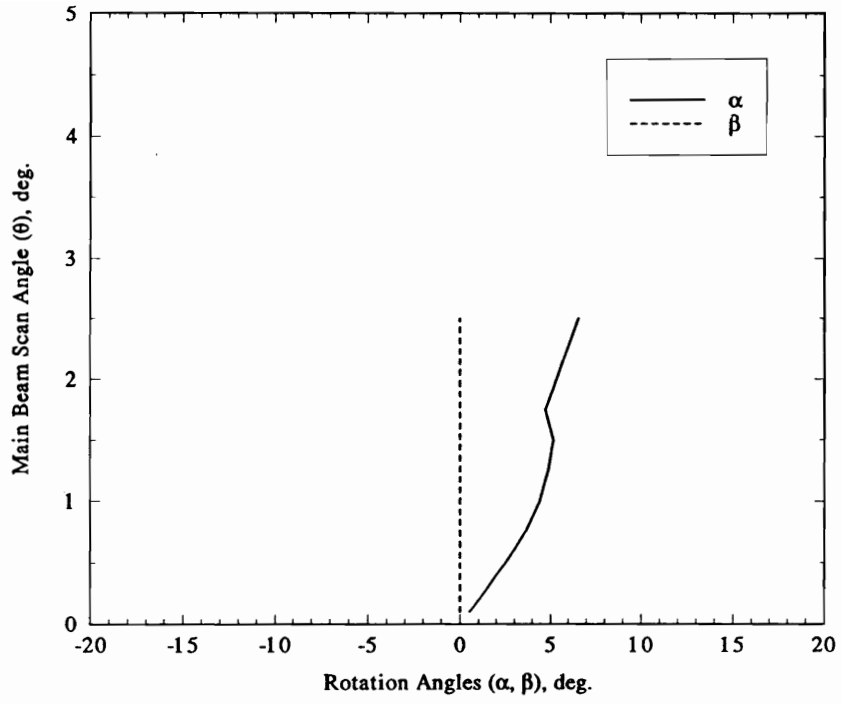

(a)

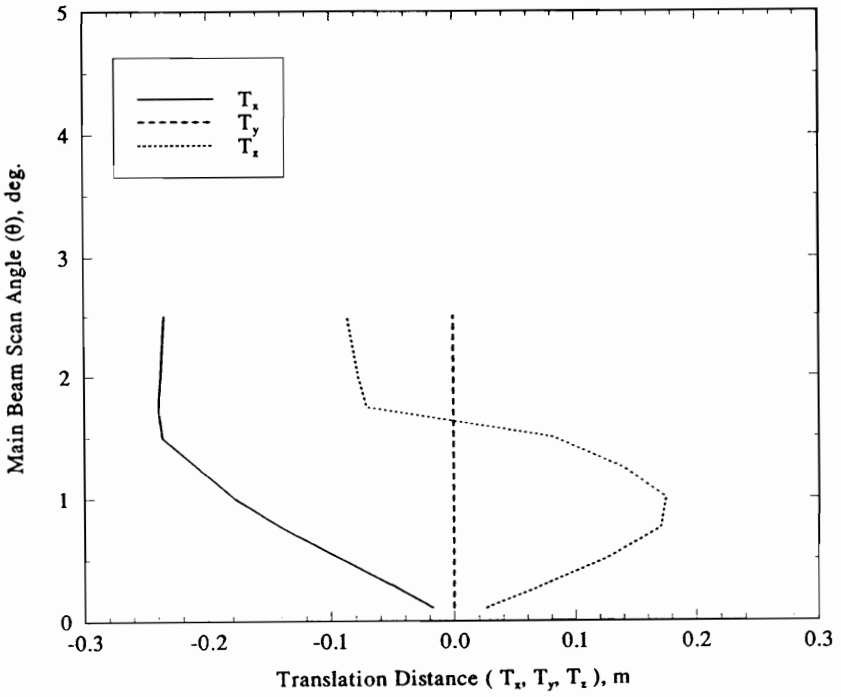

(b)

Figure 7.3-11. Cassegrain II configuration tertiary reflector rotation angles α and β and translation distances T_x, T_y and T_z used to scan the main beam over the range $\theta = 0.1°$-$2.5°$ with $\phi = 0.0°$. (a) Rotation angles. (b) Translation distances.

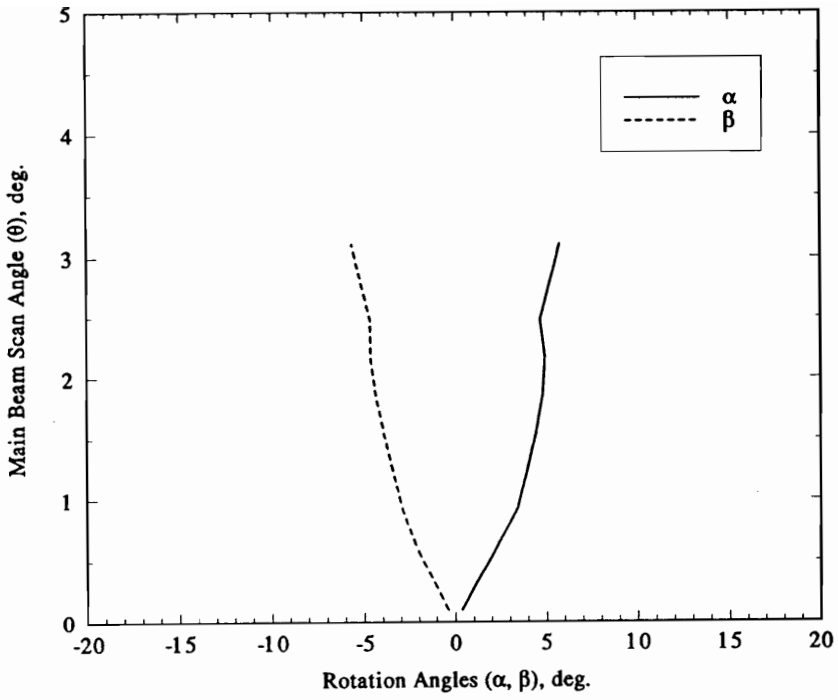

(a)

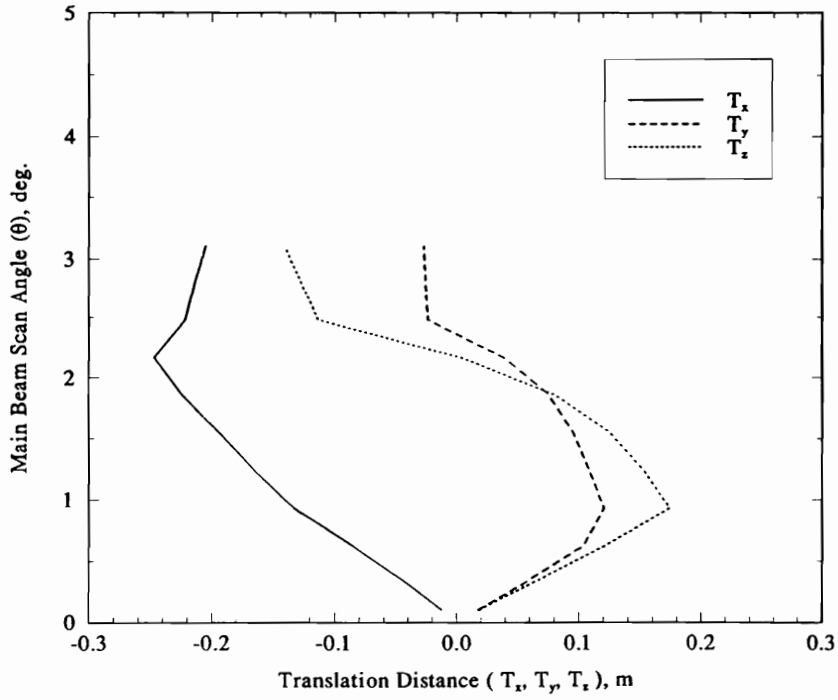

(b)

Figure 7.3-12. Cassegrain II configuration tertiary reflector rotation angles α and β and translation distances T_x, T_y and T_z used to scan the main beam over the range $\theta = 0.1°$-$3.1°$ with $\phi = 45.0°$. (a) Rotation angles. (b) Translation distances.

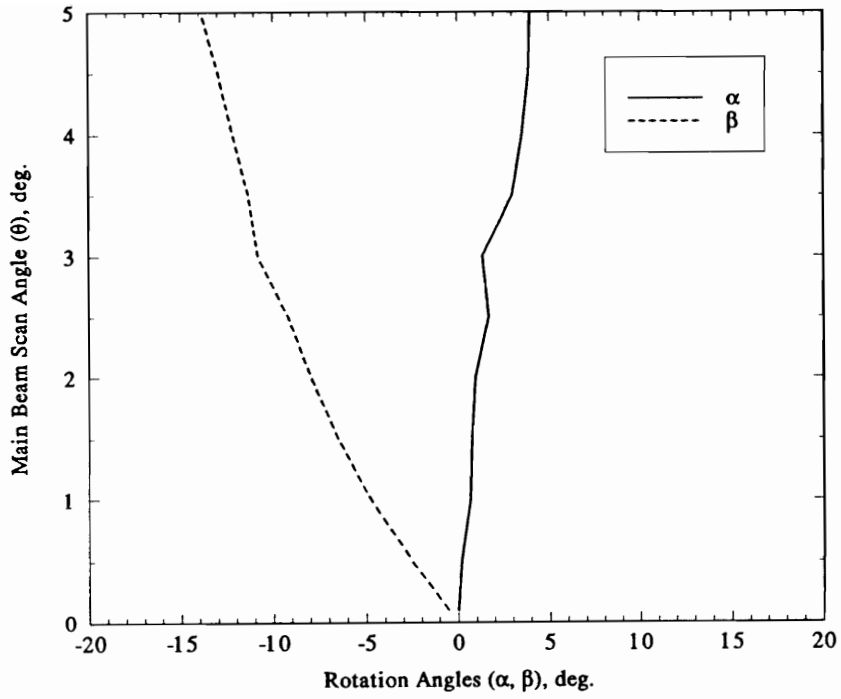

(a)

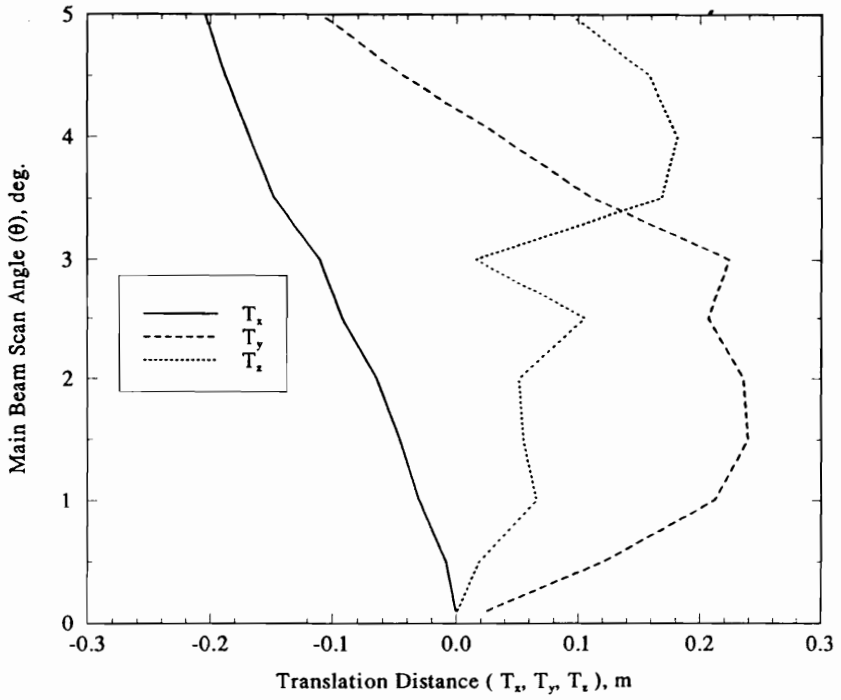

(b)

Figure 7.3-13. Cassegrain II configuration tertiary reflector rotation angles α and β and translation distances T_x, T_y and T_z used to scan the main beam over the range $\theta = 0.1°$-$5.0°$ with $\phi = 90.0°$. (a) Rotation angles. (b) Translation distances.

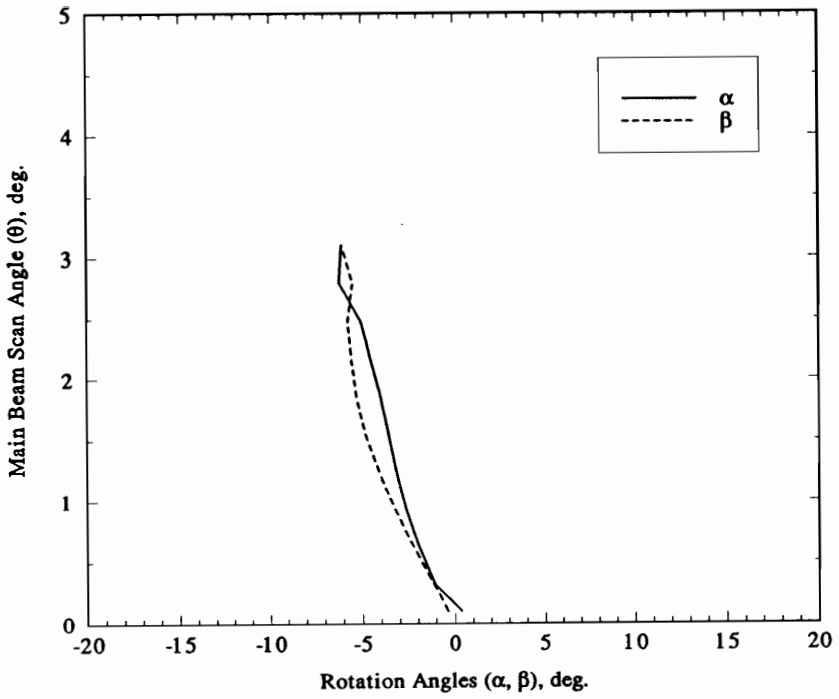

(a)

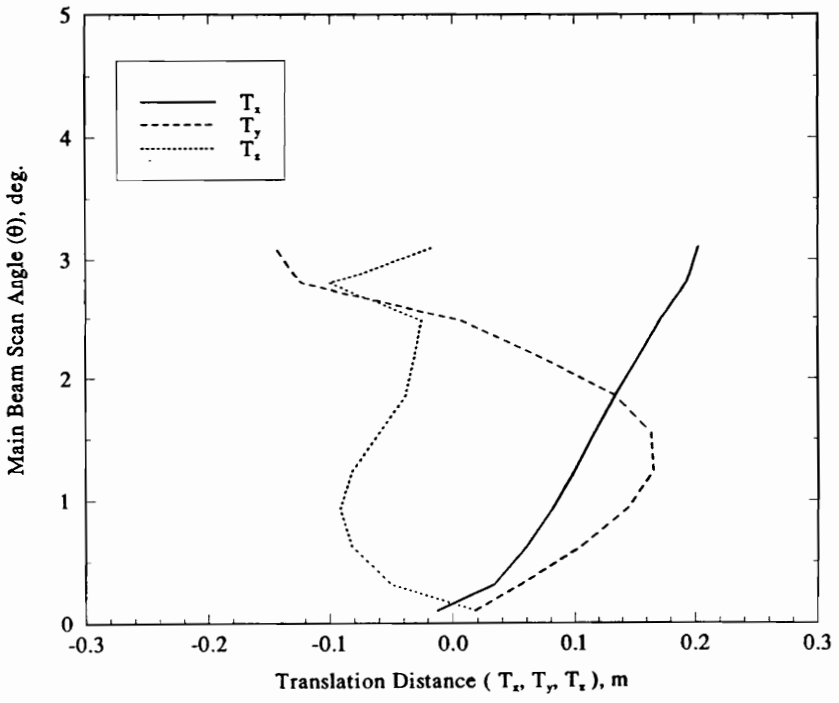

(b)

Figure 7.3-14. Cassegrain II configuration tertiary reflector rotation angles α and β and translation distances T_x, T_y and T_z used to scan the main beam over the range $\theta = 0.1°$-$3.1°$ with $\phi = 135.0°$. (a) Rotation angles. (b) Translation distances.

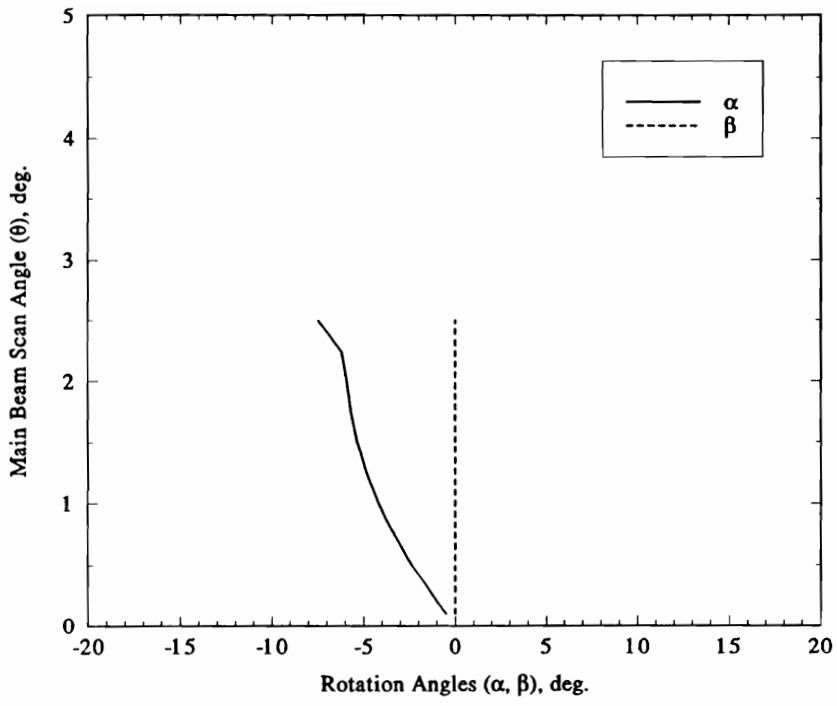

(a)

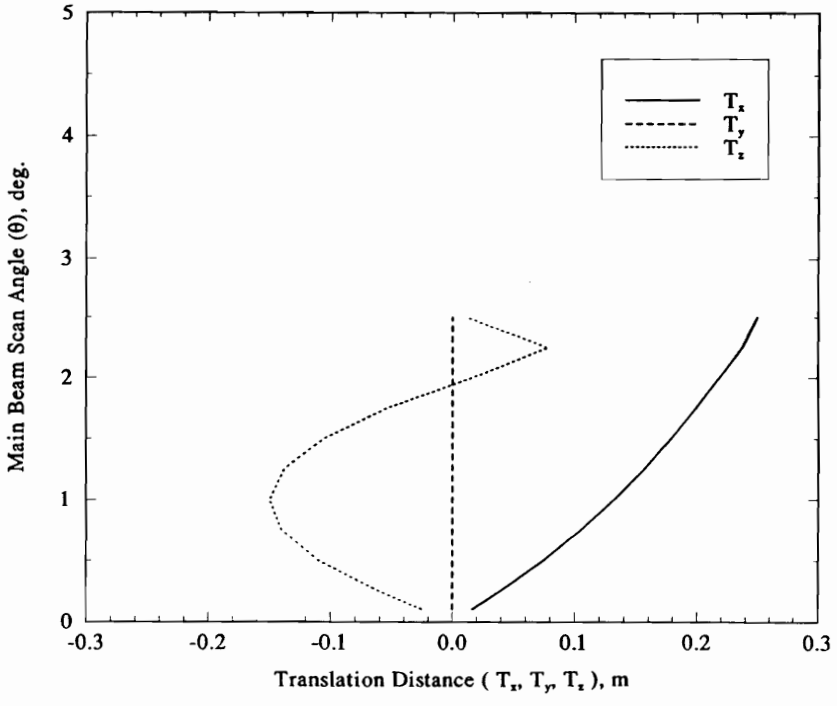

(b)

Figure 7.3-15. Cassegrain II configuration tertiary reflector rotation angles α and β and translation distances T_x, T_y and T_z used to scan the main beam over the range $\theta = 0.1°$-$2.5°$ with $\phi = 180.0°$. (a) Rotation angles. (b) Translation distances.

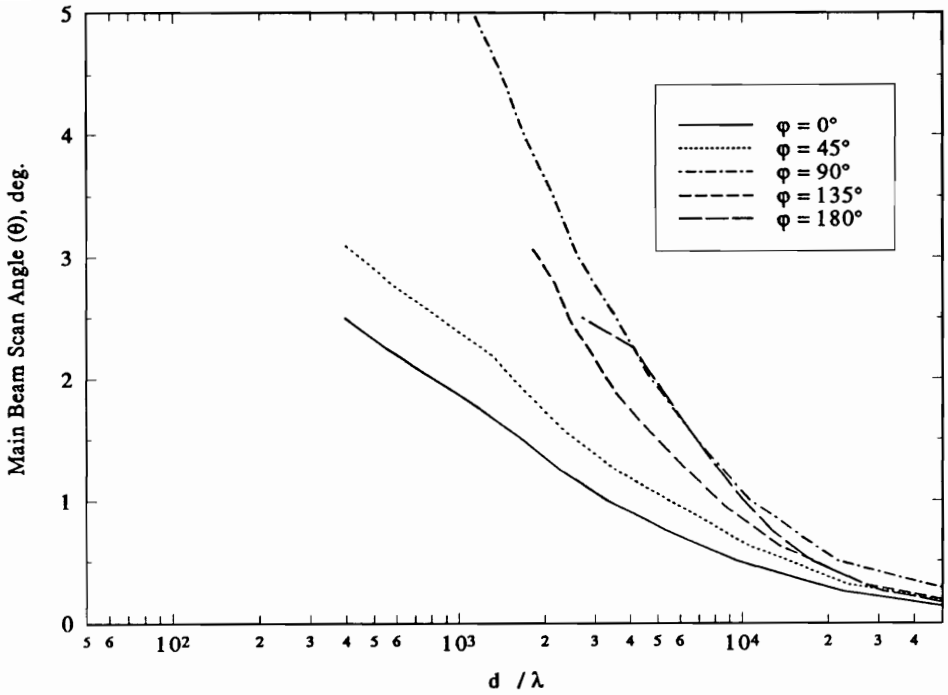

Figure 7.3-16 Normalized aperture diameter d/λ for the Cassegrain II configuration subject to 1 dB maximum gain loss due to scan induced phase errors. Tertiary reflector motion is allowed two degrees of rotational freedom and three degrees of translational freedom. The scan range is given by (7-1).

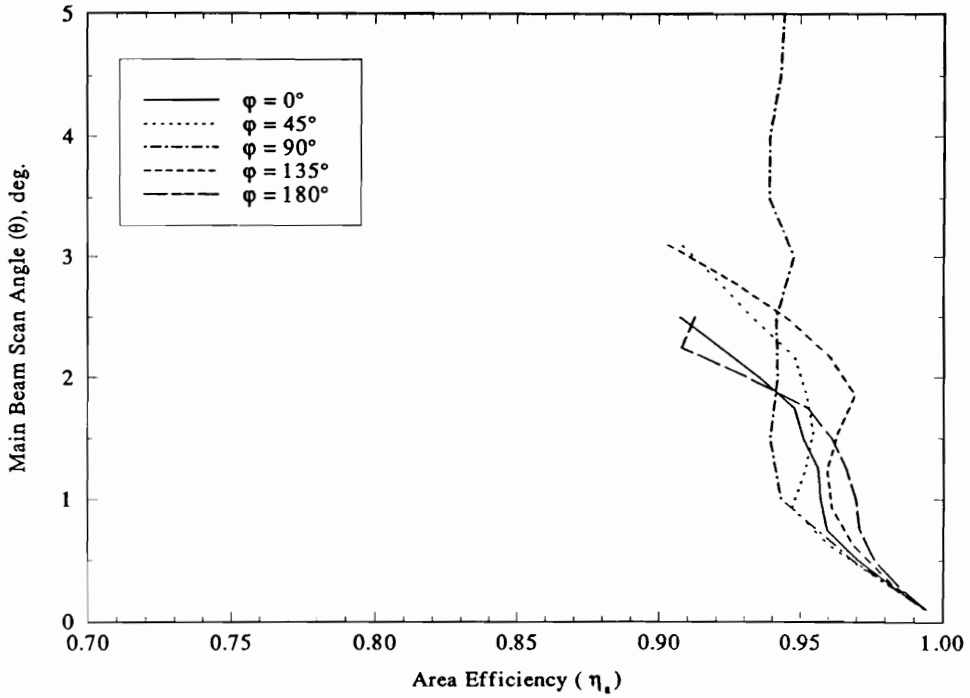

Figure 7.3-17. Primary aperture area efficiency η_a for the Cassegrain II configuration. Tertiary reflector motion is allowed two degrees of rotational freedom and three degrees of translational freedom. The scan range is given by (7-1).

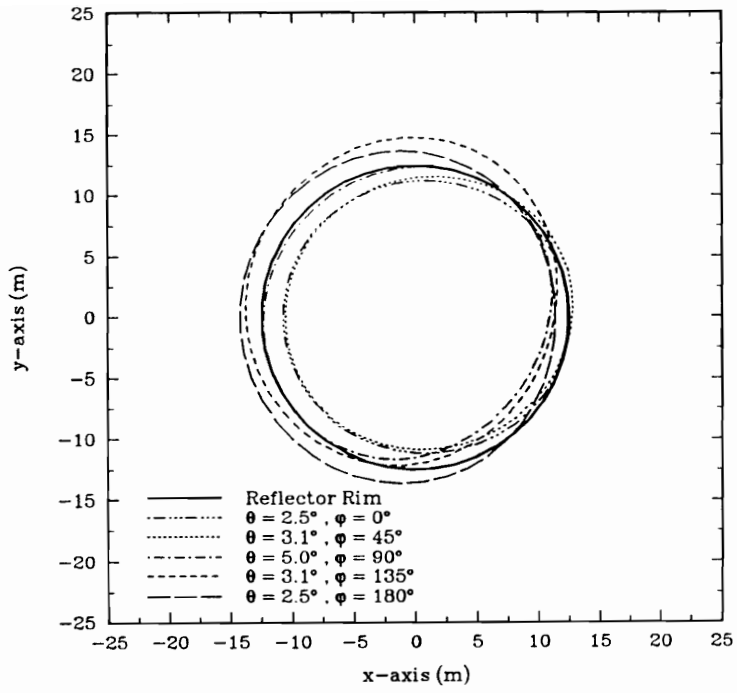

Figure 7.3-18. Primary aperture plane vignetting for the Cassegrain II configuration for the limiting scan directions in (7-1) and tertiary reflector motion allowed two degrees of rotational freedom and three degrees of translational freedom.

7.3.3 Scan Performance for Two Degrees of Rotational Freedom and One Degree of Translational Freedom

Scan performance was calculated with the tertiary reflector allowed two degrees of rotational freedom and one degree of translational freedom with the maximum translation distance constrained to 0.5 m. Motion optimization was performed with $P_r = F_2'$ and $T_{max} = 0.5$ m as discussed in Chapter 6. The direction of tertiary translation was along the line between the focus point F and the secondary reflector focal point F_2'. The slope of this line is

$$M = \frac{F_{2x}' - F_x}{F_{2z}' - F_z}. \tag{7.3-1}$$

Substitution of the appropriate values from Table 7.3-1 yields $M = 2.0$. Therefore tertiary reflector motion parameters T_x and T_z are related by

$$T_x = 2\,T_z \tag{7.3-2}$$

and $T_y = 0.0$. The distance of tertiary reflector motion is given by the scalar parameter T where

$$T = sign(T_z) \cdot \sqrt{T_x^2 + T_z^2} \tag{7.3-3}$$

and a positive value of T indicates motion away the feed and a negative value indicates motion toward the feed.

Calculated values for motion parameters α, β, and T are plotted versus scan angle θ for the five values of ϕ indicated in (7.1) in Figs. 7.3-19 - 7.3-23. The corresponding values of the normalized aperture diameter d/λ and primary reflector area efficiency η_a are plotted versus θ in Figs. 7.3-24 and 7.3-25. The results of the above performance calculations for the limiting scan directions in (7-1) are summarized on Table 7.3-4.

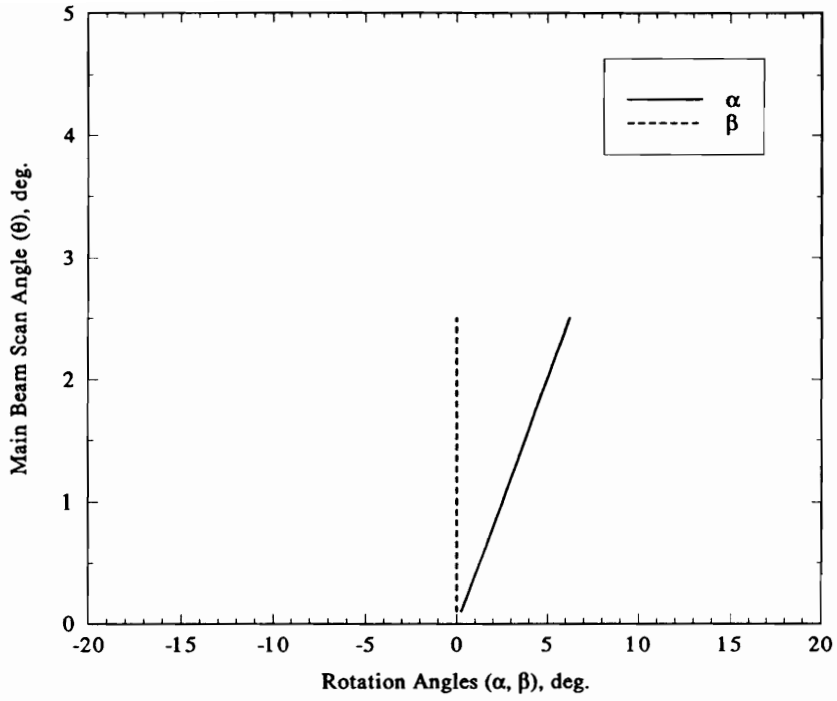

(a)

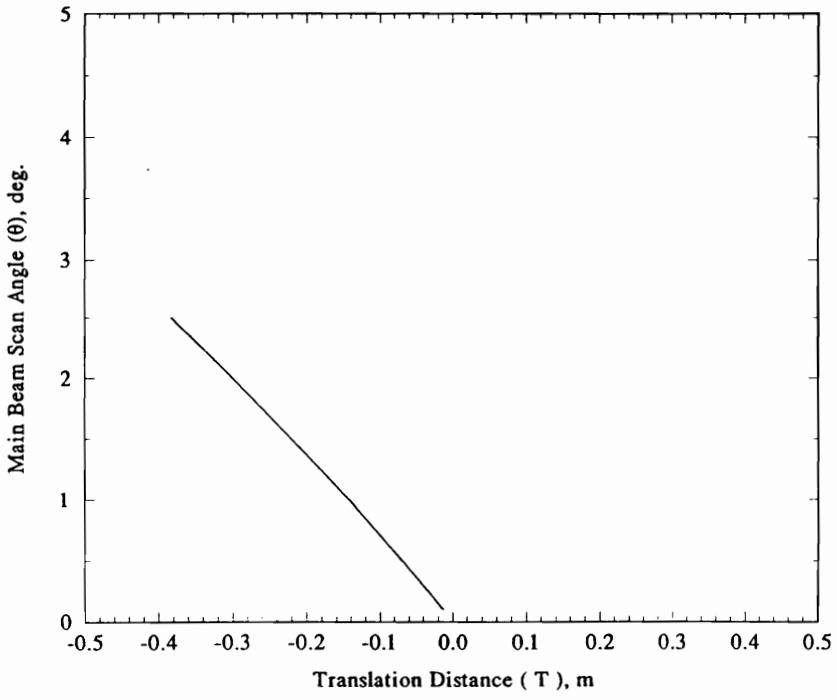

(b)

Figure 7.3-19. Cassegrain II configuration tertiary reflector rotation angles α and β and translation distance T used to scan the main beam over the range $\theta = 0.1°$-$2.5°$ with $\phi = 0.0°$. (a) Rotation angles. (b) Translation distances.

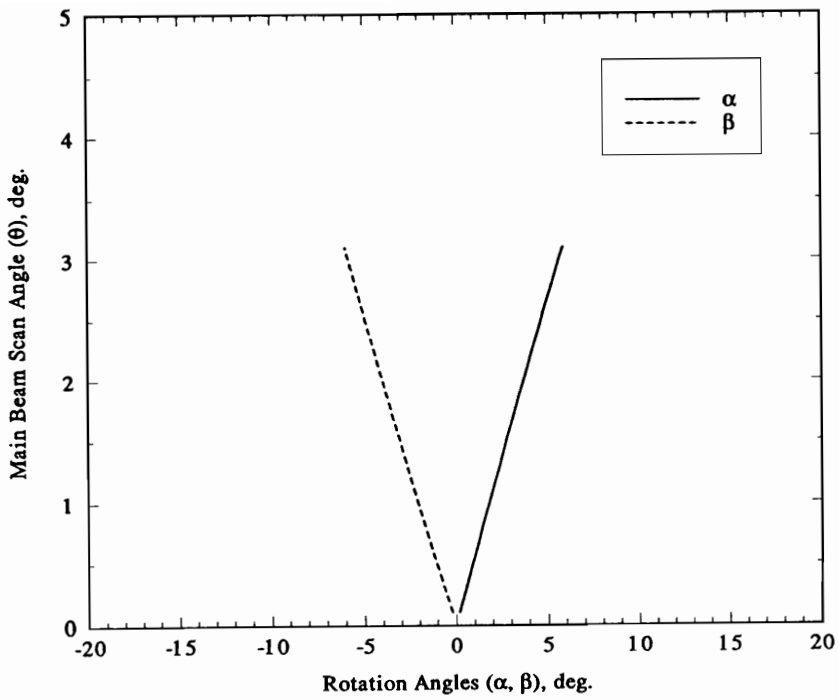

(a)

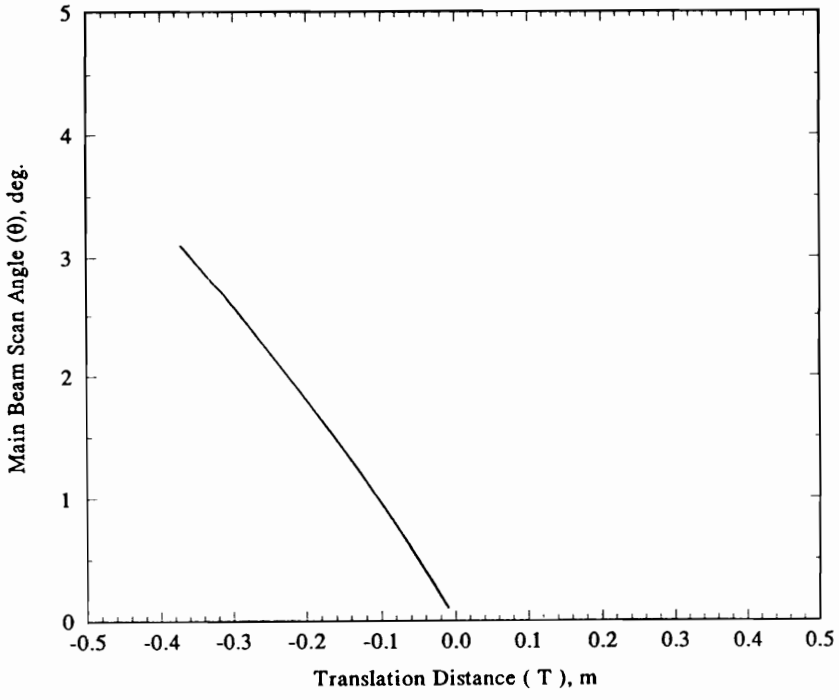

(b)

Figure 7.3-20. Cassegrain II configuration tertiary reflector rotation angles α and β and translation distance T used to scan the main beam over the range $\theta = 0.1°$-$3.1°$ with $\phi = 45.0°$. (a) Rotation angles. (b) Translation distances.

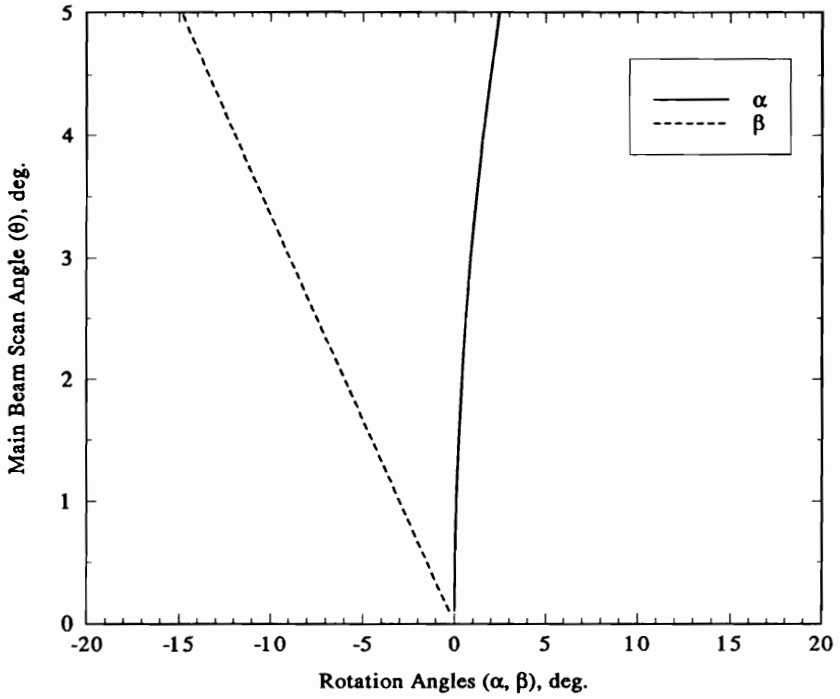

(a)

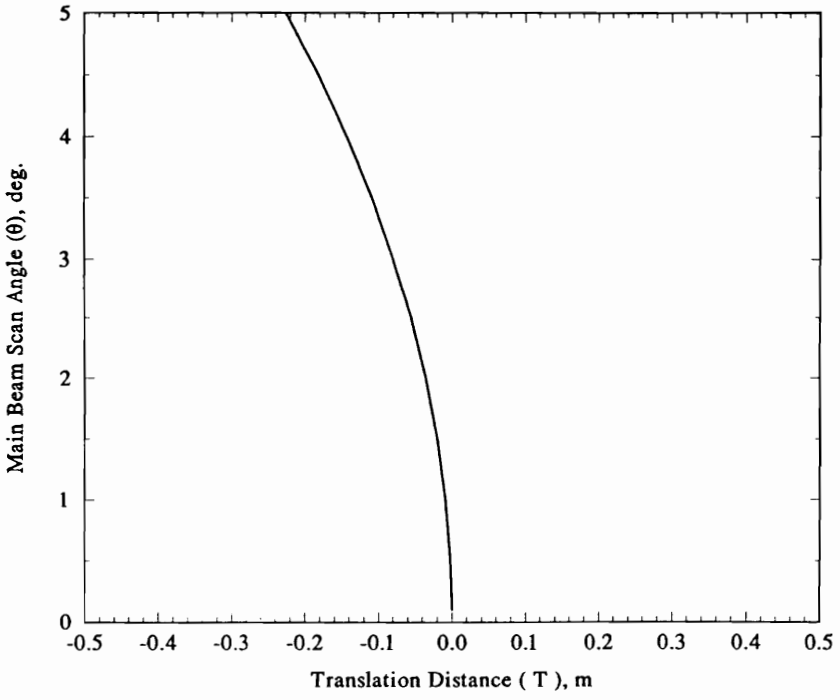

(b)

Figure 7.3-21. Cassegrain II configuration tertiary reflector rotation angles α and β and translation distance T used to scan the main beam over the range $\theta = 0.1°$-$5.0°$ with $\phi = 90.0°$. (a) Rotation angles. (b) Translation distances.

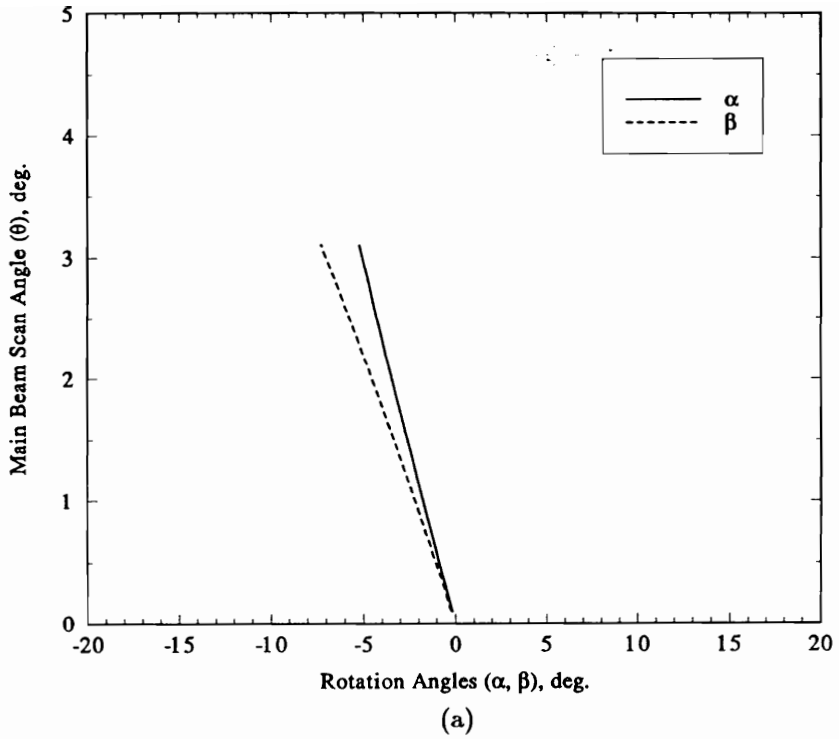

(a)

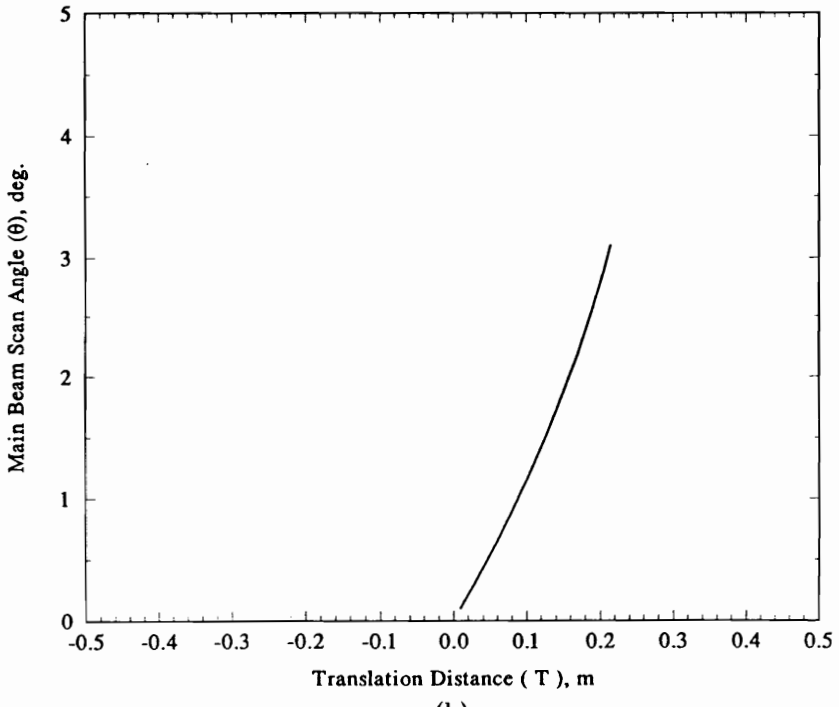

(b)

Figure 7.3-22. Cassegrain II configuration tertiary reflector rotation angles α and β and translation distance T used to scan the main beam over the range $\theta = 0.1°$-$3.1°$ with $\phi = 135.0°$. (a) Rotation angles. (b) Translation distances.

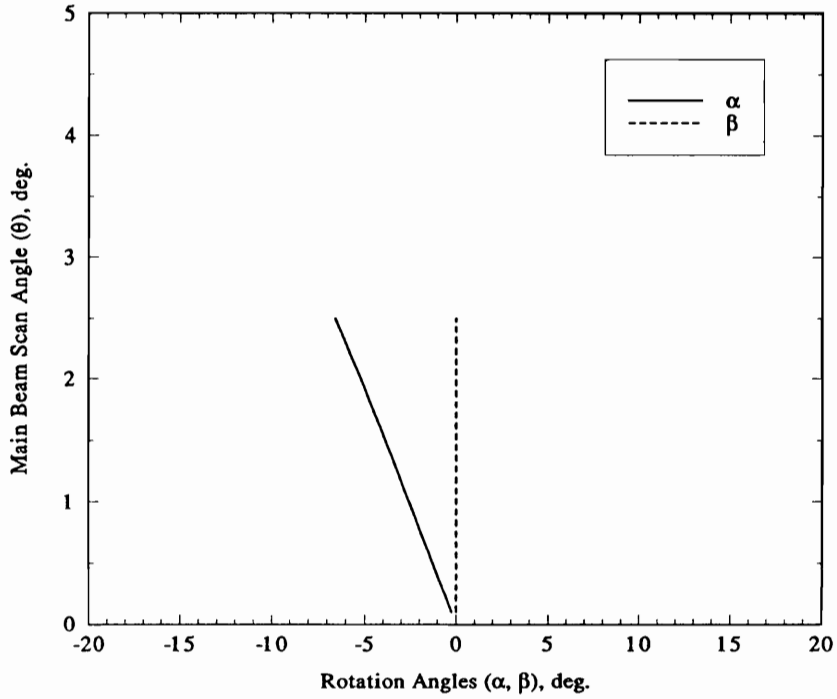

(a)

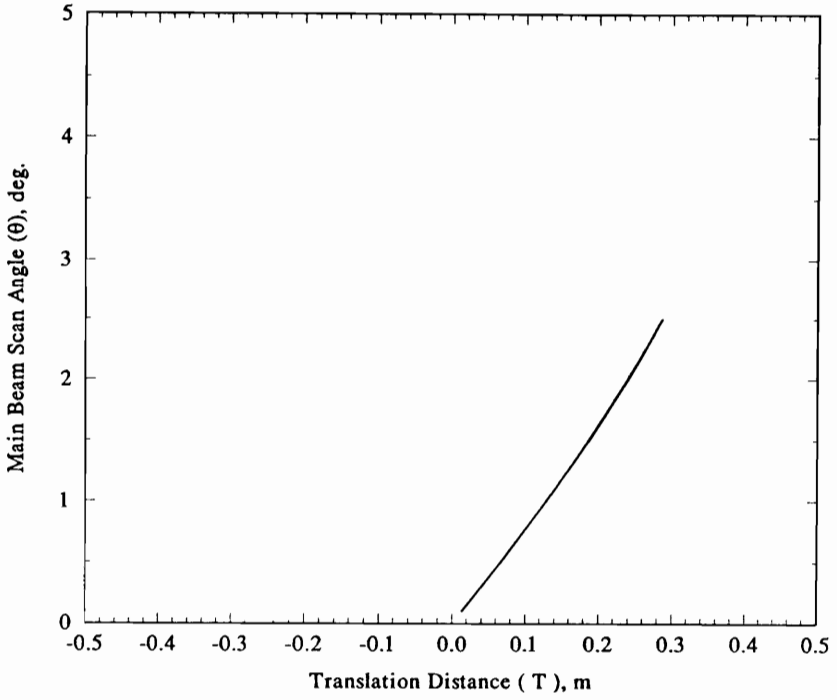

(b)

Figure 7.3-23. Cassegrain II configuration tertiary reflector rotation angles α and β and translation distance T used to scan the main beam over the range $\theta = 0.1°$-$2.5°$ with $\phi = 180.0°$. (a) Rotation angles. (b) Translation distances.

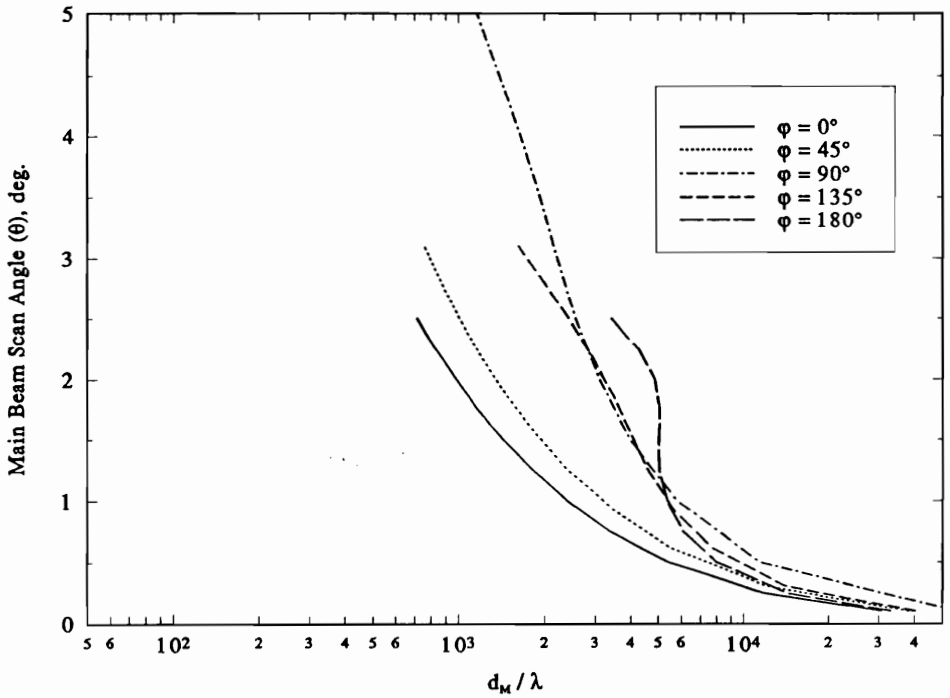

Figure 7.3-24. Normalized aperture diameter d/λ for the Cassegrain II configuration subject to 1 dB maximum gain loss due to scan induced phase errors. Tertiary reflector motion is allowed two degrees of rotational freedom and one degree of translational freedom. The scan range is given by (7-1).

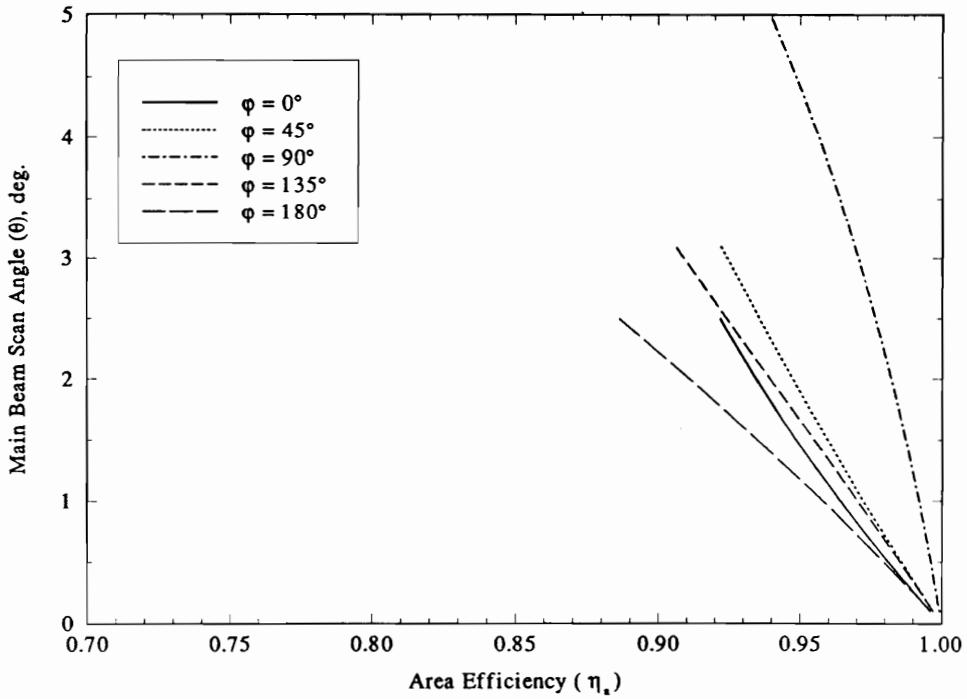

Figure 7.3-25. Primary aperture area efficiency η_a for the Cassegrain II configuration. Tertiary reflector motion is allowed two degrees of rotational freedom and one degree of translational freedom. The scan range is given by (7-1).

Table 7.3-4

Cassegrain II Performance Results

Three Degrees of Tertiary Reflector Motion (α, β, T)

$P_r = F_2', \ T_{max} = 0.5$

ϕ (deg)	θ (deg)	α (deg)	β (deg)	T (m)	d/λ	η_a
0	2.5	6.20	0.0	-0.38	716	0.92
45	3.1	5.87	-5.99	-0.37	759	0.92
90	5.0	2.45	-14.85	-0.23	1159	0.94
135	3.1	-5.21	-7.28	0.21	1626	0.91
180	2.5	-6.58	0.0	0.29	3437	0.88

The maximum translational motion is 0.38 m and, therefore, the constraint of $T_{max} = 0.5$ was never reached. The highest frequency for which this configuration can operate over the entire scan range with less than 1 dB of gain loss due to scan induced phase errors is that for which $d/\lambda = 716$. For the 25 m aperture this corresponds to a maximum operating frequency of $f_M = 8.59$ GHz. Figure 7.3-26 shows vignetting at the primary aperture plane for the limiting scan directions.

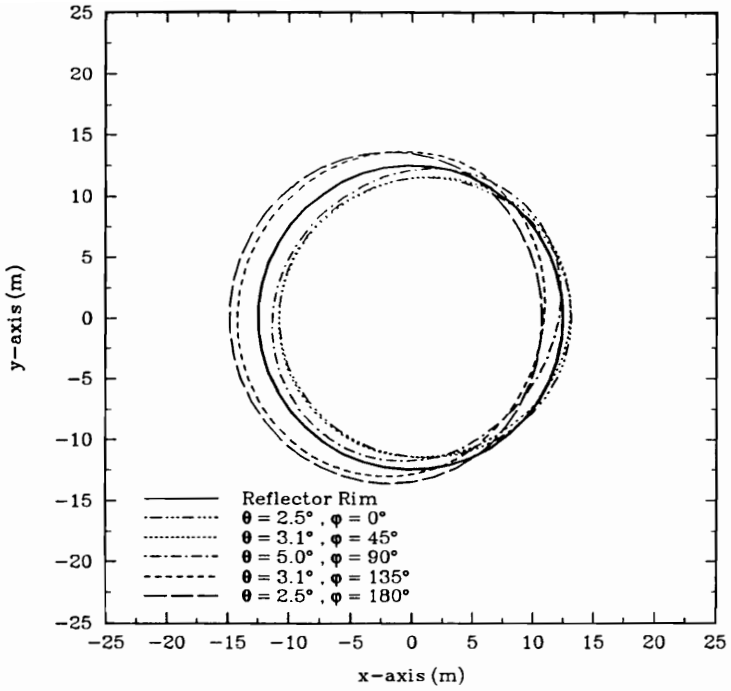

Figure 7.3-26. Primary aperture plane vignetting for the Cassegrain II configuration for the limiting scan directions in (7-1) and tertiary reflector motion allowed two degrees of rotational freedom and one degree of translational freedom.

7.3.4 Scan Performance for Two Degrees of Rotational Freedom About an Optimum Rotation Point P_r

Scan performance was calculated with the tertiary reflector constrained to two degrees of angular motion about the point $P_r = (9.37, 0.0, 36.40)$. It was found by trial and error that rotation about this point reduces scan induced phase errors. The point P_r is shown in relation to the Cassegrain II configuration in Fig. 7.3-27. Motion optimization was performed with $T_{max} = 0$ as discussed in Chapter 6. Calculated values for motion parameters α and β are plotted versus scan angle θ for the five values of ϕ indicated in (7.1) in Figs. 7.3-28 - 7.3-32. The corresponding values of the normalized aperture diameter d/λ and primary reflector area efficiency η_a are plotted versus θ in Figs. 7.3-33 and 7.3-34. The results of the above performance calculations for the limiting scan directions in (7-1) are summarized on Table 7.3-5.

Table 7.3-5

Cassegrain II Performance Results

Two Degrees of Tertiary Reflector Motion (α, β)

$P_r = (9.37, 0.0, 36.40)$, $T_{max} = 0$

ϕ (deg)	θ (deg)	α (deg)	β (deg)	d/λ	η_a
0	2.5	7.32	0.0	721	0.92
45	3.1	6.97	-6.48	776	0.92
90	5.0	3.14	-15.92	643	0.93
135	3.1	-6.07	-7.76	644	0.94
180	2.5	-7.73	0.0	650	0.93

The highest frequency for which this configuration can operate over the entire scan range with less than 1 dB of gain loss due to scan induced phase errors is that for which $d/\lambda = 643$. For the 25 m aperture this corresponds to a maximum operating frequency of $f_M = 7.72$ GHz. Figure 7.3-35 shows vignetting at the primary aperture plane for the limiting scan directions.

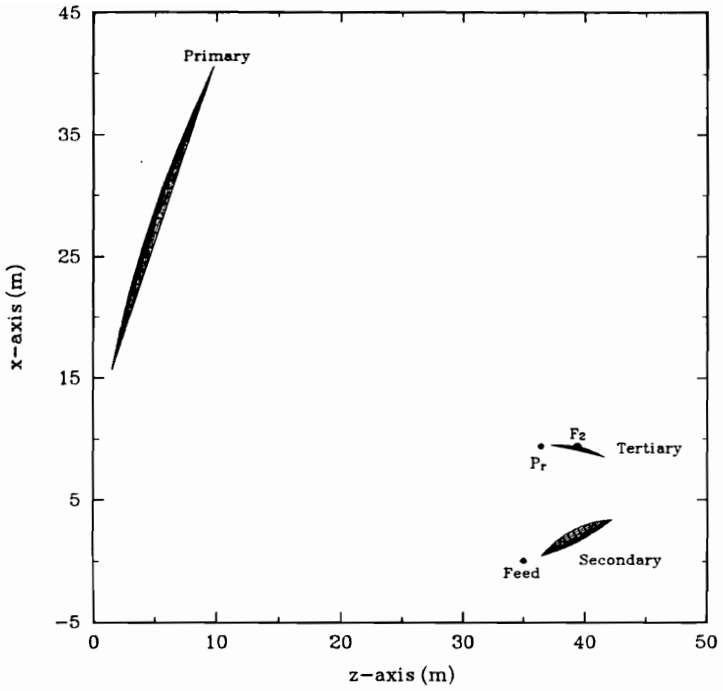

Figure 7.3-27. Side view of the Cassegrain II reflector configuration showing the relative location of the optimum rotation point P_r.

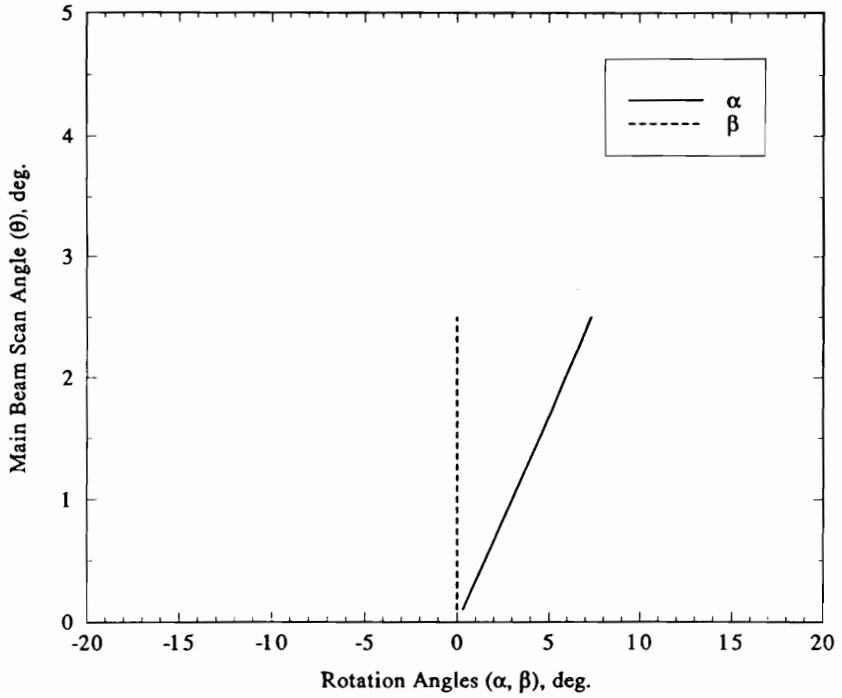

Figure 7.3-28. Cassegrain II configuration tertiary reflector rotation angles α and β used to scan the main beam over the range $\theta = 0.1°$-$2.5°$ with $\phi = 0.0°$.

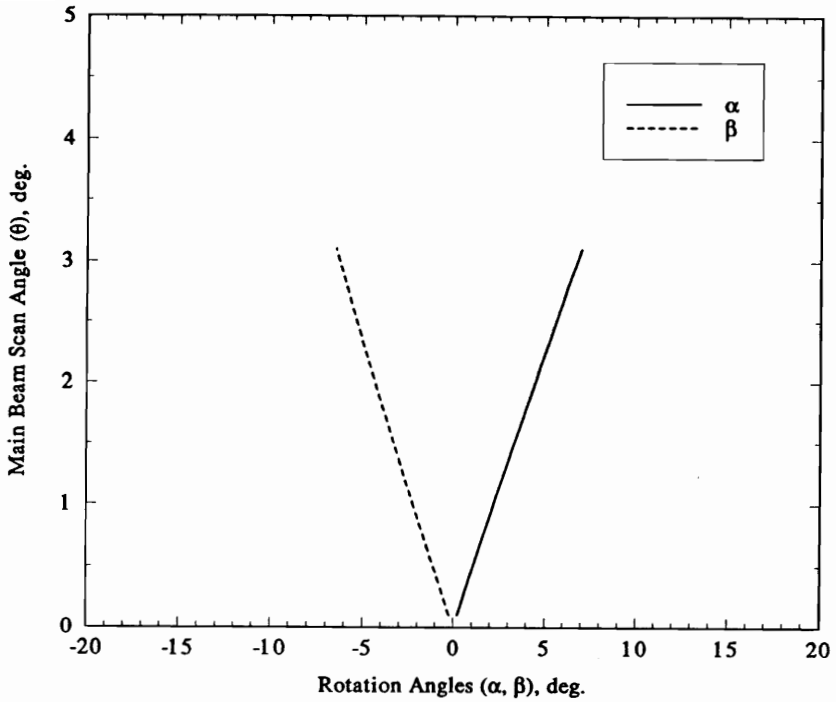

Figure 7.3-29. Cassegrain II configuration tertiary reflector rotation angles α and β used to scan the main beam over the range $\theta = 0.1°$-$3.1°$ with $\phi = 45.0°$.

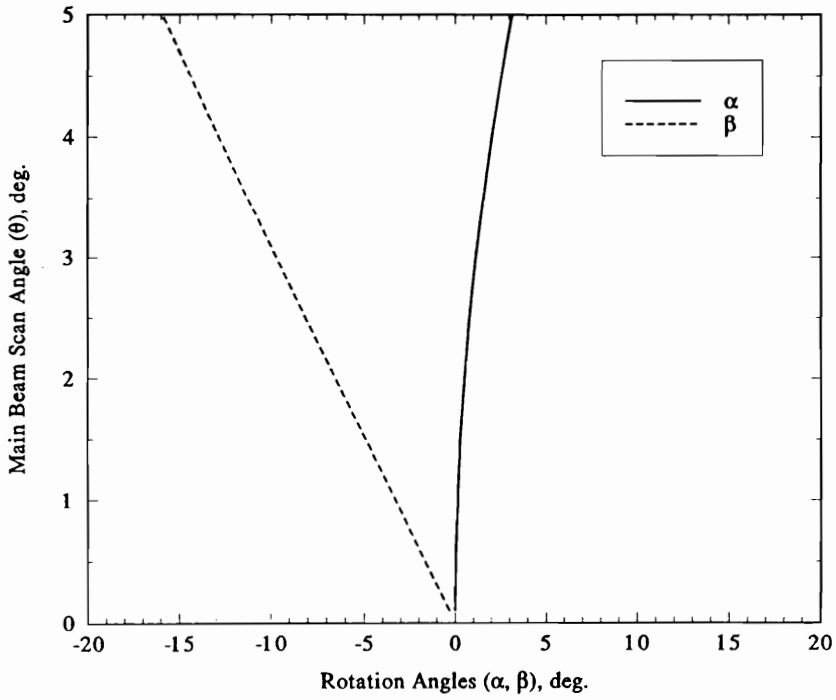

Figure 7.3-30. Cassegrain II configuration tertiary reflector rotation angles α and β used to scan the main beam over the range $\theta = 0.1°$-$5.0°$ with $\phi = 90.0°$.

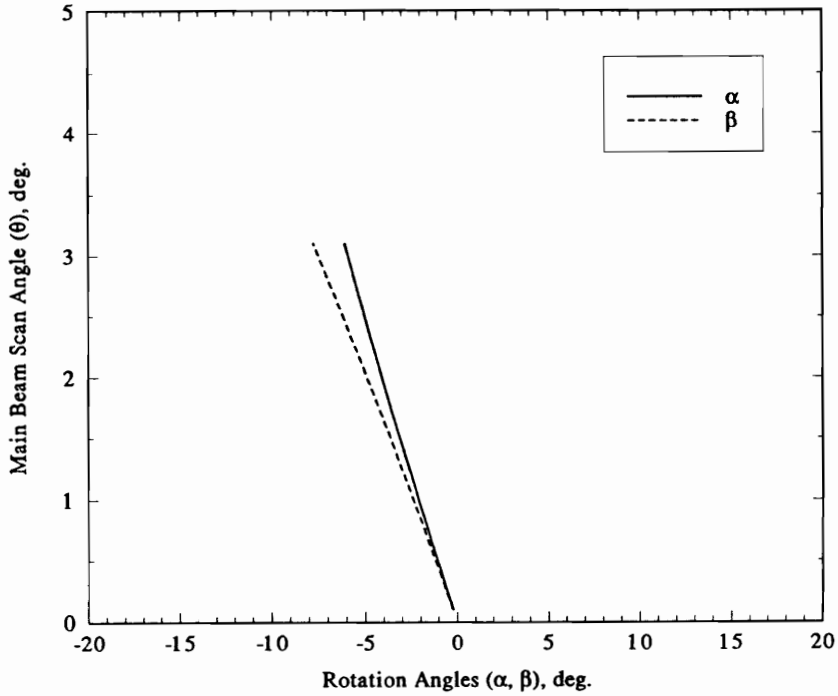

Figure 7.3-31. Cassegrain II configuration tertiary reflector rotation angles α and β used to scan the main beam over the range $\theta = 0.1°$-$3.1°$ with $\phi = 135.0°$.

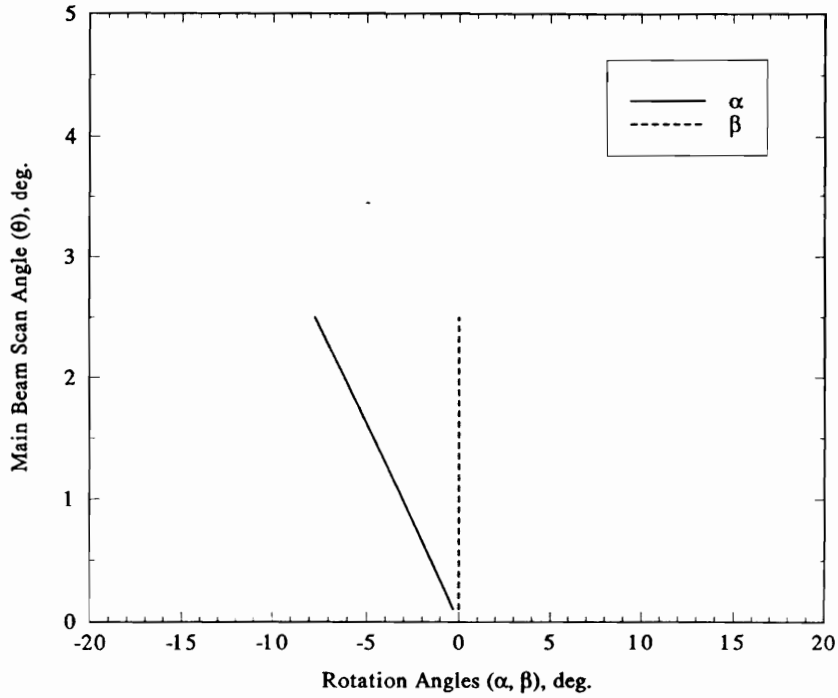

Figure 7.3-32. Cassegrain II configuration tertiary reflector rotation angles α and β used to scan the main beam over the range $\theta = 0.1°$-$2.5°$ with $\phi = 180.0°$.

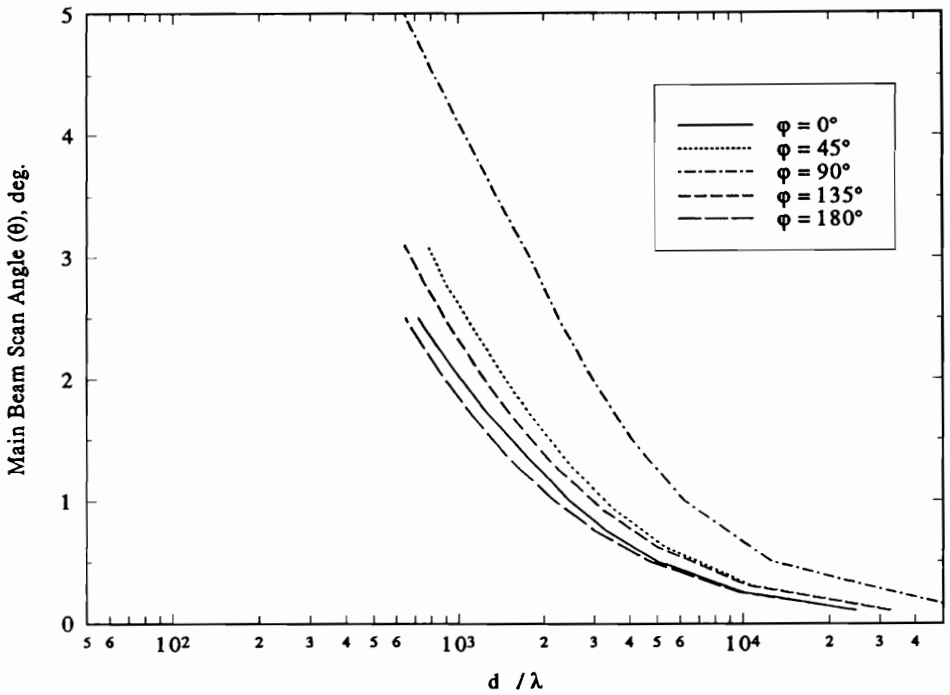

Figure 7.3-33. Normalized aperture diameter d/λ for the Cassegrain II configuration subject to 1 dB maximum gain loss due to scan induced phase errors. Tertiary reflector motion is constrained to two degrees of rotational freedom about the point $P_r = (9.37, 0.0, 36.40)$. The scan range is given by (7-1).

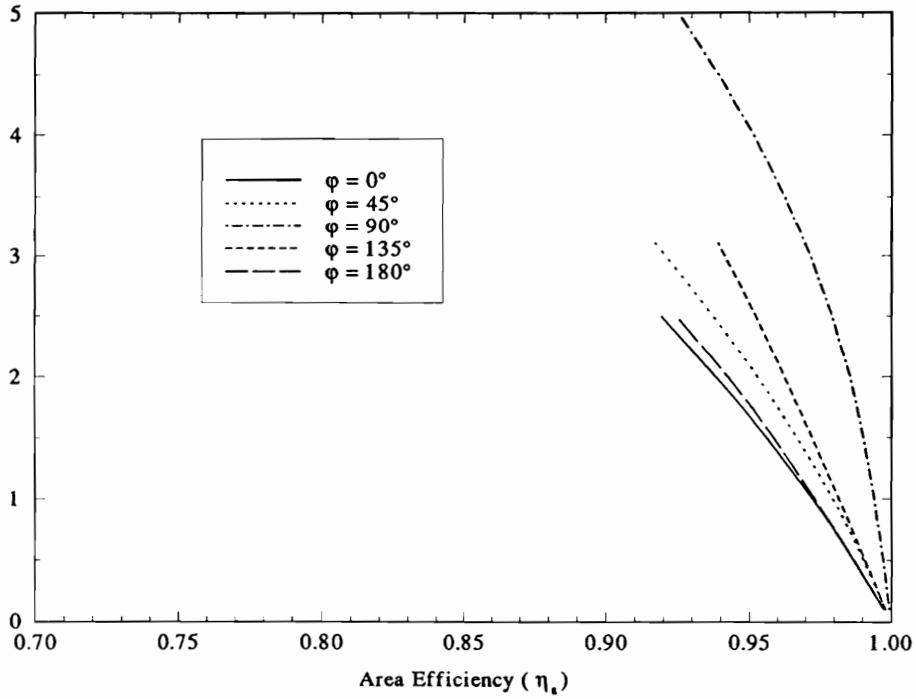

Figure 7.3-34. Primary aperture area efficiency η_a for the Cassegrain II configuration. Tertiary reflector motion is constrained to two degrees of rotational freedom about the point $P_r = (9.37, 0.0, 36.40)$. The scan range is given by (7-1).

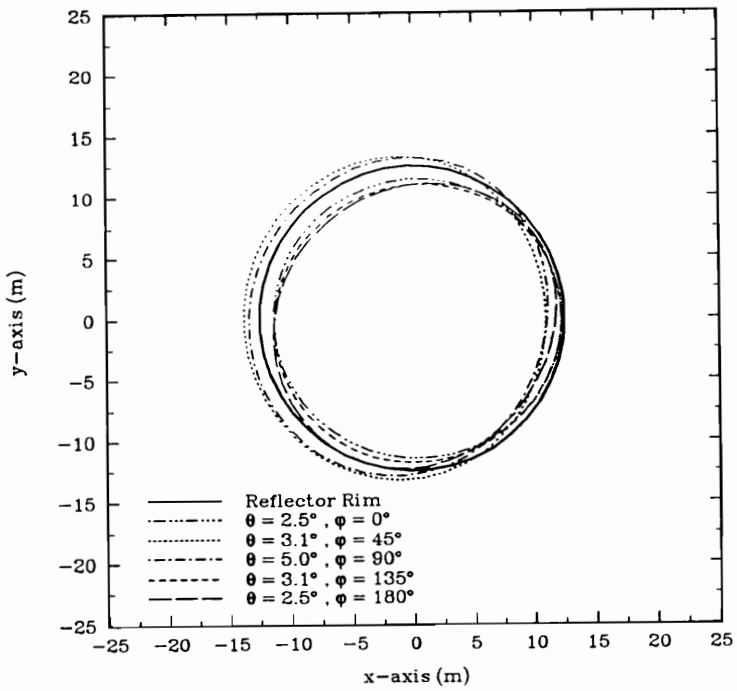

Figure 7.3-35. Primary aperture plane vignetting for the Cassegrain II configuration for the limiting scan directions in (7-1) and tertiary reflector motion constrained to two degrees of rotational freedom about point $P_r = (9.375, 0.0, 36.40)$.

7.4 The Prime Focus Parabolic Reflector

A side view of the offset prime focus parabolic reflector considered is shown in Fig. 7.4-1. The reflector is identical to the prime reflector used in the Cassegrain II configuration shown in Fig. 7.3-2. The diameter of the reflector is $d = 25$ m, the offset height is $H = 15.625$ m (see Fig. 4.1-9) and the F/D value is 1.69. The feed is pointed such that the beam peak strikes the center of the reflector. For boresight operation the average half angle subtended by the reflector as viewed from the feed is $\theta'_{ave} = 15.22^{\circ}$ for which (7.4) yields $q = 48.36$. For a pyramidal horn the corresponding aperture dimension as approximated by (7.1-1) is $d_f \simeq 5.93\ \lambda$.

With the prime focus parabolic reflector beam scanning is accomplished exclusively by feed displacement. In the following section the scan performance of the prime focus parabolic reflector shown in Fig. 7.4-1 is investigated using the G.O. techniques developed in Chapter 6.

7.4.1 Scan Performance for Three Degrees of Feed Translation

To accomplish beam scanning the feed is allowed three degrees of translational motion defined by the vector

$$\vec{T} = T_x\,\hat{x} + T_y\,\hat{y} + T_z\,\hat{z}. \tag{7.4-1}$$

This vector indicates the distance and direction of feed displacement from the reflector focal point. In Figs. 7.4-2 - 7.4-6 motion parameters T_x, T_y and T_z are plotted versus scan angle θ for the five values of ϕ indicated in (7.1). The corresponding values of the normalized aperture diameter d/λ are plotted versus θ in Fig. 7.4-7. The results of these calculations for the limiting scan directions are shown on Table 7.4-1.

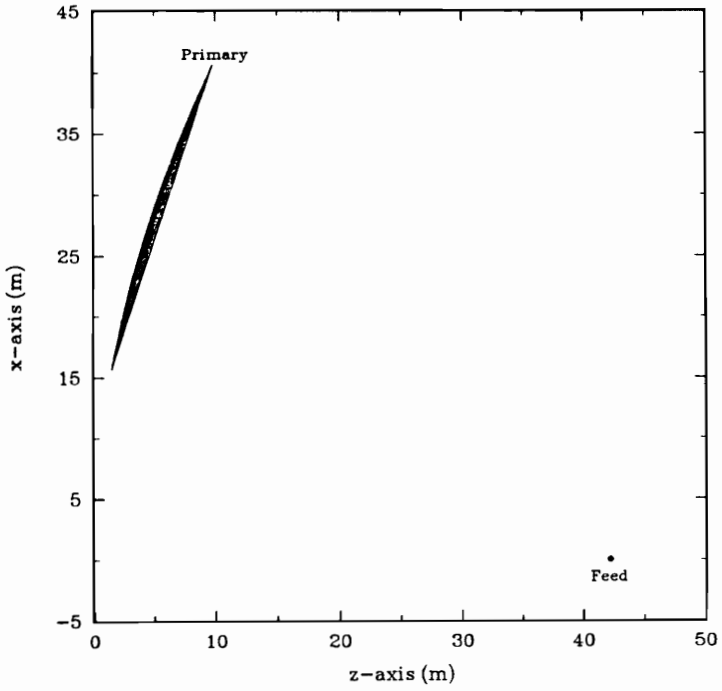

Figure 7.4-1. Side view of the prime focus parabolic reflector.

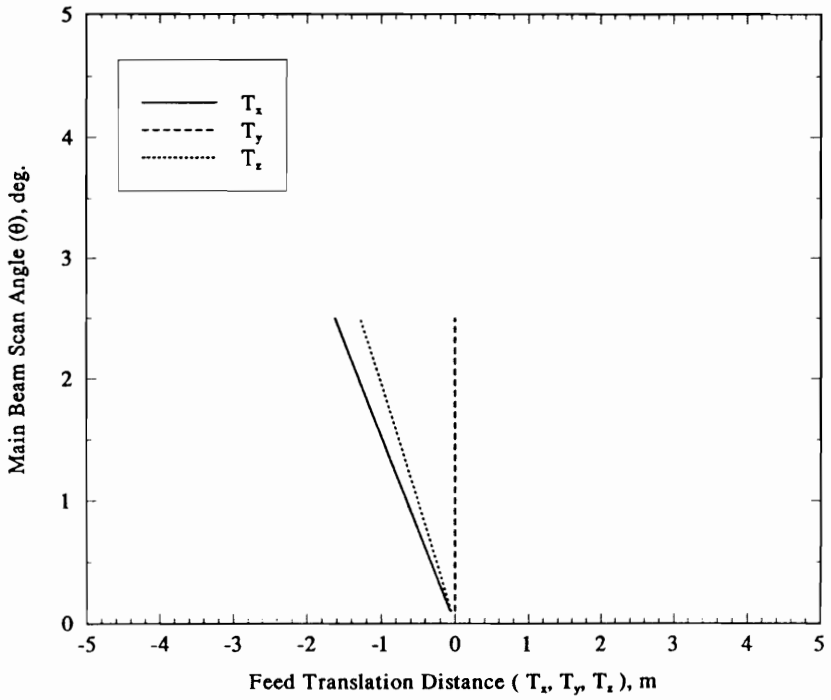

Figure 7.4-2. Prime focus parabolic reflector feed translation distances T_x, T_y and T_z used to scan the main beam over the range $\theta = 0.1°$-$2.5°$ with $\phi = 0.0°$.

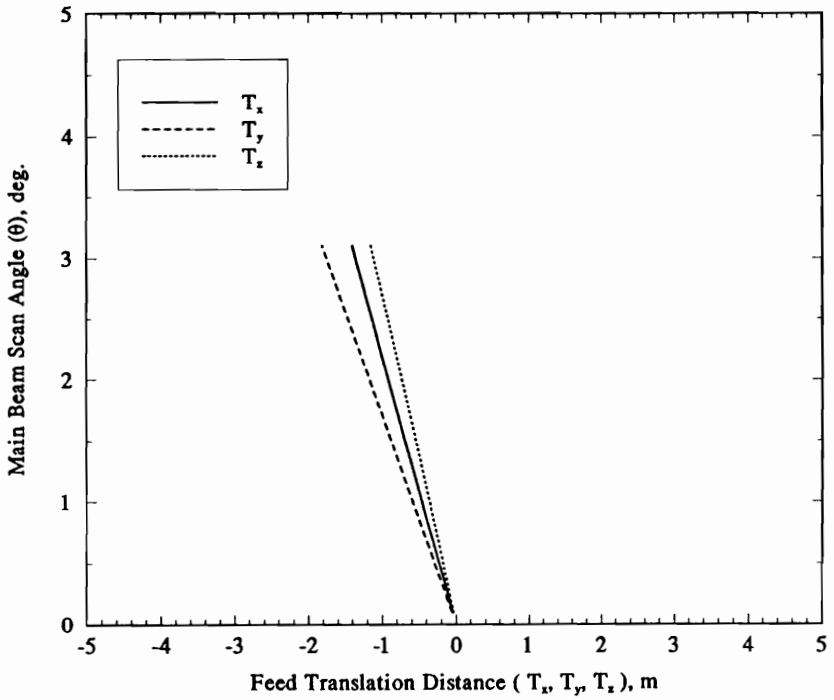

Figure 7.4-3. Prime focus parabolic reflector feed translation distances T_x, T_y and T_z used to scan the main beam over the range $\theta = 0.1°$-$3.1°$ with $\phi = 45.0°$.

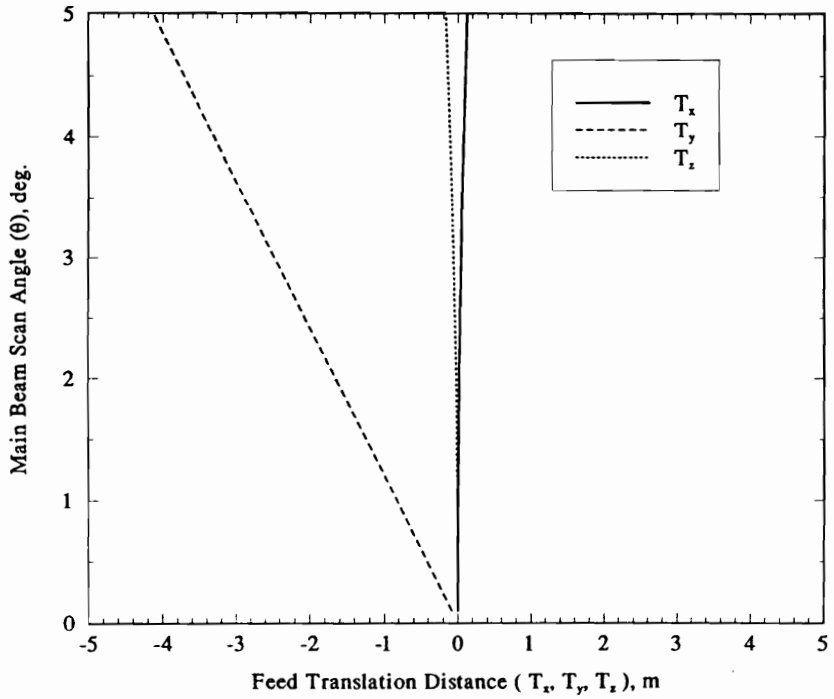

Figure 7.4-4. Prime focus parabolic reflector feed translation distances T_x, T_y and T_z used to scan the main beam over the range $\theta = 0.1°$-$5.0°$ with $\phi = 90.0°$.

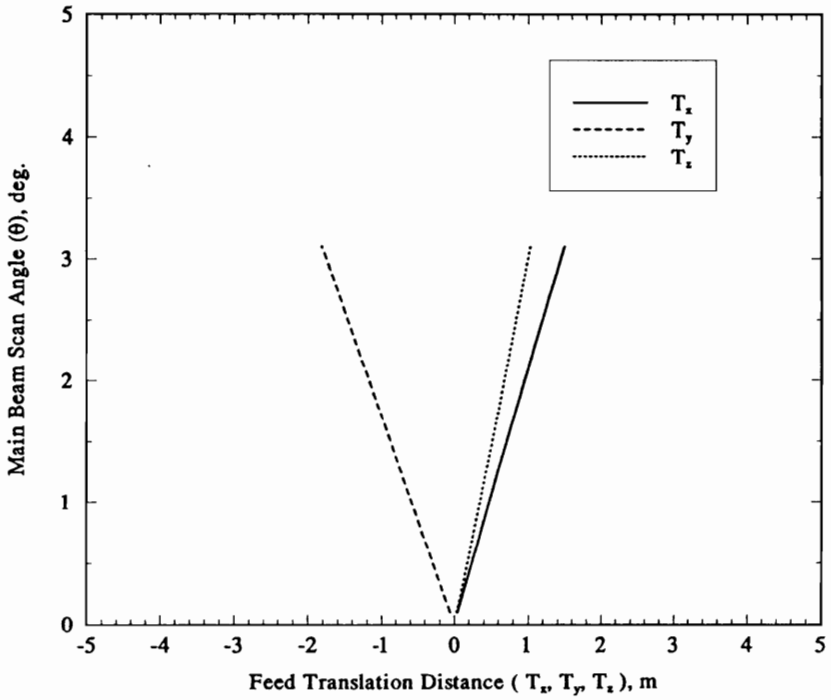

Figure 7.4-5. Prime focus parabolic reflector feed translation distances T_x, T_y and T_z used to scan the main beam over the range $\theta = 0.1°$-$3.1°$ with $\phi = 135.0°$.

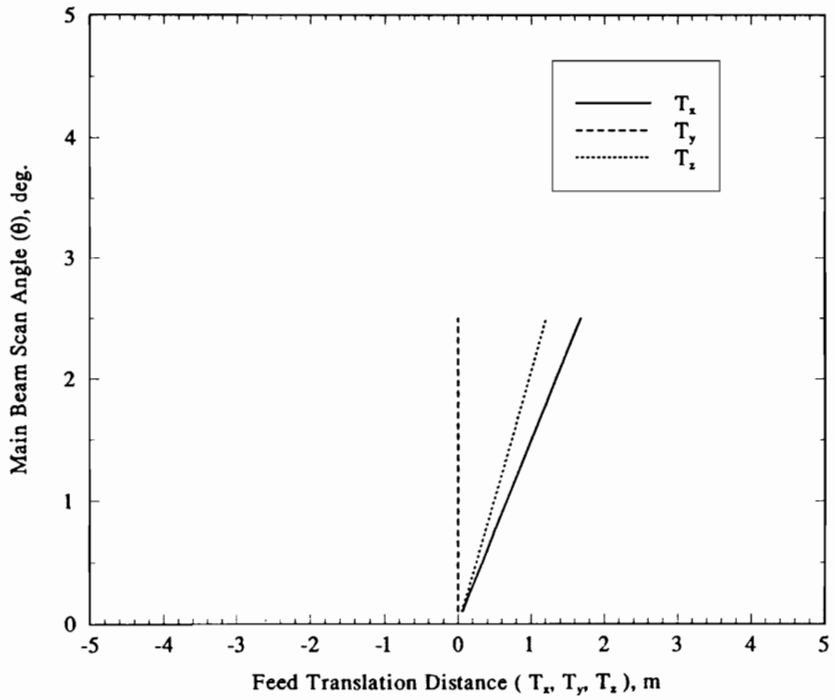

Figure 7.4-6. Prime focus parabolic reflector feed translation distances T_x, T_y and T_z used to scan the main beam over the range $\theta = 0.1°$-$2.5°$ with $\phi = 180.0°$.

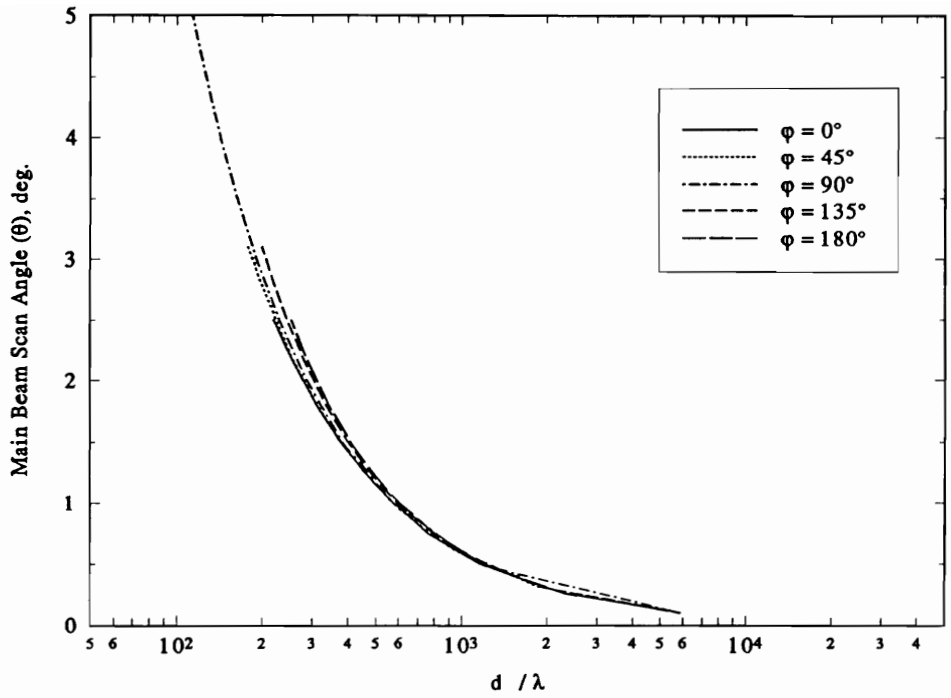

Figure 7.4-7. Normalized aperture diameter d/λ for the prime focus parabolic reflector subject to 1 dB maximum gain loss due to scan induced phase errors. The scan range is given by (7-1).

Table 7.4-1

Prime Focus Parabolic Reflector Performance Results

Three Degrees of Feed Motion (T_x, T_y, T_z)

ϕ (deg)	θ (deg)	T_x (m)	T_y (m)	T_z (m)	d/λ
0	2.5	-1.62	0.0	-1.28	219
45	3.1	-1.40	-1.81	-1.16	178
90	5.0	-0.12	-4.12	-0.16	113
135	3.1	1.50	-1.81	1.03	200
180	2.5	1.69	0.0	1.19	253

The highest frequency for which this configuration can operate over the entire scan range with less than 1 dB of gain loss due to scan induced phase errors is that for which $d/\lambda = 113$. For the 25 m aperture this corresponding to a maximum operating frequency of $f_M = 1.35$ GHz. Note, the maximum feed translation is in the $\phi = 90^\circ$ scan direction for which $|\vec{T}| = 4.12$ m.

7.5 Summary of Geometrical Optics Performance Results

A summary of the electrical performance results for the four reflector configurations investigated in Secs. 7.1-7.4 is presented on Table 7.5-1. The scan range considered is given by (7-1). On Table 7.5-1 parameter f_M indicates the maximum frequency of operation over the scan range for a 25 m primary reflector aperture and a maximum gain loss of 1 dB due to scan induced phase errors and parameter η_a indicates the lowest calculated aperture area efficiency over the scan range. A summary of the physical attributes of the reflector configurations is presented in Table 7.5.2. Specific conclusions follow.

1. Cassegrain I Tri-reflector:
   - The most desirable tertiary reflector location for placement of motion actuators.
   - The smallest overall dimensions.
   - With tertiary reflector motion limited to rotation about F_2' suffers from high aperture plane phase errors during beam scanning resulting in a low operating frequency.
   - Unacceptably high aperture plane vignetting.

2. Gregorian Tri-reflector:
   - Undesirable tertiary reflector location for placement of motion actuators.
   - Largest overall dimensions.
   - With tertiary reflector motion limited to rotation about F_2' suffers from high aperture plane phase errors during beam scanning resulting in a low operating frequency.
   - Allowing tertiary reflector translation results in only a small improvement in aperture plane phase errors during beam scanning.
   - Low aperture plane vignetting.

3. Cassegrain II Tri-reflector:
   - Undesirable tertiary reflector location for placement of motion actuators.
   - Reduced overall dimensions compared to the Gregorian tri-reflector.
   - With tertiary reflector motion limited to rotation about F_2' suffers from high aperture plane phase errors during beam scanning resulting in a low operating frequency.
   - Allowing for more complex tertiary reflector motions results in a substantial reduction in aperture plane phase errors during beam scanning.
   - Low aperture plane vignetting.

Table 7.5-1

Summary of Computed Electrical Performance Results for Three Example Conjugate Tri-Reflector Configurations and an Offset Prime Focus Parabolic Reflector

Configuration Type	Degrees of Tertiary Tertiary Motion	f_M (GHz)	η_a	Vignetting	Tertiary Motion
Cassegrain I	(α, β) †	0.68	0.78	High	Simple
Gregorian	(α, β) †	2.04	0.84	Medium	Simple
	$(\alpha, \beta, T_x, T_y, T_z)$ ‡	2.53	0.83	Medium	Complex
Cassegrain II	(α, β) †	1.82	0.86	Medium	Simple
	$(\alpha, \beta, T_x, T_y, T_z)$ ‡	4.75	0.90	Medium	Complex
	(α, β, T) *	8.59	0.88	Medium	Medium
	(α, β) **	7.72	0.92	Low	Medium
Parabolic	(T_x, T_y, T_z) ††	1.35			Complex

† rotation about point $P_r = F_2'$.

‡ rotation about point $P_r = F_2'$ and 0.25 m max translation in all directions.

* rotation about $P_r = F_2'$ and 0.382 m max translation along a linear path.

** rotation about an optimum rotation point.

†† Three degrees of feed translation.

Table 7.5-2

Summary of Physical Attributes of the

Three Example Conjugate Tri-reflector Configurations

Configuration Type	Sub Surface Area (% Primary Aperture)	Tertiary Surface Area (% Primary Aperture)	Overall Length (m)	Overall Height (m)
Cassegrain I	11.36	2.4	39	38
Gregorian	10.73	1.78	48	38
Cassegrain II	10.30	3.1	42.5	40.6

7.6 References

1. Y. Rahmat-Samii, P. Cramer, K. Woo and S. W. Lee, "Realizable Feed-Element Patterns for Multibeam Reflector Antenna Analysis," *IEEE Trans. on Ant. and Prop.*, vol. 29, no. 6, pp. 961-964, November 1981.

Chapter 8

Conjugate Tri-reflector P.O. Performance Results

In Chapter 7 synthesis and analysis of several example conjugate tri-reflector configurations was performed using geometrical optics (G.O.). In this chapter more accurate physical optics (P.O.) analysis is applied to two example configurations to confirm the results presented in Chapter 7. The example configurations considered are the Cassegrain II configuration with tertiary reflector motion constrained to two degrees of rotational motion about the optimum point P_r as discussed in Sec. 7.3.4 and the prime focus parabolic reflector discussed in Sec. 7.4. The Cassegrain II configuration was chosen because it represents the best compromise between tertiary reflector motion complexity and scan performance. The prime focus parabolic reflector, which is identical to the prime reflector in the Cassegrain II configuration, was chosen to highlight the effects of the Cassegrain II suboptics on beam scanning performance.

The P.O. results presented in this section where obtained using the reflector code GRASP7 [1]. For the prime focus parabolic reflector the surface was represented by an analytic second order equation. For the Cassegrain II configuration P.O. integration was performed on all three reflector surfaces and the primary and secondary reflector surfaces were represented by analytic second order equations while the tertiary reflector surface was represented by a set of surface points. Surface interpolation must be performed twice on the set of

tertiary reflector surface points during radiation pattern calculation and this is a potential source of error.

8.1 P.O. Results for the Cassegrain II Configuration

The feed pattern used for the Cassegrain II configuration was a Gaussian distribution with a -15 dB edge taper at the average half angle subtended by the tertiary reflector, θ'_{ave}. For this configuration $\theta'_{ave} = 12.94^{\circ}$ (see Sec. 7.3). The feed boresight direction was directed toward the secondary reflector focal point F'_2 and the feed was kept stationary for all scan directions. The feed polarization was parallel to the xz-plane shown in Fig. 7.3-27. The frequencies 5.76 GHz and 7.68 GHz were considered, which correspond to $d/\lambda = 480$ and 640, respectively. For both frequencies radiation patterns were calculated for the following scan directions (see Fig. 6.2-2):

$$\begin{aligned}
&\phi = 0.0^{\circ}, \quad \theta = 0.0^{\circ} \quad \text{(boresight direction)} \\
&\phi = 0.0^{\circ}, \quad \theta = 2.5^{\circ} \\
&\phi = 45.0^{\circ}, \quad \theta = 3.1^{\circ} \\
&\phi = 90.0^{\circ}, \quad \theta = 5.0^{\circ} \\
&\phi = 135.0^{\circ}, \quad \theta = 3.1^{\circ} \\
&\phi = 180.0^{\circ}, \quad \theta = 2.5^{\circ}
\end{aligned} \tag{8.1-1}$$

These scan directions correspond to the boresight direction and the limiting scan directions for the scan range given by (7-1).

8.1.1 Cassegrain II 5.76 GHz P.O. Results

Normalized contour plots of the co-polarized and cross-polarized radiation patterns calculated at 5.76 GHz are shown in Figs. 8.1-1 - 8.1-6. Principal plane

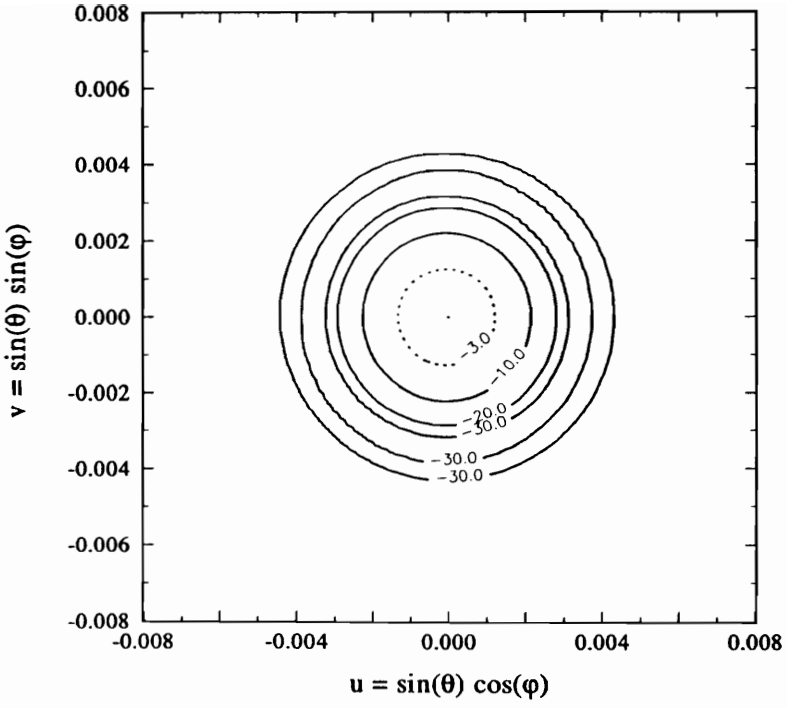

(a)

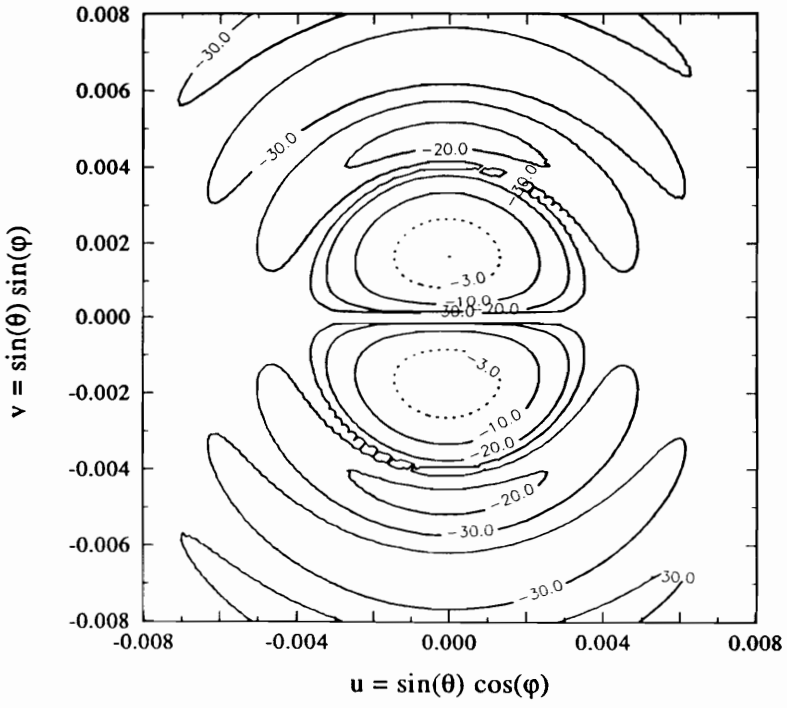

(b)

Figure 8.1-1. Normalized contour plots of co-polarized (a) and cross-polarized (b) radiation patterns in the $\theta = 0^{\circ}$, $\phi = 0^{\circ}$ scan direction calculated at 5.76 GHz for the Cassegrain II configuration with tertiary reflector rotation about point P_r as shown in Fig. 7.3-27.

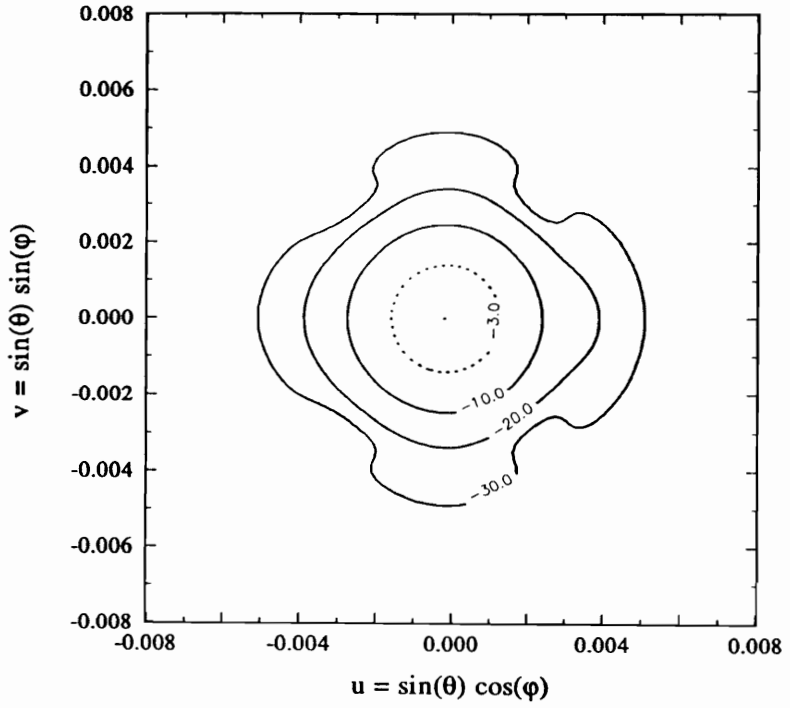

(a)

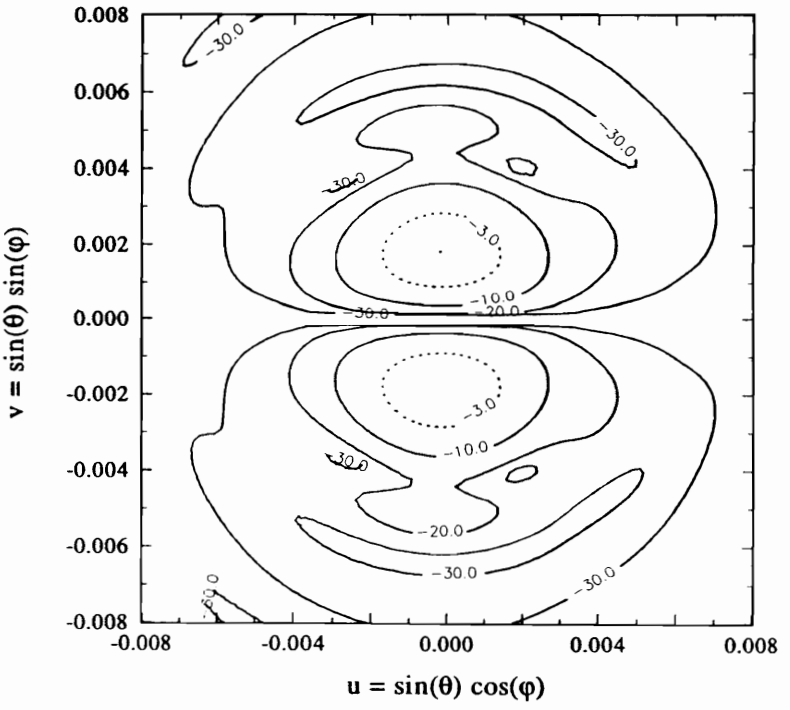

(b)

Figure 8.1-2. Normalized contour plots of co-polarized (a) and cross-polarized (b) radiation patterns in the $\theta = 2.5$, $\phi = 0^{\circ}$ scan direction calculated at 5.76 GHz for the Cassegrain II configuration with tertiary reflector rotation about point P_r as shown in Fig. 7.3-27.

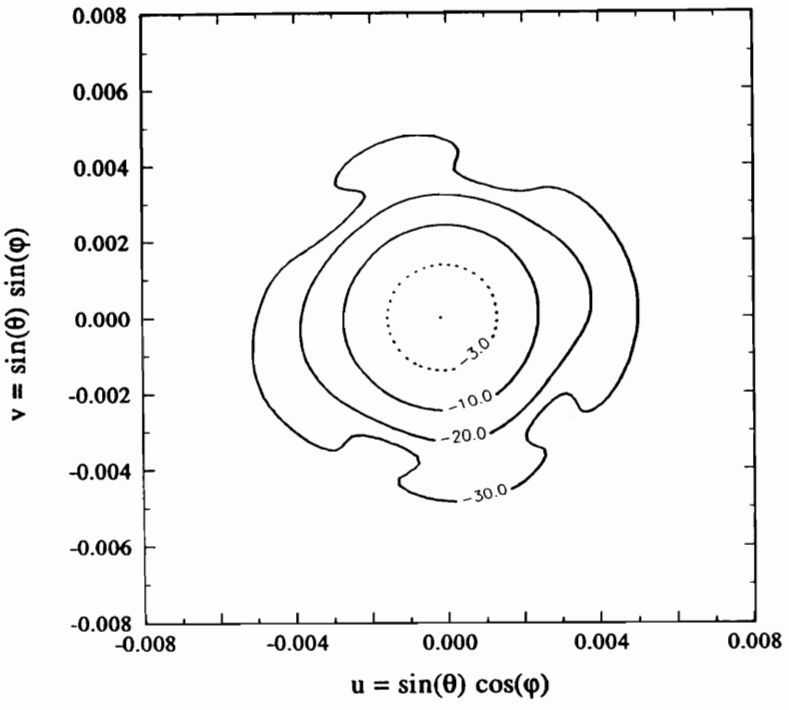

(a)

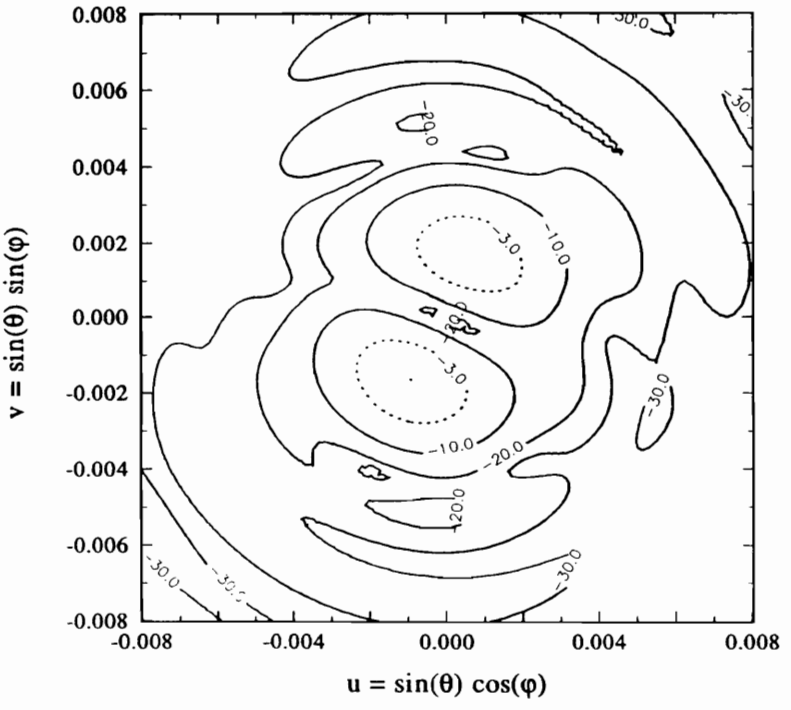

(b)

Figure 8.1-3. Normalized contour plots of co-polarized (a) and cross-polarized (b) radiation patterns in the $\theta = 3.1^{\circ}$, $\phi = 45^{\circ}$ scan direction calculated at 5.76 GHz for the Cassegrain II configuration with tertiary reflector rotation about point P_r as shown in Fig. 7.3-27.

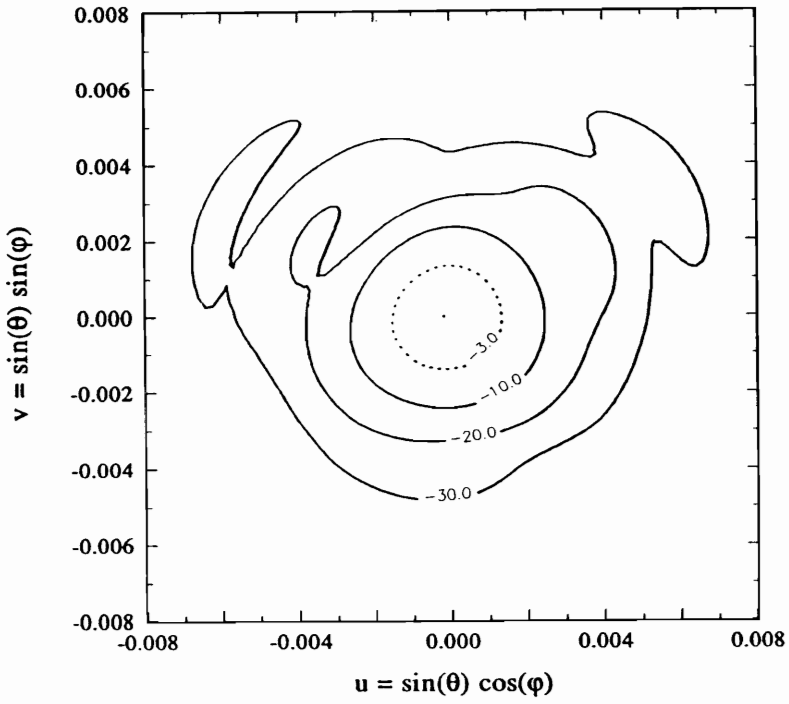

(a)

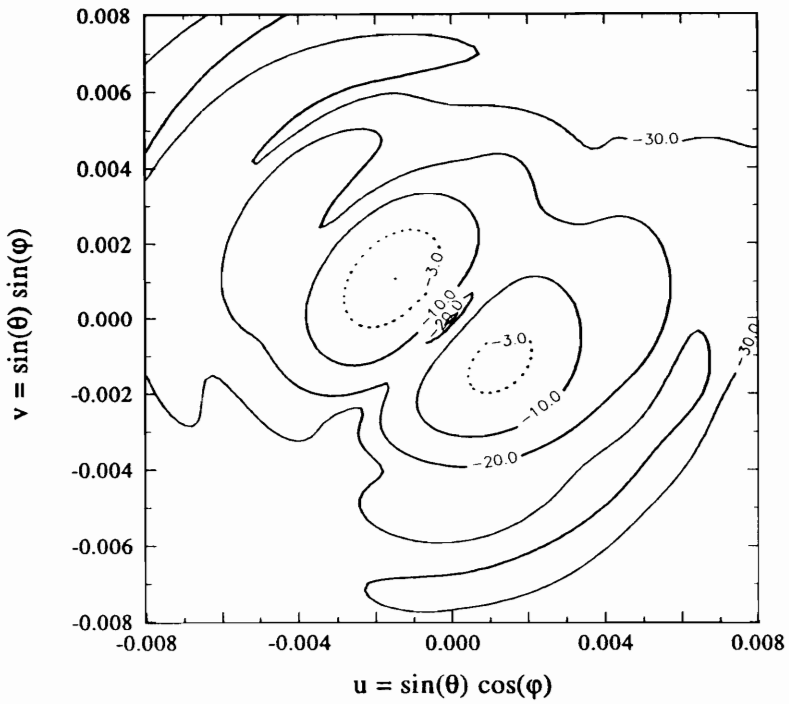

(b)

Figure 8.1-4. Normalized contour plots of co-polarized (a) and cross-polarized (b) radiation patterns in the $\theta = 5°$, $\phi = 90°$ scan direction calculated at 5.76 GHz for the Cassegrain II configuration with tertiary reflector rotation about point P_r as shown in Fig. 7.3-27.

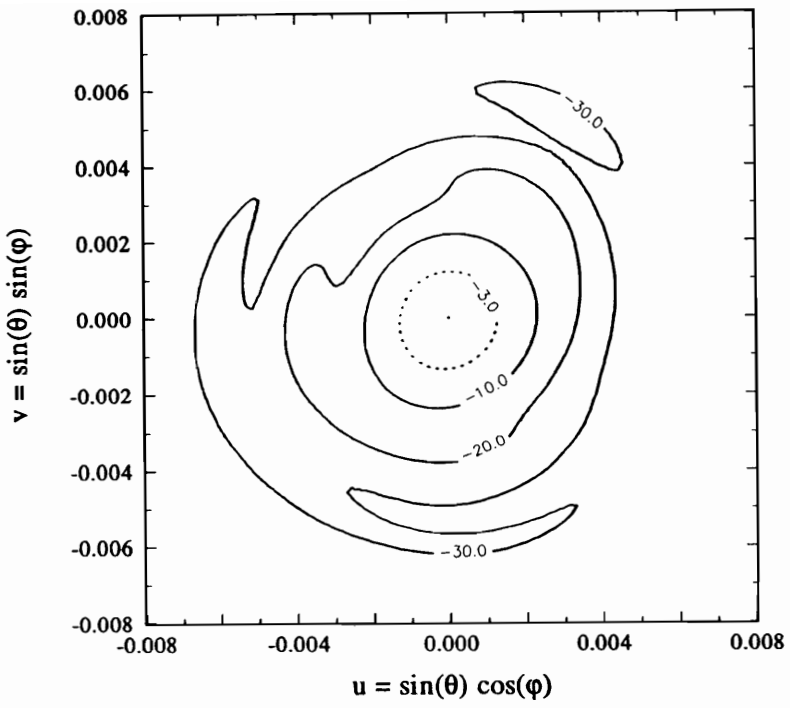

(a)

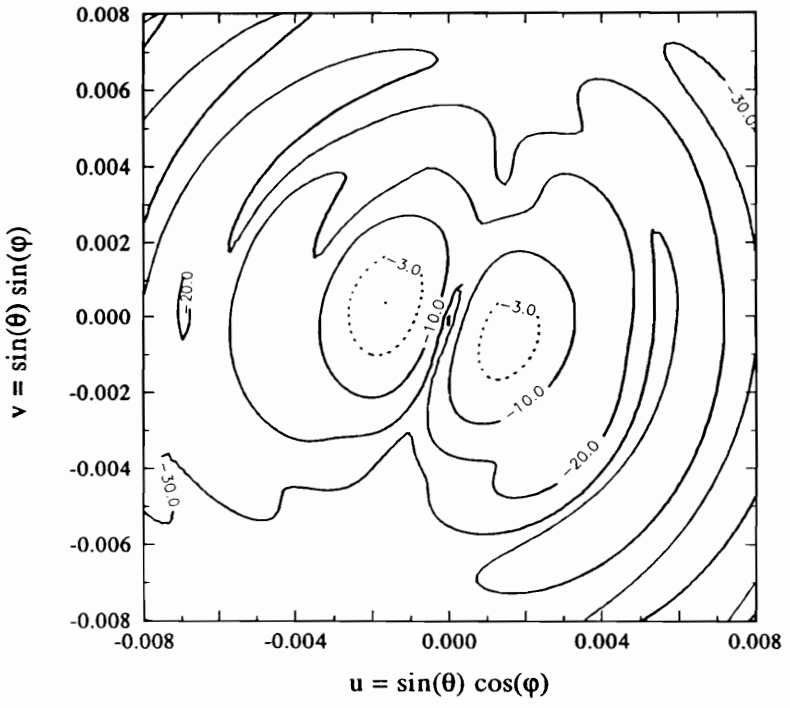

(b)

Figure 8.1-5. Normalized contour plots of co-polarized (a) and cross-polarized (b) radiation patterns in the $\theta = 3.1^{\circ}$, $\phi = 135^{\circ}$ scan direction calculated at 5.76 GHz for the Cassegrain II configuration with tertiary reflector rotation about point P_r as shown in Fig. 7.3-27.

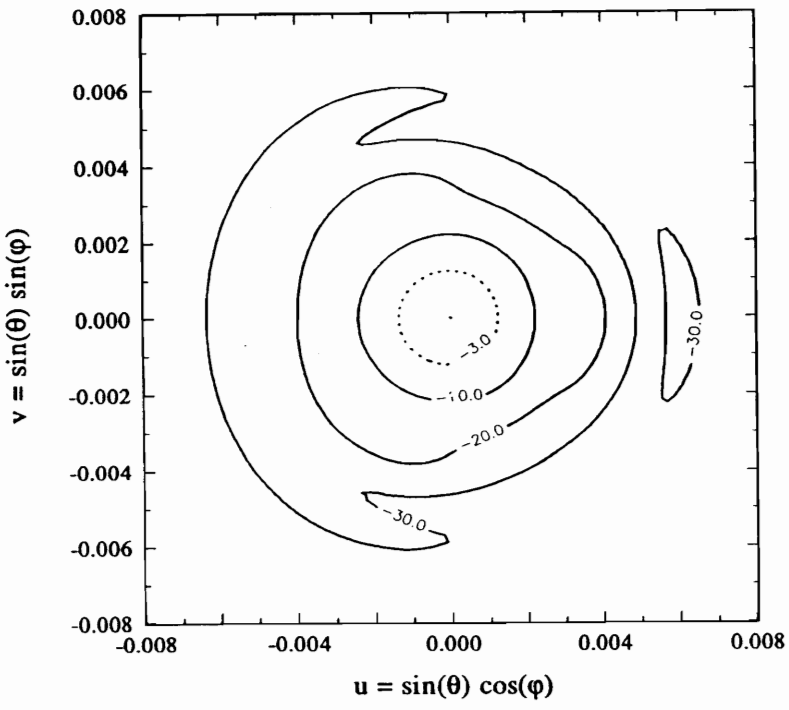

(a)

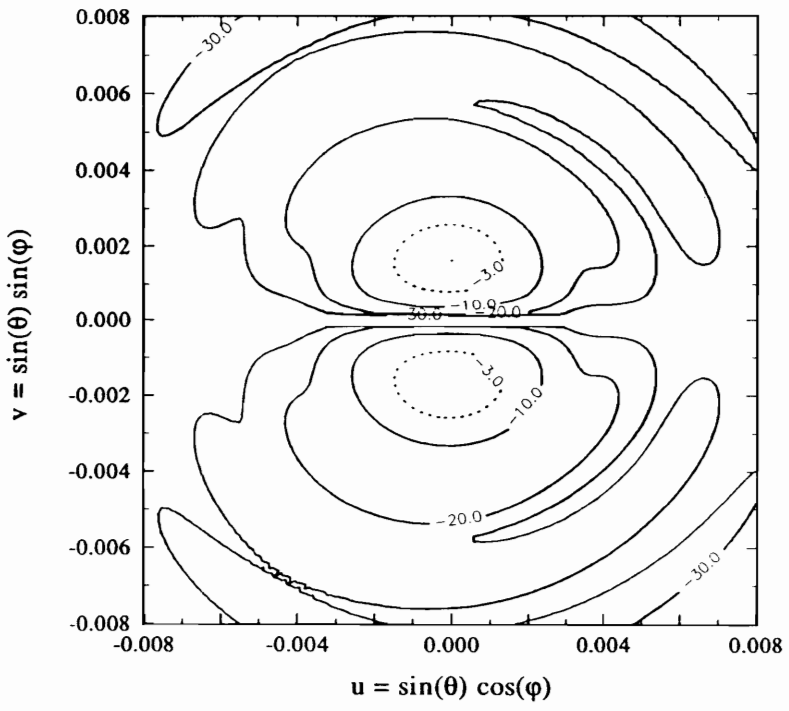

(b)

Figure 8.1-6. Normalized contour plots of co-polarized (a) and cross-polarized (b) radiation patterns in the $\theta = 2.5°$, $\phi = 180°$ scan direction calculated at 5.76 GHz for the Cassegrain II configuration with tertiary reflector rotation about point P_r as shown in Fig. 7.3-27.

patterns showing beam scanning in the $\phi = 0^\circ$ plane ($\phi = 0^\circ, \theta = \pm 2.5^\circ$), the $\phi = 45^\circ$ plane ($\phi = 45^\circ, \theta = \pm 3.1^\circ$) and the $\phi = 90^\circ$ plane ($\phi = 90^\circ, \theta = \pm 5.0^\circ$) are shown in Figs. 8.1-7 - 8.1-9. Gain, aperture efficiency ϵ_{ap} (see (3.1-4)), half-power beamwidth (HPBW) and relative cross-polarization level (XPOL) are tabulated on Table 8.1-1 for the scan directions considered. The scan range encompasses approximately 30 HPBW in the $\phi = 0^\circ$ plane and 60 HPBW in the $\phi = 90^\circ$ plane with a total gain variation of 1.05 dB.

Table 8.1-1

Cassegrain II Physical Optics Results

$f = 5.76$ GHz, $d/\lambda = 480$

ϕ (deg)	θ (deg)	Gain (dB)	ϵ_{ap} (%)	HPBW (deg)	XPOL (dB)
0	0.0	62.44	77	0.155	-28.37
0	2.5	61.39	60	0.171	-31.61
45	3.1	61.41	61	0.170	-30.10
90	5.0	61.39	61	0.172	-25.24
135	3.1	61.91	68	0.154	-24.91
180	2.5	61.90	68	0.155	-25.38

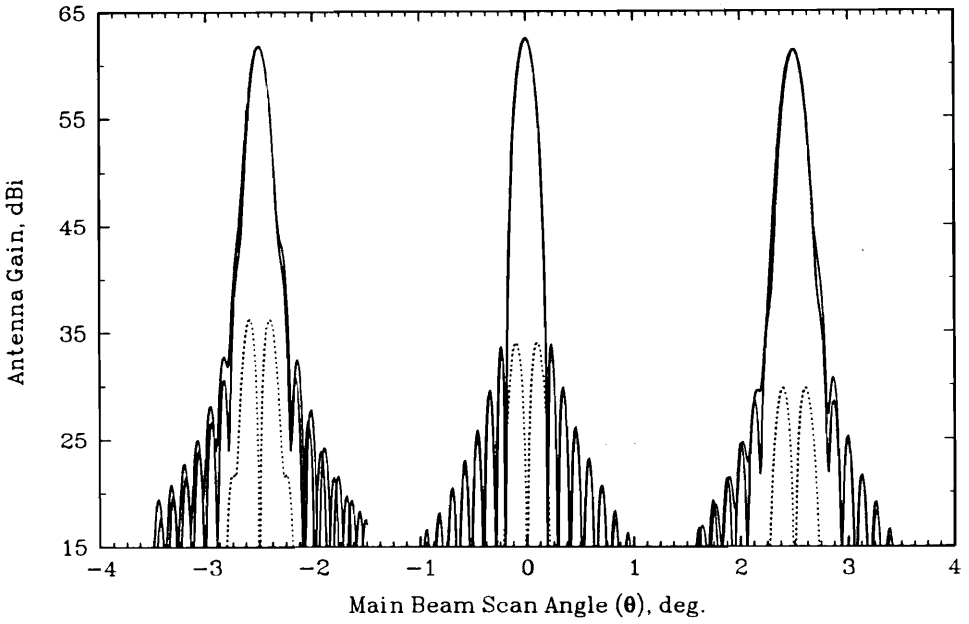

Figure 8.1-7. Principal plane patterns in the $\phi = 0°$ plane calculated at 5.76 GHz for the Cassegrain II configuration shown in Fig. 7.3-27. Beam scanning is accomplished by tertiary reflector rotation about the point P_r shown in Fig. 7.3-27. Co-polarized E- and H-plane patterns-solid; cross-polarized E- and H-plane patterns-dashed.

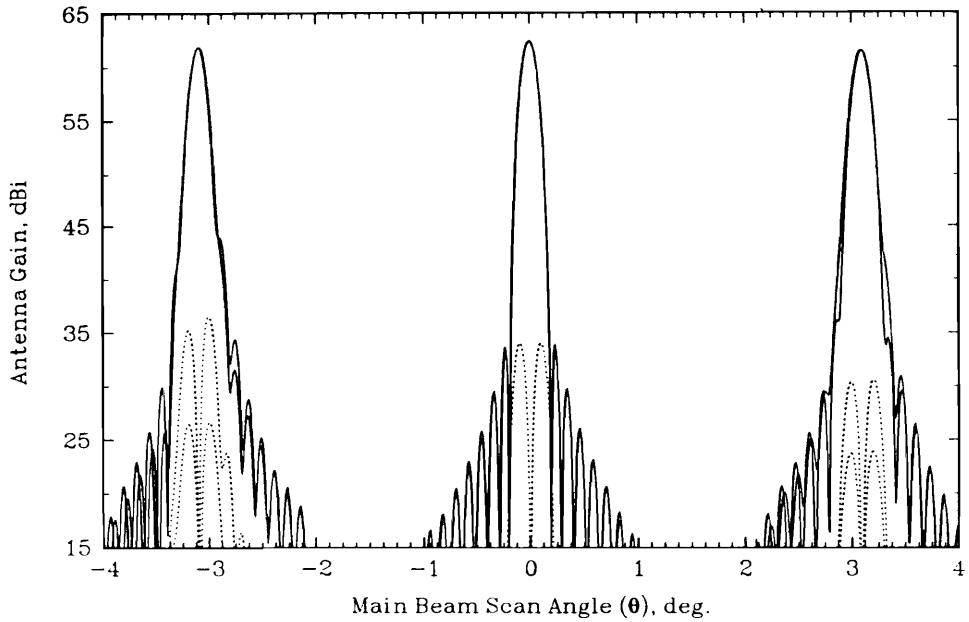

Figure 8.1-8. Principal plane patterns in the $\phi = 45°$ plane calculated at 5.76 GHz for the Cassegrain II configuration shown in Fig. 7.3-27. Beam scanning is accomplished by tertiary reflector rotation about the point P_r shown in Fig. 7.3-27. Co-polarized E- and H-plane patterns-solid; cross-polarized E- and H-plane patterns-dashed.

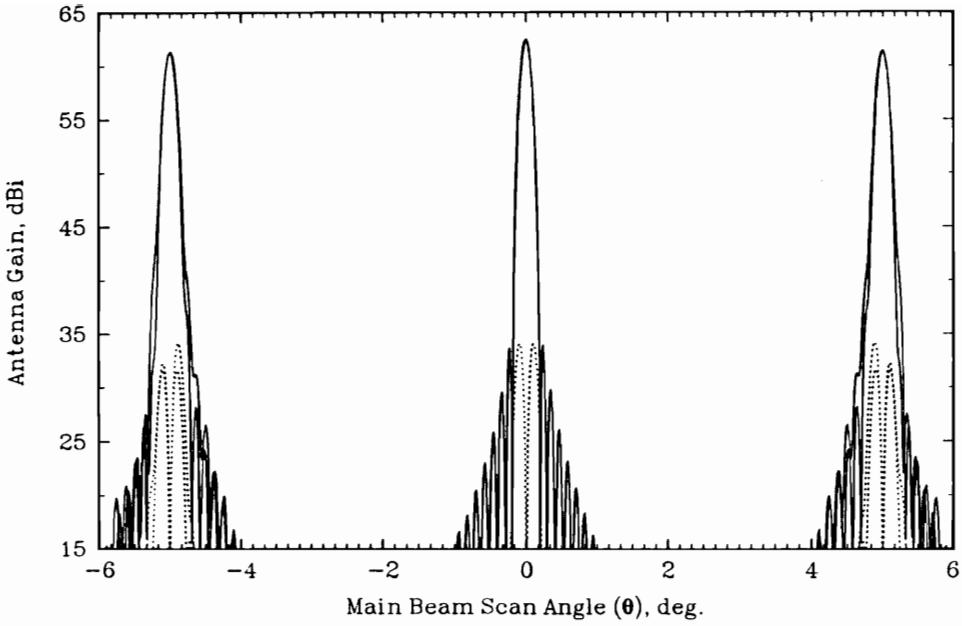

Figure 8.1-9. Principal plane patterns in the $\phi = 90^\circ$ plane calculated at 5.76 GHz for the Cassegrain II configuration shown in Fig. 7.3-27. Beam scanning is accomplished by tertiary reflector rotation about the point P_r shown in Fig. 7.3-27. Co-polarized E- and H-plane patterns-solid; cross-polarized E- and H-plane patterns-dashed.

8.1.2 Cassegrain II 7.68 GHz P.O. Results

Normalized contour plots of the co-polarized and cross-polarized radiation patterns calculated at 7.68 GHz are shown in Figs. 8.1-10 - 8.1-15. Principal plane patterns showing beam scanning in the $\phi = 0^\circ$ plane ($\phi = 0^\circ, \theta = \pm 2.5^\circ$), the $\phi = 45^\circ$ plane ($\phi = 45^\circ, \theta = \pm 3.1^\circ$) and the $\phi = 90^\circ$ plane ($\phi = 90^\circ, \theta = \pm 5.0^\circ$) are shown in Figs. 8.1-16 - 8.1-18. Gain, aperture efficiency ϵ_{ap} (see (3.1-4)), half-power beamwidth (HPBW) and relative cross-polarization level (XPOL) are tabulated on Table 8.1-2 for the scan directions considered. The scan range encompasses approximately 40 HPBW in the $\phi = 0^\circ$ plane and 78 HPBW in the $\phi = 90^\circ$ plane with a total gain variation of 1.37 dB. This is in good agreement with the 1 dB gain variation predicted by G.O. in Sec. 7.3.4.

Table 8.1-2
Cassegrain II Physical Optics Results
$f = 7.68$ GHz, $d/\lambda = 640$

ϕ (deg)	θ (deg)	Gain (dB)	ϵ_{ap} (%)	HPBW (deg)	XPOL (dB)
0	0.0	64.96	77	0.123	-28.35
0	2.5	63.67	58	0.128	-31.67
45	3.1	63.72	58	0.128	-30.21
90	5.0	63.59	57	0.129	-25.01
135	3.1	63.99	62	0.122	-24.88
180	2.5	63.96	62	0.123	-25.54

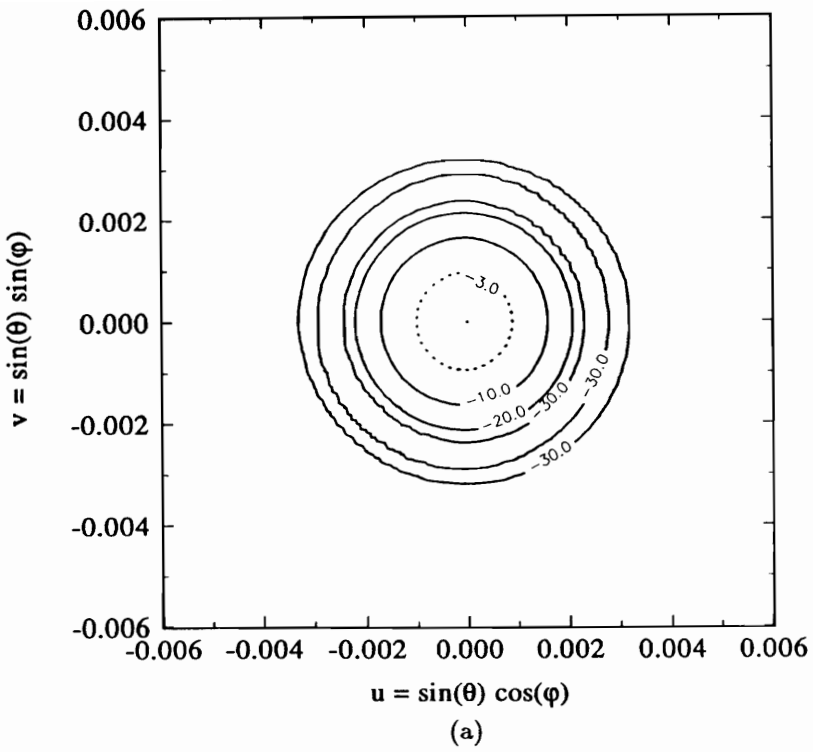

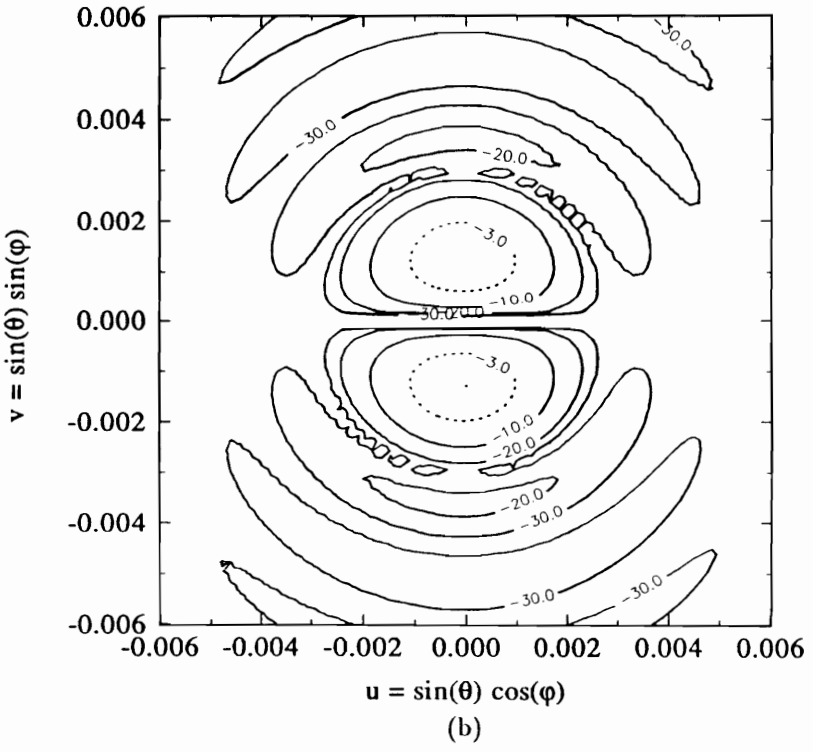

Figure 8.1-10. Normalized contour plots of co-polarized (a) and cross-polarized (b) radiation patterns in the $\theta = 0°$, $\phi = 0°$ scan direction calculated at 7.68 GHz for the Cassegrain II configuration with tertiary reflector rotation about point P_r as shown in Fig. 7.3-27.

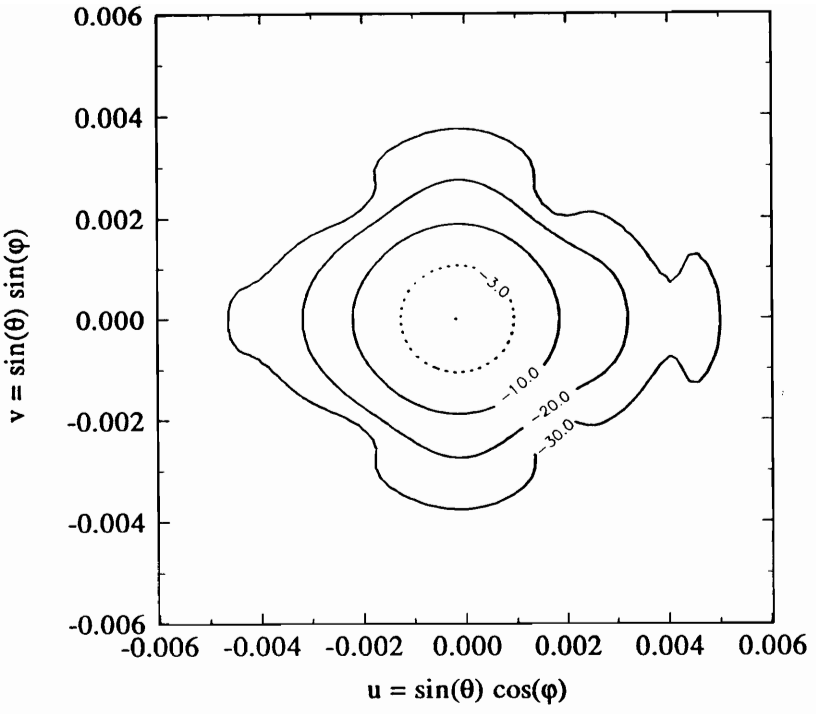

(a)

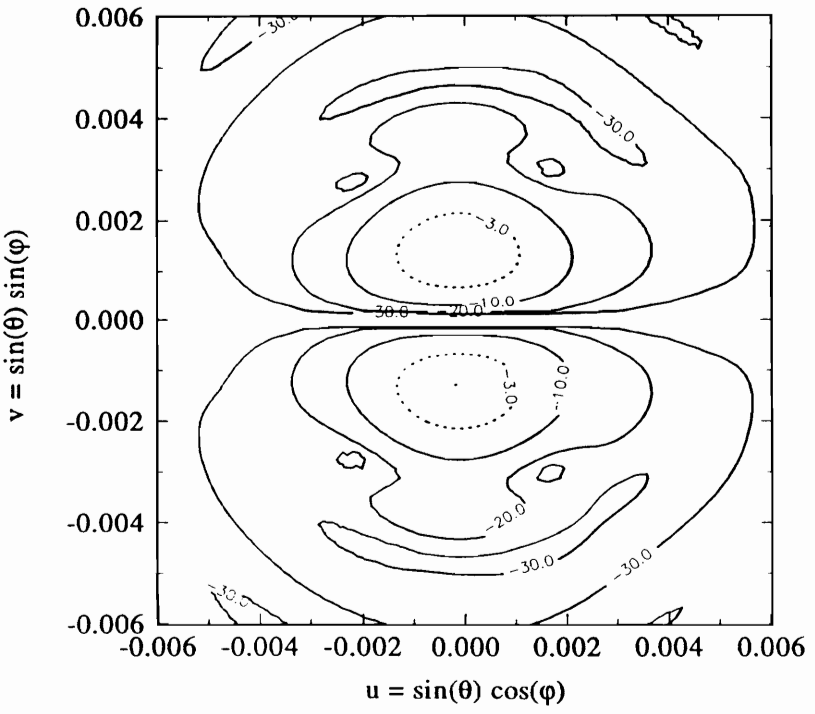

(b)

Figure 8.1-11. Normalized contour plots of co-polarized (a) and cross-polarized (b) radiation patterns in the $\theta = 2.5$, $\phi = 0^{\circ}$ scan direction calculated at 7.68 GHz for the Cassegrain II configuration with tertiary reflector rotation about point P_r as shown in Fig. 7.3-27.

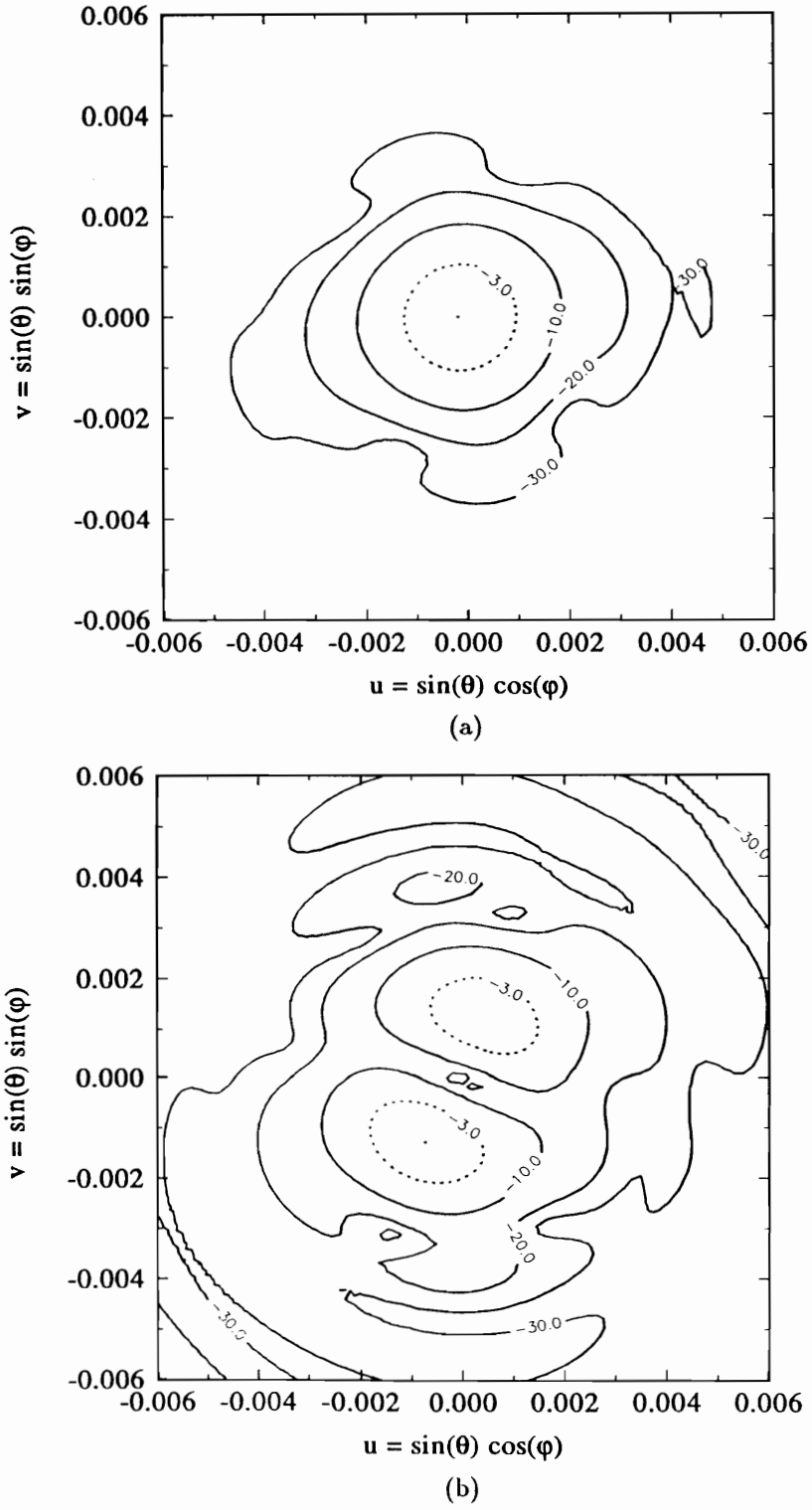

Figure 8.1-12. Normalized contour plots of co-polarized (a) and cross-polarized (b) radiation patterns in the $\theta = 3.1°$, $\phi = 45°$ scan direction calculated at 7.68 GHz for the Cassegrain II configuration with tertiary reflector rotation about point P_r as shown in Fig. 7.3-27.

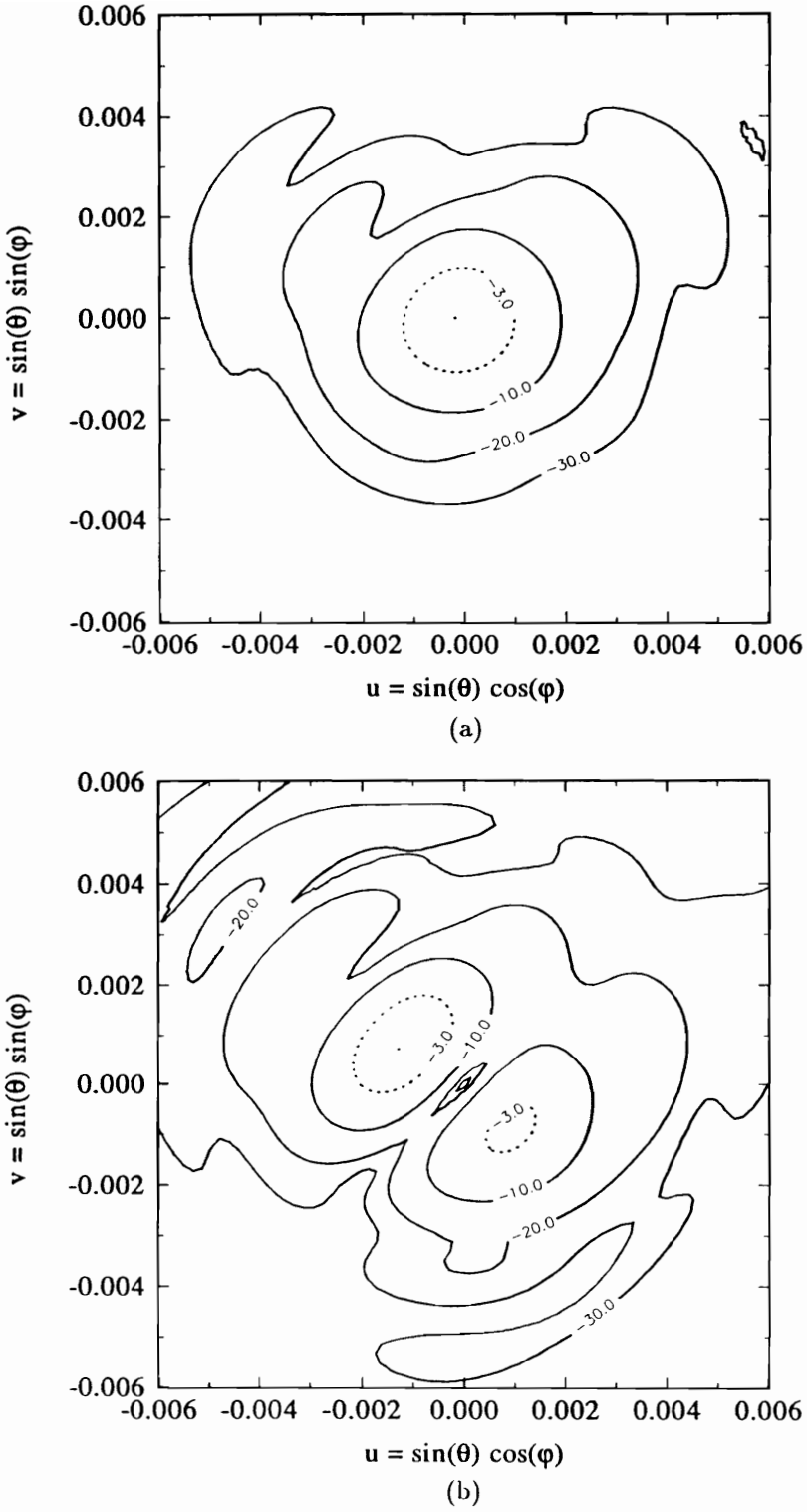

Figure 8.1-13. Normalized contour plots of co-polarized (a) and cross-polarized (b) radiation patterns in the $\theta = 5°$, $\phi = 90°$ scan direction calculated at 7.68 GHz for the Cassegrain II configuration with tertiary reflector rotation about point P_r as shown in Fig. 7.3-27.

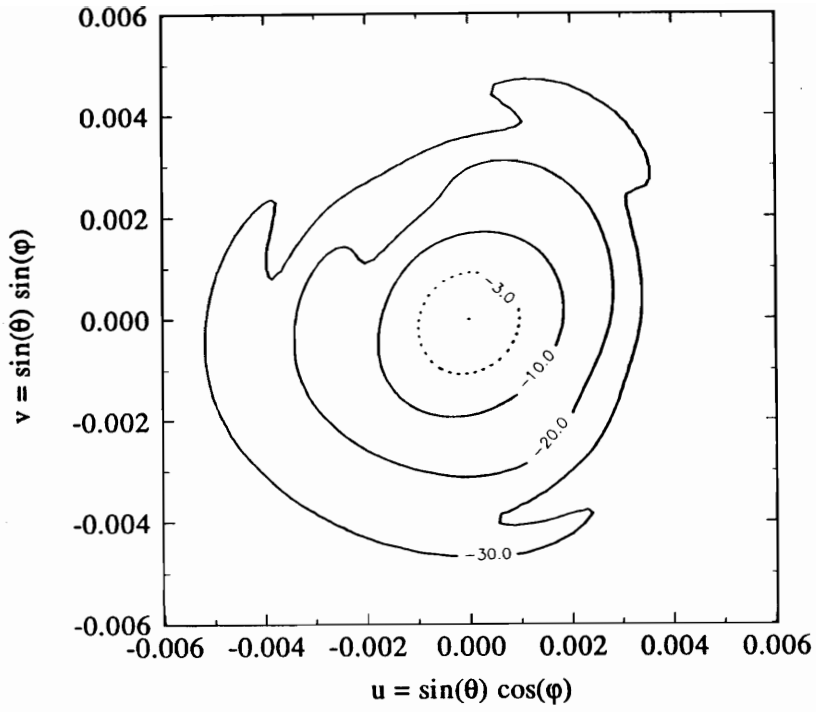

(a)

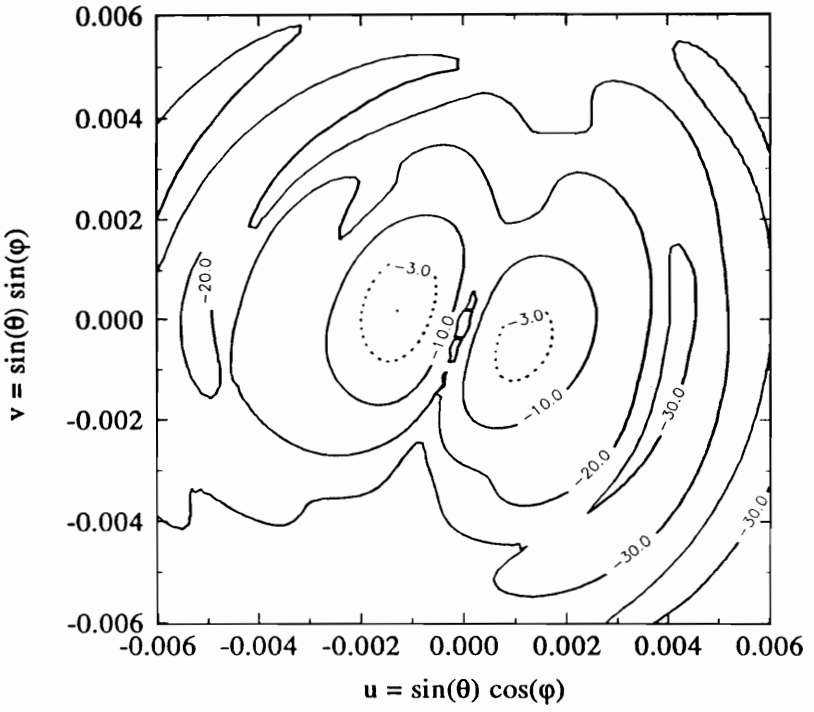

(b)

Figure 8.1-14. Normalized contour plots of co-polarized (a) and cross-polarized (b) radiation patterns in the $\theta = 3.1^{\circ}$, $\phi = 135^{\circ}$ scan direction calculated at 7.68 GHz for the Cassegrain II configuration with tertiary reflector rotation about point P_r as shown in Fig. 7.3-27.

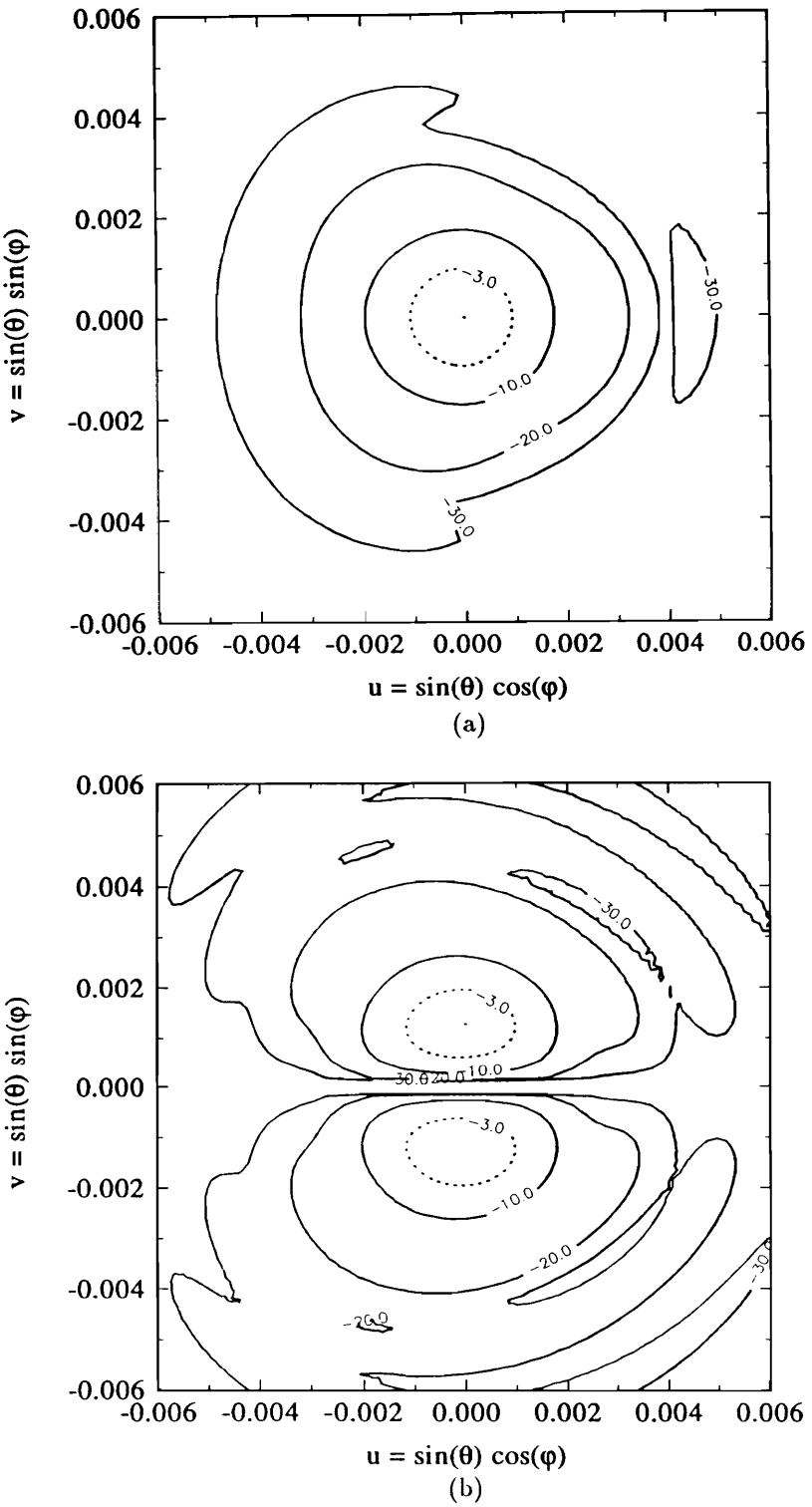

Figure 8.1-15. Normalized contour plots of co-polarized (a) and cross-polarized (b) radiation patterns in the $\theta = 2.5°$, $\phi = 180°$ scan direction calculated at 7.68 GHz for the Cassegrain II configuration with tertiary reflector rotation about point P_r as shown in Fig. 7.3-27.

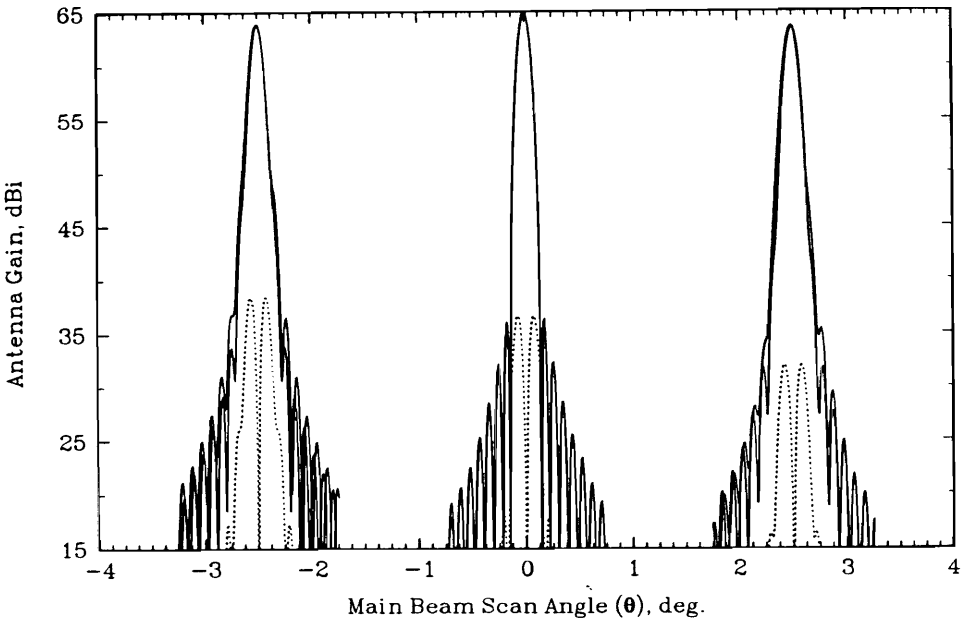

Figure 8.1-16. Principal plane patterns in the $\phi = 0°$ plane calculated at 7.68 GHz for the Cassegrain II configuration shown in Fig. 7.3-27. Beam scanning is accomplished by tertiary reflector rotation about the point P_r shown in Fig. 7.3-27. Co-polarized E- and H-plane patterns-solid; cross-polarized E- and H-plane patterns-dashed.

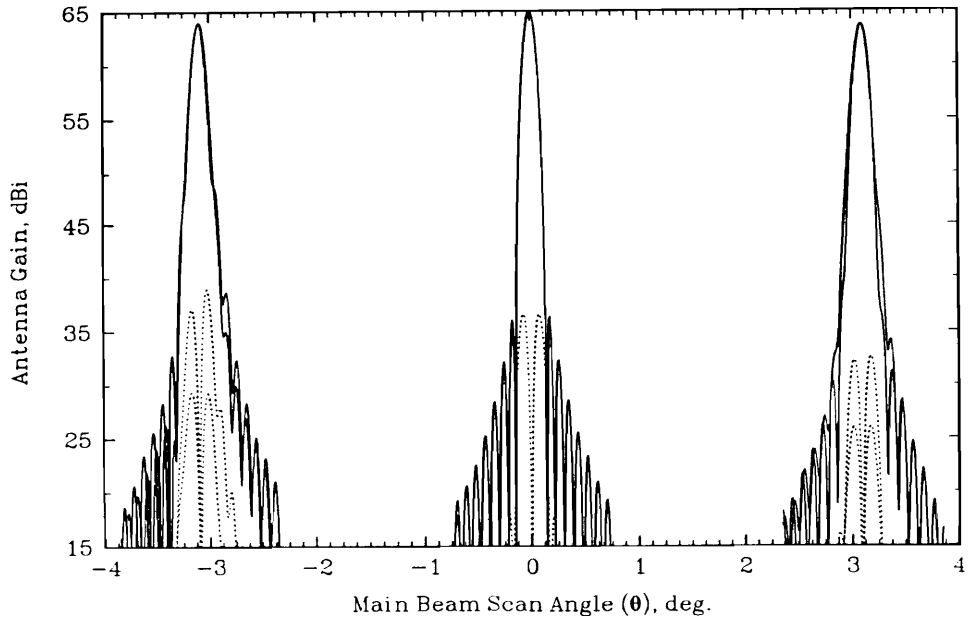

Figure 8.1-17. Principal plane patterns in the $\phi = 45°$ plane calculated at 7.68 GHz for the Cassegrain II configuration shown in Fig. 7.3-27. Beam scanning is accomplished by tertiary reflector rotation about the point P_r shown in Fig. 7.3-27. Co-polarized E- and H-plane patterns-solid; cross-polarized E- and H-plane patterns-dashed.

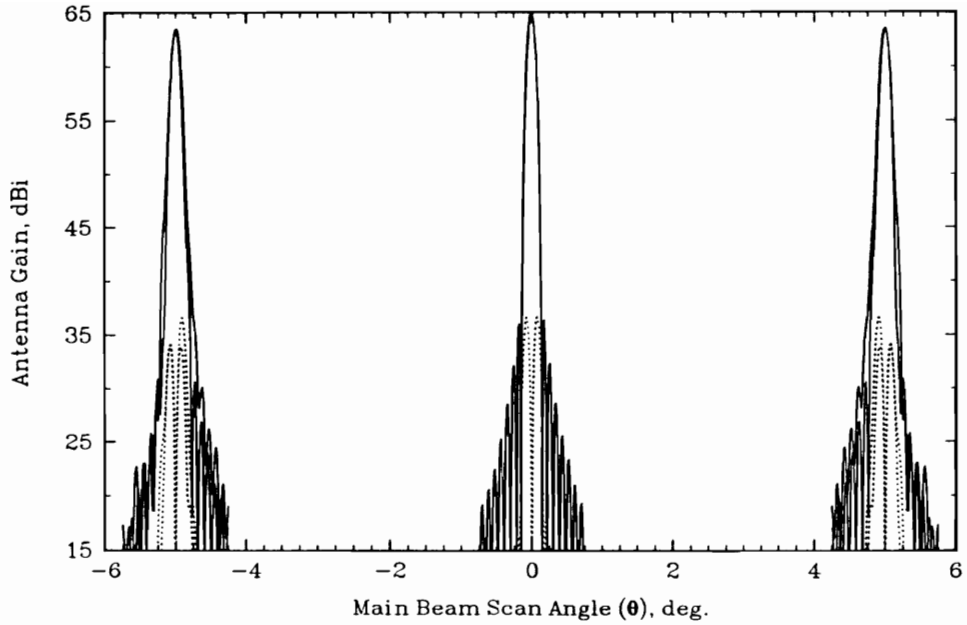

Figure 8.1-18. Principal plane patterns in the $\phi = 90^{\circ}$ plane calculated at 7.68 GHz for the Cassegrain II configuration shown in Fig. 7.3-27. Beam scanning is accomplished by tertiary reflector rotation about the point P_r shown in Fig. 7.3-27. Co-polarized E- and H-plane patterns-solid; cross-polarized E- and H-plane patterns-dashed.

8.2 P.O. Results for the Prime Focus Parabolic Reflector

The feed pattern used for the prime focus parabolic reflector was a Gaussian distribution with a -15 dB edge taper at the average half angle subtended by the reflector, θ'_{ave}. For this configuration $\theta'_{ave} = 15.22^\circ$ (see Sec. 7.4). The feed boresight direction was directed toward the center of the reflector and the feed pointing angle was kept constant as the feed was displaced to effect beam scanning. Feed polarization was parallel to the xz-plane shown in Fig. 7.4-1. Calculations were performed at 1.2 GHz, which corresponds to $d/\lambda = 100$. Radiation patterns were calculated for the following scan directions (see Fig. 6.2-2):

$$\begin{aligned} &\phi = 0.0^\circ, \quad \theta = 0.0^\circ \quad \text{(boresight direction)} \\ &\phi = 0.0^\circ, \quad \theta = 2.5^\circ \\ &\phi = 90.0^\circ, \quad \theta = 5.0^\circ \\ &\phi = 180.0^\circ, \quad \theta = 2.5^\circ \end{aligned} \tag{8.2-1}$$

Beam scanning in the diagonal planes given by $\phi = 45^\circ$ and $\phi = 135^\circ$ was not considered.

Principal plane patterns showing the calculated co-polarized and cross-polarized radiation patterns in the $\phi = 0^\circ$ plane ($\phi = 0^\circ, \theta = \pm 2.5^\circ$) and the $\phi = 90^\circ$ plane ($\phi = 90^\circ, \theta = \pm 5.0^\circ$) are shown in Figs. 8.1-1 and 8.1-2, respectively. Gain, aperture efficiency ϵ_{ap} (see (3.1-4)), half-power beamwidth (HPBW) and relative cross-polarization level (XPOL) are tabulated on Table 8.2-1 for the scan directions considered. The scan range encompasses approximately 6.3 HPBW in the xz-plane and 12.3 HPBW in the yz-plane with a total gain variation of 1.22 dB. This is in close agreement with the 1 dB gain variation predicted by G.O. in Sec. 7.4.

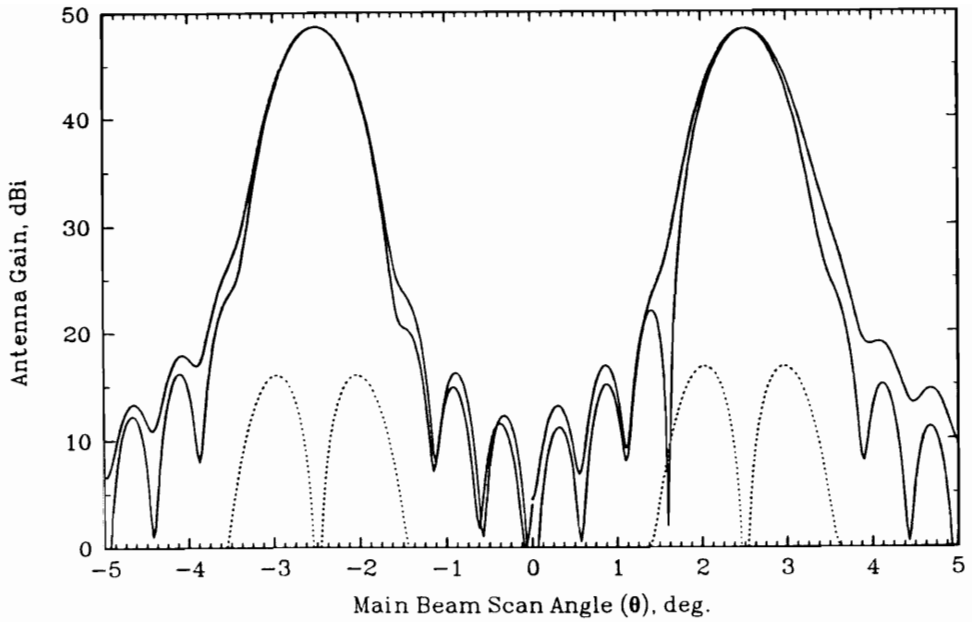

Figure 8.2-1. Principal plane patterns in the $\phi = 0^{\circ}$ plane calculated at 1.2 GHz for the Cassegrain II configuration shown in Fig. 7.3-27. Beam scanning is accomplished by tertiary reflector rotation about the point P_r shown in Fig. 7.3-27. Co-polarized E- and H-plane patterns-solid; cross-polarized E- and H-plane patterns-dashed.

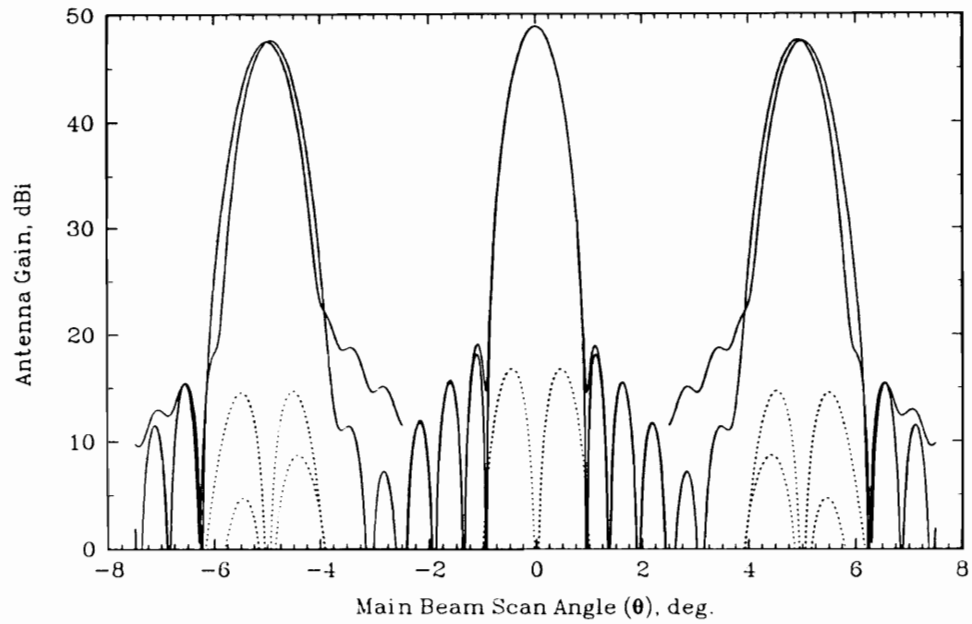

Figure 8.2-2. Principal plane patterns in the $\phi = 90^{\circ}$ plane calculated at 1.2 GHz for the Cassegrain II configuration shown in Fig. 7.3-27. Beam scanning is accomplished by tertiary reflector rotation about the point P_r shown in Fig. 7.3-27. Co-polarized E- and H-plane patterns-solid; cross-polarized E- and H-plane patterns-dashed.

Table 8.2-1

Prime Focus Parabolic Reflector Physical Optics Results

$f = 1.2$ GHz, $d/\lambda = 100$

ϕ (deg)	θ (deg)	Gain (dB)	ϵ_{ap} (%)	HPBW (deg)	XPOL (dB)
0	0.0	48.84	78	0.700	-32.06
0	2.5	48.38	70	0.793	-32.57
90	5.0	47.63	59	0.814	-32.74
180	2.5	48.68	75	0.807	-32.65

8.3 References

1. S. B. Sorensen and P. H. Nielson, "Manual for Grasp 7 Package," TICRA Document S-359-07, November 1988.

Chapter 9

Conclusions and Recommendations

The goal of this work was the design of a high gain reflector configuration capable of beam scanning and suitable for use on a geostationary platform. The following design constraints were established: elimination of feed motion; small feed array size; simple reflector motion; and high primary aperture utilization for all scan directions. The conjugate tri-reflector configuration was established as a candidate for meeting these constraints. Investigation of the conjugate tri-reflector configuration involved the development of effective geometrical optics synthesis and analysis techniques. The techniques used are presented in Chapter 6.

Three types of conjugate tri-reflector configurations were identified and compared in terms of both mechanical and electrical suitability. This comparison is performed in Chapter 7. The Cassegrain II configuration showed the most promising results. Specifically, the Cassegrain II configuration with tertiary reflector motion restricted to two degrees of rotational freedom about the optimum point P_r(shown in Fig. 7.3-27) represents a good compromise between tertiary reflector motion complexity and beam scan performance.

Physical optics analysis using GRASP7 was performed on the Cassegrain II configuration shown in Fig. 7.3-27 for several limiting scan directions over an elliptical scan range that subtends $\pm 2.5^\circ$ in the $\phi = 0^\circ$ plane (see Fig. 6.2-2) and $\pm 5.0^\circ$ in the $\phi = 90^\circ$ plane. The results of these calculations are presented in Chapter 8. The reflector configuration demonstrated the

capability of scanning 48 HPBW (half-power beamwidths) in the $\phi = 0^\circ$ plane and 78 HPBW in the $\phi = 90^\circ$ plane with a gain variation of only 1.37 dB. However, the configuration suffers from moderately high cross-polarization with relative cross-polarization in the range of -25 dB.

Future efforts should place emphasis on the Cassegrain II configuration. Specific areas of concentration should be:

- A detailed trade-off study between tertiary reflector motion complexity and scan performance.

- Efforts to reduce the dimensions of the tertiary reflector as compared to the dimensions of the primary and secondary reflectors.

- Efforts to increase scan performance using reflector surface optimization.

- Efforts to reduce cross-polarization.

- An investigation into the use of array feeds to improve scan performance.

Vita

Paul Werntz was born on December 22, 1962 in Washington D.C.. He graduated from Gonzaga High School in June 1981 and from Catholic University in May 1986 with a Bachelor of Science in Electrical Engineering. In September 1986 he became a student at Virginia Tech where he held a graduate teaching assistantship and in September 1988 earned a Master of Science in Electrical Engineering. From 1988 to 1989 he worked as a graduate research assistant investigating rough surface scattering and spent the summer of 1989 at the Naval Research Laboratory in Washington D.C.. He joined the Virginia Tech Satellite Communications Group in September 1989 and worked as a graduate project assistant investigating high gain beam scanning reflector configurations for the NASA Mission to Planet Earth Project. Between October 1992 and February 1993 he was a visiting scientist at the Technischen Universität Braunschweig in Germany.